



University
of Glasgow

Aghamoradi, Fatemeh (2012) *The development of high quality passive components for sub-millimetre wave applications*. PhD thesis.

<http://theses.gla.ac.uk/3214/>

Copyright and moral rights for this thesis are retained by the Author

A copy can be downloaded for personal non-commercial research or study, without prior permission or charge

This thesis cannot be reproduced or quoted extensively from without first obtaining permission in writing from the Author

The content must not be changed in any way or sold commercially in any format or medium without the formal permission of the Author

When referring to this work, full bibliographic details including the author, title, awarding institution and date of the thesis must be given

THE DEVELOPMENT OF HIGH QUALITY PASSIVE
COMPONENTS FOR SUB-MILLIMETRE WAVE APPLICATIONS

A THESIS SUBMITTED TO
THE DEPARTMENT OF ELECTRONICS AND ELECTRICAL ENGINEERING
SCHOOL OF ENGINEERING
UNIVERSITY OF GLASGOW
IN FULFILMENT OF THE REQUIREMENTS
FOR THE DEGREE OF
DOCTOR OF PHILOSOPHY

By
Fateme Aghamoradi
November 2011

© Fateme Aghamoradi 2011
All Rights Reserved

Abstract

Advances in transistors with cut-off frequencies $>400\text{GHz}$ have fuelled interest in security, imaging and telecommunications applications operating well above 100GHz . However, further development of passive networks has become vital in developing such systems, as traditional coplanar waveguide (CPW) transmission lines, the most fundamental passive component, exhibit high losses in the millimetre and sub-millimetre wave regime.

This work investigates novel, practical, low loss, transmission lines for frequencies above 100GHz and high-Q passive components composed of these lines. At these frequencies, transmission line losses are primarily due to the influence of the waveguide substrate. We therefore focus on structures which elevate transmission line traces above the substrate using air-bridge technology. Thorough analysis is performed on a range of elevated structures, and analytic / semi-analytic formulae for component figures of merit obtained. These, along with comprehensive 2 and 3D simulations are used to design discrete lines and distributed passive networks, with a focus on the $140\text{-}320\text{GHz}$ frequency range. Innovative fabrication and detailed characterisation of the components are also carried out.

The key result is the development of a novel MMIC compatible transmission line structure, Elevated-Grounded CPW, with a relatively simple fabrication process. EGCPW provides high substrate isolation, resulting in a low losses and high-quality passive networks. 50Ω EGCPW transmission line shows an insertion loss of 2.5dB/mm at 320GHz , 2.5dB/mm less than CPW. EGCPW passive networks, including resonators and filters, show higher performance than both conventional CPW and other forms of elevated CPW. 30-80% improvements in quality factor are shown, and an EGCPW band-pass filter with the centre frequency of 220GHz shows a 12% reduction in bandwidth and 4.5dB reduced in-band loss compared with its CPW counterpart.

Due to the superior performance of MMIC-compatible EGCPW, as well as its ability to support a wide range of characteristic impedances, this structure is suggested as a candidate for widespread use in sub-millimetre wave circuits in order to increase efficiency and reduce losses.

Acknowledgements

I would like to dedicate this thesis to my parents for their unwavering support and understanding throughout my studies.

I would also like to take this opportunity to express my thanks to the many people who supported me during the completion of this project.

My genuine thanks to Scott Roy for his supervision, support and constructive feedback throughout the writing of this thesis. Without Scott's support I would not have been able to complete this project. I would also like to thank Iain Thayne for the support he provided to me as my second supervisor.

My special thanks to Ian McGregor. I am greatly indebted to Ian for the knowledge of millimeter-wave design and measurement that he imparted to me and also for his expert advice throughout the project. Thanks also to Lai Bun Lok for familiarizing me with high frequency measurement set-up and calibration and HFSS simulation.

The entire academic and technical staff in the department of Electrical and Electronic Engineering and James Watt Nanofabrication Centre (JWNC) deserve thanks for the knowledge and skills they successfully passed onto me. Special thanks to Helen McLelland and Susan Ferguson for their help and support during the fabrication of airbridge devices.

Heart full thanks to my family and friends who have supported me through my studies. Undertaking this work has been made possible with the constant love, support and encouragement of Martin whose unweaving belief and patience have enabled me to stay sane.

Finally, to all my friends and colleagues who are too many to name, but who have made such a huge difference, Thanks to you all!

Contents

1	Introduction	1
1.1	Motivation for use of millimetre and sub-millimetre waves	1
1.2	Aims and Objectives	3
1.3	Thesis Organisation	4
1.4	Sub-millimetre wave passive networks : research review	7
2	Theoretical and Experimental Study of Coplanar Waveguide	18
2.1	Introduction to CPW transmission line	18
2.2	CPW Analysis	21
2.2.1	Conformal mapping technique	22
2.2.2	CPW with finite substrate and finite ground planes without backside metallization	25
2.2.3	CPW with finite substrate and backside metallisation	31
2.3	Losses in CPW	35
2.3.1	Conductor loss	35
2.3.2	Dielectric loss:	40
2.3.3	Radiation loss	41
2.4	Modelling and measurement of CPW transmission lines	47
2.4.1	Measurement	47
2.4.3	CPW transmission line on GaAs substrate without backside metallisation	48
2.4.4	CPW transmission line on GaAs substrate with backside metallization	56
2.5	CPW Resonators	67
2.5.1	Quarter-wavelength CPW open-circuited stub	68

2.5.2	Quarter-wavelength CPW short-circuited stub	76
2.6	CPW quarter-wave resonator filters	83
2.6.1	Quarter-wavelength CPW band-pass Filter	84
2.6.2	Quarter-Wavelength Band-stop Filter	89
2.7	Summary	98
3	Fabrication of Elevated Structures	100
3-1	Introduction	100
3-2	Overview of the process flow	100
3-3	Sample preparation	102
3-4	Markers and Bondpad definition	103
3-4-1	Resist coating and development	106
3-4-2	Electron-Beam Lithography	109
3-4-3	Metallisation and lift-off	110
3-5	Definition of elevated structures	111
3-5-1	Photolithography	113
3-5-2	Photoresist and development	115
3-5-3	Metallisation	117
3-6	Summary	122
4	All-elevated Coplanar Waveguide	123
4-1	Introduction to Elevated CPW structures	123
4-2	All-elevated CPW (ECPW) Analysis	129
4-2-1	The structure of all-elevated CPW	130
4-2-2	Analysis in terms of capacitances for finite substrate height and finite conductor thickness	131
4-2-3	Comparison between the empirical approach and previously reported series capacitance approach	139
4-2-4	Comparison between theory, simulation and measurement for elevated CPW	141
4-2-5	Analysis of frequency dependent effects arising from CPW feed/post section/elevated section discontinuities	146

4-2-6	Losses in all-elevated CPW	150
4.3	Modeling and measurement of all-elevated CPW transmission line	157
4-3-1	all-elevated and conventional CPW transmission lines	158
4-3-2	Effect Of CPW/ Elevated CPW Transition Feeds	162
4-3-3	Effect of the size and distance between supporting posts:	164
4-3-4	Effect of elevation height	167
4.4	All-elevated CPW (ECPW) resonators	171
4.4.1	Quarter-wavelength ECPW Short-circuited stub	171
4.4.2	Quarter-wavelength ECPW open-circuited stub	181
4.5	All-elevated CPW quarter-wavelength resonator filter	187
4.5.1	Quarter-wavelength ECPW Band-pass filter	188
4.4.2	Quarter-wavelength ECPW Band-Stop filter	195
4.5	Summary	201
5	Study of Signal-Elevated Coplanar Waveguide Structures	205
5-1	Signal-elevated CPW (SECPW) transmission line	205
5-1-1	SECPW Analysis	206
5-1-2	Losses in signal-elevated CPW	209
5-1-3	Signal-elevated, all-elevated and conventional CPW transmission lines	216
5-1-4	Effect of size and distance of supporting posts	219
5-1-5	Effect of elevation height	221
5-2	Signal-elevated CPW (SECPW) resonators	226
5-2-1	Quarter-wavelength SECPW short-circuited stub	226
5-2-2	Quarter-wavelength SECPW open-circuited stub	236
5-3	Summary	243
6	Elevated-Grounded Coplanar Waveguide Structures	246
6-1	Introduction to Elevated-grounded CPW structure	246
6-2	Elevated grounded CPW (EGCPW) Analysis	248
6-2-1	The structure of elevated grounded CPW	248

6-2-2	Synthesis of thick elevated grounded CPW resting on dielectric substrate	250
6-2-3	Analysis of thick elevated grounded CPW resting on dielectric substrate with the gap in bottom ground	257
6-2-4	Analysis of post section	259
6-2-5	Quasi-static characteristics of composite line	260
6-2-6	Losses in elevated-grounded CPW lines	261
6-3	Modelling and measurement of elevated-grounded CPW transmission line	268
6-3-1	Transition to Coplanar waveguide	273
6-4	Elevated-grounded CPW (EGCPW) Resonators	276
6-4-1	Quarter-wavelength EGCPW Short-circuited stub	276
6-4-2	Quarter-wavelength EGCPW open-circuited stub	282
6-5	Elevated-grounded CPW quarter-wavelength resonator filter	286
6-5-1	Quarter-wavelength ECPW Band-pass filter	286
6-5-2	Quarter-wavelength EGCPW Band-stop filter	289
6-7	Summary	292
7	Conclusions and Future Work	295
7-1	Conclusions	295
7-1-1	Coplanar Waveguides	295
7-1-2	Elevated Waveguides	297
7-1-3	Elevated Passives	298
7-1-4	Elevated-Grounded Waveguides	300
7-1-5	Elevated-Grounded Passives	301
7.2	Future work	303
	References	305

List of Tables

3.1	Experimental thickness achieved for PMMA resists used in this work	108
4.1	Comparison between simulated, calculated and measured characteristic impedance of ECPW line for various geometries.	143
5.1	Table showing the extracted effective permittivities for various signal and all-elevated open circuit resonators. The CPW ground width is 100 μ m.	242
6.1	Comparison between calculated and simulated characteristic impedance for various geometries	253

List of Figures

1.1	WR-10 silicon micromachined waveguide. a) The waveguide is split into half sections b) One half section of waveguide [55].....	18
1.2	(a), (b) Membrane microshield transmission lines. c) Dielectric micromashield line. d) Conventional coplanar waveguide [56]	19
1.3	Different transmission line structures considered in this work: a) Conventional CPW, b) All-elevated CPW, c) Signal-elevated CPW and d) Ground-elevated CPW w-plane [16]	22
2.1	Structure of the Coplanar Waveguide transmission line with finite substrate thickness and (a) infinite and (b) finite ground widths.	18
2.2	Coplanar mode(a) and Coupled Slotline mode(b) field configurations	19
2.3	Mapping between a circle in z-plane and a line segment in w-plane [16]	22
2.4	The Schwartz-Christoffel transformation [111]	23
2.5	Cross section of CPW on finite substrate with finite ground planes	25
2.6	Conformal mapping for upper half plane (air layer) of CPW with finite substrate and finite ground widths	27
2.7	Conformal mapping for lower half plane (dielectric layer) of CPW with finite substrate and finite ground widths.	28
2.8	(a) Characteristic impedance and (b) Effective permittivity of a CPW with finite substrate thickness and finite ground widths	30
2.9	Cross Section of Conductor-backed CPW with finite substrate thickness.....	31

2.10	Conformal mapping of conductor-backed CPW with finite substrate to calculate free space capacitance.....	32
2.11	Conformal mapping of conductor-backed CPW with finite substrate to calculate the dielectric capacitance	33
2.12	(a) Characteristic impedance and (b) Effective permittivity of a conductor-backed CPW with finite substrate thickness	34
2.13	Plot of simulated and calculated conductor loss of CPW lines with three different lateral dimensions (2b) of 30, 60 and 120 μ m for various shape ratios (signal width/lateral dimensions).....	37
2.14	Plot of simulated conductor loss of CPW lines for various lateral dimensions(2b) each simulated by once keeping the signal width constant at 10 μ m and varying the gap size (b-a) and once varying the signal width (2a) when the gap size is constant, 5 μ m.....	39
2.15	Plot of simulated and calculated substrate loss of CPW lines with three different lateral dimensions (2b) of 30, 60 and 120 μ m for various shape ratios.....	41
2.16	(a) 2-D and 3-D Simulation plots of total attenuation and (b) 3-D simulation and calculation results of a radiation loss of a CPW line with lateral dimension (2b) of 120 μ m.....	44
2.17	(a) 2-D and 3-D Simulation plots of total attenuation and (b) 3-D simulation and calculation results of a radiation loss of a CPW line with lateral dimension of 30 μ m.....	45
2.18	Micrograph of a 50 Ω CPW transmission line. The design dimensions are: W=35, S=25 and W _g =100. All the dimensions are in micron.	49
2.19	Measured and simulated S-parameters for a 50 Ω CPW transmission line insertion loss.	49

2.20	Measured and simulated S-parameters for a 50Ω CPW transmission line return loss.	50
2.21	Measured and Simulated attenuation for 50Ω CPW transmission line.	51
2.22	Measured and Simulated loss factor for 50Ω CPW transmission line.	52
2.23	Profile of electric-field distribution modeled for CPW transmission line with finite grounds on a thick substrate and without backside metallisation at 50, 150 and 320GHz.	53
2.24	3-D simulation and calculation results of a radiation loss for 50Ω CPW transmission line.	54
2.25	Simulated Insertion loss of the CPW with characteristic impedances of 50Ω, 20Ω and 94Ω.	56
2.26	Measured Insertion loss for 50Ω CPW line on a 50μm thin substrate.	57
2.27	Measured Return loss for 50Ω CPW line on a 50μm thin substrate.	57
2.28	Profile of electric-field distribution modeled at 280-GHz for finite-ground conductor-backed CPW on (a) 600μm substrate, (b) 50μm substrate.	58
2.29	Modeled transmission response of CBCPW (without vias) on 50μm substrate with different widths of finite-ground.	60
2.30	(a) The layout and (b) Cross sectional view of the conductor-backed CPW transmission line with via holes connecting the top and bottom grounds.	61
2.31	Modeled transmission response of finite-ground CBCPW on 50μm substrate with different via hole separation pattern.	62
2.32	Profile of electric-field distribution modeled at 280-GHz for finite-ground conductor-backed CPW on (a) 50μm substrate without via holes, and (b) 50μm substrate with via holes.	63

2.33	Modeled transmission response of finite-ground CBCPW with vias on 50 μm and 100 μm thickness substrate.....	64
2.35	Measured transmission response of finite-ground CBCPW: <i>with</i> via holes (via spacing: X=150 μm and Y=70 μm) and <i>without</i> via holes.....	65
2.34	Top view optical picture of fabricated finite-ground CBCPW test structure with via holes separated by X=150 μm and Y=70 μm	65
2.36	Comparison of transmission response for finite-ground CBCPW without via holes.	66
2.37	Transmission response of finite-ground CBCPW with grounding via holes. Via hole center-to-center separation X=150 μm and Y=70 μm	66
2.38	A lumped-element equivalent circuit of an open-ended transmission line used as a resonator. $l = (2n - 1)\lambda/4$	68
2.39	Simulated S-parameters for a quarter-wave length open- circuited stub with a fixed feed impedance of 50 Ω and various impedances at the stub.....	71
2.40	Structure of an open-circuited matching stub implemented by CPW transmission line.	72
2.41	Micrograph of the CPW open-circuited Stub.....	73
2.42	Measured and simulated S-parameters for a CPW open-end shunt stub.....	74
2.43	Simulated S-parameters for open-end shunt stub with various feed and stub impedances.....	76
2.44	The lumped-element equivalent circuit of a short-ended transmission line used as a resonator. $l = (2n - 1)\lambda/4$	77
2.45	Simulated S-parameters for a quarter-wave length short-circuited stub with a fixed feed impedance of 50 Ω and various impedances at the stub.....	78

2.46	Structure of a short-circuited matching stub implemented by CPW transmission line.....	79
2.47	Micrograph of the CPW short-circuited shunt stub.....	80
2.48	Measured and simulated S-parameters for a CPW short-end shunt stub at G-band (140-220GHz).....	80
2.49	Measured and simulated S-parameters for a CPW open-end shunt stub at H-band (220-320GHz).....	81
2.50	The substrate electric field plot of a short-circuited CPW shunt stub at the centre frequency of 220GHz.....	82
2.51	Modelled S-parameter response of a short-circuited shunt stub with various impedances at feed and stub sections.	83
2.52	Micrograph of a 3-rd order quarter-wavelength CPW band-pass filter.....	86
2.53	Measured and simulated S-parameters for a CPW band-pass filter.....	86
2.54	The substrate electric field plot of a CPW band-pass filter at the centre frequency of 220GHz.....	87
2.55	Simulated CPW band-pass filter implemented by double short-circuited stubs (BPF1) and Single short-circuited stubs (BPF2)	88
2.56	Simulated results for 3rd-order quarter-wavelength bandpass filter with a) same 50Ω impedance for all sections (BPF1), and b) various impedances for different sections, 50Ω feed lines, 45Ω stubs and 55Ω connection lines (BPF2).....	89
2.57	Micrograph of a 3-rd order quarter-wavelength CPW band-stop filter.....	91
2.58	Measured and simulated S-parameters for a CPW bandstop filter.....	91
2.59	The substrate electric field plot of a CPW band-stop filter at (a)the centre frequency of 220GHz and (b)above stop-band frequency of 420GHz.....	92

2.60	Simulated results for 3rd-order quarter-wavelength bandstop filter with a) same 50Ω impedance for all sections (BSF1), and b) various impedances for different sections, 50Ω feed lines, 55Ω stubs and 45Ω connection lines (BSF2).....	93
2.61	Simulated results for 3rd-order quarter-wavelength bandstop filter with a) same 50Ω impedance for all sections (BSF1), and b) various impedances for different sections, 50Ω feed and connection lines and 94Ω stubs (BSF2).....	94
2.62	Simulated CPW band-stop filter implemented by double short-circuited stubs (BSF1) and Single short-circuited stubs (BSF2)	95
2.63	Simulated results for bandstop filter using single open stubs with a) same 50Ω impedance for all sections (BSF1), and b) various impedances for different sections, 50Ω feed and connection lines and 94Ω stubs (BSF2).....	95
2.64	Simulated results for 3rd-order quarter-wavelength bandstop filter with two parallel open stubs at each junction (BSF1), and b) a parallel short and open stubs at each junction (BSF2)	96
2.65	Simulated results for 3rd-order quarter-wavelength bandstop filter with single open stubs at each junction (BSF1), and b) a parallel short and open stubs at each junction (BSF2).....	97
2.66	Simulated results for band-stop filter using short and open stubs with a) same 50Ω impedance for all sections (BSF1), and b) various impedances for different sections, 50Ω feed lines, 45Ω short circuit stubs and 55Ω open circuit stubs (BSF2).....	97
3.1	General process flow of the fabrication steps required to form elevated passive structures.....	101
3.2	Fabrication steps (1-4) of markers and bondpad layers.....	104
3.3	Layout of alignment markers.....	105

3.4	Optical and SEM pictures of the structure with probe positioning marks.....	106
3.5	Schematic of metal lift-off with undercut resist profile	107
3.6	Fabrication steps (1-6) of airbridge process	112
3.7	Developed holes with minimum size of $10 \times 10 \mu\text{m}$ on 13μ thick resist to form supporting posts in elevated structures	116
3.8	Continued fabrication steps of Fig.3.6, (6-9) when the supporting posts need to be filled.	119
3.9	Fabricated elevated structures at: a and b) post section, c and d) cross-section, e and f) angled view.....	121
4.1	Profile of electric-field distribution modeled for (a) CPW line directly on the substrate and (b) CPW line $5 \mu\text{m}$ elevated above the substrate.....	124
4.2	Elevated CPW structure with (a) all traces elevated (b) signal trace elevated, and (c) ground traces elevated.	125
4.3	Measured S-parameters of elevated CPW with 3 different configurations: all-elevated CPW, signal-elevated CPW and ground-elevated CPW	127
4.4	Measured loss-factor of all-elevated, signal-elevated and ground-elevated CPW structures.....	128
4.5	Cross section of an elevated CPW line.....	130
4.6	Angled 3-D conceptual view of a section of an all-elevated CPW line resting on posts.	131
4.7	One half of all-elevated CPW cross section with various discrete capacitances [137].....	133
4.8	Calculated characteristic impedance of all-elevated CPW from (4.12) for varying $2a$, $b=2a+20$, $c=b+100$, $h=2,8$ and 14 . All dimensions are in micron.	136

4.9	Calculated effective permittivity of all-elevated CPW from (4.11) for varying $2a$, $b=2a+20$, $c=b+100$, $h=2,8$ and 14 . All dimensions are in micron.	138
4.10	Characteristic impedance obtained for ECPW line by simulation, calculation from empirical approach (4.12) and calculation from [135]	140
4.11	Comparison between modeled and calculated characteristic impedances for $2a=40\mu\text{m}$, $b=40+(15, 40 \text{ and } 65)\mu\text{m}$, $c=b+100$ and varying air gap thickness, h_2 . conductor thickness, t , is $2\mu\text{m}$ and substrate is GaAs with $600\mu\text{m}$ thickness. ...	142
4.12	Equivalent circuit model of the transmission line [29]	144
4.13	Diagram of CPW/ECPW transition feeds	146
4.14	Comparison between measured and calculated effective characteristic impedance for the structure with CPW/thick CPW/elevated-CPW sections.....	148
4.16	Plot of simulated (a) conductor loss and (b) substrate loss of ECPW lines for various lateral dimensions($2b$) and three elevation height of $5,10$ and $15\mu\text{m}$	153
4.17	2-D and 3-D Simulation plots of total attenuation of a $5\mu\text{m}$ -elevated ECPW line with lateral dimension of (a) $120\mu\text{m}$ and (b) $30\mu\text{m}$	155
4.18	Micrograph of an all-elevated CPW transmission line at (a) and (b) top view, (c) angled view.	158
4.19	Comparison between measured Insertion loss of 60Ω all-elevated and conventional CPW lines. CPW1 has a dimension of: $(50-35-50)\mu\text{m}$ and CPW2 has a dimension of $(25-17-25)$	159
4.20	(a) Measured and simulated S-parameters for ECPW transmission line, and (b) Comparison between measured insertion loss of 60Ω ECPW and CPW transmission lines at G-band ($140-220\text{GHz}$) and H-band ($220-320\text{GHz}$).	161

4.21	Micrograph of two different structures for ECPW probing by (a) using CPW/ECPW transition feeds and (b) using two close supporting posts to facilitate probing on top of elevated lines.....	162
4.22	Measured insertion loss of ECPW transmission lines with and without CPW/ECPW tapers at G-band (140-220GHz).....	163
4.23	Measured insertion loss of ECPW transmission lines with and without CPW/ECPW tapers up to 320GHz.	164
4.24	Comparison between measured insertion loss of all-elevated CPW transmission lines with different size and distance of supporting posts at G-band(140-220 GHz).....	165
4.25	Comparison between measured insertion loss of two ECPW transmission lines with different supporting post distances up to 320GHz.	166
4.26	Measured loss factor of two ECPW transmission lines with different supporting post distances up to 320GHz.	166
4.28	Comparison between the measured loss factor of 13 μ m elevated ECPW transmission lines with different supporting post distances.	169
4.29	Profile of electric-field distribution modeled for ECPW line with (a) 5 μ elevation, (b) 10 μ m elevation and (c) 70 μ m elevation.....	170
4.30	Micrograph of a short-circuited ECPW stub at (a) angled and (b) top view.....	172
4.31	Measured and simulated S-parameters for ECPW short-end shunt stub with 6 μ m elevation with resonance frequency at (a)160GHz and (b)240GHz.....	174
4.32	Comparison between measured S-parameters for 6 μ m elevated ECPW and conventional CPW short-end shunt stubs at (a) G-band (140-220GHz) and (b) H-band (220-320GHz).	175

4.33	The substrate electric field plot of a short-circuited shunt stub with (a) ECPW and (b) CPW structures at the centre frequency of 170 and 165GHz, respectively.	176
4.34	Comparison between simulated S-parameters for short-circuited stub designed with all similar impedance lines(50Ω) and the stub designed with various impedance lines (high impedance at feeds and low impedance at stub section).	178
4.35	Comparison between measured S-parameters of ECPW short-end stubs with 6μm and 13μm elevations.	179
4.36	Comparison between measured S-parameters of 6μm elevated CPW short-end stubs with different number of supporting posts.	180
4.37	Comparison between measured S-parameters of ECPW short-end shunt stubs with 6μm and 13μm elevation heights.	181
4.38	Micrograph of a open-circuited ECPW shunt stub	182
4.39	Measured and simulated S-parameters for ECPW open-end shunt stub with 6μm elevation.	182
4.40	Comparison between measured S-parameters for 6μm-elevated ECPW and conventional CPW open-end shunt stubs at (a) G-band (140-220GHz) and (b) H-band (220-320GHz).	184
4.41	Comparison between simulated S-parameters for ECPW open-circuited stub with all 50Ω lines, various impedance lines and CPW with various impedance lines (low impedance feeds and high impedance stubs).	185
4.42	Comparison between measured S-parameters of double and single open-end ECPW shunt stubs	186
4.43	Comparison between measured S-parameters of open-end ECPW shunt stubs with 6μm and 13μm elevation heights	187
4.44	Micrograph of the 3rd order quarter-wavelength band-pass ECPW Filter	188

4.45	Measured and simulated S-parameters for a 3rd order ECPW band-pass filter with elevation height of $6\mu\text{m}$	189
4.46	Comparison between measured S-parameters for $6\mu\text{m}$ -elevated ECPW and conventional CPW bandpass filters with centre frequency of 240GHz	190
4.47	Top view of electric-field distribution in the substrate modeled for (a) CPW and (b) ECPW band-pass filters at the centre frequency.....	191
4.48	Comparison between simulated S-parameters for ECPW and CPW band-pass filters designed with identical high impedance connecting lines and low impedance stubs.....	192
4.49	Measured and simulated S-parameters for a 3rd order ECPW band-pass filter with elevation height of $13\mu\text{m}$	193
4.50	Comparison between measured S-parameters of 3rd-order bandpass ECPW filters with $6\mu\text{m}$ and $13\mu\text{m}$ elevation heights	193
4.51	Comparison between measured S-parameters of a $13\mu\text{m}$ -elevated ECPW and conventional CPW bandpass filters.....	195
4.52	Micrograph the 3rd order quarter-wavelength ECPW band-stop Filter.....	196
4.53	Measured and simulated S-parameters for a 3rd order ECPW band-stop filter with elevation height of $6\mu\text{m}$	196
4.54	Comparison between measured S-parameters of $6\mu\text{m}$ -elevated ECPW and conventional CPW band-stop filters.....	197
4.55	Comparison between simulated S-parameters for band-stop filter with high impedance connecting lines and low impedance stubs (BSF1) and filter with low impedance connecting lines and high impedance stubs (BSF2).....	198
4.56	Comparison between simulated S-parameters for band-stop filter using double open stubs (BSF1) and single open stubs (BSF2).....	199

4.57	Comparison between simulated S-parameters for band-stop filter using single open stubs (BSF1) and band-stop filter utilising combination of short and open stubs (BSF2).	200
4.58	Comparison between simulated S-parameters for ECPW and CPW band-stop filters utilising short/open topology.	201
5.1	Cross section of a signal-elevated CPW line.....	207
5.2	Simulated characteristic impedance of signal-elevated CPW for varying 2a, b=2a+20, c=b+100, h=2,8 and 14. All dimensions are in micron	208
5.3	Simulated effective permittivity of signal-elevated CPW from for varying 2a, b=2a+20, c=b+100, h=2,8 and 14. All dimensions are in micron	209
5.4	Plot of simulated (a) conductor loss and (b) substrate loss of SECPW lines with three different lateral dimensions (2b) of 30, 60 and 120 μ m for various ratios of signal width to lateral dimensions (a/b).	210
5.5	Plot of simulated (a) conductor loss and (b) substrate loss of SECPW lines for various lateral dimensions (2b) and three elevation height of 5,10 and 15 μ m.	212
5.6	2-D and 3-D Simulation plots of total attenuation of a 5 μ m-elevated SECPW line with lateral dimension of 120 μ m.	214
5.7	2-D and 3-D Simulation plots of total attenuation of a 5 μ m-elevated SECPW line with lateral dimension of 30 μ m.	215
5.8	Micrograph of a signal-elevated CPW transmission line at (a) and (b) top view, (c) angled view.....	216
5.9	Comparison between measured S-parameters of signal-elevated, all-elevated and conventional CPW transmission lines	217
5.10	Measured loss factor of signal-elevated, all-elevated and conventional CPW transmission lines.....	218

5.11	Measured insertion loss of signal-elevated, all-elevated and conventional CPW transmission lines per unit wavelength.	219
5.12	Comparison between measured insertion loss of signal-elevated CPW transmission lines with different size and distance of supporting posts at G-band(140-220 GHz).	220
5.13	Measured loss factor of two SECPW transmission lines with different supporting post distances up to 325GHz.	221
5.14	Comparison between measured reflection coefficient of SECPW transmission lines with elevation heights of 6 μ m and 13 μ m.....	222
5.15	Comparison between the measured loss factor of SECPW transmission lines with elevation heights of 6 μ m and 13 μ m.	223
5.16	Comparison between measured loss factor of 13 μ m-elevated SECPW transmission lines with different supporting post distances.	224
5.17	Comparison between measured loss factor of 13 μ m-elevated ECPW and SECPW transmission lines with conventional CPW line.	225
5.18	Micrograph of a short-circuited SECPW stub at (a) angled and (b) top view....	227
5.19	Measured and simulated S-parameters for SECPW short-end shunt stub with 6 μ m elevation with resonance frequency at (a)160GHz and (b)240GHz.....	228
5.20	Comparison between measured S-parameters of SECPW, ECPW and conventional CPW short-circuited stubs at (a) G-band (140-220GHz) and (b) H-band (220-320GHz). The elevation height for elevated structures is 6 μ m.....	230
5.21	The substrate electric field plot of a short-circuited (a)SECPW, (b)CPW shunt stub at the centre frequency of 170 and 165GHz, respectively.	231
5.22	Comparison between measured S-parameters of SECPW short-end stubs with 6 μ m and 13 μ m elevations.....	232

5.23	Comparison between measured S-parameters of SECPW and ECPW short-end stubs with 13 μ m elevations	233
5.24	Comparison between measures S-parameters of 6 μ m-elevated SECPW short-circuited stubs with different number of supporting posts	234
5.25	Comparison between measures S-parameters of 6 μ m-elevated SECPW short-circuited stubs with different size of supporting posts	234
5.26	Micrograph of a open-circuited SECPW shunt stub	236
5.27	Measured and simulated S-parameters for SECPW open-end shunt stub with 6 μ m elevation.....	237
5.28	Comparison between measured S-parameters for 6 μ m-elevated SECPW and conventional CPW open-end shunt stubs	238
5.29	Comparison between simulated S-parameters for SECPW open-circuited stubs implemented with all 50 Ω lines and various impedance lines. (Low impedance feeds and high impedance stubs)	239
5.30	Comparison between measured S-parameters for 6 μ m-elevated SECPW and ECPW open-end shunt stubs.....	240
5.31	Comparison between simulated S-parameters for SECPW, ECPW and CPW open-circuited stubs implied with various impedance lines (Low impedance feeds and high impedance stubs).....	241
6.1	Angled 3-D conceptual view of a section of a elevated-grounded CPW line resting on posts and fed by CPW	249
6.2	Cross section of an elevated-grounded CPW line	249
6.3	Simulated characteristic impedance of elevated grounded CPW for varying $2a$, $b=2a+20$, $c=b+100$, $h=2, 8$ and 14 . All dimensions are in microns.	254

6.4	Simulated effective permittivity of elevated grounded CPW for varying $2a$, $b=2a+20$, $c=b+100$, $h=2, 8$ and 14 . All dimensions are in microns.	255
6.5	Simulated characteristic impedance of elevated grounded CPW for varying elevation height (h_2), $2a=40$, $b=2a+(15,40$ and $65)$ and $c=b+100$. All dimensions are in micron.	256
6.6	Cross section of a grounded elevated CPW section with gap on the lower ground	257
6.7	Mapping between physical (z) plane, intermediate t -plane and final t' plane for the intermediate post section.....	258
6.8	Cross section of EGCPW post section	259
6.9	Comparison between simulated and calculated frequency dependent characteristic impedance for seven section line.....	260
6.10	Simulated conductor loss of EGCPW lines with three different lateral dimensions ($2b$) of $30, 60$ and $120\mu\text{m}$ for various ratios of signal width to lateral dimensions (a/b).....	261
6.11	Simulated conductor loss of EGCPW lines for various lateral dimensions($2b$) and three elevation height of $5,10$ and $15\mu\text{m}$	263
6.12	2-D and 3-D Simulation plots of total attenuation of a $5\mu\text{m}$ -elevated EGCPW line with $120\mu\text{m}$ lateral dimension without added supporting posts.	264
6.13	2-D and 3-D Simulation plots of total attenuation of a $5\mu\text{m}$ -elevated EGCPW line with $30\mu\text{m}$ lateral dimension without added supporting posts.	264
6.14	2-D and 3-D Simulation plots of total attenuation of a $5\mu\text{m}$ -elevated EGCPW line with $30\mu\text{m}$ lateral dimension and added supporting posts to connect ground planes.	266

6.15	2-D and 3-D Simulation plots of total attenuation of a 5 μ m-elevated EGCPW line with 120 μ m lateral dimension and added supporting posts to connect ground planes.	267
6.16	Top view micrograph of EGCPW transmission line. The line dimensions are: W=24, S=25 and Wg=105. All dimensions are in micron	268
6.17	Measured and simulated S-parameters for a EGCPW and CPW (a) Insertion loss per mm (b) Reflection Coefficient (dB)	270
6.18	Micrograph of a EGCPW line with supporting posts placed in close distance to support probing on top of the elevated structure	271
6.20	Measured loss factor of EGCPW and CPW transmission lines.....	274
6.21	Micrograph of EGCPW line with transition pads to Coplanar waveguide	274
6.22	Measured S-parameters for a tapered EGCPW, de-embedded EGCPW and CPW transmission lines insertion loss/mm.	274
6.23	Micrograph of short circuited stub	277
6.24	Measured and simulated S-parameters for EGCPW short-end shunt stub with 6 μ m elevation.	277
6.25	Measured and simulated S-parameters for a 6 μ m-elevated EGCPW short-end shunt stub compared with the measured S-parameters for a CPW short stub.	278
6.26	Measured and S-parameters for EGCPW short-end shunt stub with 13 μ m elevation compared with CPW short-circuited stub.	279
6.27	(a) Micrograph of a stub at the junction with additional supporting posts in order to suppress the unwanted modes. (b) Measured results of the short circuit stub without supporting posts at the junction	282
6.28	Micrograph of open circuited stub.....	283
6.29	Measured and simulated S-parameters for a EGCPW open-end shunt stub.	283

6.30	Measured and simulated S-parameters for a EGCPW open-end shunt stub compared with the measured S-parameters for CPW open-end stub.....	286
6.31	Measured S-parameters for EGCPW open-end shunt stub with different elevation heights.....	286
6.32	Micrograph of the 3rd order quarter-wavelength band-pass Filter.....	287
6.33	Measured and simulated S-parameters for a EGCPW band-pass filter.....	287
6.34	Measured and simulated S-parameters for a EGCPW band-pass filter compared with the measured S-parameters for CPW band-pass filter.....	288
6.35	Micrograph the 3rd order quarter-wavelength band-stop Filter.....	289
6.36	Measured and simulated S-parameters for a EGCPW band-stop filter.....	290
6.37	Measured and simulated S-parameters for a EGCPW band-stop filter compared with (a) measured CPW band-stop filter with just open stubs in its configuration and (b) modelled CPW band-stop filter with same configuration.....	291

Associated Publications

The work of this thesis has led to the publication of a number of journal papers and peer reviewed conference papers which were given as oral presentation at IEEE conferences, including the following

- F. AGHAMORADI, I. MCGREGOR, S. ROY, AND K. ELGAID, "Low-Loss Grounded Elevated Coplanar Waveguide for Sub-Millimeter wave MMIC Applications," *Progress in Electromagnetic Research Journal, PIER B*, vol. 34, 2011.
- F. AGHAMORADI, I. MCGREGOR, AND K. ELGAID, "Performance enhancement of millimetre-wave resonators using elevated CPW," *Electronics Letters*, vol. 45. pp. 1326-1328, Dec 2009.
- I. MCGREGOR, F. AGHAMORADI, AND K. ELGAID, "An Approximate Analytical Model for the Quasi-Static Parameters of Elevated CPW Lines," *IEEE Transactions on Microwave Theory and Techniques*, vol. 58, Part. 1, pp. 3809 - 3814, 2010.
- F. AGHAMORADI, I. MCGREGOR, AND K. ELGAID, "H-Band elevated CPW band-pass filters on GaAs substrate," *IEEE Microwave Conference (EuMC), Paris*. pp. 9-12, Sep 2010.
- F. AGHAMORADI, I. MCGREGOR, AND K. ELGAID, "High Performance Resonators for MM-Wave ICs," *IEEE Microwave Conference (APMC), Yokohama*. pp. 833-836, Dec 2010.

Chapter1

Introduction

1.1 Motivation for use of millimetre and sub-millimetre waves

Applications which utilize frequencies in the sub millimetre wave regions of the electromagnetic spectrum, i.e. between 0.1-2.0 THz, are currently stimulating great commercial and academic interest. The applications of millimetre and sub-millimetre waves are widespread and include security and weapon detection [1], the biological and biomedical fields [2], pharmaceutical screening and drug identification [3], security and surveillance [4], collision avoidance radar systems [5], information and communications technology [6], astronomy and space science [7, 8] and passive imaging systems [9]. In particular, millimetre-wave imaging systems have received much interest because numerous materials (e.g. plastic, fabric, wood), fog, smoke and dust are transparent to mm-wave radiation. This allows imaging systems to see that which is invisible to optical systems - e.g. through clothes, walls, sandstorms etc. In addition, submillimeter-wave radiation is non-ionizing so the health risks are minimal compared with X-rays. In particular, the atmospheric windows at 94, 140, 220 and 320 GHz are in great interest for high-resolution active and passive imaging. Also, as operating frequencies are pushed ever higher, the resolution of imaging systems increases in proportion. An

increase in operating frequency also enables communication systems with larger bandwidths and, therefore, higher data transfer rates. Sub-millimetre-wave radios thus represent the next generation of ultra high speed wireless communications.

Recent advances in high electron mobility transistors (HEMTs) and hetero-junction bipolar transistors (HBTs) with cut-off frequencies greater than 400GHz [10, 11], and also high frequency diodes [12], have opened the door to the fabrication of integrated circuits operating in the low sub-millimetre wave regimes (140-320 GHz). Examples of sub-millimetre wave circuits include several G-band (140-220) and H-band (220-320) low noise amplifiers developed for high-bandwidth radar and high resolution imaging systems [13-21]. Also measurement results of G-band oscillator, phase-shifter and T/R modules have been reported [22-25]. A 380GHz fully integrated transceiver using quadrature push-push circuitry has been fabricated and tested recently using SiGe BiCMOS technology [26]. All above-mentioned advances and researches in millimetre and sub-millimetre wave regime show the growing interest as well as the existing potential of developing a fully integrated circuits with optimum performance at frequencies above 100GHz.

However, a significant obstacle to the implementation of submillimeter-wave circuits and systems is the poor performance of the passive networks which accompany the active devices [14, 20, 27]. In particular, the transmission line which is the building block of microwave and millimetre-wave circuits, is found to exhibit high losses in the sub-millimetre wave regime [27-28]. These losses are primarily due to the influence of the waveguide substrate, with the presence of high permittivity substrates increasing direct losses, but also conductive and radiative losses. If the deleterious effects of the substrate can be reduced, then waveguide performance can be increased at high

frequencies, and improved passive components will become available to integrate with active semiconductor devices. This in turn will allow the design of detectors, oscillators, filters, mixers, up-convertors and amplifiers with substantially improved performance, thus increasing the performance of the microwave systems of which these are fundamental building blocks.

1.2 Aims and Objectives

The aim of this thesis is to extending the frequency range over which current transmission lines and passive networks can operate by modelling, fabricating and measuring novel, low loss transmission lines (as well as distributed passive networks composed of these lines), with the view to improving the performance of the mm-wave circuits and the systems which rely upon them. The main focus is on the frequency range 140-320GHz. In order to accomplish this aim, the research will :

- Study currently used transmission lines and investigate their performance, through analysis, modelling and experiment, at the lower end of sub-millimeter wave range, considering their performance both as discrete transmission lines and as part of distributed passive networks.
- Perform a thorough analysis into the performance of potential, low loss transmission line structures suitable for sub-millimeter wave range. Such a study will be broken down into a number of key areas :
 - Development of compact analytic / semi-analytic formulae for the figures of merit of novel transmission lines, to quickly narrow the search domain of useful structures (and facilitate later design using these structures).

- Development of fabrication processes needed to construct novel transmission lines.
- Design and fabrication of structures to allow detailed study of line performance.
- Perform analysis, modelling, simulation and physical measurement to investigate and understand the behavior of the most promising structures up to 320GHz.
- Perform a thorough analysis into the potential of foundational passive networks constructed using the transmission lines investigated above. The analysis should involve design, fabrication and measurement of low loss structures.

If the aims and objectives of this work are fulfilled, the result will be development of novel structures with low levels of attenuation and high performance when used to form passive networks for high millimetre wave frequencies. If such structures can be designed as: MMIC compatible, easily combined with presently available active and passive devices, relatively simple to fabricate, and with low attenuation characteristics, then they will be of considerable interest and benefit to both industry, and to the research community in this area.

1.3 Thesis Organisation

An introduction to the motivation and aims of this project, as well as a review of past and present research into the development of low loss transmission lines and high-Q passive networks for millimetre and sub-millimetre wave applications is given in this first chapter.

Chapter 2 presents a comprehensive investigation into the performance of the most popular transmission media for high frequency applications, coplanar waveguides, in the frequency range of 0.1-320GHz. Theoretical and experimental investigations of passive components including transmission lines, two-port short and open-circuited resonators, and band-pass and band-stop filters are presented. The problems associated with coplanar waveguides in the implementation of passive networks in the sub-millimetre wave regime are exposed, along with a discussion on how elevated structures can be used to ease these limitations.

The fabrication processes required to construct elevated structures are outlined in chapter 3, along with novel extensions to these techniques developed as part of this work.

Different elevated coplanar waveguides structures, including all-elevated, signal-elevated and ground-elevated coplanar waveguides, are studied in Chapter 4. This chapter then compares the performance of all-elevated coplanar waveguides, and all-elevated coplanar waveguide based shunt stubs, with more traditional coplanar waveguides at frequencies up to 320GHz, whilst in Chapter 5 transmission lines, resonators and filters implemented with signal-elevated coplanar waveguides are investigated in similar fashion.

In chapter 6, a new variant of elevated coplanar waveguide, the Elevated Grounded Coplanar Waveguide, is presented. This new structure offers a substrate-isolated transmission line with an effective permittivity of 1. Simple formulae for the characteristic impedance of this novel transmission line are developed along with a synthesis technique based on Newton's method. The performance of the structure is investigated by looking at the performance of the transmission line with different

geometries as well as 2 port short and open-end stubs. Band pass and band stop filters are designed with centre frequencies around 220GHz and their performances are compared with more traditional waveguides.

Conclusions are finally drawn in chapter 7.

After a general outline of the thesis in terms of motivation, aims and objectives and organisation of chapters, we continue this first chapter with an introduction to submillimeter wave passive networks past and present research in this field.

1.4 Sub-millimetre wave passive networks : research review

The transmission line is the most fundamental passive component [29] in high frequency (millimetre wave and sub-millimetre wave) integrated circuits, and therefore achieving a high performance transmission line is critical for any successful high frequency circuit design.

In general, the critical problems to be understood and overcome in the design of any high frequency transmission line are: signal attenuation (due to $\propto \sqrt{f}$ conduction losses, conductor skin effect, and substrate loss through radiation and substrate conductance), impedance dispersion (variation of Z_0 with frequency), spurious electromagnetic losses and coupling to remote structures, and the problematic generation of multiple higher order propagating modes [30].

The first planar transmission line, the strip transmission line, was proposed and fabricated by Robert M. Barrett in 1950 [31], and since then there has been ongoing attempts to achieve a transmission line able to maintain a single propagation mode over a wide frequency range coupled with low attenuation. This led to the introduction of several transmission line structures such as microstrip [32], slotline [33], suspended stripline [34], and coplanar waveguides (CPW) which will be discussed in more detail below.

Among the above transmission lines, microstrip and CPW show the greatest potential for microwave integrated circuit (MIC) and monolithic microwave integrated circuit (MMIC) applications, with CPW often the preferred choice for applications above 60GHz [35]. CPW was first introduced by C.P. Wen in 1969 [36]. At first, despite the fact that it offered many desirable properties, CPW could not compete with already established microstrip line in hybrid technology. More recently, however, with the push

to high frequencies and monolithic technologies, CPW has experienced growing popularity due to certain intrinsically properties [37-43]. For example, Pucel [37] and Browne [39] showed that CPW has the major advantage of enabling devices to be grounded, with a low inductance, on the top surface of a substrate without the need of via holes. In addition, Browne *et al.* [43] showed that CPW allows easier shunt and series surface mounting of active and passive devices while it also facilitate more convenient on-wafer probing of microwave integrated circuits. Also the existence of ground planes between any two adjacent lines implemented by CPW, reduces the cross-talk effect between adjacent lines in monolithic circuits [37, 38, 42]. Another important characteristic of CPW, compared with microstrip, described by Stegens *et al.* [40], is that the line impedance and phase velocity are more dependent on transmission line metallisation geometry than on substrate thickness. Since the conducting surfaces of a CPW structure are all printed on the same interface and are typically much smaller than the substrate thickness, careful design can efficiently confine the fields to near this air-dielectric interface. This characteristic can be beneficial as it provides control over signal leakage and unwanted parasitic coupling [35, 38].

However, studies of CPW have *also* shown the limitations of CPW at very high frequencies, above 100GHz, where the signal wavelength becomes comparable with the physical dimensions of the substrate. The sub-millimetre wave attenuation performance of CPW transmission lines up to 1THz was investigated by Frankel *et al.* [44], Cheng *et al.* [45] and Zhang *et al.* [46] using electro-optic sampling techniques. These investigations indicated that, even if CPW exhibits superior performance to microstrip lines operating at the same frequency, as this frequency enters the sub-mm wave region the increased radiation loss in CPW in the form of surface-waves complicates the

design. As a result, further reduction of parasitic radiation is required. (A way to achieve this and also to extend the operation of a coplanar waveguide into the sub-millimetre wave region is to generate a surface-wave free environment [45]). In addition, the increased attenuation of CPW mixed with the additional conductor loss introduced when used for low or high impedance lines [35, 48], makes the realisation of high Q/ low loss passive networks a challenge at sub-mm wave frequencies. The performance of CPW discontinuities including open and short-circuited stubs as well as band-pass and band-stop filters for frequency range of 0.1-110GHz, are reported in [49]. Open circuit stubs and a band-pass filter implemented with CPW are investigated in [50] up to 220GHz. These results also indicate that in order to achieve high quality stubs and narrow-band filters, an alternative structure with lower loss and less sensitivity is required.

Another problem with the conventional CPW structure arises when it is eventually packaged in a real application. Heinrich *et al.* [51] showed that the CPW structure then becomes a conductor-backed coplanar waveguide (CBCPW) which can behave like an over-moded patch antenna, supporting parallel-plate modes and exhibiting unwanted in-band resonances [52]. This problem is exacerbated when the backside metal is brought closer to the CPW, as is necessary when the substrate is thinned for reducing the thermal resistance and increasing the efficiency of heat removal from a CPW-based MMIC. To mitigate unwanted in-band resonances and ensure single-mode propagation for CBCPW, the authors used via holes connected between the top and bottom ground planes. Since the addition of via holes is a difficult and time consuming fabrication process, with inherent frequency limitations, we believe that an alternative approach is required for practical systems, with a simpler fabrication process.

These disadvantages of the CPW structure at very high frequencies, has been recognised in the literature and has led to an increased interest in the development of non conventional transmission lines. Examples of structures which have been considered as promising include: monolithic dielectric guides (including ridge, semiembedded) [53], silicon micro-machined rectangular waveguides [54, 55], micro-shield lines [56] and elevated structures in the form of thin film microstrip (TFMS, Air-TFMS) [57, 58] and elevated CPW [59-60]. These are summarised below with an indication of the advantages and disadvantages of each structure.

One of the structures which has been suggested for sub-millimetre waveguides is the ridge dielectric waveguide [53, 61]. Dielectric waveguides have been extensively studied for their performance at low-frequencies in different configurations such as strip dielectric guides, insulated image guides, strip-slab guides [62], cladded image guides [63], dielectric image guides [64], and trapped image guides [65]. In the construction of these transmission structures, a combination of layers and ridges with various permittivities are used to provide a region in which the propagating energy is well defined. Although there are some examples of use of these structures in monolithic circuits (e.g.[66]), these waveguides are mostly considered hybrid in nature. In 1991, Engel *et al.* [53] suggested that the variation of these early dielectric waveguides can be considered as a way of developing sub-millimetre wave guiding structures. The proposed ridge or semiembedded dielectric waveguide considered in their work consist of alternating layers of materials with high and low dielectric constant. These materials are available in monolithic technology and therefore the integration of active devices is possible. The abrupt changes in the permittivity are designed to optimize power confinement in the least dense material. This layer is designated as the propagation

layer, and is remote from the ground plane, resulting in minimal ground plane conductor losses. Transition from waveguide to active devices can consist of a very short length of planar transmission line i.e microstrip. The dielectric waveguides eliminate conductor losses and with careful design can reduce radiation to lower levels. However, due to fabrication constraints, these waveguides are presently more suitable for operation in the high end of the sub-mm wave spectrum (0.5-1THz). This is because the fabrication process of both suggested structures, ridge and semiembedded dielectric waveguides, require regrowth of several semiconducting layers on GaAs or InP substrates. For operating at around 0.7-3THz, layers of 5-20 μm are required which can be provided using MOCVD (Metalorganic Chemical Vapour Deposition). As the frequency of operation decreases, thicker layers are required to provide good power confinement and the time require to grow the material on the wafers become impractically long [53, 61]. In general, in the design of circuits and systems in lower frequency range i.e 0.1-0.4 THz, which also require strict monolithic integration of passive and active devices, other types of low-loss transmission lines might be more appropriate [61, 67, 68].

Kim *et al.* [54] and Yap *et al.* [55] introduced the transmission structure called silicon micromachined rectangular waveguide in 1992 to overcome the complicated and costly conventional machining techniques used for metal rectangular waveguides operating above hundred GHz (i.e. fabricating a very small waveguide with dimensions less than 0.3mm \times 0.15mm for 500-1000GHz waveguides using milling and drilling of metallic and dielectric materials) and also to solve the traditional mounting problems with these standard waveguides in integrated circuits. WR-10 silicon micromachined waveguide was investigated experimentally by Yap *et al.* [55].

This silicon based monolithic waveguide for sub-mm waves uses a micromachining technique to form the guide, Fig. 1.1.

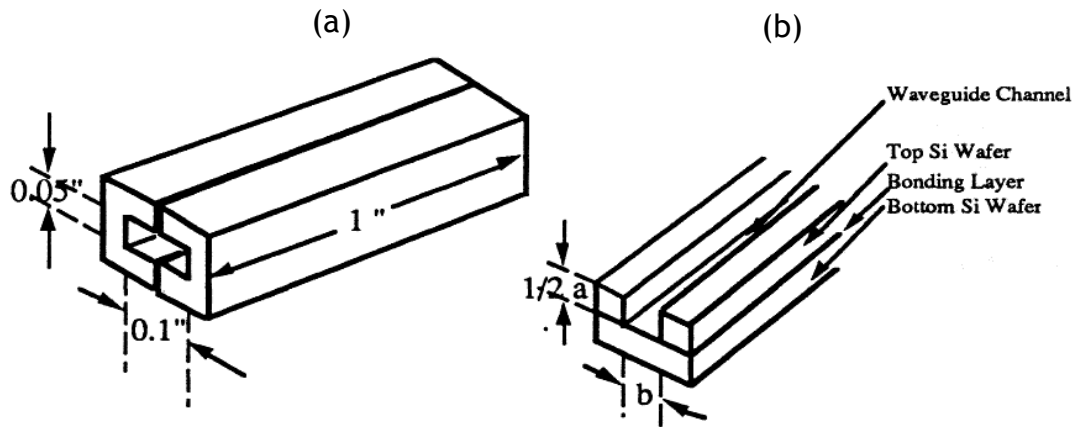


Figure 1.1: WR-10 silicon micro-machined waveguide. a) The waveguide is split into half sections b) One half section of waveguide [55].

The rectangular waveguide is split along the broad wall with each half is formed by etching and smoothing the channel through a wafer. The wafer is then bonded to another flat wafer and diced into the U-shaped half waveguides. This is then followed by depositing a gold layer on the waveguide walls. WR-10 waveguide is a rectangular channel with the dimensions of 2.54×1.27 mm with operating frequency range of 75-110GHz and is made of two half sections split along the broad wall to simplify the fabrication process and also to facilitate the integration with planar passive and active devices. The Silicon micromachined waveguides were constructed and found to offer comparable loss with commercially available rectangular waveguides i.e non-optimised WR-10 measured at 100GHz showed $0.05\text{dB}/\lambda$ compared with $0.024\text{dB}/\lambda$ for rectangular waveguide at the same frequency. Since then and with advances in micromachining technology, silicon-based waveguides have been extensively investigated utilising different fabrication techniques such as wet and dry etching, thick

photoresist (SU-8) [69] and LIGA-processes based on X-ray [70] or UV exposure [71] to achieve optimum size and performance for different frequency ranges of interest [72-75]. Also research has been conducted into optimising the integration of these structures with active and passive planar devices [76, 77]. The CPW-fed micromachined rectangular waveguide in [76] shows measured return loss better than 10dB and insertion loss around 1.5dB in the frequency range of 60-120GHz. Also the work in [77], proposes the micromachined rectangular waveguide with cavity-backed (CBCPW) coplanar waveguide transition with simulated return loss of better than 20dB and insertion loss of 1dB/mm over the frequency range of 230-245GHz. In comparison with traditional tool-based (metallic) waveguides, non-traditional mask-based (micromachined) waveguides can support much smaller sizes, i.e minimum dimensions of $>1.5\mu\text{m}$ compared with $>50\mu\text{m}$ for standard metal waveguides. Also these structures can support much higher surface quality while maintaining much lower cost [75]. However this type of line suffers a considerable disadvantage, due to considerable increased fabrication complexity, and as a fully rectangular waveguide on silicon, remains difficult to integrate with active devices and planar structures.

Micro-shield line was first fabricated in 1991 by N.I. Dib *et al.* [56] as a high performance transmission line for sub-mm-wave frequencies and studied in detail by N.I. Dib *et al.* [78], N. Yuan *et al.* [79] and Helal *et al.* [80]. Micro-shield line is fabricated using thin dielectric membrane technology and the anisotropic etching of the supporting silicon substrate, Fig.1.2.

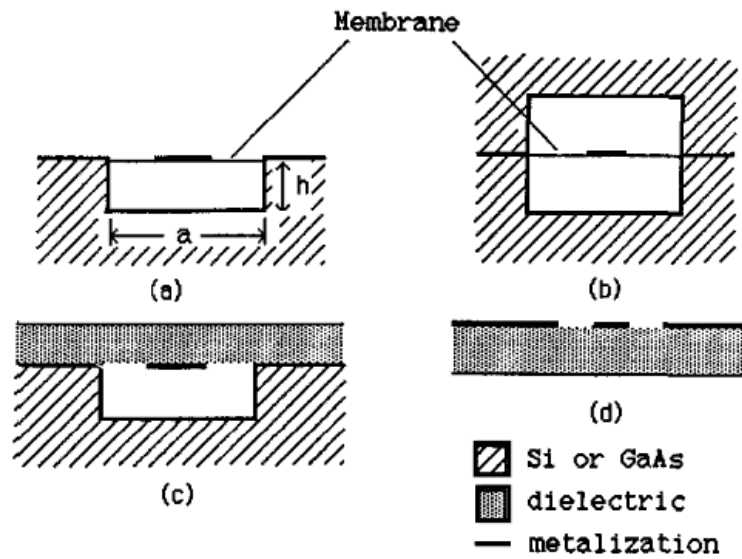


Figure 1.2: (a), (b) Membrane microshield transmission lines. c) Dielectric microshield line. d) Conventional coplanar waveguide [56]

To form the membrane, first three layers of $\text{SiO}_2/\text{Si}_3\text{N}_4/\text{SiO}_2$ is developed on top of the wafer using thermal oxidation and chemical vapour deposition. Then a window is defined on the back of the wafer using silicon-nitride mask and the wafer is etched until the transparent membrane appears. After forming the membrane, metallisation is carried to cover the cavity walls and also to realise the CPW traces on top of the membrane. At the end, the back of the cavity is shielded by bonding to another flat wafer. By providing air-substrate structure, micro-shield line is characterized by low dielectric and radiation loss, reduced electromagnetic interference, and the ability to exhibit TEM dispersion-less wave characteristics over a very wide frequency range up to 1THz. By using time-domain electro-optic sampling measurement technique, Cheng *et al.* [28] showed an attenuation of around 1dB/mm up to 1THz for CPW micro-shield line with lateral dimension of 25-40-25 μm . Weller *et al.* [81, 82] and Robertson *et al.* [83] have shown that the silicon micro-shield structure can be to construct a variety of circuit

components with low level of attenuation and high quality factor up to frequencies around 250GHz. Dupuis *et al.* [84] also showed experimental results of developed microshield transmission lines with different characteristic impedances on GaAs substrates. The measurement results for these transmission lines up to 110GHz show a constant phase velocity of 2.9×10^8 m/s and low loss for GaAs-based micromachined lines. However, a critical disadvantage of the membrane micro-shield is its long and complex fabrication process (due to the required substrate etching and membrane fabrication) and also requirement of additional steps in integration of thin dielectric membranes onto the substrates [85].

Yet another transmission line structure with good potential for sub-mm-wave applications is the elevated transmission line. This line can be in the form of elevated CPW or microstrip line. microstrip line elevated on a thin dielectric layer i.e polyamide or BCB (bisbenzo-cyclobutene), known as thin film microstrip (TFMS) was introduced to extend the frequency range of microstrip structures to millimetre and submillimeter-wave frequencies [86]. Conventional 50Ω microstrip lines require the signal width to be in the same order of magnitude as the substrate thickness, i.e. , relatively large dimension compared to CPW dimensions. This causes an increase in modal dispersion and makes the conventional microstrip unsuitable for applications in the millimetre and sub-mmwave regime. While conventional microstrip line uses the whole semiconductor substrate as a dielectric layer, in TFMS this layer consists of thin dielectric material in the range of 1-25μm on top of the semiconductor substrate, separated by metal layer [57, 86]. This allows the strip width to be scaled down, and consequently the total dimension of the line. TFMS is an attractive transmission line for millimetre and sub-mm wave applications and its performance was investigated theoretically and

experimentally in recent years [87-91]. It was experimentally shown by Six *et al* [90] that TFMS line with 20 μ m BCB fabricated on silicon substrate has an insertion loss of 0.38dB/mm at 110GHz compared with 0.06dB/mm for micromachined structures at the expense of less complex fabrication process and more MMIC compatibility. In general TFMS transmission lines show comparable performance with conventional CPW lines up to 1THz [88]. While CPW and TFMS are compatible in terms of loss performance, CPW makes it easier to integrate with transistors in layout and tend to be more compact than TFMS [96]. In 2005, Hettak *et al.* [58] fabricated TFMS lines with an air dielectric layer, Air TFMS, to improve the loss performance of low impedance TFMS lines for millimetre-wave frequencies. Air-TFMS uses the same fabrication technology as the air-elevated coplanar waveguide, called Elevated CPW.

Elevated CPW makes use of air-bridge technology to elevate some or all of the transmission line traces above the substrate, reducing substrate attributable losses, and offering an environment which is less prone to the generation of surface-waves. Elevated structures have primarily been used as high impedance/low loss lines [92-95], but have also been suggested as attractive candidates for general use at high mm-wave frequencies [20, 59, 60, 96]. Despite the potential elevated structures offer for high frequency circuits and the relatively simple fabrication process this structure requires, little analysis, and experimental confirmation of their performance at high frequencies has been conducted. This is a weakness in the literature which this work aims to correct. Elevated CPW structures are therefore considered for further investigation in this thesis to evaluate performance in the sub-millimetre wave regime. Different types of elevated configuration are studied and their performance, both intrinsically, and in implementation of some basic passive networks (resonators, filters) is investigated.

Also, the frequency range over which the performance of all of the structures in this work, including conventional and elevated, are investigated is extended up to 320GHz for the first time. The diagram of the conventional and elevated CPW structures considered in this work is shown in figure 1.3.

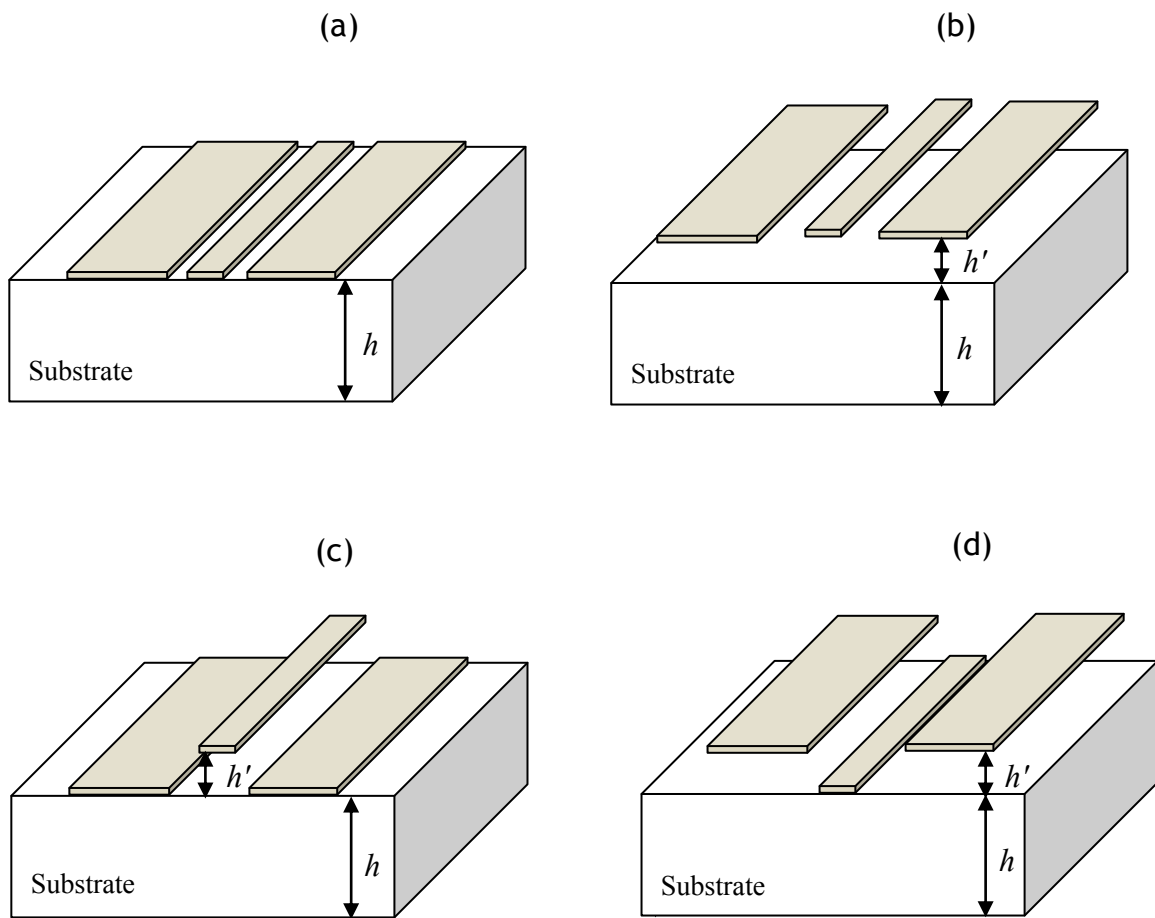


Figure 1.3: Different transmission line structures considered in this work:

a) Conventional CPW, b) All-elevated CPW, c) Signal-elevated CPW and d) Ground-elevated CPW

Chapter 2

Theoretical and Experimental Study of Coplanar Waveguide

2.1 Introduction to CPW transmission line

Widespread use of coplanar waveguides (CPW) in MICs and MMICs over recent years [13-23] is the result of an effort to improve circuit performance at operating frequencies up to sub millimetre wave bands. The structure of CPW, shown in Figure 2.1, consists of two ground planes surrounding a signal conductor which are printed on the same surface of a dielectric slab.

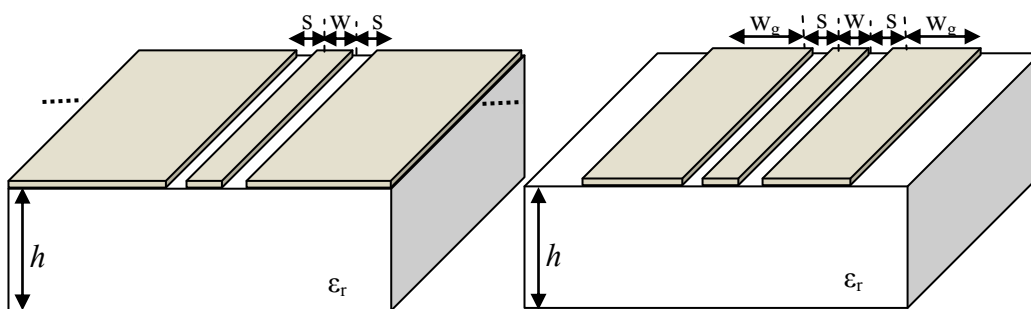


Figure 2.1: Structure of the Coplanar Waveguide transmission line with finite substrate thickness and (a) infinite and (b) finite ground widths.

The coplanar waveguide has two modes of propagation. One is a quasi-TEM mode, often called the odd mode or coplanar mode, where the electric fields in the two slots are 180° out of phase as shown in Figure 2.2(a). The other is a non-TEM mode, called

the even mode or the coupled slotline mode, where the electric fields are in phase as shown in Figure 2.2(b).

In CPW microwave circuits, the coplanar mode is desired due to its low radiation properties and zero frequency cut-off. However, one of the problems of CPW is the degeneration of the propagation mode from quasi-TEM to a balanced coupled-slotline mode - especially at discontinuities. This can be reduced by geometrical techniques to maintain the symmetry of the structure, and using airbridges or underpasses to reduce the effect of this unwanted phenomenon by physically uniting the ground plates [145, 146].

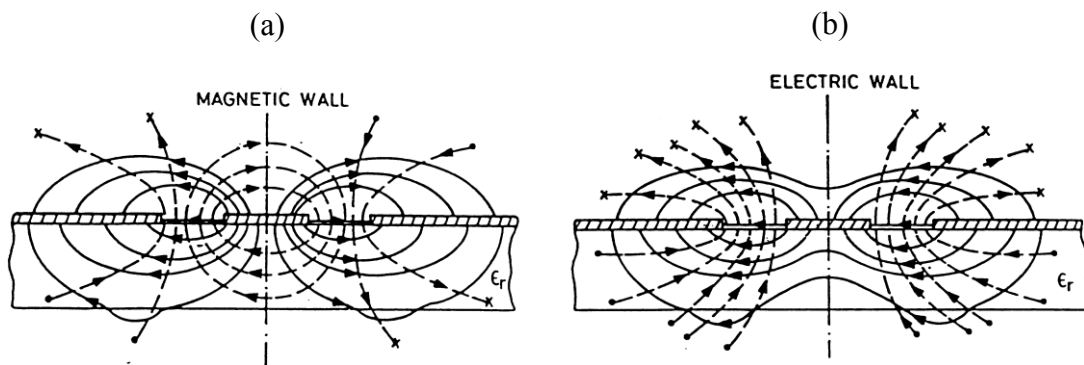


Figure 2.2: Coplanar mode(a) and Coupled Slotline mode(b) field configurations
(— Lines show the Electric Field lines and --- Lines show the Magnetic Field lines) [98]

One of the main advantages of the CPW structure over other types of transmission line such as microstrip is that it doesn't need through-substrate via holes for grounding purposes. In general, the principal advantages of the CPW can be summarised as follows:

- Devices and components can be grounded without via holes.
- It suffers from much less dispersion than microstrip, making it suitable for millimetre wave circuits [110], [117].

- A given characteristic impedance can be realized with a wide variety of track width and gap size combinations
- A considerable increase in packing density is possible because the ground planes provide shielding between adjacent CPW lines.

The attenuation characteristics of CPW transmission lines have been investigated before by Cheng *et al.* [28, 45], Frankel [44], Zhang *et al.* [46], and Zehentner *et al.* [97] up to 1THz. Despite the advantages of CPW over microstrip at low frequencies, all this previous work shows high attenuation for CPW at frequencies above 100GHz. To obtain a better understanding of the mechanisms of wave propagation in CPW and the sources of attenuation for in these structures, this chapter begins with the basic theory and analysis of coplanar waveguides. The results of a set of static and full wave simulations of the losses in CPW transmission lines are then presented in section two. The third section describes a theoretical and experimental investigation of CPW transmission lines up to 320GHz and continues with the problems that the CPW structure faces when it comes to real applications and packaging. In this section, also, one of the most common suggestions to solve this problem (use of via holes to connect the top and bottom grounds of CPW) is investigated in detail, and a method to simplify the complex fabrication procedure is given. Despite the popularity of CPW transmission line for millimetre-wave applications, there is little in the literature on the performance of CPW passive circuit implementations at frequencies above 140GHz. Therefore, section 5 and 6 present the theoretical and experimental investigation of some passive components and circuits such as resonators and filters implemented with a CPW structure in the frequency range of 0.1-320GHz. The problems that the conventional CPW structure show in implementing these components and circuits is discussed in

detail in this chapter. The chapter also provides a good background for the further research that is carried out later in this work to improve the performance and increase the functionality of submillimeter wave passive distributed circuits.

2.2 CPW Analysis

The coplanar waveguide structure was first introduced by C.P.Wen in 1969 [36]. Since then, different techniques have been used to analyse its characteristics. For example, conformal mapping was used to derive the quasi-TEM parameters (Z_0 and ϵ_{eff}) of a CPW with infinite ground planes and infinite substrate thickness [36], and has been used to obtain closed form expressions of these parameters including the effects of finite substrate thickness and shielding walls [99], finite extend ground planes [100] and mixed-dielectric substrates [101]. Numerical techniques have been used to derive the quasi-TEM properties of CPW, including: point matching method [102, 103], relaxation technique [104], generalized transverse resonance method [105] and a hybrid approach that combines the finite element method and the conformal mapping technique [106]. Since these quasi-TEM techniques cannot fully describe the high frequency behaviour of CPW, full wave analyses of CPW transmission lines have also been developed [107-110].

As the conformal mapping technique will be used later to analyse a number of the novel structures developed in this work, the technique is described immediately below, using as examples the two most commonly used CPW structures in real applications: CPW with finite ground planes and finite substrate thickness with and without backside metallisation.

2.2.1 Conformal mapping technique

Conformal mapping (CM) is a useful mathematical approach to solving many boundary problems in engineering [111]. Its main advantage is simplicity and the ability in obtaining closed-form equations for the parameters of interest. In static situations, many electromagnetic problems can be solved by employing conformal mapping. In particular, the analysis of transmission lines for RF and microwave integrated circuits.

Mapping, by itself is a very straightforward geometric technique. In general, a function, f , describing the relationship between two complex variables $z = x + jy$ ($z = re^{j\theta}$) and $w = u + jv$ ($w = \rho e^{j\phi}$) as $w = f(z)$, performs a *transformation* or *mapping* between the two points z and w . Geometrically, f maps the area containing points (x, y) to one containing the points (u, v) . Separate planes are normally used for the coordinates of z and w to provide simplicity and convenience in mathematical analysis (z-plane and w-plane). For instance, the mapping function, $f(z) = w = \ln z$, maps a circle in z-plane to a line segment in w-plane, Figure 2.3.

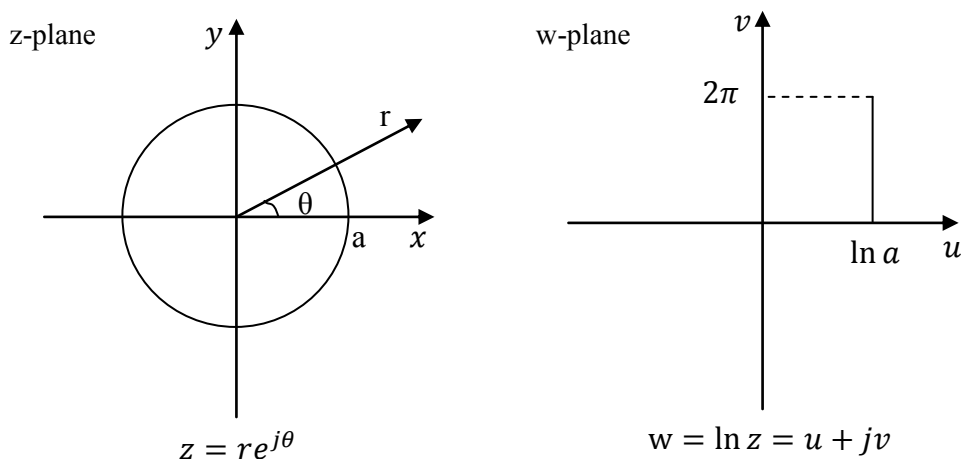


Figure 2.3: Mapping between a circle in z-plane and a line segment in w-plane [111]

The *mapping* is said to be *conformal* if the function f is *analytic* at point z , and $f'(z) = \frac{df}{dz} \neq 0$. Therefore, conformal mapping is a mapping that employs an analytic function whose derivative is never zero on the z plane where the function is defined. Geometrically a conformal map is one in which lines in one plane cross at the same angle as in the transformed plane - i.e. angles are preserved locally.

In microwave problems the complex geometries of transmission lines are mapped to simpler structures with known or easily found solutions - usually a parallel plate capacitor.

- The Schwarz-Christoffel Transformation

The most commonly used conformal transformation in transmission line analysis is the *Schwarz-Christoffel transformation*. This transformation maps the x axis and the upper half of the z -plane onto a closed polygon and its interior in the w -plane as shown in Fig.2.4.

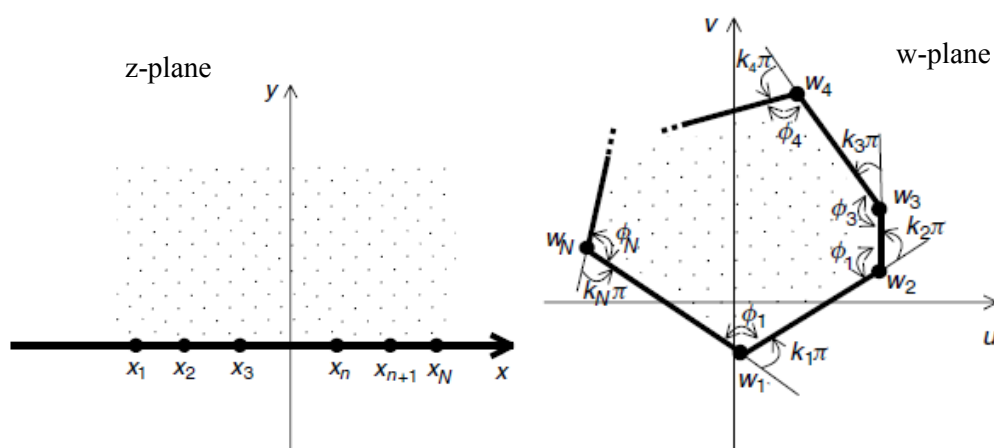


Figure 2.4 : The Schwartz-Christoffel transformation [111]

The Schwarz-Christoffel transformation can be written as:

$$w = f(z) = A \int^z \prod_{n=1}^N (z - x_n)^{\phi_n/\pi-1} dz + B \quad (2.1)$$

Where ϕ_{n+1} is the interior angle at the vertex w_{n+1} which is defined as the angle between two adjacent sides, B is an arbitrary constant which determines the position of the polygon while the magnitude and angle of constant A controls the size and orientation of polygon in w -plane. In practice, the polygon is defined in the w -plane and the Schwarz-Christoffel transformation is determined such that the x -axis of the z -plane is mapped to the polygon. This process can be done by first determining the polygon's interior angles ϕ_n and the points x_n and, then, evaluating the integral in Eq.2.1.

A simplifying assumption used in the conformal mapping of planar transmission lines is to assume a magnetic wall at the air-dielectric interfaces in the structure. This assumption is valid for structures whose electric field lies along a dielectric interface, such as planar transmission lines [98]. Under this assumption, the line capacitance can be calculated for the half-planes above and below the metallisation plane separately. The total line capacitance is then the algebraic sum of these two capacitances. In the case of finite substrate thickness, the lower half-plane capacitance can be found from the sum of a) the free space capacitance where the dielectric is replaced with air and b) the capacitance of the line with dielectric of permittivity of (ϵ_r-1) .

Using this approach, the effective dielectric constant and characteristic impedance can be obtained by:

$$\epsilon_{eff} = \frac{C}{C_{air}} \quad (2.2)$$

$$Z_0 = \frac{1}{c\sqrt{CC_{air}}} \quad (2.3)$$

Where c is speed of light in free space, C_{air} is the capacitance of the line with all the dielectrics replaced by air and C is the total capacitance of the line.

1.1.2 CPW with finite substrate and finite ground planes without backside metallization

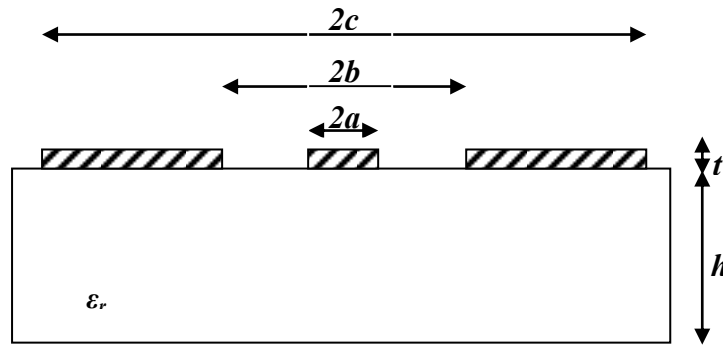


Figure 2.5: Cross section of CPW on finite substrate with finite ground planes

Figure 2.5 shows a cross sectional view of a CPW with ground planes of finite extent and a finite substrate thickness. The width of the signal line is $2a$ and the gap is $(b-a)$. The width of the ground planes are $(c-b)$. Infinitesimally thin conductors are considered and the finite thickness of the substrate layer is h . Due to symmetry, only one half of the structure need to be considered, as shown in Fig.2.6 (a).

We assume that the lower-half plane capacitance is the sum of the free space capacitance and the capacitance of the dielectric layer with permittivity of $(\epsilon_r - 1)$.

Therefore, the capacitance of the structure with all dielectric material replaced with air, C_{air} , is first calculated.

A pair of conformal transformations is used to transform the CPW into a parallel plate structure. First, the quadrant of CPW is transformed to the t -plane using the mapping integral

$$z = A \int \frac{dt}{\sqrt{t}} + B \quad (2.4)$$

From which the inverse mapping function which transforms the physical z -plane to the upper half t -plane is found to be

$$t = z^2 \quad (2.5)$$

Then, the Schwarz-Christoffel transformation is again used to map the upper half t -plane to a parallel plate structure in the w -plane, Figure 2.6 (c) as

$$w = \int_{t_0}^t \frac{dt}{\sqrt{t(t-t_1)(t-t_2)(t-t_3)}} \quad (2.6)$$

with

$$t_1 \leftrightarrow a^2$$

$$t_2 \leftrightarrow b^2$$

$$t_3 \leftrightarrow c^2$$

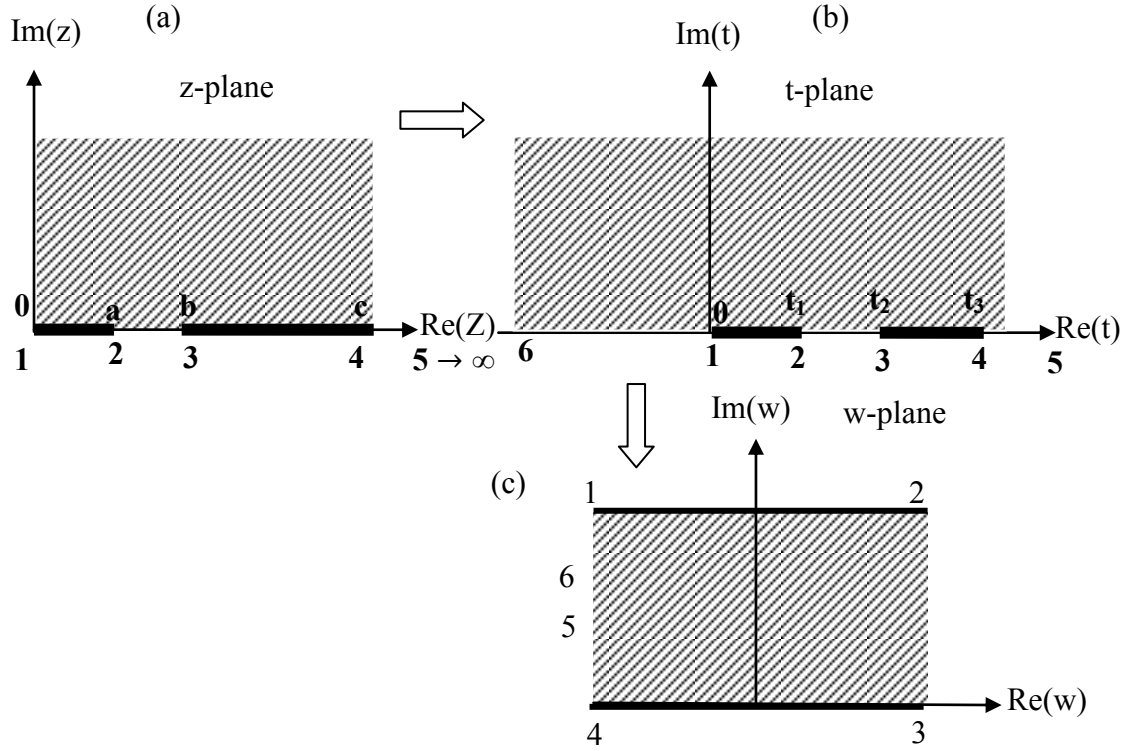


Figure 2.6: Conformal mapping for upper half plane (air layer) of CPW with finite substrate and finite ground widths: (a) original z-plane, (b) intermediate t-plane and (c) final mapping into a parallel-plane capacitor in w-plane.

The free space capacitance in the air half-plane, C_1 , is given by

$$C_1 = 2\varepsilon_0 \frac{K(k_1)}{K'(k_1)} \quad (2.7)$$

and

$$C_{air} = 2C_1 \quad (2.8)$$

Where

$$k_1 = \frac{a}{b} \sqrt{\frac{1-b^2/c^2}{1-a^2/c^2}} \quad (2.9)$$

$K(k_1)$ and $K'(k_1)$ are the complete elliptic integrals of the first kind and its complement, respectively.

To calculate the capacitance of the dielectric region, it is first mapped to the upper half of t -plane, using the mapping integral

$$z = A \int \frac{dt}{\sqrt{t(t-1)}} + B \quad (2.10)$$

from which the inverse mapping function is found to be

$$t = \cosh^2 \left(\frac{\pi z}{2h} \right) \quad (2.11)$$

The upper half t -plane is then transformed to a parallel-plate capacitor in the w -plane using the following Schwarz-Christoffel transformation

$$w = \int_{t_0}^t \frac{dt}{\sqrt{(t-1)(t-t_1)(t-t_2)(t-t_3)}} \quad (2.12)$$

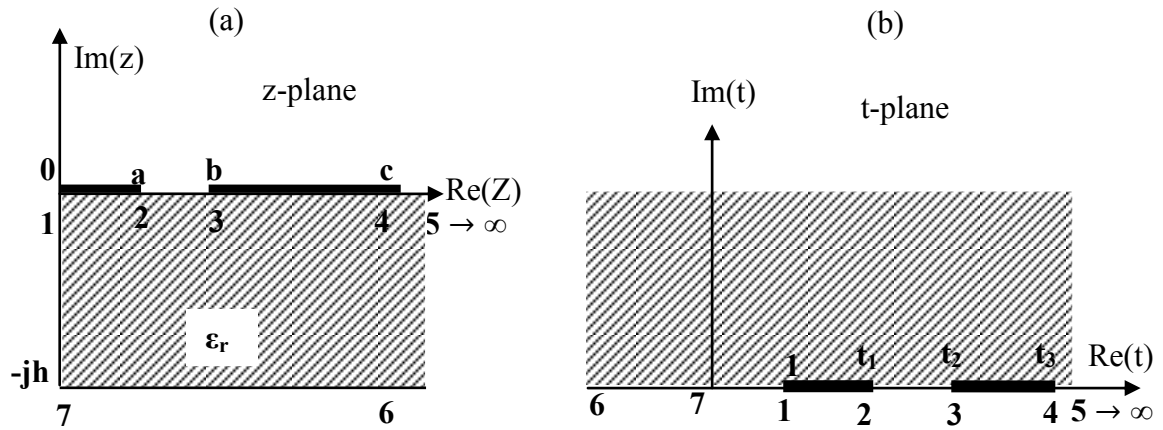


Figure 2.7: Conformal mapping for lower half plane (dielectric layer) of CPW with finite substrate and finite ground widths: (a) original z -plane, (b) intermediate t -plane.

The capacitance per unit length of the line contributed by the dielectric half plane, C_2 , is given by

$$C_2 = 2\varepsilon_0(\varepsilon_r - 1) \frac{K(k_2)}{K'(k_2)} \quad (2.13)$$

where

$$k_2 = \frac{\sinh(\pi a/2h)}{\sinh(\pi b/2h)} \sqrt{\frac{1 - \sinh^2(\pi b/2h)/\sinh^2(\pi c/2h)}{1 - \sinh^2(\pi a/2h)/\sinh^2(\pi c/2h)}} \quad (2.14)$$

The total line capacitance can be calculated from

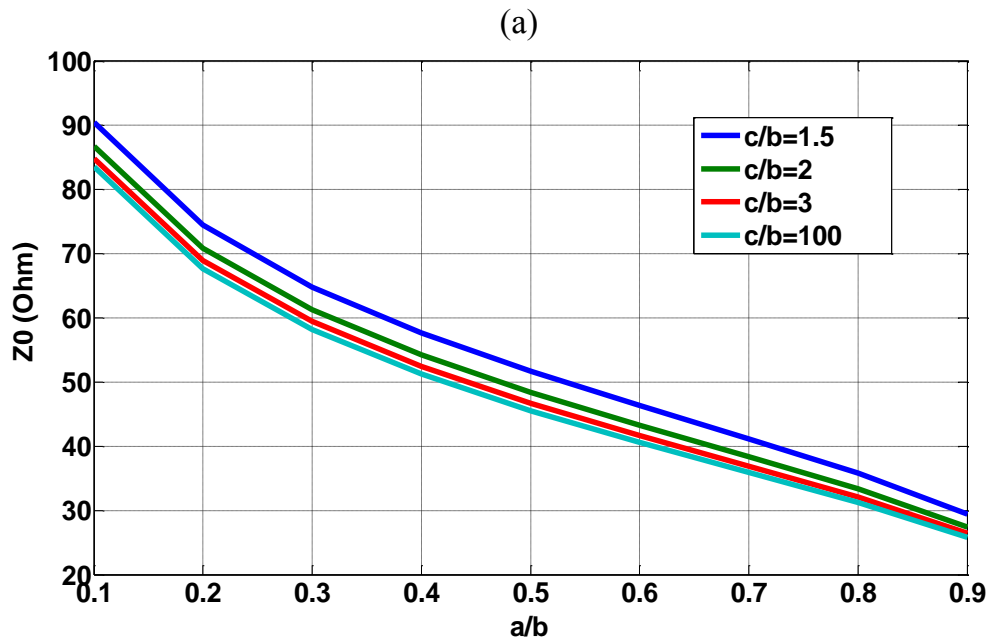
$$C = 2C_1 + C_2 \quad (2.15)$$

and total air capacitance from

$$C_{air} = 2C_1 \quad (2.16)$$

The effective permittivity and characteristic impedance of the CPW can be calculated from equations (2.2) and (2.3).

Using these equations, the graphs of Figures 2.8(a) and 2.8(b) are plotted, showing the variation of CPW characteristic impedance and effective permittivity as a function of aspect ratio a/b with c/b as a parameter.



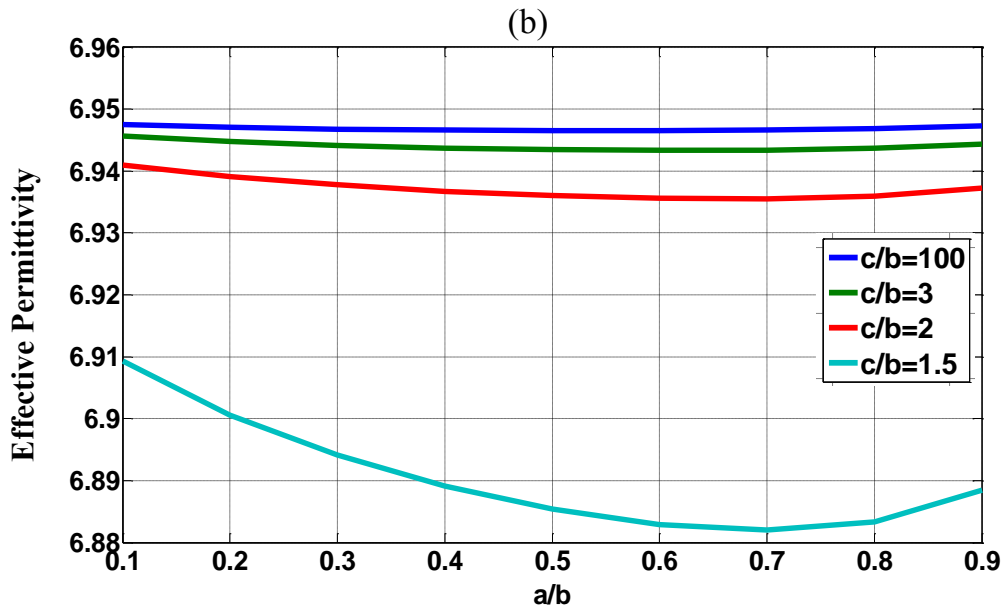


Figure 2.6: (a) Characteristic impedance and (b) Effective permittivity of a CPW with finite substrate thickness and finite ground widths. The substrate has a thickness of $h = 600\mu\text{m}$ and dielectric constant of $\epsilon_r = 12.9$.

For the graphs above, the substrate thickness is considered to be $600\mu\text{m}$ which is large enough not to affect the results in this case. It is for the thicknesses comparable to the dimension of the line, i.e. c , that the substrate thickness starts to have an effect on the characteristic impedance. For example for $c = 150\mu\text{m}$, the substrate height becomes effective on impedance at thicknesses around $300\mu\text{m}$ and decreasing the substrate thickness to lower values results in an increase in impedance. The increase in characteristic impedance by decreasing the substrate height is a result of smaller total capacitance with dielectric present. It also can be seen in graphs that increasing the aspect ratio a/b of CPW transmission line, by increasing the signal width or decreasing the gap size, results in a decrease in characteristic impedance while the effective permittivity stays almost constant. Whereas, increasing the ground size results in an increase in total capacitance and decrease in characteristic impedance and increase in effective permittivity of a CPW line. The preceding analysis provides an understanding

of the CPW line characteristics which are useful in the design process and also provides the background for analysis of the structures suggested in this work (Elevated CPW structure, Chapter 4)

2.2.3 CPW with finite substrate and backside metallisation

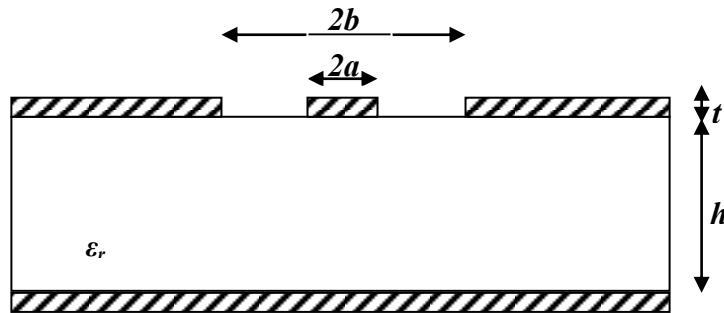


Figure 2.7: Cross Section of Conductor-backed CPW with finite substrate thickness.

In real applications, when a CPW is packaged, it becomes a conductor-backed CPW (CBCPW), as shown in Figure 2.9, and has different propagation characteristics. This structure can improve the power dissipation problem of CPW [99]. The additional ground plane forms a mixed coplanar-microstrip structure whose propagation characteristics are determined by the CPW dimensions (signal and slot width) and also the substrate thickness. The quasi-TEM analysis of this structure was performed using conformal mapping by Ghione [112].

To calculate the line capacitance, first the free space capacitance is calculated by mapping the upper half of the z -plane to the parallel plate structure in the w -plane using the Schwarz-Christoffel transformation:

$$w = \int_{z_0}^z \frac{dz}{\sqrt{(z-a)(z-b)}} \quad (2.17)$$

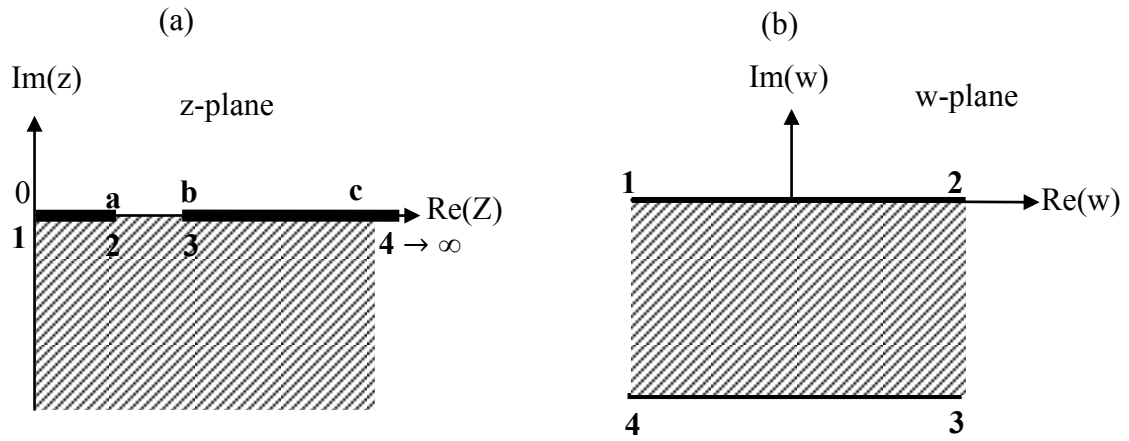


Figure 2.10: Conformal mapping of conductor-backed CPW with finite substrate to calculate free space capacitance : (a) original z-plane, (b) final mapping into a parallel-plane capacitor in w-plane.

The capacitance due to the electric field in the upper half plane, C_1 , is given by

$$C_1 = 2\varepsilon_0 \frac{K(k_1)}{K'(k_1)} \quad (2.18)$$

$$k_1 = a/b \quad (2.19)$$

$$C_{air} = C_1 \quad (2.20)$$

To calculate the capacitance contributed from the dielectric half-plane, the structure is mapped to the t -plane using the transformation function

$$t = \cosh^2 \left(\frac{\pi z}{2h} \right) \quad (2.21)$$

and then the Schwarz-Christoffel transformation being is used to map the new geometry to the parallel plate structure in the w -plane.

$$w = \int_{t_0}^t \frac{dt}{\sqrt{t(t-1)(t-t_2)(t-t_3)}} \quad (2.22)$$

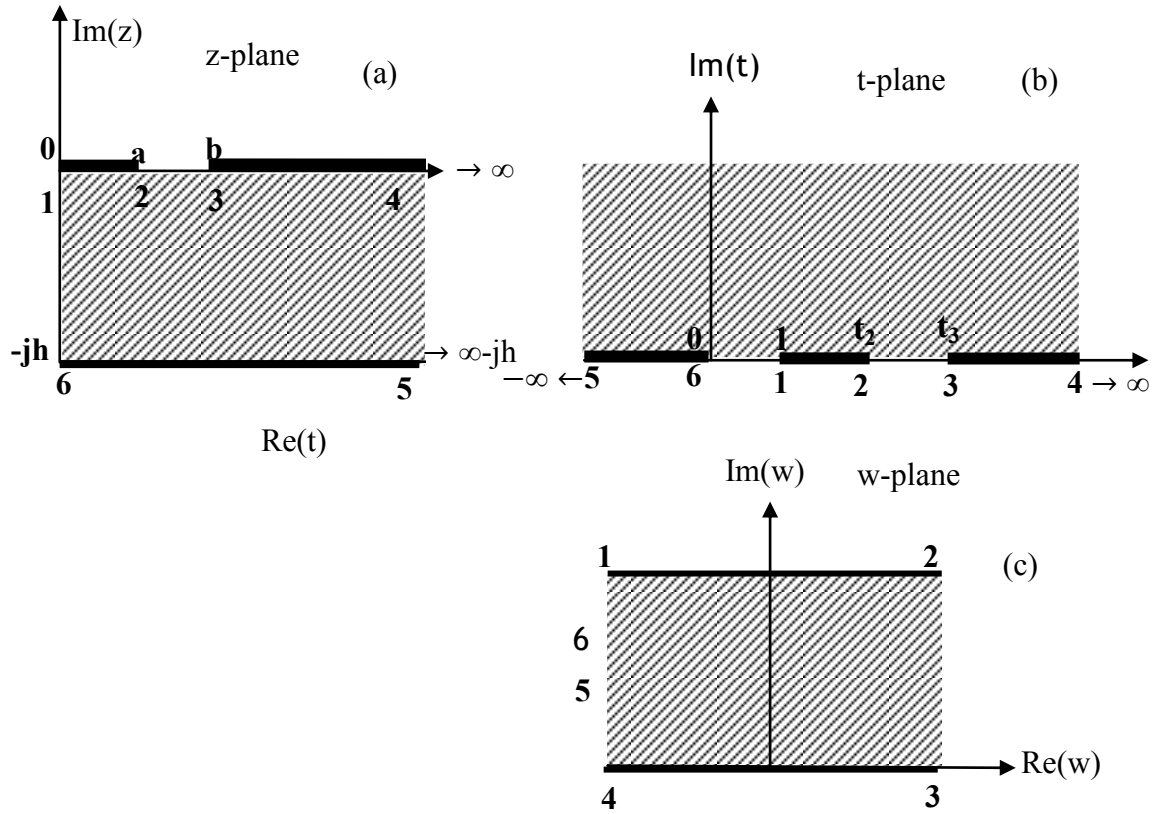


Figure 2.11: Conformal mapping of conductor-backed CPW with finite substrate to calculate the dielectric capacitance: (a) original z-plane, (b) intermediate t-plane and (c) final mapping into a parallel-plane capacitor in w-plane.

The capacitance therefore is :

$$C_2 = \epsilon_0 \epsilon_r \frac{K(k_2)}{K'(k_2)} \quad (2.23)$$

where

$$k_2 = \frac{\tanh(\pi a/2h)}{\tanh(\pi b/2h)} \quad (2.24)$$

Then the total line capacitance, C , is

$$C = C_{air} + 2C_2 + 2 \frac{C_2}{\epsilon_r} \quad (2.25)$$

The effective permittivity and characteristic impedance of a CBCPW can be calculated using equations (2.2) and (2.3). From these equations, Figures 2.12(a) and 2.12(b) can

be obtained, which show the variation of CBCPW characteristic impedance and effective permittivity as a function of aspect ratio a/b with h/b as a parameter.

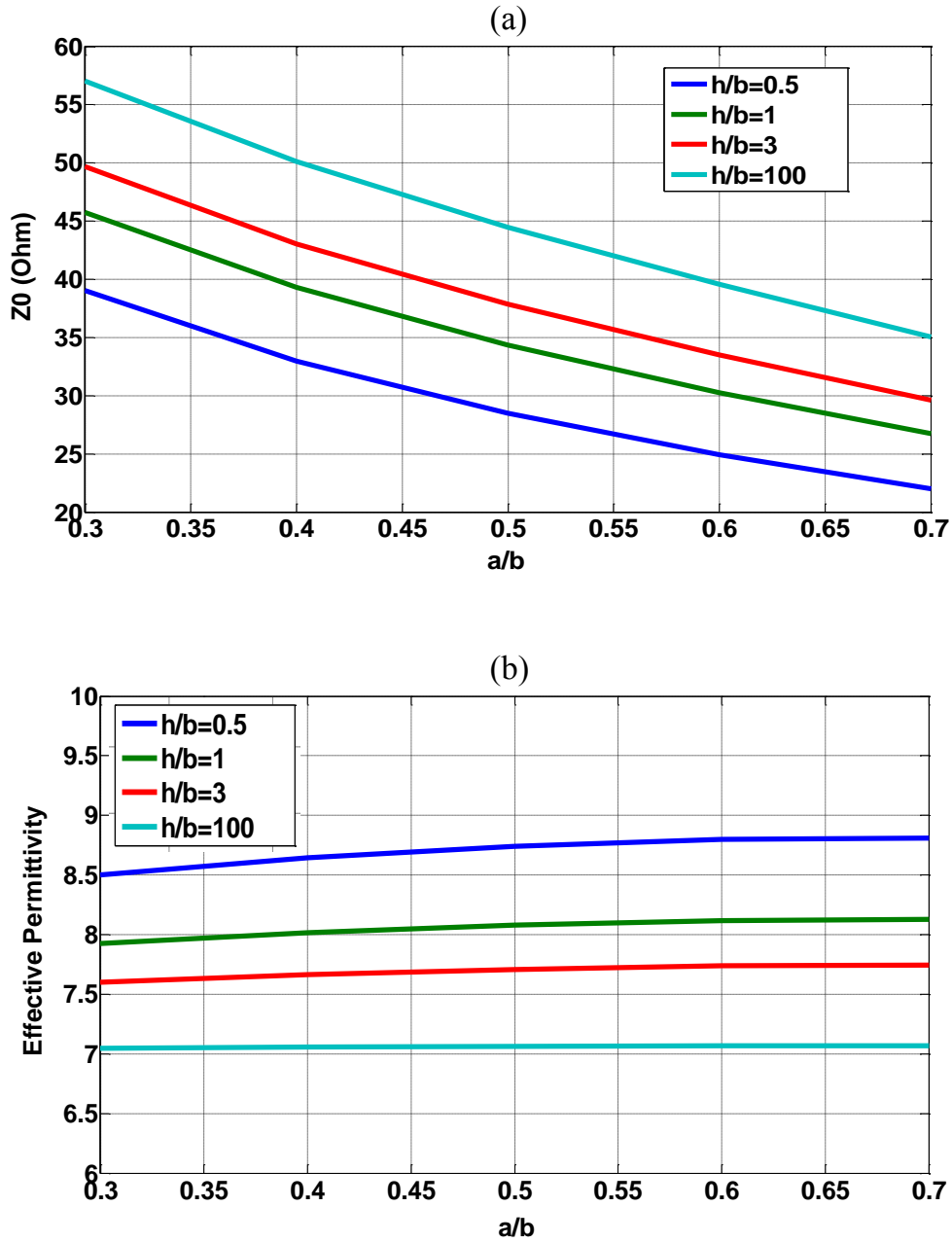


Figure 2.12: (a) Characteristic impedance and (b) Effective permittivity of a conductor-backed CPW with finite substrate thickness. The substrate has a dielectric constant of $\epsilon_r = 12.9$.

It can be seen in above graphs that decreasing the substrate thickness in conductor-backed CPW results in an increase in the line's capacitance and decrease in

characteristic impedance. However, the effective permittivity of the line increases by decreasing the substrate thickness. Also the effective permittivity is more sensitive to the line's aspect ratio at lower substrate heights compared with the thicker substrates. Similar to the CPW without backside metallisation, the lines impedance decreases with wider signal width or narrower gaps (increasing a/b). Apart from providing useful design insight, understanding the preceding analysis provides the basic background for the analysis of the novel structures suggested later in this work (Elevated Grounded CPW, Chapter 6).

2.3 Losses in CPW

As mentioned earlier in this chapter, the Coplanar Waveguide is the most popular transmission line in the design of millimetre wave circuits. This is due to a large extent to its advantages over microstrip technology. Therefore, to start our research on the development of low loss transmission line for millimetre- and submillimeter-wave applications, a comprehensive understanding of the loss mechanisms in CPW is vital. In this section, we will look at theoretical loss analyses of CPW structures on thick substrates without backside metallisation.

When electromagnetic waves propagates in a CPW structure, they suffer from three types of attenuation - conductor (ohmic) loss, dielectric loss and radiation loss.

2.3.1 Conductor loss

The attenuation due to the conductor loss, α_c , is evaluated in terms of surface resistivity and the line inductivity which is related to the skin depth, δ , which causes the effective

resistance of the conductor to increase as frequency increases. The skin depth is a function of frequency, resistivity and relative permeability, given by:

$$\delta = \sqrt{\frac{2\rho}{2\pi f \mu_0 \mu_r}} \quad (2.26)$$

where ρ , is the bulk resistivity, $\mu_0 = 4\pi \times 10^{-7}$ Henry/meter and $\mu_r = 1$ is the relative permeability. In MMIC designs, the metal thickness is usually required to be at least 5 times the skin depth in the frequency range of interest [113], which still allows thin metals to be used for millimetre-wave applications without significant conductor losses. For example, the skin depth of gold is $\sim 0.25\mu\text{m}$ at 100GHz, and components can be designed with conductor thicknesses $< 1.2\mu\text{m}$ for 100GHz and above.

The conductor loss of a CPW transmission line, α_c is given as [114]:

$$\alpha_c = 8.867 \frac{R_c + R_g}{2Z_0} \text{ dB/meter} \quad (2.27)$$

Where Z_0 is the characteristic impedance of the CPW, R_c is the series resistance of the centre conductor (2a) in ohm per unit length and is given by

$$R_c = \frac{R_s}{4(2a)(1-k_0^2)K^2(k_0)} \left[\pi + \ln\left(\frac{4\pi(2a)}{t}\right) - k_0 \ln\left(\frac{1+k_0}{1-k_0}\right) \right] \quad (2.28)$$

And R_g is the series resistance of the ground planes in ohm per unit length and is given by

$$R_g = \frac{k_0 R_s}{4(2a)(1-k_0^2)K^2(k_0)} \left[\pi + \ln\left(\frac{4\pi(2b)}{t}\right) - \frac{1}{k_0} \ln\left(\frac{1+k_0}{1-k_0}\right) \right] \quad (2.29)$$

Where $k_0 = \frac{a}{b}$, $K(k_0)$ is the empirical integral of first kind and R_s is the skin effect surface resistance and is given by

$$R_s = \frac{1}{\delta\sigma} \text{ ohms} \quad (2.30)$$

Where σ is the conductor conductivity in Siemens/meter and δ is the skin depth can be calculated from (2.26).

As can be seen, the conductor loss is a geometry dependant factor which depends on the CPW dimensions. To develop a clearer view on this type of attenuation, the conductor loss for CPW on GaAs substrate with different geometries is obtained from the 2D solver at the frequency of 60GHz and is plotted in Figure 2.13. These results are in very close agreement with the calculations-which validates our approximations.

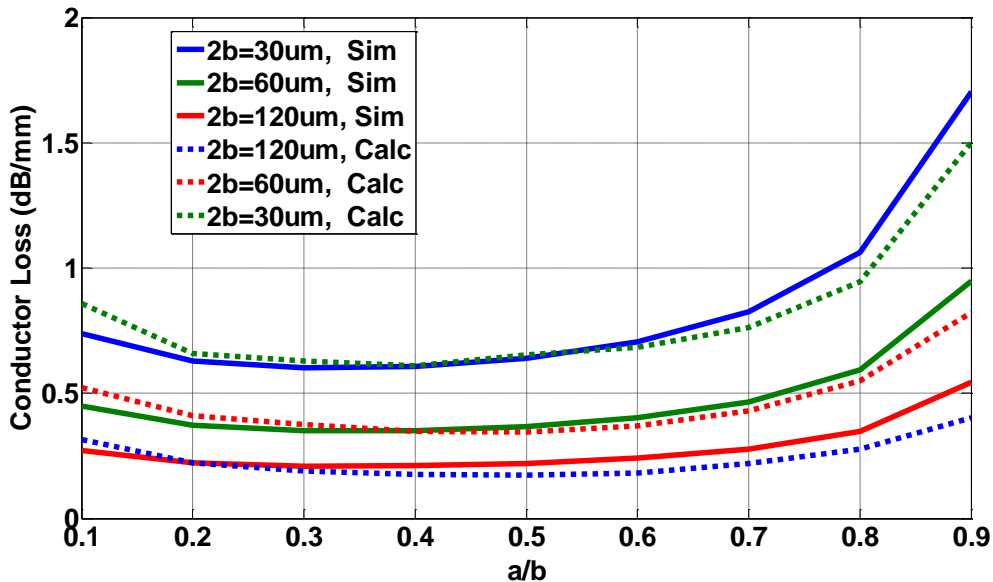


Figure 2.13: Plot of simulated and calculated conductor loss of CPW lines with three different lateral dimensions ($2b$) of 30, 60 and 120 μm for various shape ratios (signal width/lateral dimensions).

To obtain the simulation results of Figure 2.13, Ansys Q3D a 2D finite element solver is used. The software derives the quasi-static parameters, such as the loss due to the metallisation's finite conductivity, by solving Poisson's and/or Laplace's equations and is therefore unable to solve for the radiation characteristics. For modelling, a substrate relative permittivity of 12.9 is assumed, with a value of 0.0016 for the loss tangent of the substrate, and gold CPW traces with initial conductivities of 4.1×10^7 S/m and of thicknesses $2\mu\text{m}$ are used. The simulations are then repeated, replacing the gold with an ideal conductor, and the results of the two simulations subtracted to obtain the conductor losses. Since the 2D solver doesn't consider the radiation loss, this is a valid way to obtain the conductor loss.

Figure 2.13 shows that CPW with larger dimensions ($2b$) results in lower conductor loss than one with a smaller cross-section. Also the conductor loss increases by decreasing the signal width/increasing the gap or decreasing the gap/increasing the signal width for a fixed CPW dimension. Also, looking at the Figure 2.13, we can see that small signal widths and small gaps, which are required for high and low impedances, results in an increase in conductor loss. Also it can be seen in Figure 2.14 that when a fixed CPW dimension is required, having a wider gap ($b-a$) results in significantly lower conductor loss compared with having a wider signal trace ($2a$). This is mainly due to the high current density at the edges of conductors when small gaps are used, resulting in increased conductor loss. Therefore the lower impedance transmission lines are more subject to conductor loss than the high impedance lines in CPW implementations.

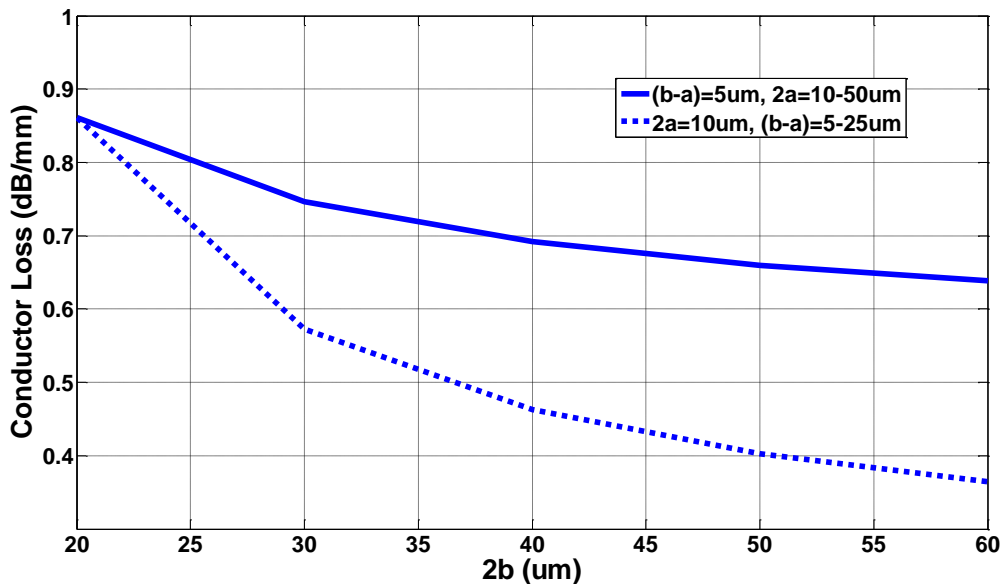


Figure 2.14: Plot of simulated conductor loss of CPW lines for various lateral dimensions ($2b$) each simulated by once keeping the signal width constant at $10\mu\text{m}$ and varying the gap size ($b-a$) and once varying the signal width ($2a$) when the gap size is constant, $5\mu\text{m}$.

2.3.2 Dielectric loss:

Dielectric loss is proportional to the loss tangent of the substrate and the CPW loss due to the dielectric effect can be written as [115]:

$$\alpha_d = 8.867 \frac{\tan\delta_c}{\lambda_0} \frac{\epsilon_r}{\sqrt{\epsilon_{re}}} \frac{\epsilon_{re}-1}{\epsilon_r-1} \pi \text{ dB/meter} \quad (2.31)$$

where λ_0 is the free space wavelength in meters, ϵ_r is the relative permittivity of the substrate, $\tan\delta_c$ is the loss tangent of the dielectric and ϵ_{re} is the simplified effective dielectric constant of the CPW and can be expressed as

$$\epsilon_{re} = \frac{(\epsilon_r+1)}{2} \quad (2.32)$$

Dielectric loss is strongly influenced by the conductivity of the substrate and also dielectric relaxation frequency. In high-quality semiconductor substrates, with relaxation frequencies in the range of terahertz and low conductivity, the dielectric loss is very small. Figure 2.15 shows the dielectric loss of CPWs with different geometries on GaAs substrate at 60GHz. The plots are from the simulation results using a 2D solver, Ansys Q3D, and are an almost exact match with the calculated values from (2.31).

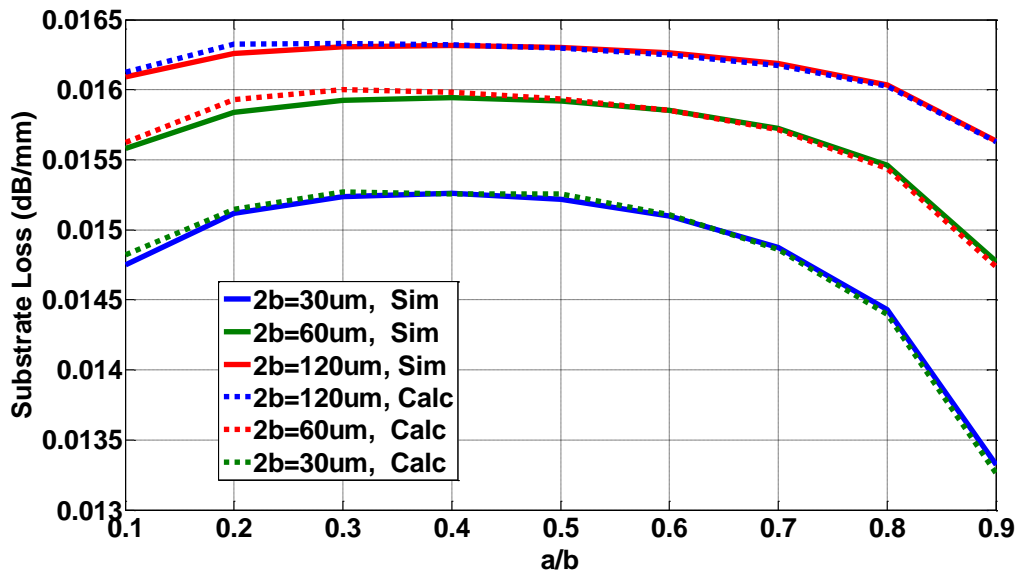


Figure 2.15: Plot of simulated and calculated substrate loss of CPW lines with three different lateral dimensions ($2b$) of 30, 60 and $120\mu\text{m}$ for various shape ratios (signal width/lateral dimensions).

The results of Figure 2.15 are achieved by simulating ideal CPW lines on GaAs substrate with loss tangent of 0.0016, to eliminate any conductor loss. Comparing the results of Fig.2.13 and Fig.2.15 shows that for the CPW structure, the dielectric losses are negligible compared with conductor losses, and that substrate losses have an opposite trend to that of conductor losses as a function of geometry.

2.3.3 Radiation loss

Beside the above mentioned losses, another kind of loss which occurs in CPW lines at higher frequencies is radiation loss due to parasitic modes such as surface waves and space modes. These losses can be controlled by substrate thickness and, permittivity, and CPW dimensions.

Excitation of different types of parasitic modes depends on the structure of the CPW. For instance, parasitic modes for the open structure of CPW are surface and space

modes, whilst the parallel plate transmission line mode is the most likely parasitic mode to be propagated for the partially covered CPW structures (like grounded CPW). Other modes which exist in CPW structure are Slotline (even) as well as CPW (odd) modes [116, 117]. In CPW with finite substrate thickness, leakage happens because of the surface wave modes of the substrate. In situations where the substrate thickness and wavelength are comparable, stronger coupling of modes to the substrate will occur [118]. Excitation of substrate modes depends on the polarization and symmetries of the substrate mode and transmission line mode. In fact, dispersion and radiation will happen when the phase velocity of the guided CPW mode exceeds the phase velocity of the substrate mode (surface wave mode). In this case, the coupling between CPW mode and substrate mode forces the energy to radiate from transmission line into the substrate. This is not the case at lower frequencies, when the phase velocity of the surface modes is much higher than CPW modes. However, as frequency increases, the phase velocity of the surface mode decreases to a value less than that of the CPW mode. Radiation begins to occur when the phase velocity of the two modes are equal. Above this critical frequency the power radiated from the line increases as the operating frequency increases [19]. In order to keep this intersection point far above the maximum operating frequency, the substrate thickness can be set such that $h < 0.15 \lambda_d$ for the lowest TM mode and $2h \approx 0.25 \lambda_d$ for the next mode - the TE_0 mode. To avoid all potential problems the following condition is required [118]:

$$h < 0.12 \lambda_d \quad (2.33)$$

A thin substrate which pushes the cut off frequency of the surface modes above the operating frequency, minimizes the leakage. In the structure with finite ground planes

(Figure 2.1(b)), due to the large non-metalized area of the line on both sides, the most significant mode is the full slab mode of substrate. Therefore, this structure has the zero cut off TE_0 and TM_0 modes and TE_0 is the first mode which interacts with CPW mode. To prevent this interaction, an even thinner substrate is required, with [118]:

$$h = 0.1 \lambda_d \quad (2.34)$$

However this rule can be difficult to meet in practical cases. For instance, λ_d for a wave propagating in GaAs substrate is $\sim 500\mu\text{m}$ at 200GHz, requiring a substrate of less than $50\mu\text{m}$. A substrate of less than $35\mu\text{m}$ is required to push the cut-off frequency of surface modes above 300GHz. Such substrates are not practical due to mechanical fragility.

In order to analyse radiations from a CPW structure with finite substrate thickness and ground planes, a set of 2-D and 3-D simulations are carried out. Ansys Q3D is used to derive the quasi-static parameters and Ansoft HFSSTM, a 3-D full wave electromagnetic simulation tool, is used to extract the frequency dependent response and radiation losses of the lines by solving the full Maxwell equations. Quasi-static simulation results show that the CPWs with smaller lateral dimension ($2b$), have lower attenuation than the larger ones. Therefore, two CPW lines with lateral dimensions of $30\mu\text{m}$ ($7.5\text{-}15\text{-}7.5$) μm and $120\mu\text{m}$ ($30\text{-}60\text{-}30$) μm are considered for comparison. The lines are simulated up to 320GHz by HFSS, a 3-D solver and Q3D, a 2-D solver. Figure 2.16 shows the results for a CPW line with $120\mu\text{m}$ lateral dimension;

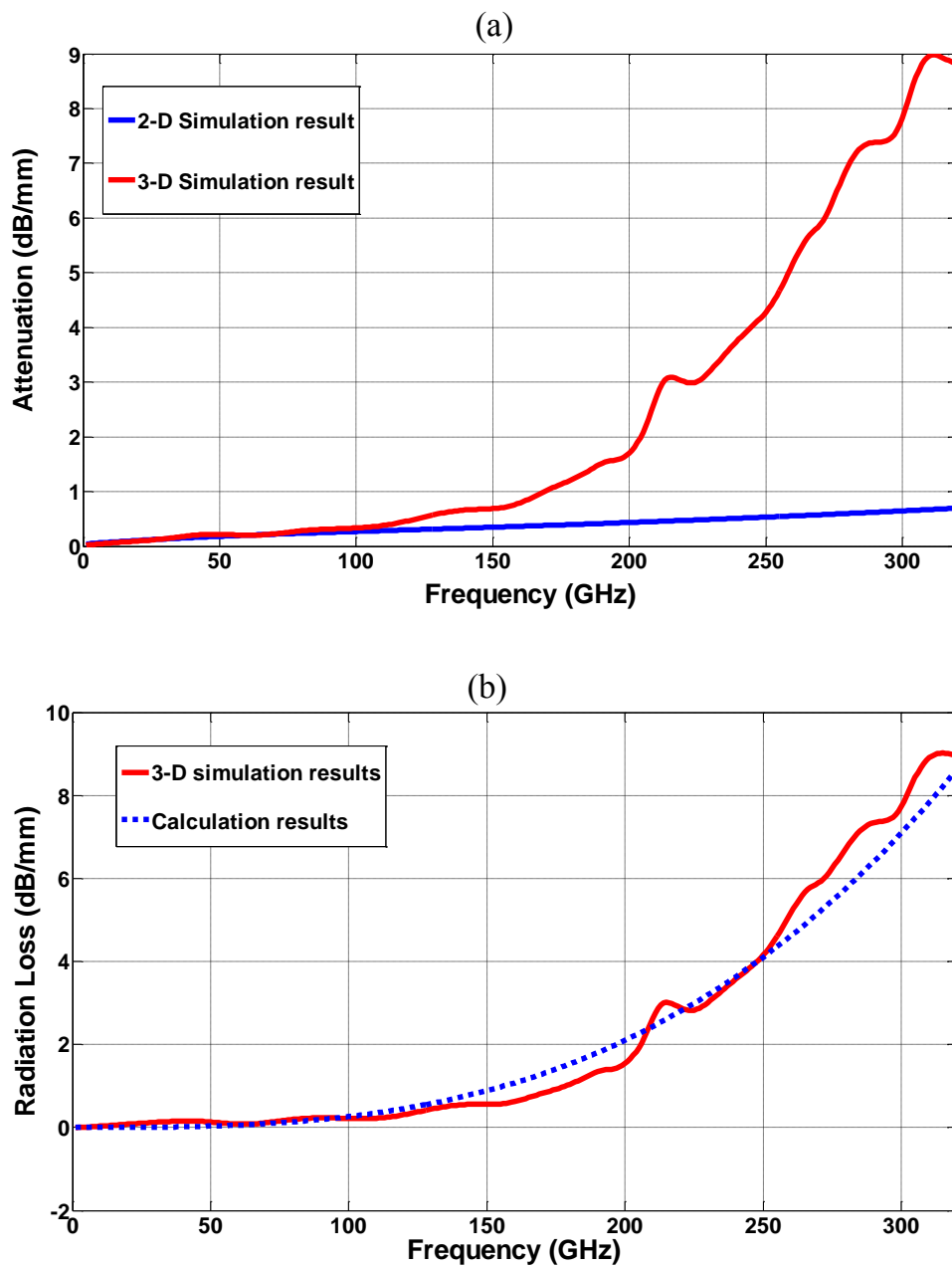


Figure 2.16: (a) 2-D and 3-D Simulation plots of total attenuation and (b) 3-D simulation and calculation results from (2.23) of a radiation loss of a CPW line with lateral dimension ($2b$) of $120\mu\text{m}$.

The 2-D simulation results account only for dielectric and conductive losses while the 3-D simulation results also include radiation losses, the difference in results which is shown in Figure 2.16 (b) indicating the radiation losses alone. As can be seen, the 3-D

results track the 2-D results at lower frequencies where the conductor losses dominate. At frequencies above 100GHz, the structure starts to radiate, and the 3-D results shows losses of almost 8dB/mm at 300GHz due to radiation.

From Figure 2.17, we can see that the CPW radiation losses can be reduced significantly by using a smaller lateral dimensions - in this case $30\mu\text{m}$.

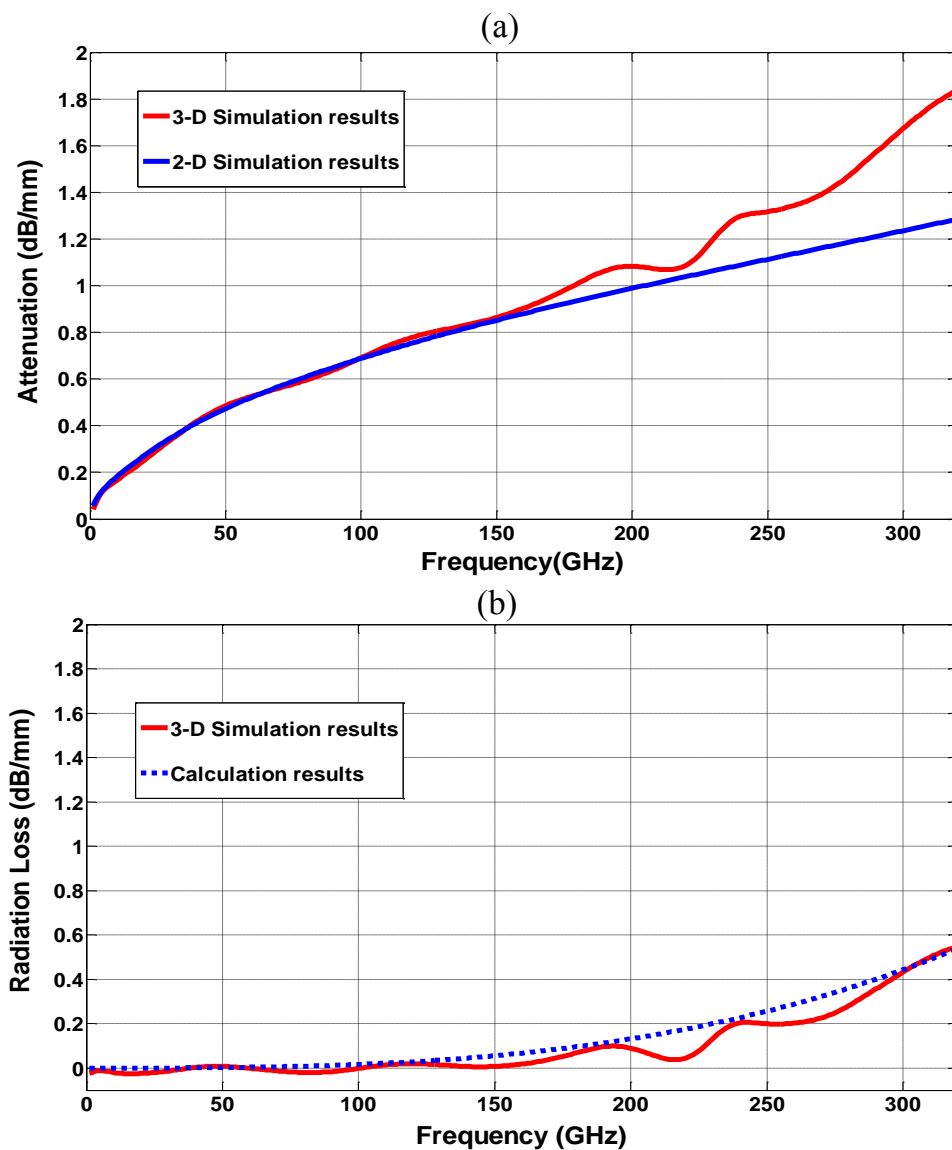


Figure 2.17: (a) 2-D and 3-D Simulation plots of total attenuation and (b) 3-D simulation and calculation results of a radiation loss of a CPW line with lateral dimension of $30\mu\text{m}$.

As can be seen in Fig. 2.17(b), these results are in agreement with those from the analytic result given in [119] as:

$$\alpha_r = 8.686 \left(\frac{\pi}{2}\right)^5 \frac{1}{\sqrt{2}} \frac{(1-1/\epsilon_r)^2}{\sqrt{1+1/\epsilon_r}} \frac{(2b)^2 \epsilon_r^{3/2}}{c^3 K'(k)K(k)} f^3 \text{ dB/meter} \quad (2.35)$$

where c is the speed of light in free space, f is the frequency, ϵ_r is the relative permittivity of the substrate, $k = \frac{a}{b}$ is a geometry dependant parameter, $K(k)$ is the complete elliptic integral of the first kind and $K'(k) = K(\sqrt{1-k^2})$.

Decreasing CPW lateral dimensions to values as low as $30\mu\text{m}$, significantly lowers radiation loss and total attenuation at high frequencies. However, implementing high and low impedance lines at these lateral dimensions is challenging. For example, to achieve a 25Ω line by keeping the lateral dimension constant at $30\mu\text{m}$, the CPW line needs to have a gap size of $2.1\mu\text{m}$ with signal width of $24\mu\text{m}$. A CPW line with these dimensions not only shows excessive loss due to the very narrow gap, but also has an impedance highly sensitive to small variations in gap size, which makes it very difficult to fabricate. Also, to achieve a 80Ω line with this lateral dimension, the CPW line should have signal width of $2.5\mu\text{m}$ and gap width of $13.5\mu\text{m}$. Having such a small centre conductor, the CPW is also subject to high conductive attenuation and sensitivity to small geometrical variations. The theoretical analysis in this section and the very good agreement between theory and our simulation results, gives us confidence in the loss analysis we will carry out for novel structures in the following chapters.

2.4 Modelling and measurement of CPW transmission lines

This section continues the description of the characteristics of CPW with an experimental investigation of its performance up to 325GHz. The previous reports of the attenuation characteristics of CPW at high frequencies, i.e. up to 1THz, used Electro-optic sampling techniques [44-46]. However, in this work we perform our measurements using network analysers up to 325GHz for the first time. Comparing our results with previously reported data, validates our measurement and simulations and also provides us with a reference for comparison with novel transmission lines.

Therefore, a comprehensive investigation of fabricated CPW transmission lines with different structures is now described. This includes the simulation and measurement of CPW lines on GaAs substrates with and without backside metallisation. The measurement and simulation results covers the frequency range 0.1-320GHz.

2.4.1 Measurement

On-wafer S-parameter measurements were performed with an Agilent PNA network analyzer over the range 140-220GHz and 220-320GHz (G and H-band) using 50 μ m-pitch WR-05 and WR-03 waveguide probes and 10MHz-110GHz using 100 μ m-pitch probes. The system was calibrated using the SOLT method with alumina ISS standards placed on an absorbing material. We checked the validity of the SOLT calibration through the measurement of long CPW lines on the ISS calibration substrate [120] which were compared with careful EM simulations. Also, the results were compared with those obtained from a TRL calibration. The two results were essentially identical but those from the SOLT calibration were smoother and so these were used in subsequent analysis. The reference planes for the measurements were placed at the

probe tips. To ensure the correct placement of the reference planes in all frequency bands, we checked that the phase of S_{21} was continuous at the cross-over frequencies. The samples were placed on thick quartz during the measurements. The Quartz spacer is used to eliminate any possible microstrip-like mode caused by the metal chuck from propagating.

2.4.2 Modelling

Simulations were carried out using three different commercial simulators - the Momentum solver in Agilent ADS 2008, Ansoft HFSSTM, a 3-D full wave electromagnetic simulation tool and Ansys Q3D a 2D finite element solver. Ansoft HFSS is used to extract the frequency dependent response and radiation losses of the components by solving Maxwell's equations. The Q3D is used here to extract the loss due to the finite metallisation conductivity and non-zero substrate conductance. The software drives this quantities by solving Poisson's and/or Laplace's equations and is therefore unable to solve for the radiation characteristics.

2.4.3 CPW transmission line on GaAs substrate without backside metallisation

We initially consider the performance of conventional CPW transmission lines at frequencies between 0.1GHz and 320GHz; specially, a set of lines with different characteristic impedances on 600 μ m thick Semi-insulating GaAs substrate whose propagation characteristics were analysed in section 2.3 above. First the performance of 50 Ω CPW transmission line with design dimensions shown in Figure 2.18 was investigated.

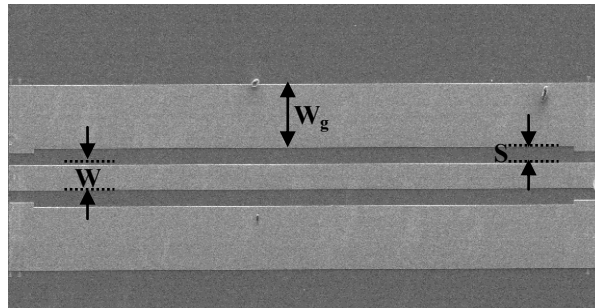


Figure 2.18: Micrograph of a 50Ω CPW transmission line. The design dimensions are: $W=35$, $S=25$ and $W_g=100$. All the dimensions are in micron.

The measurement and simulation results for this transmission line are shown in Figures 2.19 to 2.20, and can be seen to be in good agreement with one another.

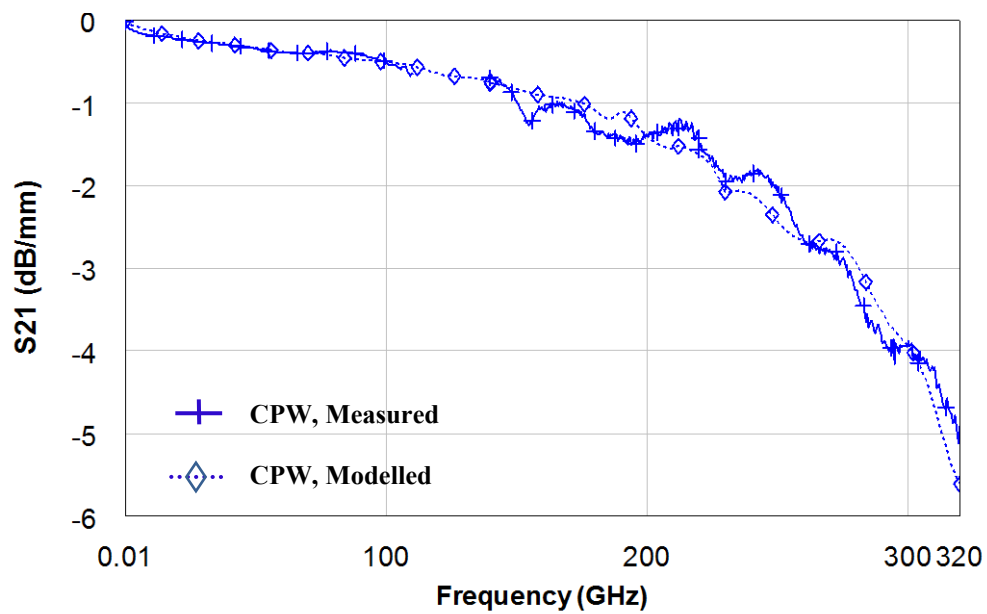


Figure 2.19: Measured and simulated S-parameters for a 50Ω CPW transmission line insertion loss.

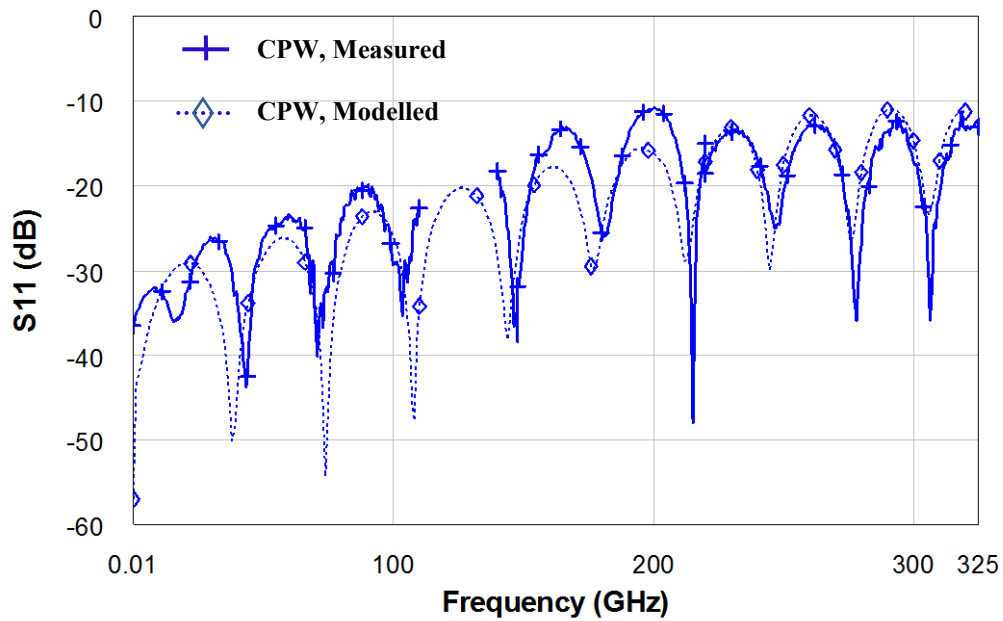


Figure 2.20: Measured and simulated S-parameters for a 50Ω CPW transmission line return loss.

Figure 2.19, shows a sharp rise in the insertion loss of these conventional CPW lines on thick GaAs substrates at frequencies above 150GHz, and it can be seen in Figure 2.20 that they suffer significant impedance dispersion at high frequencies.

The attenuation of the CPW transmission line was calculated based on following equation [46]

$$\alpha = -\frac{1}{2l} \ln (|S_{11}|^2 + |S_{21}|^2) \quad (2.36)$$

and plotted in Figure 2.21. These attenuation results are in very good agreement with the results in [44, 45].

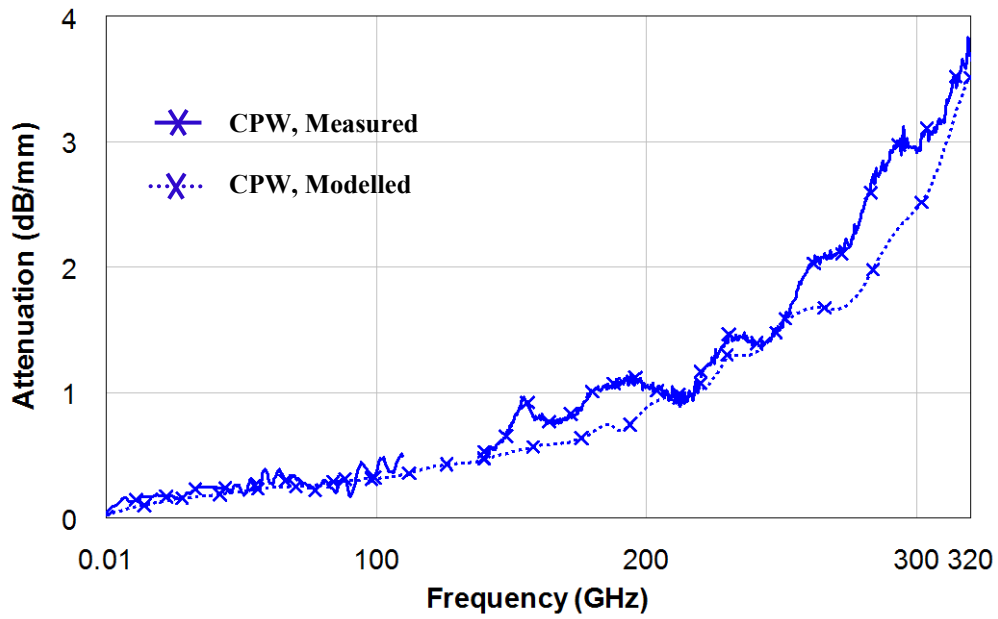


Figure 2.21: Measured and Simulated attenuation for 50Ω CPW transmission line.

Another figure of merit in evaluating the performance of passive components is the loss factor which can be written as [121]:

$$LF = 1 - |S_{11}|^2 - |S_{21}|^2 \quad (2.37)$$

By this definition, the loss factor is the difference between a normalised input power, the power transferred to the output and the power reflected from the input ports and thus it is a measure of the power loss due dielectric, conductor or radiative loss mechanisms.

The measured and modelled forward loss factors for these CPW transmission lines are shown in Figure 2.22.

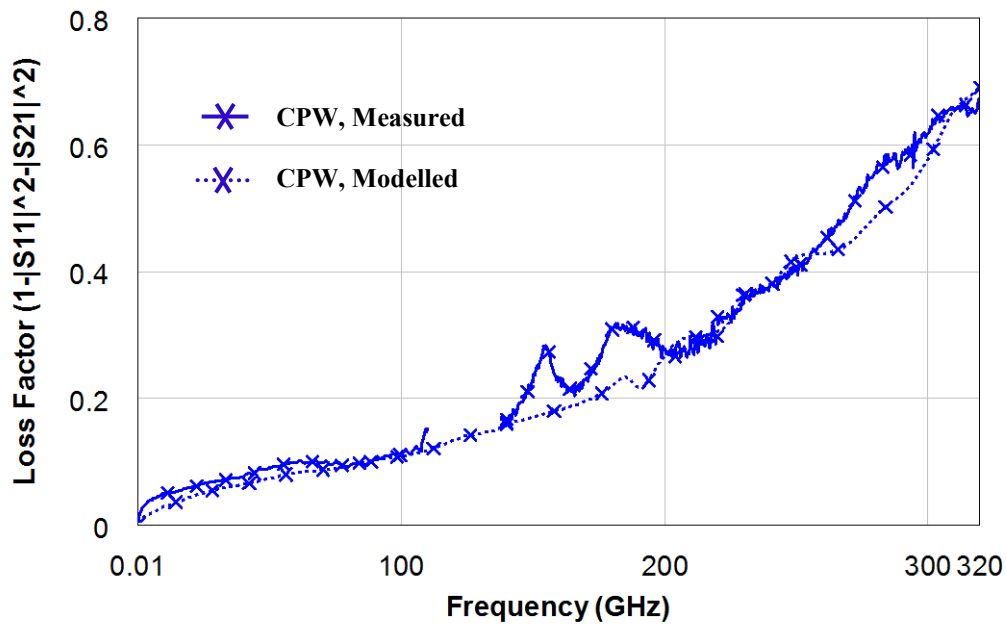


Figure 2.22: Measured and Simulated loss factor for 50Ω CPW transmission line.

It can be observed that the loss factor rises to very high values at frequencies above 150GHz and becomes around 0.7 at 320GHz. For comparison, a CPW line with the same geometry but with substrate completely removed has a loss factor of approximately 0.2. Therefore, it is desired to achieve a transmission line with a loss factor as close to this value as possible. In this way, we will know by how much we have reduced the deleterious effect of the substrate. To have a better understanding of the propagation characteristics of conventional CPW line, the cross sectional view of the electric field is plotted in Fig.2.23 for frequencies of 50, 150 and 320GHz, respectively.

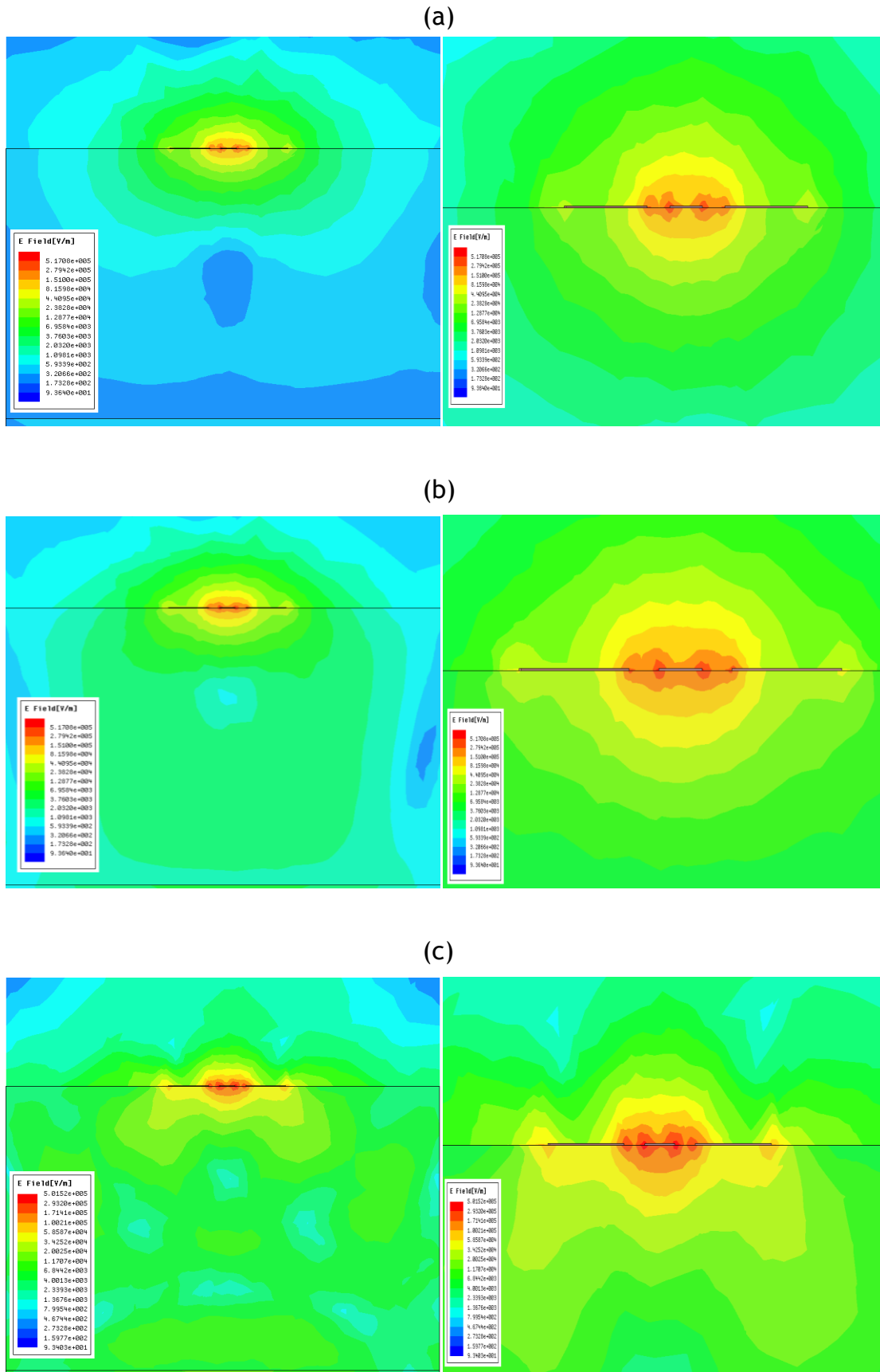


Figure 2.23: Profile of electric-field distribution modelled for CPW transmission line with finite grounds on a thick substrate and without backside metallisation at a)50, b)150 and c)320GHz, each at two different magnifications.

It can be seen in above figures that by increasing the frequency (and reducing the wavelength as a result) there is greater penetration of the electric field into the lossy substrate, increasing signal attenuation. As mentioned in the previous section, this is due to the increase in the velocity of CPW mode to values higher than the substrate mode as the operating frequency increases, as can be seen in Fig.2.23, and forces the energy to radiate to the substrate. This can be clearly seen in the radiation loss of this structure plotted in Figure 2.24 in the same way described in the last section.

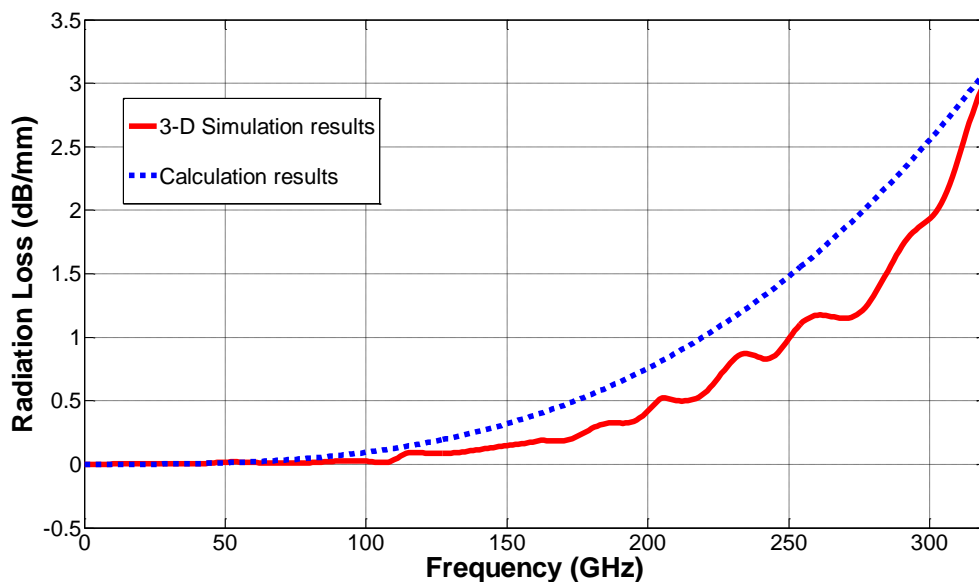


Figure 2.24: 3-D simulation and calculation results of a radiation loss for 50Ω CPW transmission line.

Figure 2.24 indicates that the radiation loss of this CPW transmission line starts at frequencies around 100GHz and increases as the frequency increases. Comparing with Figure 2.21 shows that, at higher frequencies, radiation loss dominates the total losses of the structure. In this case, radiation loss accounts for approximately 82% of total attenuation of the line while the combination of conductor and dielectric losses accounts for 18% of the total attenuation. Besides, the calculated radiation loss using (2.35) is

plotted in this figure along with the simulation results and shows reasonable agreement with our simulation results.

It was observed that a 50Ω CPW transmission line has a very high insertion loss at high frequencies. Also, it should be mentioned that CPW transmission line shows excessive loss at the impedance extremes and this further limits the usable impedance range of CPW for MMIC applications. In order to achieve a high impedance transmission line with CPW, a very narrow centre conductor is required which results in high conductor loss. For example, for a CPW line with a lateral dimension of $85\mu\text{m}$, the centre conductor width should decrease from $35\mu\text{m}$ to $5\mu\text{m}$ to increase the impedance from 50Ω to 92Ω . From the loss analysis of the previous section, the conductor loss increases from 0.2dB/mm to 0.6dB/mm by increasing the impedance from 50 to 92Ω at 60GHz .

Also in this case, the impedance becomes extremely sensitive to the CPW aspect ratio (signal to gap width ratio) and small changes in the transverse dimensions causes significant changes in the impedance. For instance, for a 90Ω line with a nominal $3\mu\text{m}$ wide centre conductor, a typical 5% change in transverse dimension produces a 4.3% change in impedance. This change is 1.8% for a 54Ω line with $20\mu\text{m}$ width centre conductor.

This makes the electrical performance of the line and consequently the circuit more greatly influenced by fabrication uncertainties [95]. On the other hand, to implement very low impedance lines, very narrow gaps are required. This causes high current density at the edges and a subsequent increase in the conductor loss [116]. In fact the common applicable impedance range of CPW for MMIC applications is considered to be from $30\text{-}80\Omega$ [58]. Fig.2.25 compares the loss factor of a 50Ω transmission line with

the $25\Omega(5\text{-}80\text{-}5\mu\text{m})$ and $94\Omega(40\text{-}5\text{-}40)$ lines, confirming the points made in discussion above.

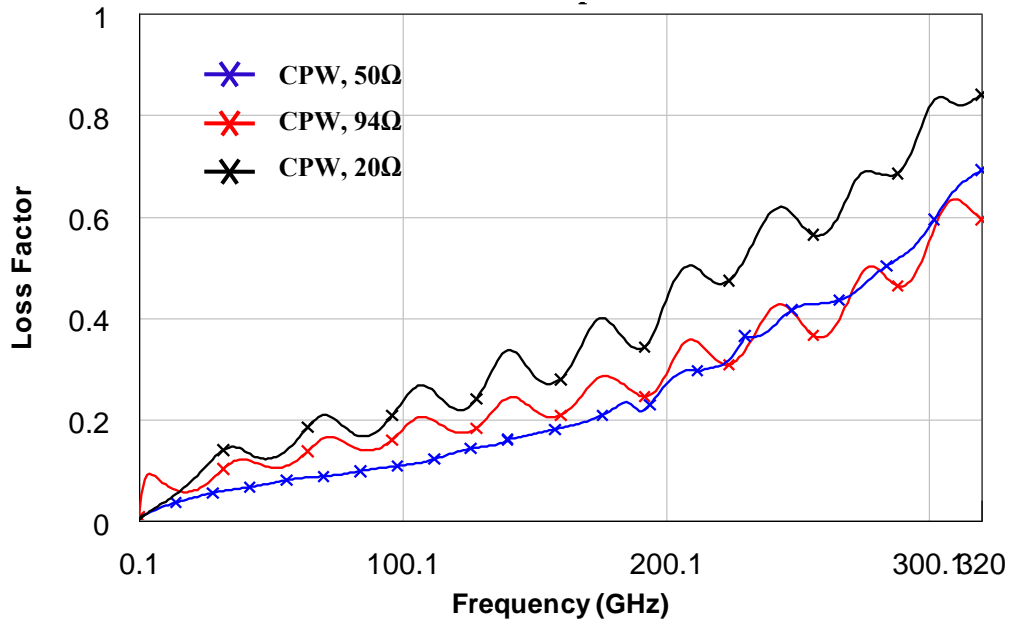


Figure 2.25: Simulated Insertion loss of the CPW with characteristic impedances of 50Ω , 20Ω and 94Ω .

Figure 2.25 shows that losses are worse for low impedance CPW, i.e. a 20Ω line with $1.4\mu\text{m}$ gap and $40\mu\text{m}$ signal width.

2.4.4 CPW transmission line on GaAs substrate with backside metallization

The measurement and simulation results of the last section shows very high insertion losses for conventional CPW at millimetre-wave frequencies. However, additional problems become manifest when the waveguides are eventually packaged for real applications. In this case, CPW structure then becomes a conductor-backed coplanar waveguide (CBCPW) which can behave like an over-moded patch antenna supporting parallel-plate modes, and can exhibit unwanted in-band resonances [52]. This problem

is exacerbated when the backside metal is brought closer to the CPW, as is necessary when the substrate is thinned to reduce thermal resistance in a CPW-based MMIC.

Figure 2.26 shows measurement results for a 50 Ω CBCPW line on a 50 μm semi-insulating GaAs substrate

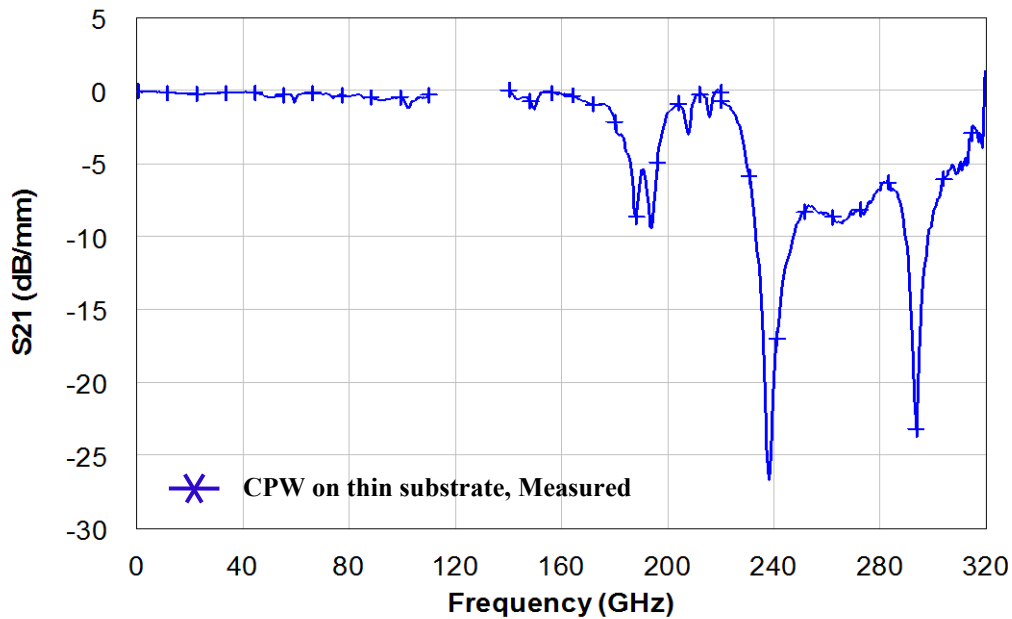


Figure 2.26: Measured Insertion loss for 50 Ω CPW line on a 50 μm thin substrate

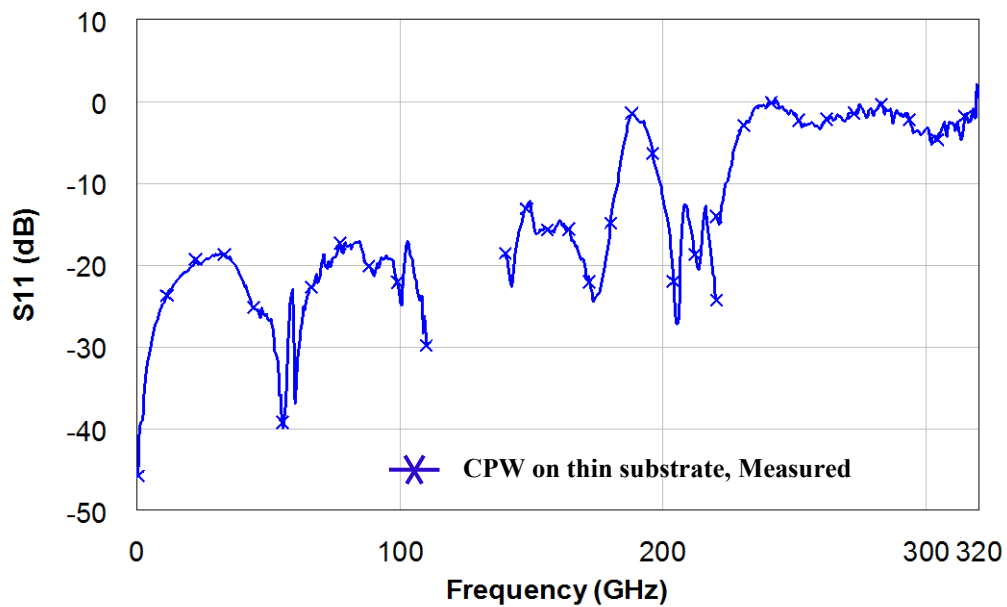


Figure 2.27: Measured Return loss for 50 Ω CPW line on a 50 μm thin substrate

These measurement results show very sharp unwanted resonances when the frequency enters the G-band. These unwanted resonances are the result of microstrip-like parasitic modes which are introduced to the line by shrinking the substrate and bringing the top and bottom metals close to each other. The electric field plots of Figure 2.28 clearly shows the changes in propagation characteristics from CBCPW line on a thick substrate to the counterpart line on a thin substrate.

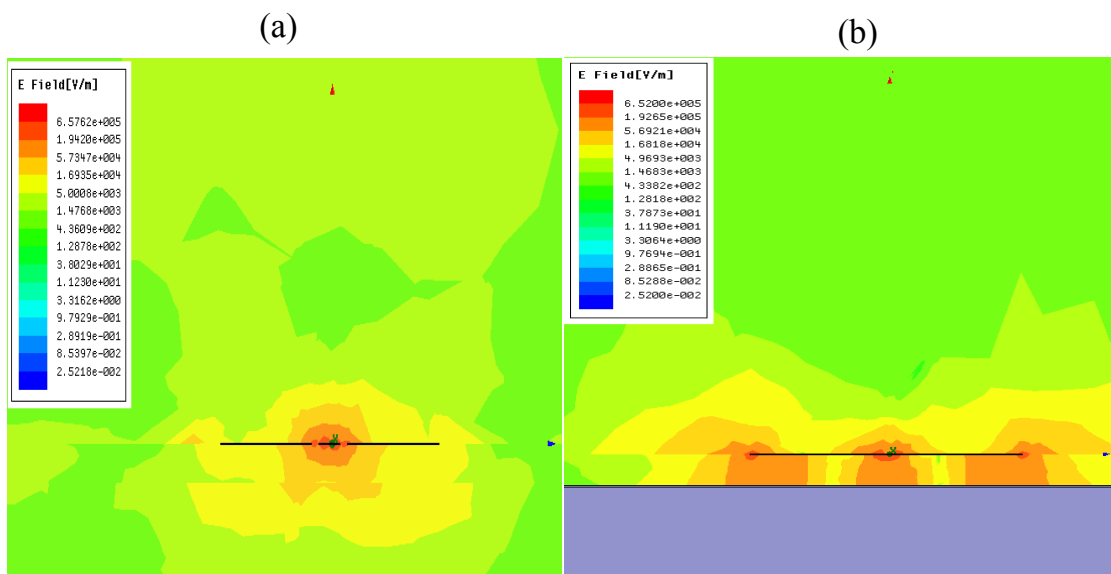


Figure 2.28: Profile of electric-field distribution modelled at 280-GHz for finite-ground conductor-backed CPW on (a) 600 μm substrate, (b) 50 μm substrate (Top ground plane width = 200 μm for all cases).

To mitigate these unwanted in-band resonances and ensure single-mode propagation for CBCPW, the addition of via holes on infinitely-wide ground planes [52], or the reduction of ground plane width [51, 122] have been previously reported. In this section, we study the effect of using via holes with finite-ground CBCPW transmission lines on 50 μm semi-insulating GaAs substrate from 10MHz to 325GHz. The work in [52] includes the results of adding via holes to infinitely-wide ground planes on a 100 μm thick GaAs substrate with measurement results up to 220GHz. In their work, they achieved suppression of resonances to a frequency of approximately 90GHz by

using vias in $100\mu\text{m}$ square and centre to centre spacing of $240\mu\text{m}$. On the other hand, none of the results on the use of finite ground width reported in [51, 122] are suggesting a resonance free CBCPW line up to 320GHz on a thin substrate ($\sim 50\text{-}100\mu\text{m}$). Therefore, in this work we are combining these two techniques – CBCPW with finite ground width and addition of via holes – with the aim of achieving resonance free lines up to 320GHz on a $50\mu\text{m}$ thick GaAs substrate.

First, comprehensive modelling was done using ADS (Agilent) to study the effect of ground width, via holes and substrate thickness and to design a transmission line with optimum ground width and via configuration on a thin substrate. Then, based on these modelling results, an optimized CBCPW was fabricated and measured. The modelling results are summarised as follows.

2.4.4.1 Modelling results

A. Effect of topside ground plane width (without Vias)

Reducing the width of the topside ground planes in order to have finite-ground CBCPW without vias is a simple method that has been suggested to ensure single-mode propagation. This method has been shown to work well with thick substrates but when the substrate is thinned to around $50\mu\text{m}$, resonances at frequencies around 150GHz can appear. In fact, at frequencies where the wavelength becomes comparable to the lateral line dimensions, the topside ground planes of CBCPW can act as patch antennas which support unwanted modes and cause numerous resonances [52]. The modelling results shown in Figure 2.29 highlight the fact that resonances are strongly dependent upon the topside ground widths. For CBCPW with $400\mu\text{m}$ -wide grounds on $50\mu\text{m}$ substrate, resonances begin at around 100GHz . Reducing the width of the CPW ground planes can

push the onset of these resonances to higher frequencies, with 200 μm wide grounds exhibiting resonances that start at 210GHz and 100 μm -wide grounds showing only minor resonance peaks up to 320GHz.

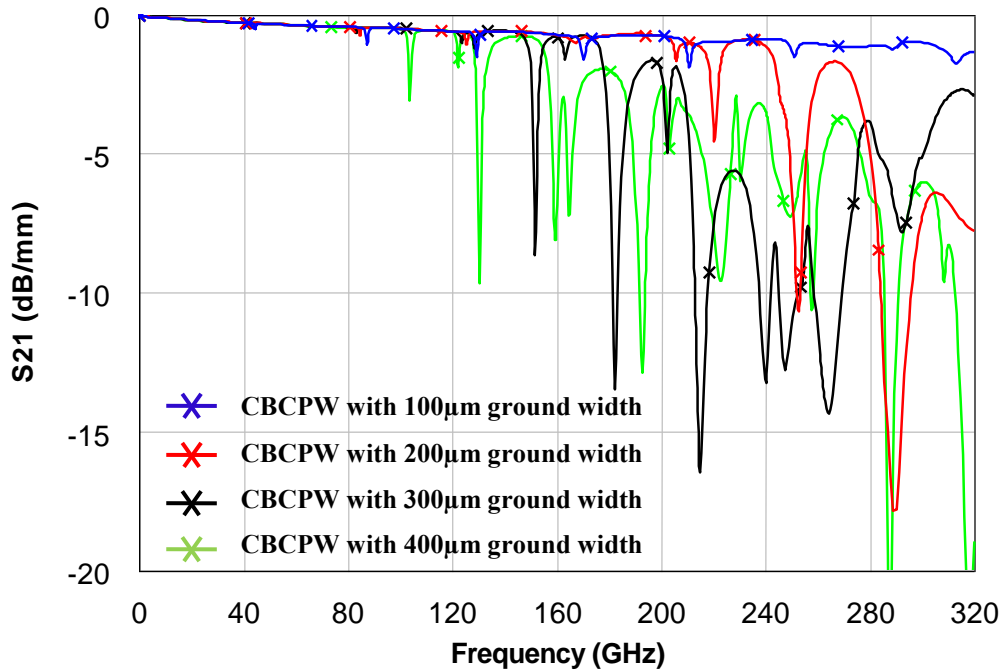


Figure 2.29: Modelled transmission response of CBCPW (without vias) on 50 μm substrate with different widths of finite-ground.

B. Effect of via holes separation

Another method of suppressing parasitic modes for CBCPW was suggested by Haydl [52]. It was indicated that parasitic resonance suppression up to 90GHz could be achieved by inclusion of via holes in an infinite ground CPW on 100 μm GaAs substrate. The cross-sectional view of a CBCPW with via holes connecting the top and bottom grounds is shown in Figure 2.30.

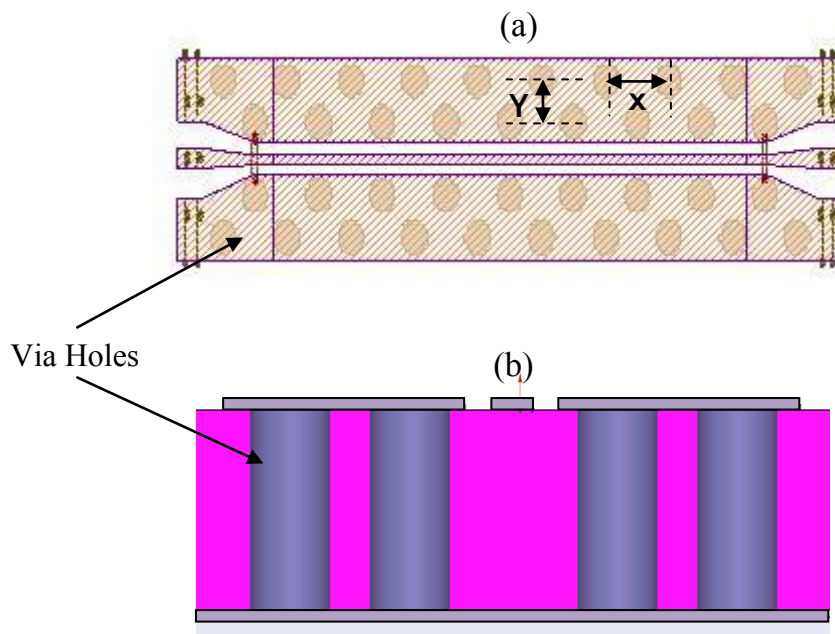


Figure 2.30: (a) The layout and (b) Cross sectional view of the conductor-backed CPW transmission line with via holes connecting the top and bottom grounds.

Building on this work, and with the goal of achieving resonance-free transmission lines which are compatible with packaging requirements for MMIC applications to at least 320GHz, we investigated the effect of distance and configuration of these via holes on the performance of finite-ground CBCPW on 50 μm thickness substrate. Cylindrical thru-substrate vias were placed at various horizontal and vertical separation distances within the 200 μm -wide top ground planes. The simulated performance of 50 μm thick CBCPW with different via configurations are compared in Figure 2.31.

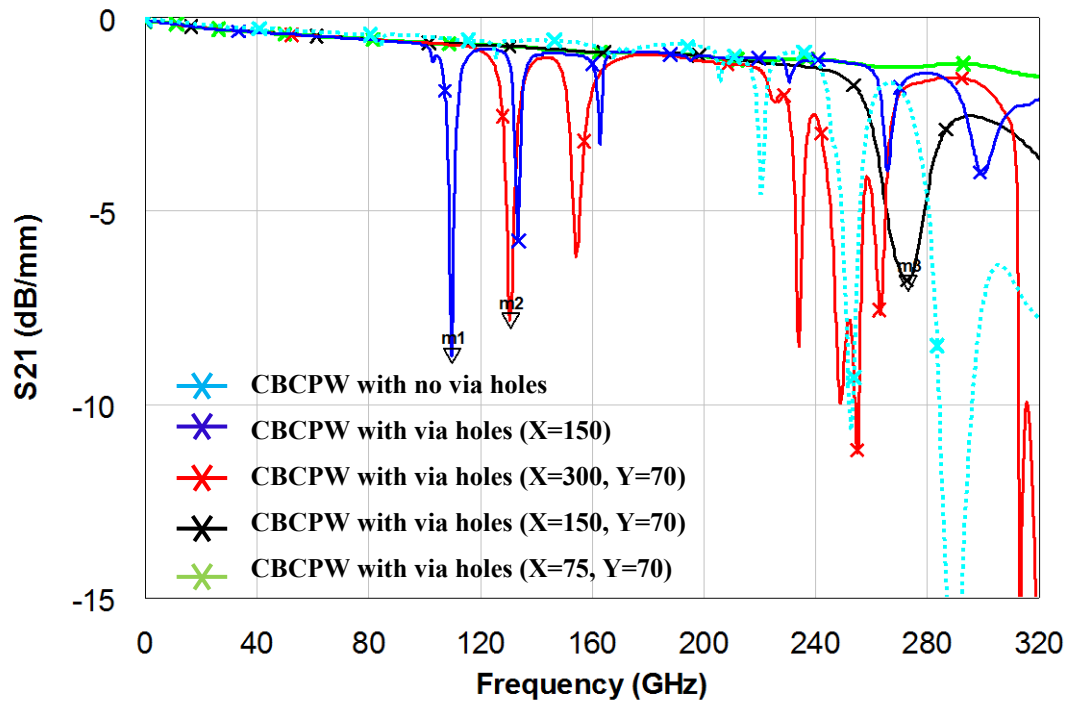


Figure 2.31: Modelled transmission response of finite-ground CBCPW on $50\mu\text{m}$ substrate with different via hole separation pattern. Top ground plane width= $200\mu\text{m}$ in all cases.(X and Y are shown on the layout in Fig.2.30).

Looking at Fig.2.31, we can see that just adding via holes to the structure, doesn't make significant difference to the structure. In fact, the density of the vias is a major factor in suppressing the resonances in the frequency range of interest. For example, Figure 2.31 reveals that in order to achieve a resonance free transmission line for frequency range of 0.1-320GHz, via holes as dense as around $70\mu\text{m}$ in both X and Y directions are required. Also this figure shows that the structure with vias of $150\mu\text{m}$ horizontal and $70\mu\text{m}$ vertical separation, exhibits a resonance frequency at around 280GHz (black curve). Also our experiments show that via holes situated in random patterns do not necessarily improve the performance and resonance separation still depends on the via spacing.

To illustrate the transmission mode behaviour at resonance, we used the 3D full-wave solver (HFSSTM) to inspect the cross-sectional electric-field distribution of the finite-

ground CBCPW transmission lines. Figure 2.32 shows that the microstrip-like mode caused by the bottom metal can be effectively suppressed by adding via holes as expected. However, the placement of via holes still has a crucial impact on the extent to which resonances can be suppressed. Fig.2.31 shows that the most dense pattern of vias gives the most effective suppression up to 320GHz.

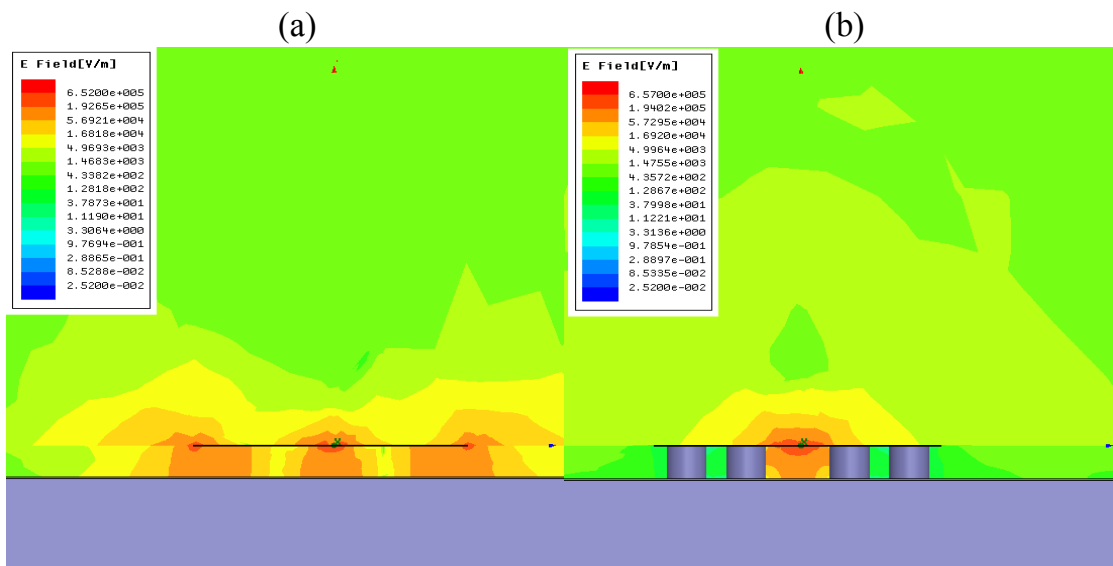


Figure 2.32: Profile of electric-field distribution modelled at 280-GHz for finite-ground conductor-backed CPW on (a) 50 μ m substrate without via holes, and (b) 50 μ m substrate with via holes. (Top ground plane width = 200 μ m for all cases).

C. Effect of substrate thickness

Finally, to examine the effect of substrate thickness on the performance of CBCPW with finite-grounds, we modelled, for the first time, the structure of Fig.2.30 on both 50 μ m and 100 μ m thick substrates. A comparison of the transmission response is shown in Fig.2.33. This clearly shows that a smoother transmission loss response with higher resonant frequency is obtained for the 50 μ m substrate. These observations may be attributed to the reduction of via hole inductance at sub-millimetre-wave frequencies for the thinner substrate. Since the work in [52] uses a 100 μ m thick GaAs, this comparison

gives us an indication of ultimate substrate thickness for CBCPW line with the presence of via holes.

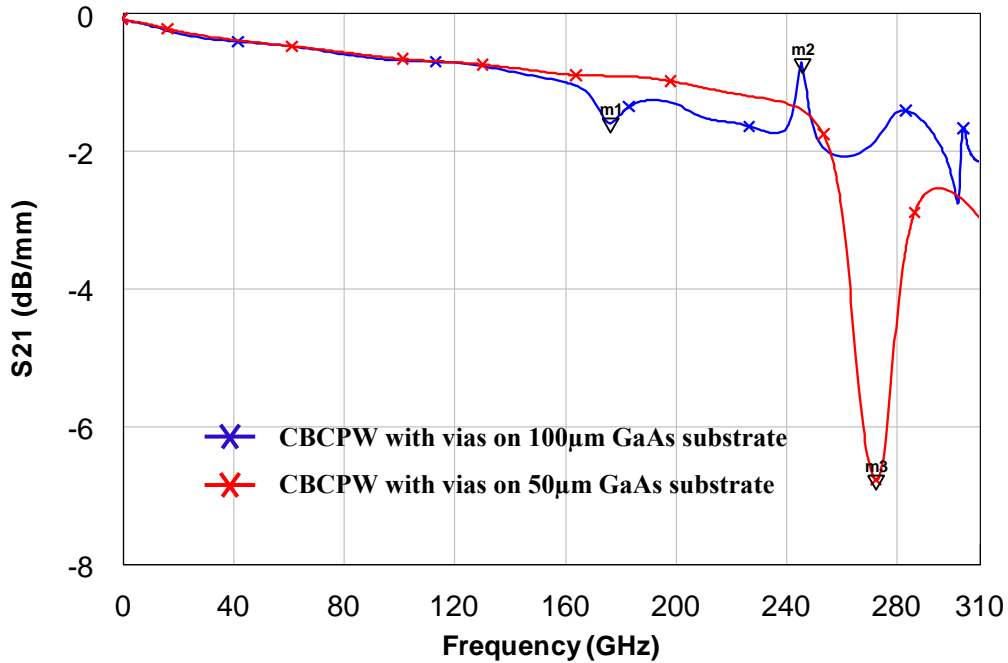


Figure 2.33: Modelled transmission response of finite-ground CBCPW with vias on 50 μm and 100 μm thickness substrate. (Top ground width=200 μm , via spacing: X=150 μm and Y=70 μm)

2.4.4.2 Experimental results

To verify the modelling results experimentally, a set of uniform finite-ground CBCPW transmission lines (with and without grounding vias) was fabricated initially on a thick semi-insulating GaAs substrate. The substrate was then thinned to 50 μm using a mechanical lapping process followed by a chemical stress relief etch. Thru-substrate via holes of 30 μm diameter were patterned and fabricated using a dry-etch process with backside alignment. Finally electroplated gold was formed in the via holes and over the complete backside of the substrate. Figure 2.34 shows a micrograph of the fabricated structure with very closely spaced via holes.

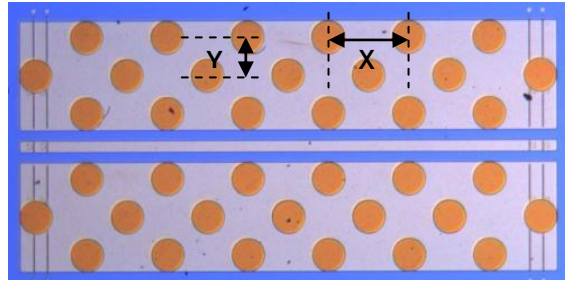


Figure 2.34: Top view optical picture of fabricated finite-ground CBCPW test structure with via holes separated by $X=150\mu\text{m}$ and $Y=70\mu\text{m}$.

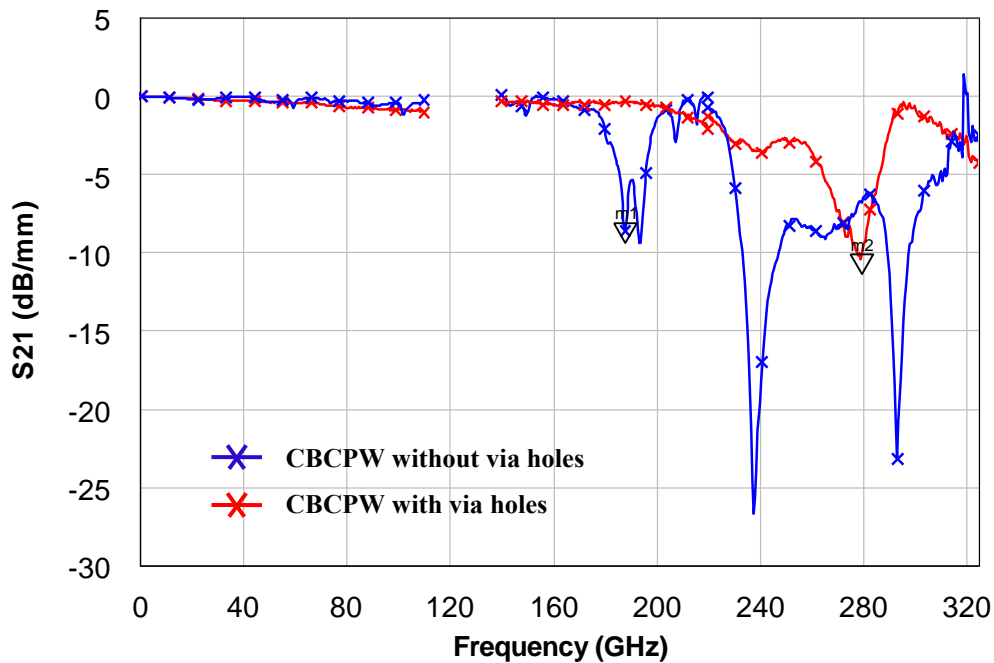


Figure 2.35: Measured transmission response of finite-ground CBCPW: *with* via holes (via spacing: $X=150\mu\text{m}$ and $Y=70\mu\text{m}$) and *without* via holes. (m_1 : 187.6GHz, m_2 : 279.3GHz)

The measured response of the finite-ground CBCPW with and without via holes are compared in Figure 2.35. This shows that inclusion of via holes is vital to pushing the unwanted resonance to higher frequency, in this case around 280GHz, as indicated in our modelling.

To verify our modelling approach, we compared the results from section 2.4.4.1 with measurements. Figs. 2.36 and 2.37 show the good agreement obtained up to 320GHz.

The insertion loss of finite-ground CBCPW with grounding vias was 1.01dB/mm at 200GHz.

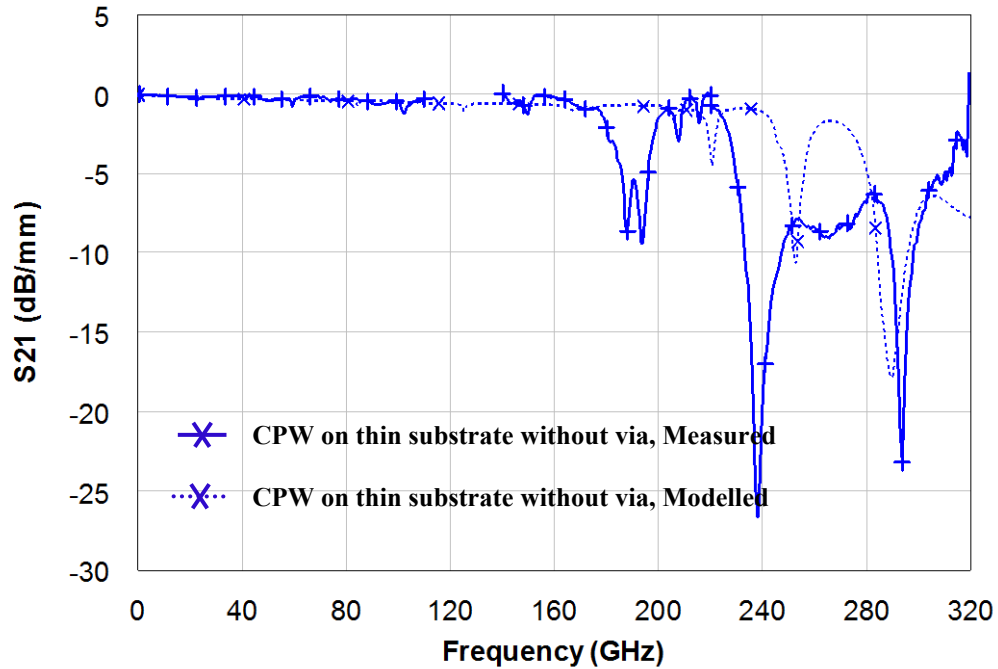


Figure 2.36: Comparison of transmission response for finite-ground CBCPW without via holes.

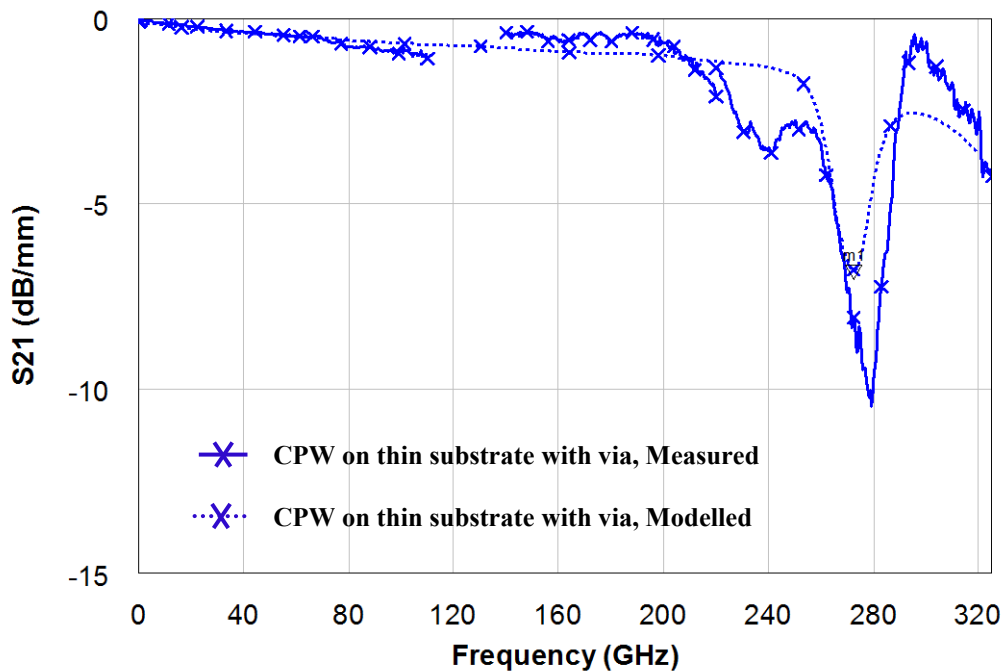


Figure 2.37: Transmission response of finite-ground CBCPW with grounding via holes. Via hole centre-to-centre separation $X=150\mu\text{m}$ and $Y=70\mu\text{m}$. Topside ground width = $200\mu\text{m}$.

This study shows that the frequencies of transmission resonance of a CPW on thin substrate are dependent on (i) the topside ground plane widths and (ii) the density of via holes which connect the topside and backside ground planes. To maintain a superior performance with finite-ground CBCPW transmission lines, the centre-to-centre separation distance between via holes should be kept less than $\lambda/4$ for the highest frequency of interest. A reduction in insertion loss and smoother results were also observed on substrates which were thinned to $50\mu\text{m}$ thickness.

As both modelling and experiment shows, adding via holes is an effective way of pushing transmission resonances to higher frequencies, but even the most densely arranged via holes cannot suppress the resonances completely at sub-mm-wave frequencies. In addition, the fabrication process required for adding via holes is difficult and time consuming. These facts, prompted us to consider an alternative transmission line with a simpler fabrication process called elevated coplanar waveguide as a more manufacturable solution to suppressing resonances at mm-wave frequencies - a solution discussed in detail in chapter 4 and subsequent chapters.

In the following sections, we are continuing our research on the investigation of some essential passive networks on thick substrate CPW theoretically and experimentally. Since to the authors knowledge, there is very little in literature on the performance of these networks at frequencies up to 320GHz, these investigations gives us a ground for comparison which will be made later in this thesis on elevated structures.

2.5 CPW Resonators

Resonators form the basic design elements in many microwave components. They can be used in filters, oscillators, frequency meters and tuned amplifiers. Advances in

microwave and millimetre-wave integrated circuits mandate that high performance planar resonators be used as building blocks for low-cost and highly sophisticated communication systems. Today, while the subject of resonators is mature, there is relatively little literature on coplanar waveguide (CPW) resonators in the millimetre-wave regimes. The performance of the CPW open and short circuited quarter-wavelength resonators in W-band (0.1-110GHz) is studied in [49] and the CPW open stub at 203GHz is reported at [50]. However there is no report on the performance of the CPW short circuit resonator in G-band and neither of them in H-band (220-320GHz). Therefore the novelty of our work compared to the previous works is the frequency extension.

A series of open and short circuit matching stubs (quarter-wavelength resonators) were designed and fabricated for different frequencies in G and H frequency bands. The theoretical and experimental studies of these components are discussed below.

2.5.1 Quarter-wavelength CPW open-circuited stub

An open-circuited length of transmission line will act as a practical resonator. As shown in Fig.2.38, it behaves as a series resonant circuit at frequencies of multiples of $\lambda/4$ [29].

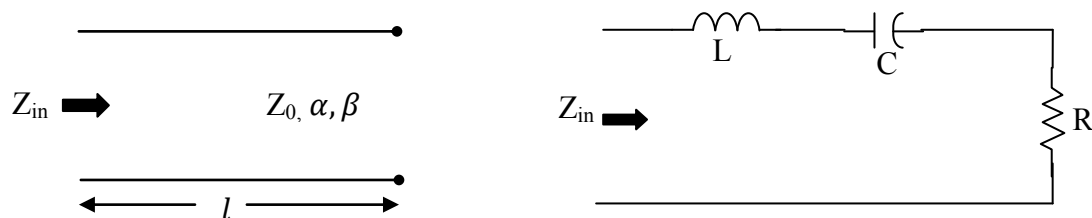


Figure 2.38: A lumped-element equivalent circuit of an open-ended transmission line used as a resonator. $l = (2n - 1)\lambda/4$

One of the important parameters of a resonant circuit is Q , or quality factor which is a measure of the loss of the resonant circuit – lower loss implies a higher Q . The Q of this resonator can be expressed as

$$Q = \omega \frac{\text{(average energy stored)}}{\text{(energy loss/second)}} \quad (2.38)$$

$$Q = \omega \frac{W_m + W_e}{P_{loss}} \quad (2.39)$$

$$Q = \frac{\omega_0 L}{R} = \frac{1}{\omega_0 RC} = \frac{\pi}{4\alpha l} = \frac{\beta}{2\alpha} \quad (2.40)$$

Which shows that Q increases as the attenuation of the line decreases, as expected. Therefore in order to achieve an open-circuited resonator with high quality factor, one needs to obtain a transmission line with minimum attenuation.

In order to take the effect of input and output loading into account, the quality factor of a resonator can be broken down to the loaded (Q_L), unloaded (Q_u) and external (Q_{ext}) quality factors. The loaded Q is the quality factor which considers the loading effects of the resonator itself and also the external circuits. Q_L is the only quality factor of a resonator that can be actually measured, while Q_u and Q_{ext} needed to be extrapolated. The loaded Q of an open-circuited resonator obtained from measured S-parameters can be written as [123]:

$$Q_L = \frac{f_0}{\Delta f_{3dB}} \quad (2.41)$$

Where f_0 is the resonant frequency and Δf_{3dB} is the 3dB bandwidth of S_{11} . The external and loaded Q of the band-stop resonator (open stub) then can be obtained from:

$$Q_{ext} = \frac{Q_L}{S_{11}(f_0)} \quad (2.42)$$

$$Q_u = \frac{Q_L}{1 - S_{11}(f_0)} \quad (2.43)$$

where $S_{11}(f_0)$ is the reflection coefficient at centre frequency. In distributed networks, reducing the total attenuation of a transmission lines, improves unloaded and loaded quality factors of the resonator circuit.

Besides, to clearly observe the relationship between the quality factor of the loaded stub and characteristic impedance of the employed transmission lines, we consider the scattering parameters of a quarter-wavelength shunt open-circuited stub given by [125]

$$S_{21} = \frac{1}{1 + j \frac{Z_0}{2Z_{0s}} \tan \theta} \quad (2.44)$$

$$S_{11} = -j \frac{Z_0}{2Z_{0s}} \tan \theta S_{21} \quad (2.45)$$

Where Z_0 is the impedance of the feeds and Z_{0s} is the impedance of the stub. and

$$\theta = \beta l = \frac{2\pi}{\lambda_g} l = \frac{2\pi f \sqrt{\epsilon_{eff}}}{c} \quad (2.46)$$

Where c is the speed of light and ϵ_{eff} is the effective permittivity of the line.

The plot of the S_{11} and S_{21} is given in Fig.2.39 for the shunt open stubs with constant feed impedance of 50Ω and various impedances at the stub.

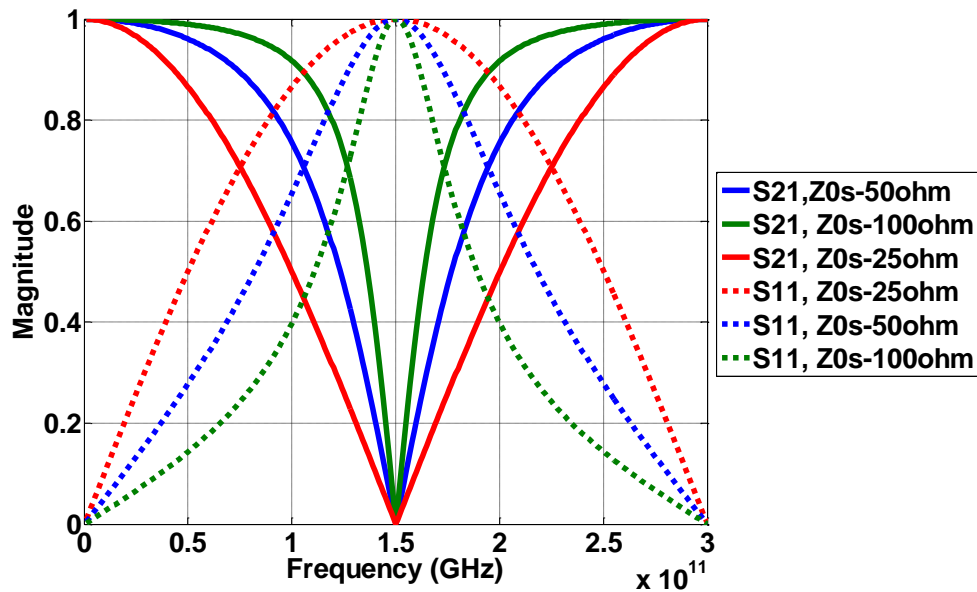


Figure 2.39: Simulated S-parameters for a quarter-wave length open-circuited stub with a fixed feed impedance of 50Ω and various impedances at the stub.

With the impedance of the feed lines constant, one can improve the loaded quality factor of the shunt open-circuited stub by utilising high impedance stub lines. Further improvement is given by decreasing the impedance of the feed lines. In fact, the best performance is achieved by using very low impedance feed lines and very high impedance stub lines. Increasing or decreasing the impedance of both feed and stub together makes no significant change in the performance of the open-circuited stub.

Therefore, transmission lines with low loss at high and low-range impedances are required to achieve the best performing open-circuit matching network.

A series of open circuit stubs were designed with CPW line for different frequencies at G and H-band.

The MMIC CPW open circuit stub is depicted in Figure 2.40 [124].

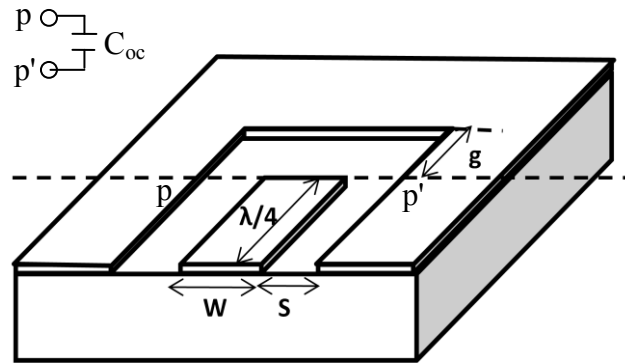


Figure 2.40: Structure of an open-circuited matching stub implemented by CPW transmission line.

The stop-band resonance of the stub occurs when the mean length is $\lambda_{eff}/4$ and the pass-band resonance occurs when the stub length is $\lambda_{eff}/2$. The resonant frequency of the open circuit stub, f_0 , is theoretically predicted as

$$f_0 = \frac{c}{4L\sqrt{\epsilon_{eff}}} \quad (2.47)$$

ϵ_{eff} is almost 7 for CPW on a GaAs substrate.

In order to design the open circuit stub for a certain frequency, the stub length (L)

$$L = \frac{c}{4f_0\sqrt{\epsilon_{eff}}} \quad (2.48)$$

is calculated from the above equation. The other issue which should be considered in the design of open stubs is the so-called length extension, l_{ext} . This effect appears as a result of the end capacitance due to the fringing electric fields across the end gap, g . This end capacitance increases the capacitive reactance which is seen at the plane p-p' due to the open end of the centre conductor. This causes the apparent position of the end circuit to be beyond the physical end of the centre conductor by l_{ext} . In CPW open circuits with fixed geometries, the length extension decreases by increasing the end gap, g and eventually saturates. Based on [124], in order to minimize the parasitic length

extension, it is sufficient to choose the end gap, g , equal to the CPW ground to ground spacing, $d = W + 2S$. This rule was considered in our design and g was chosen to be $2d$. Under this condition, the parasitic length extension to open stub is reported to be

$$l_{ext} \approx \frac{1}{4} \cdot d \quad (2.49)$$

Without considering the length extension, we designed our open stubs for the frequencies of 185GHz and 354GHz. The stub length considered for the open at 185GHz is $(L_1 - S_1) = 154\mu\text{m}$, Fig.2.41) and for the open at 354GHz is $80.5\mu\text{m}$.

Figure 2.41 shows the micrograph of the designed open circuit for G-band with the designed dimensions.

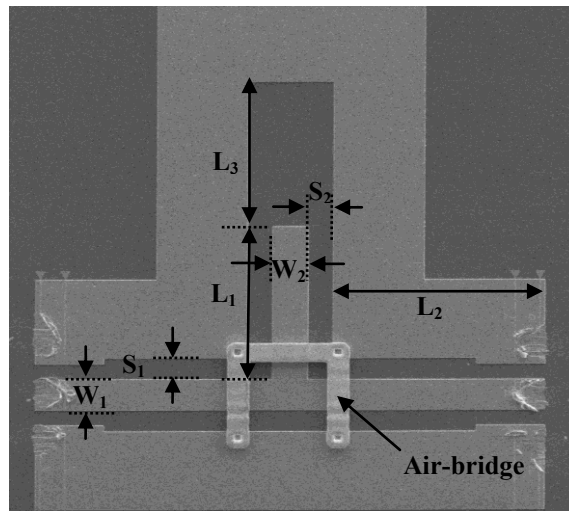


Figure 2.41: Micrograph of the CPW open-circuited Stub. The stub dimensions are: $W_1=35$, $W_2=35$, $S_1=25$, $S_2=25$, $L_1=179$ (G-band), $L_1=105.5$ (H-band), $L_2=215$, $L_3=170$. All dimensions are in micron.

Simulation and measurement results of the CPW open stub in G-band are presented in Fig.2.42 and show good agreement.

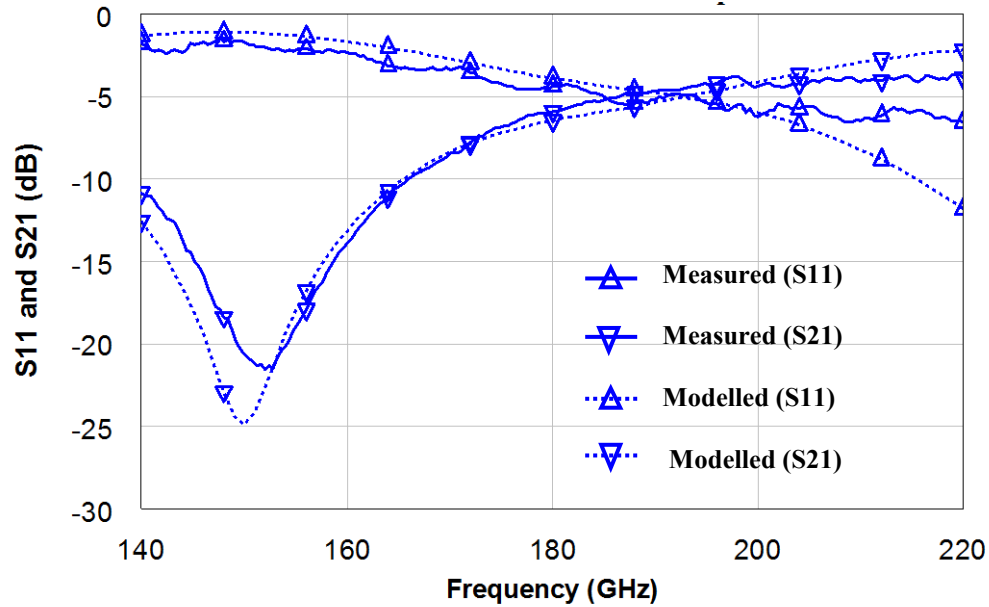


Figure 2.42: Measured and simulated S-parameters for a CPW open-end shunt stub.

Figure 2.42 reveals a 3dB-bandwidth of 105GHz (69% fractional bandwidth), a loaded quality factor (Q_L) of 1.7 and unloaded quality factor (Q_u) of 8.08. The CPW open stub shows a return loss of -2.07dB and an insertion loss of -22dB at its centre frequency. This open stub resonates at 152GHz although it was designed for 185GHz. The discrepancy in the resonant frequency is due to the length extension phenomena explained above. The length extension in this case is $l_{ext} = 33.2\mu m$ which is equal to $l_{ext} = d/2.56$. The other open stub designed for 354GHz, resonates at 247.5GHz with a length extension of $l_{ext} = 34.7\mu m = d/2.4$.

Looking at the results of the CPW open circuit stubs in [49] we can see length extension of $d/3$ for the stubs at W-band (with resonant frequency of 72.77GHz). Considering these results, we can conclude that the length extension is a frequency dependent phenomenon and increases with operating frequency. Our observation shows an

increase of 15% for length extension from 72.77 to 185GHz and 4.8% from 185 to 247.5GHz. The effect of increasing length extension from $l_{ext} = d/4$ by increasing the frequency is mentioned in [124] up to 100GHz. However, looking at the results reported in [50] for 203GHz CPW open stub, we can see the length extension is $d/8$.

This report shows the CPW open stub designed for centre frequency of 203GHz with an insertion loss more than 20dB and return loss of -1.09dB at the centre frequency. The higher rejection for the stub reported in this work (compared with our open stub) may be due to the smaller lateral dimensions used. As mentioned in section 2.3.3, using smaller lateral dimensions for CPW structures reduces the radiation and therefore improves the performance of an open stub. However the measurement results in that paper peak at 220GHz and therefore it is not possible to get an idea about the bandwidth performance of their stub. The open stub designed here for H-band frequency range, shows -17dB insertion loss and return loss of -2.5dB at centre frequency of 247GHz.

As described earlier in this section, increasing the impedance of the stubs or decreasing the impedance of feed lines is predicted to improve the quality factor of the circuit. To investigate this, an open-circuited stub with 50Ω lines is compared with one with the stub impedance increased to 100Ω as well as the one with a 25Ω feed line and 100Ω stub. Fig.2.43 shows the simulation results of this comparison.

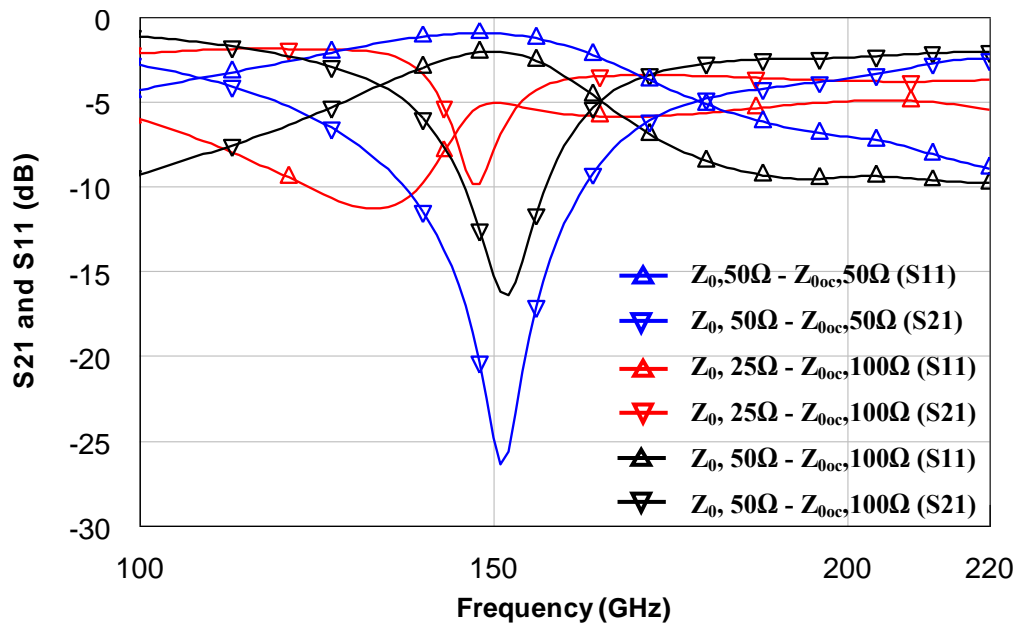


Figure 2.43: Simulated S-parameters for open-end shunt stub with various feed and stub impedances.

Increasing the impedance of the CPW line at the stub section to 100Ω, decreases the bandwidth of the open-circuit stubs but also increases the in-band loss of the stub. increasing the impedance of the stub to 100Ω whilst at the same time decreasing the feed line impedance to 25Ω, results in a very narrow band with high in-band loss. This is due to the increased loss of a CPW line at impedance extremes.

The result show that, in order to achieve a CPW open-circuit stub with a high quality factor, a low loss transmission line suitable for mid to high characteristic impedances coupled with low loss is required.

2.5.2 Quarter-wavelength CPW short-circuited stub

A parallel resonance can be achieved using a short-circuited transmission line with characteristic impedance Z_0 , propagation constant β , and attenuation constant α . At the frequency $\omega = \omega_0$, the length of the line is $l = \lambda/4$. A short-circuited length of transmission line and its equivalent lumped circuit are shown in Fig.2.44 [29].

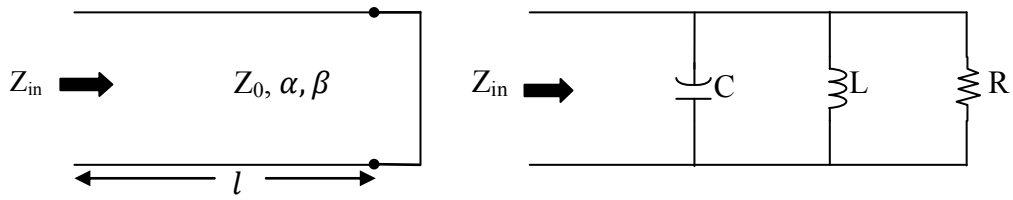


Figure 2.44: The lumped-element equivalent circuit of a short-ended transmission line used as a resonator. $l = (2n - 1)\lambda/4$

The Quality factor of this circuit can be written as

$$Q = \omega_0 RC = \frac{\pi}{4\alpha l} = \frac{\beta}{2\alpha} \quad (2.50)$$

which clearly indicates that by decreasing attenuation, α , the quality factor will increase.

Also the loaded Q (Q_L) and unloaded Q (Q_u) of the short-ended resonator with input output loading can be obtained from [123]:

$$Q_L = \frac{f_0}{\Delta f_{3dB}} \quad (2.51)$$

$$Q_u = \frac{Q_L}{1 - S_{21}(f_0)} \quad (2.52)$$

Where f_0 is the resonant frequency, Δf_{3dB} is the 3 dB bandwidth of the S_{21} response and $S_{21}(f_0)$ is the transmission coefficient at resonance for a band-pass resonator (short-circuited stub). Similar to the open stub, reduction in the attenuation of transmission line, results in the improved loaded and unloaded quality factor of a distributed short-circuit stub.

On the other hand, looking at the scattering parameter equations of the loaded shunt quarter-wavelength short-circuited stubs, gives us an indication of the impedance dependent performance of this component [125].

$$S_{21} = \frac{1}{1 - j \frac{Z_0}{2Z_{0s}} \cot\theta} \quad (2.53)$$

and

$$S_{11} = j \frac{Z_0}{2Z_{0s}} \cot\theta S_{21} \quad (2.54)$$

Where Z_0 is the characteristic impedance of the feed lines and Z_{0s} is the impedance of the short-circuited stub. Plots of S_{21} and S_{11} are given in Fig.2.45 for a network with the feed line characteristic impedance held constant at 50Ω and with three different values of stub characteristic impedance - low(25Ω), mid(50Ω) and high(100Ω).

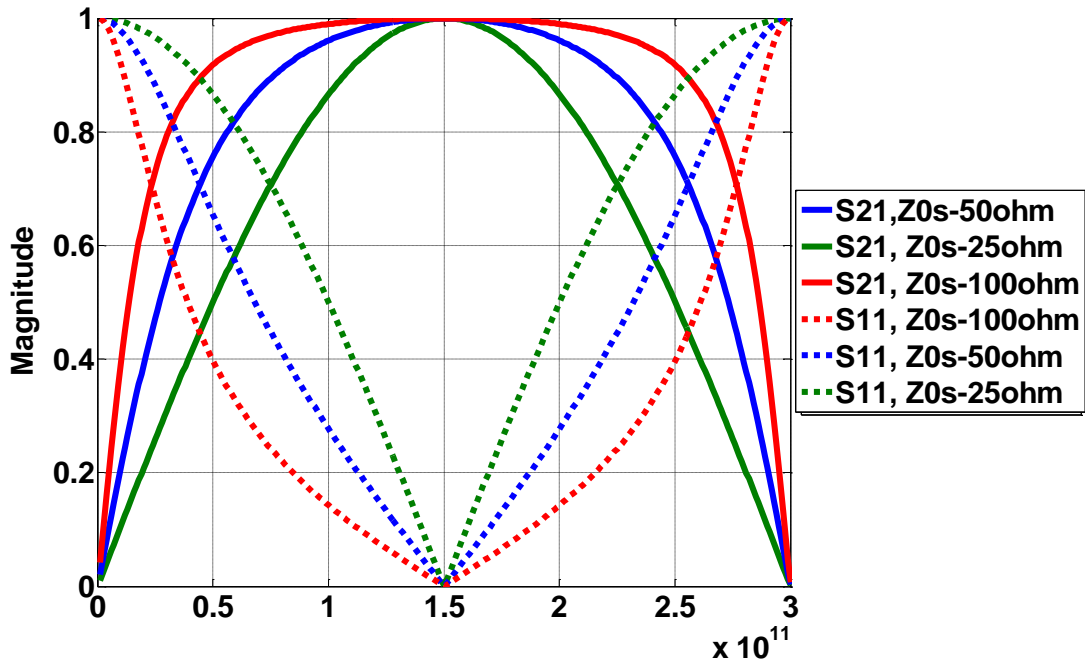


Figure 2.45: Simulated S-parameters for a quarter-wave length short-circuited stub with a fixed feed impedance of 50Ω and various impedances at the stub.

It can clearly be seen that in order to decrease the bandwidth and increase the quality factor of a shunt short circuit stub, low impedance transmission lines should be used to implement the stub section. Also increasing the characteristic impedance of the feed lines, further improves the performance of short-circuited stub. And, similar to open

circuit stub, the more the difference between the impedance of the feed and stub section, the better the performance of short stub. Therefore, in order to achieve the best performance for short-circuited matching stub, low loss transmission line at high and low impedance ranges is required.

To investigate the performance of the short-circuit stub with Coplanar Waveguide, a series of stubs were designed for different resonance frequencies at G and H-band using this transmission line.

Figure 2.46 presents the MMIC CPW short circuit stub.

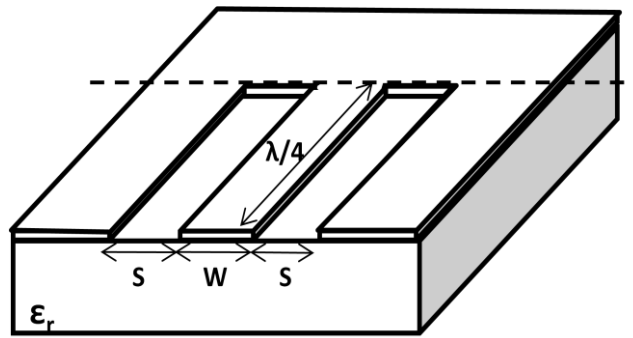


Figure 2.46: Structure of a short-circuited matching stub implemented by CPW transmission line.

A similar analysis to that carried out for the open circuit stub, calculates a stub length for a given centre frequency of

$$L = \frac{c}{4f_r \sqrt{\epsilon_{eff}}} - l_{ext} \quad (2.55)$$

Where the parasitic length extension is defined by the end inductance and can be expressed as [124]

$$l_{ext} \approx \frac{1}{8} \cdot d \quad (2.56)$$

Micrograph of the shunt CPW short circuit stub along with the designed dimensions are presented in Fig.2.47.

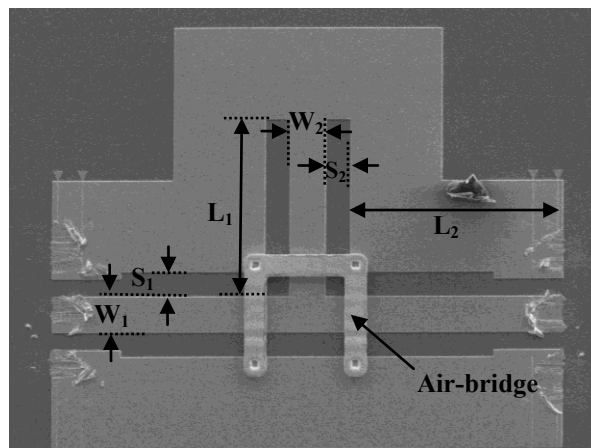


Figure 2.47: Micrograph of the CPW short-circuited shunt stub. The stub dimensions are: $W_1=35$, $S_1=25$, $S_2=25$, $L_1=105$ (H-band), 180 (G-band), $L_2=215$. All dimensions are in micron.

Measurement and simulation results for the CPW short circuit stub are in close agreement in both G and H-bands, Figs 2.48 and 2.49, and show very poor performance for this component, with very wide 3-dB bandwidth and high insertion loss at centre frequency (-1.8dB) for both the G and H-bands.

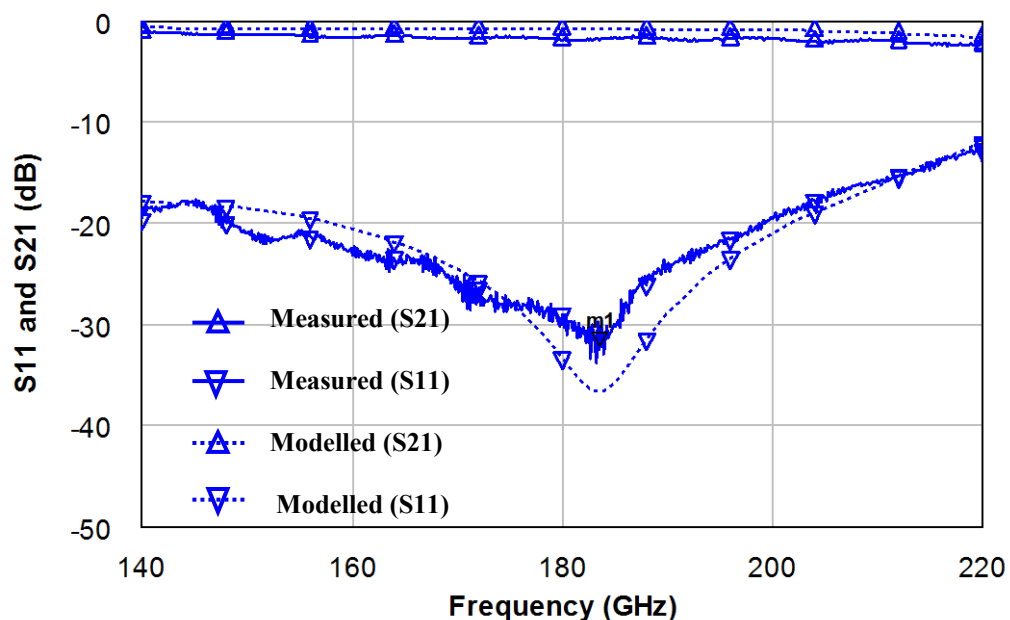


Figure 2.48: Measured and simulated S-parameters for a CPW short-end shunt stub at G-band (140-220GHz), $m1$: -31.2 dB @183.44GHz.

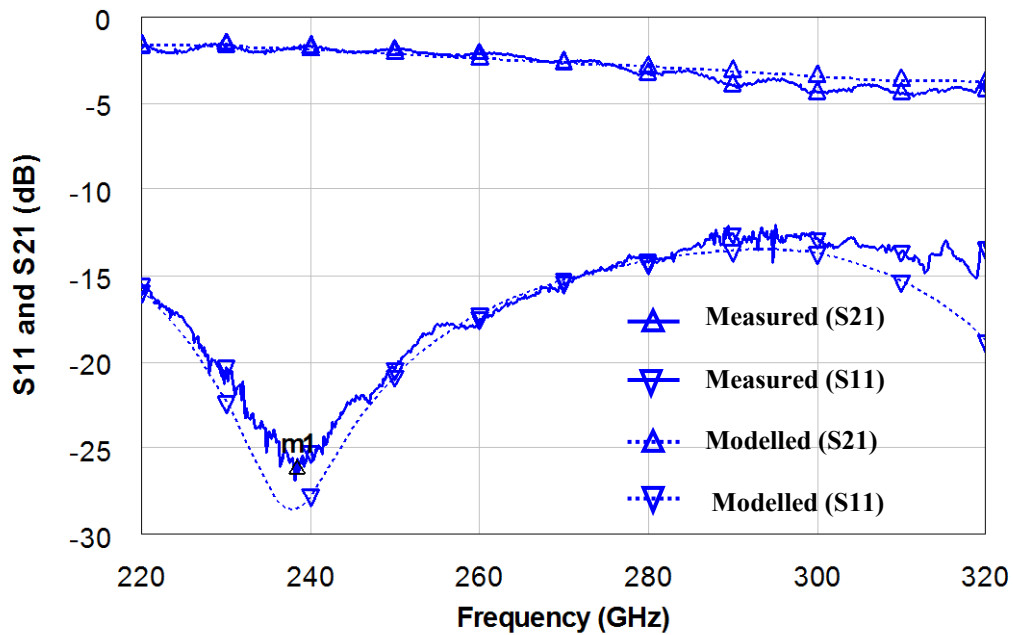


Figure 2.49: Measured and simulated S-parameters for a CPW short-end shunt stub at H-band (220-320GHz), $m1: -26.16@238.8$ GHz.

The G-band CPW short stub has a 3dB bandwidth of 210GHz (115% fractional bandwidth), the loaded Q (Q_L) of approximately 0.8 and unloaded Q (Q_u) of 4.6. Also the H-band CPW short stub has a 3dB bandwidth of 238GHz (118% fractional bandwidth), the Q_L of less than 0.8 and Q_u of approximately 4.27.

It should be mentioned that there is also a shift to lower frequencies in the resonances of the CPW stubs in both G-band (by 5GHz) and H-band (by 118GHz). However, unlike open stub, the resonance frequency of the short-circuited stub depends on the feeds sizes as well as the stub size. Therefore it is not possible to calculate the length extension of these stubs in the same way as was done for open stubs.

Looking at the electric field plot in the substrate region of the CPW short circuit stub at the centre frequency of 165 GHz, Fig. 2.50, we can see there is significant leakage of energy and penetration of the field to the lossy substrate. This energy leakage explains the poor performance of the CPW short circuit stub.

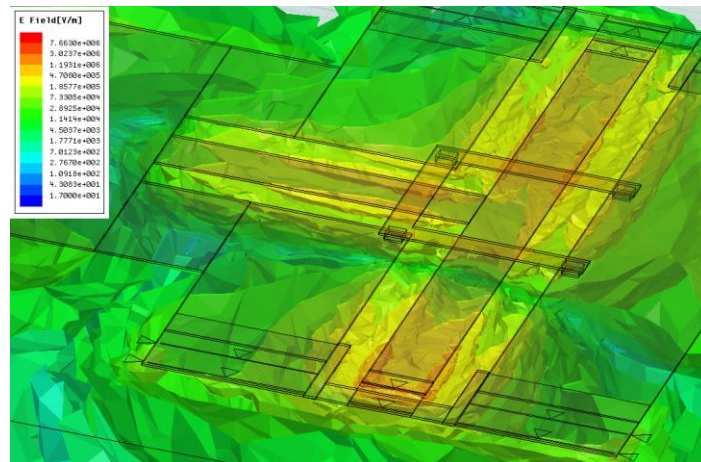


Figure 2.50: The substrate electric field plot of a short-circuited CPW shunt stub at the centre frequency of 220GHz.

Therefore, in order to improve the performance of CPW short circuited resonators, one should isolate the CPW traces from the substrate and reduce the substrate effect. This can be achieved by using elevated structures and is explained in the following chapters. Also, as in section 2.5.1, further investigation is done to investigate the effect of changing the characteristic impedance of the stub and feed section on the performance of CPW short-circuited stubs. A short-circuit stub with 50Ω feed (Z_0) and stub (Z_{0sc}) is compared with the short stub with 50Ω feed and 25Ω stub and also with the short stub with 100Ω feed and 25Ω stub in Figure 2.51.

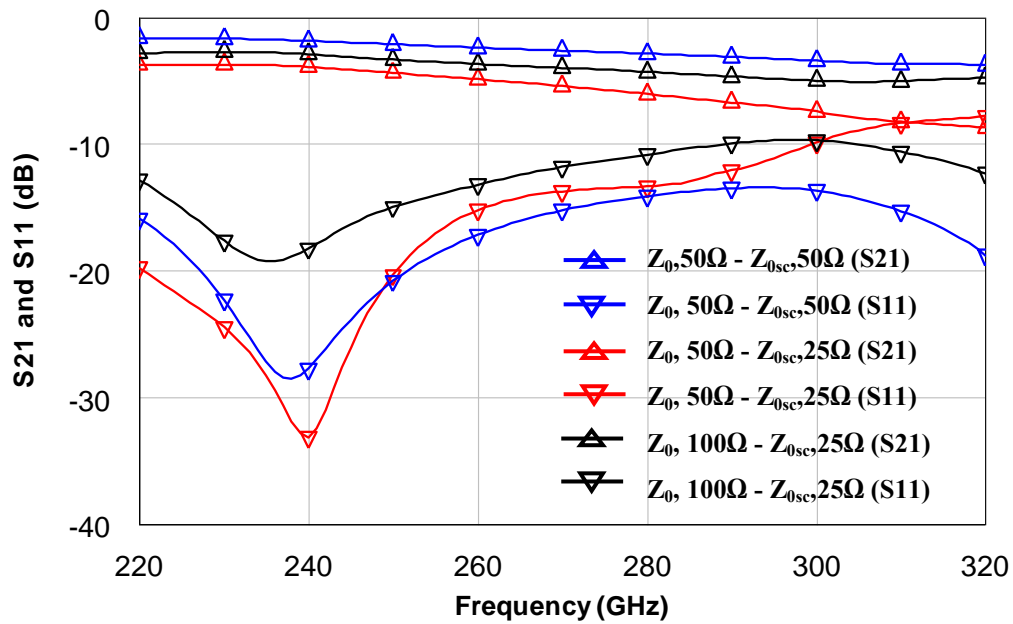


Figure 2.51: Modelled S-parameter response of a short-circuited shunt stub with various impedances at feed and stub sections.

Figure 2.51 shows that using low impedance CPW transmission lines to implement the stub decreases the bandwidth but also increases the in-band loss. The in-band loss increases even more when the high impedance lines replaces at the feeds. This can be explained, as it was discussed earlier, by the high insertion loss of the CPW line at impedance extremes.

All the above mentioned experience indicates that the ultimate performance for short-circuited can be achieved by using highly substrate isolated transmission line which also shows low loss at the impedance extremes.

2.6 CPW quarter-wave resonator filters

Filters are important blocks in microwave circuits and are among the first circuit elements studied in the development of any new technology. While the subject of filters is mature, there is little literature on coplanar waveguide (CPW) filter performance at

sub-mm-wave frequencies. This section describes band-pass and band-stop filters using CPW quarter-wave resonator filters for sub-mm-wave frequencies.

As noted above, quarter-wavelength open-circuited or short-circuited transmission line stubs act as series or parallel resonant circuits. Therefore, they can be used as shunts along a transmission line to implement band-pass or band-stop filters [29]. Quarter-wavelength sections of line between the stubs act as admittance inverters to effectively convert alternate shunt resonators to series resonators. The stubs and the transmission line sections are $\theta = \lambda/4$ long at the center frequency, ω_0 . The complete analysis of these types of stub filters is given in [29]. However, in this part of the work, we are aiming to apply the same design methods used in the centimetric domain to achieve filters for sub-mm wave regime.

2.6.1 Quarter-wavelength CPW band-pass Filter

As discussed in section 2-5-2, a short-circuited stub can be approximated as a shunt LC resonator when its length is near 90° . Therefore when two short circuited stubs are connected by quarter-wavelength transmission lines, they can implement a bandpass filter structures. Based on [29], the design equations for the required stub characteristic impedances, Z_{0n} , can be derived through the use of an equivalent circuit. this can be written as

$$Z_{0n} = \frac{\pi Z_0 \Delta}{4g_n} \quad (2.57)$$

Where Δ is the fractional bandwidth of the filter, Z_0 is the internal impedance of the stub filter which is usually 50Ω in microwave circuits, and g_n is the low-pass prototype parameters. It can be seen from equation (2.57) that, in order to decrease the bandwidth, lower impedance transmission lines should be used for the stubs, for example, by using

double shunt stubs to reduce the equivalent impedance seen at the junction of the two stubs. This design rule stays the same when the frequency enters to the millimetre and submillimetre-wave regime.

In addition, the performance of a quarter-wavelength filter can be improved by allowing the characteristic impedance of the interconnecting lines to be variable [29, 125]. In our experience, it was found that by increasing the impedance of the quarter-wavelength section line between stubs, further improvement can be achieved for the band-pass filter in terms of loss and bandwidth. In fact, the more the difference between the impedance of these sections, the better the filter performance. Here, the need for low-loss transmission line at low and high impedance extremes becomes pronounced. 3rd-order shunt stub bandpass filters were reported for W-band(0.1-110GHz) and G-band(140-220GHz) frequencies in [49] and [50]. In comparison with these reported works, the novelty of our work is essentially the frequency extension up to 320GHz. The work in [49] reports shunt stub band-pass filters with centre frequency of around 80GHz with fractional bandwidths of 82%, 58% and 36%. Also the band-pass reported in [50] has a centre frequency of 165GHz with fractional bandwidth of 57%. Since the insertion loss of CPW transmission line shows roll off at frequencies specially above 200GHz, it would be interesting to investigate the performance of the filters designed for centre frequencies above this point. Therefore, a 3rd order quarter-wavelength resonator band pass filter using CPW transmission line is designed for the centre frequency of 210GHz. The CPW filter was designed and then fabricated using 50 Ω impedance feed lines, stubs and connectors. By considering double stubs in the design of this filter, the overall impedance of the stubs is 25 Ω . Micrograph and the design dimensions of this filter are

shown in Fig.2.52 and the measurement and simulation results, which are clearly in close agreement, are presented in Figure 2.53.

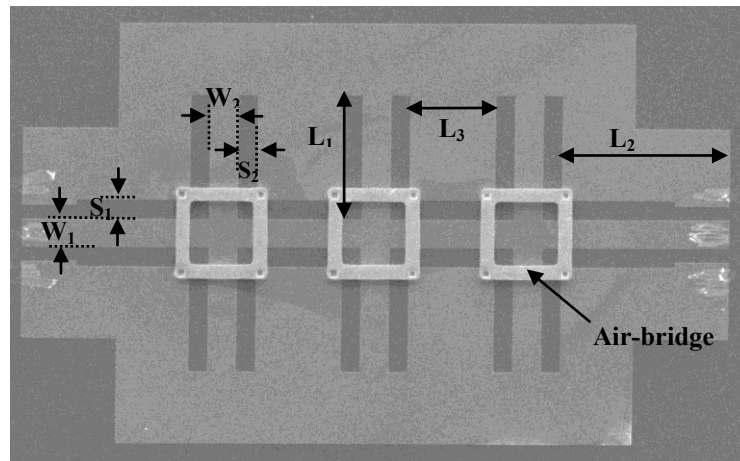


Figure 2.52: Micrograph of a 3-rd order quarter-wavelength CPW band-pass filter. The filter dimensions are: $W_1=35$, $W_2=35$, $S_1=25$, $S_2=25$, $L_1=117$, $L_2=215$, $L_3=67$. All dimensions are in micron.

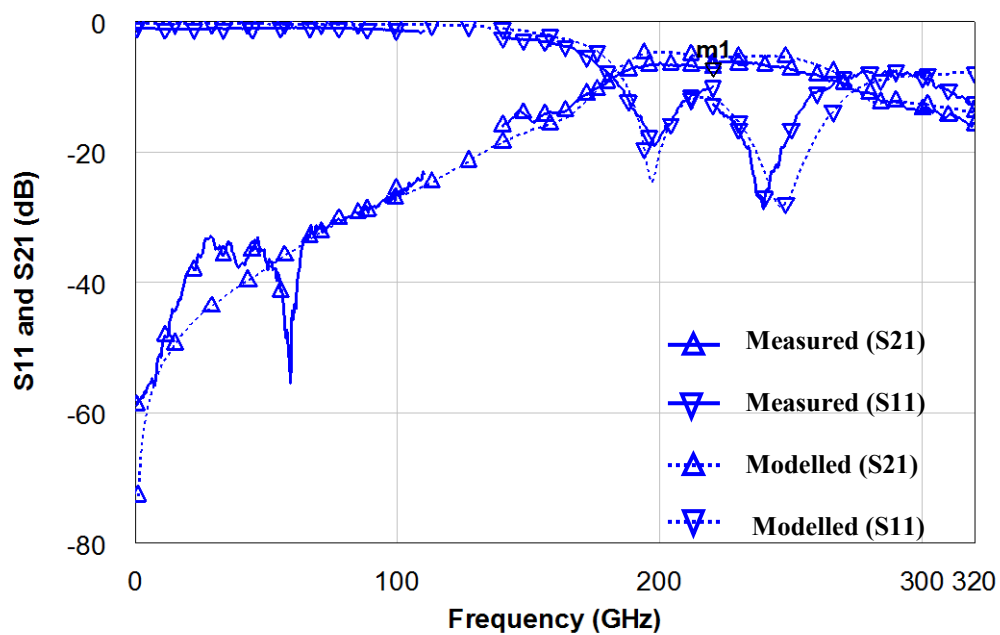


Figure 2.53: Measured and simulated S-parameters for a CPW band-pass filter. ($m1$:-6.998dB @220GHz)

A 3-dB bandwidth of 103GHz (45% fractional bandwidth) and very high insertion loss of 6.99 dB at the centre frequency is observed for this filter.

Looking at the electric field plot of this filter at centre frequency shows the high energy penetration of the substrate for this structure. This results in a great amount of energy loss in the substrate and poor performance of the filter as a result.

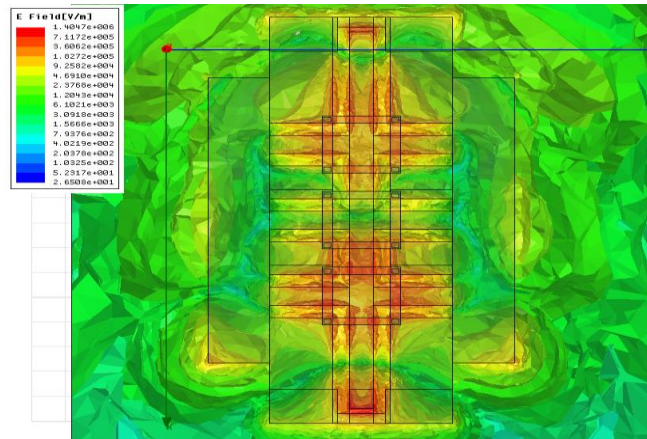


Figure 2.54: The substrate electric field plot of a CPW band-pass filter at the centre frequency of 220GHz.

In order to investigate the performance of this filter in more detail with the aim of performance enhancement, a series of simulations are carried out. The simulation results show that implementing the bandpass filter with single short-circuited stubs rather than double stubs, improves the insertion loss of the filter but results in a much wider bandwidth and also degraded upper roll-off characteristics, as shown in Figure 2.55.

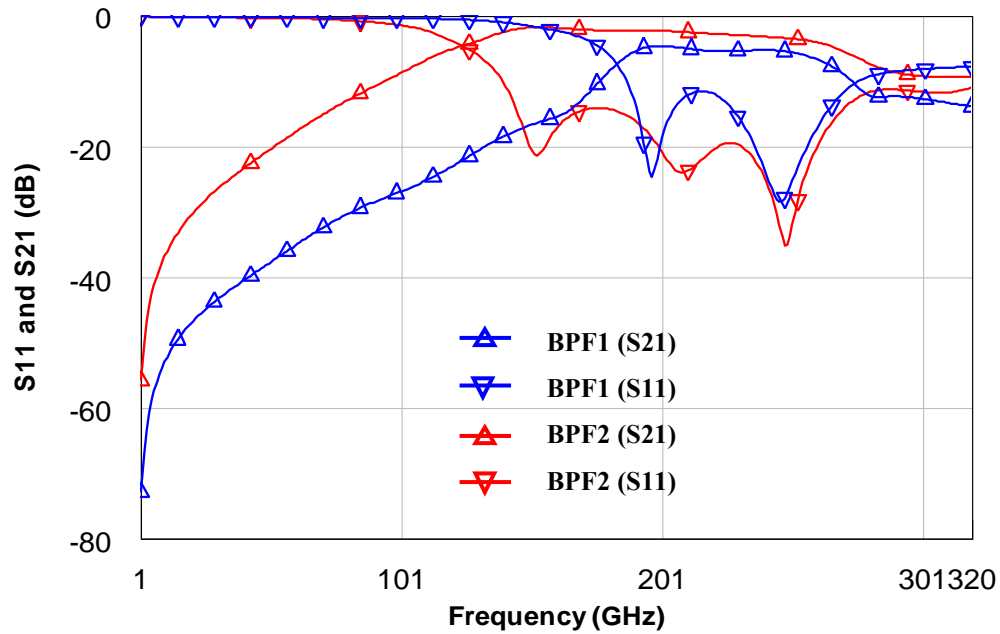


Figure 2.55: Simulated CPW band-pass filter implemented by double short-circuited stubs (BPF1) and Single short-circuited stubs (BPF2)

The narrower bandwidth observed in the filter with double stubs is the result of the lower impedance achieved by this method for the stub sections. Due to its better performance, we continued our experiments with this configuration.

To implement the design rule in equation (2.57) and achieve a better performance for the CPW band-pass filter in terms of bandwidth, a 3-rd order resonator filter was designed and simulated by increasing the impedance of connecting lines and decreasing the impedance of the stubs, with the impedance of feed lines kept to 50Ω . An impedance of 55Ω was employed for the connecting lines and 45Ω for the stubs (which results in an overall impedance of 22.5Ω at stub sections). The simulation results of this filter compared with the all- 50Ω impedance CPW filter is shown in Figure 2.56.

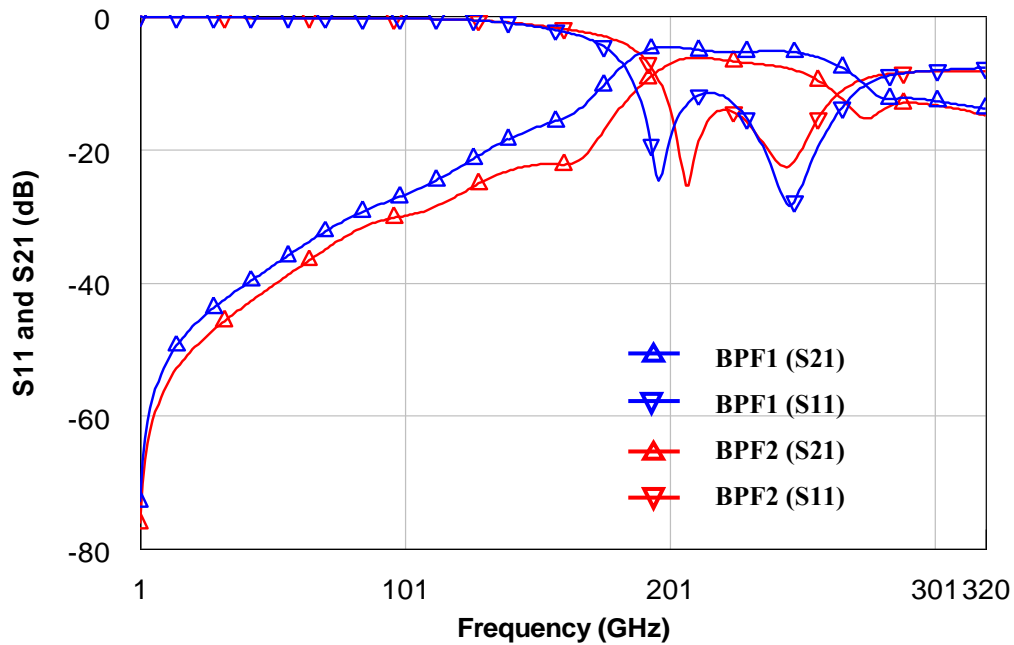


Figure 2.56: Simulated results for 3rd-order quarter-wavelength band-pass filter with a) same 50Ω impedance for all sections (BPF1), and b) various impedances for different sections, 50Ω feed lines, 45Ω stubs and 55Ω connection lines (BPF2)

It can be seen that even small variations in impedance for different parts of the filter, can make a significant change in filter performance. The results reveal that, although a narrower bandwidth is achieved for this filter, the in-band insertion loss is increased by almost 2dB. This is due to the fact that the CPW structures suffer from higher and higher losses as the characteristic impedance approaches either the high or low extremes of the possible impedance range. All of these results and also the reports in [49] and [50], emphasize the need for a transmission lines which couple characteristic impedances at the lower and upper bounds of feasibility with low loss. Such lines would greatly facilitate the design of low loss, narrow-band filters operating at sub mm-wave frequencies.

2.6.2 Quarter-Wavelength Band-stop Filter

As noted in section 2-5-1, an open-circuited stub can be approximated as a series LC resonator. Therefore this element with the combination of quarter-wavelength

transmission line connectors can implement a band-stop filter.

Based on conventional synthesis in [29], characteristic impedance of the stub section can be achieved from

$$Z_{0n} = \frac{4 Z_0}{\pi g_n \Delta} \quad (2.58)$$

Where Z_0 is the input and output and connecting lines impedance, Δ is the fractional bandwidth of the filter and g_n is the low-pass prototype.

It can be seen from equation (2.58) that high impedance transmission line is required for stub part in order to decrease the bandwidth of the filter. Similar to the band-pass filter, these design rules still apply to submillimeter-wave band-stop filters. While the performance of CPW open-circuited stubs at W and G-band frequencies has been investigated before [49, 50], to the best of our knowledge there is no report on this type of filter. Therefore, in order to investigate the submillimeter-wave performance of this filter in detail, a MMIC 3rd-order quarter-wavelength band-stop filter was designed by connecting three double CPW open stubs for the centre frequency of 220GHz. Fig.2.57 shows the micrograph and design dimensions of the CPW quarter-wavelength band-stop filter.

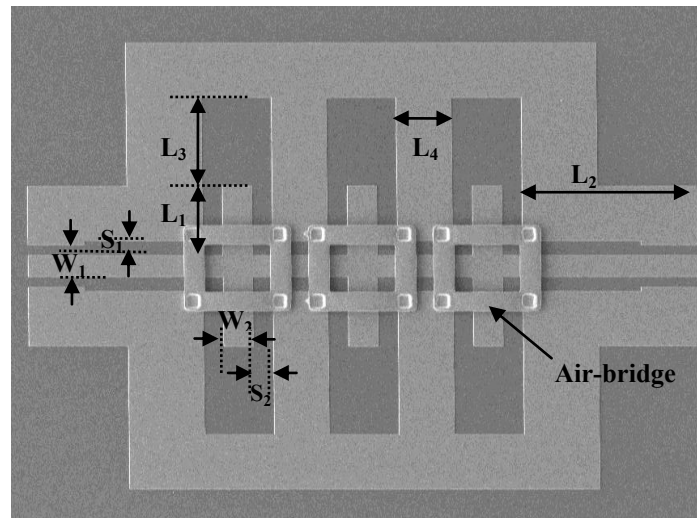


Figure 2.57: Micrograph of a 3-rd order quarter-wavelength CPW band-stop filter. The filter dimensions are: $W_1=35$, $W_1=35$, $S_1=25$, $S_2=25$, $L_1=117$, $L_2=215$, $L_3=150$, $L_4=67$. All dimensions are in micron.

Measured /simulated results for the CPW bandstop filter are shown in Figure 2.58.

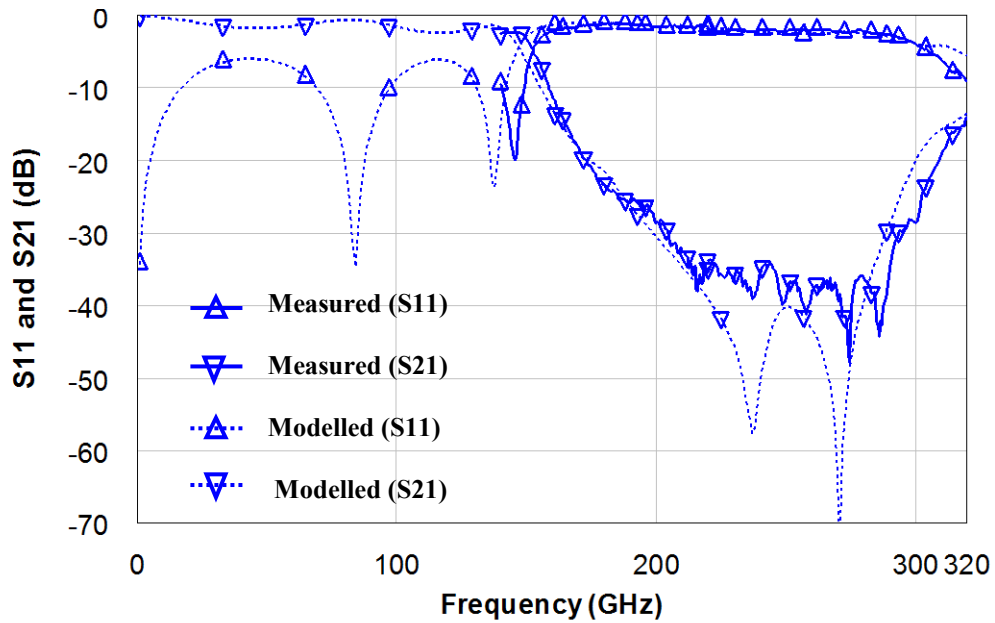


Figure 2.58: Measured and simulated S-parameters for a CPW band-stop filter.

A 3-dB bandwidth of 154GHz (fractional bandwidth of ~71%) and insertion loss of above 40dB at the centre frequency of 235GHz was achieved for this filter. As can be seen, this filter structure exhibits poor performance. In particular, a very poor upper roll-off characteristic was observed along with a very high insertion loss after the stop-band. Looking at the substrate electric field plot at frequencies above stop-band, e.g.420GHz, shows high energy penetration of the substrate which results in a poor performance.

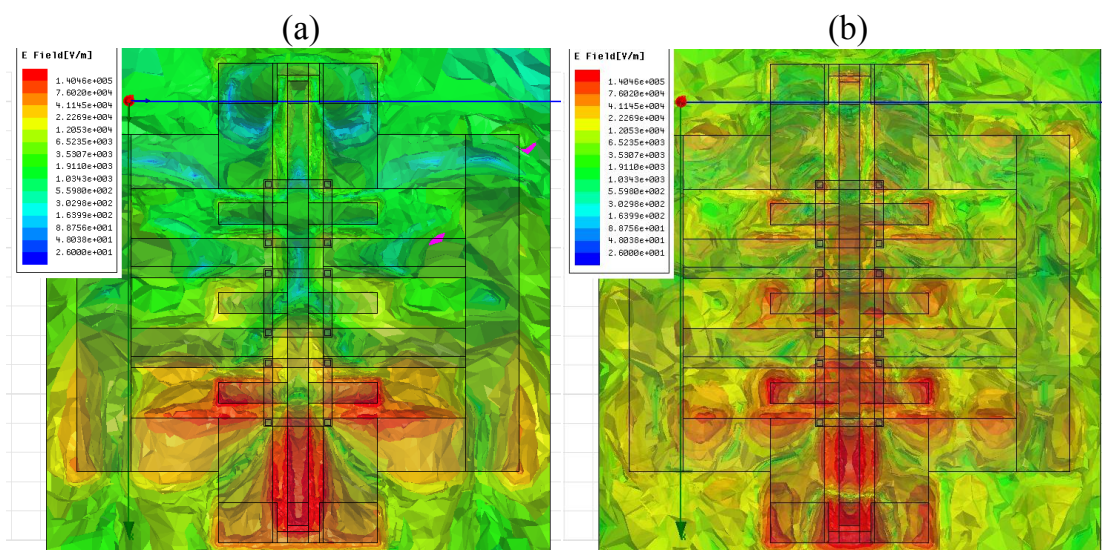


Figure 2.59: The substrate electric field plot of a CPW band-stop filter at (a)the centre frequency of 220GHz and (b)above stop-band frequency of 420GHz.

In order to optimize the performance for this filter, a series of simulations were carried out which are summarised as follow. First, the CPW band-stop filter design was adjusted by increasing the characteristic impedance of the stubs to 55Ω and decreasing the impedance of the connecting sections to 45Ω . As Figure 2.60 shows a narrower filter bandwidth can be achieved, although the magnitude of the improvement is not significant for this change of characteristic impedance, and no degradation of in-band loss was observed.

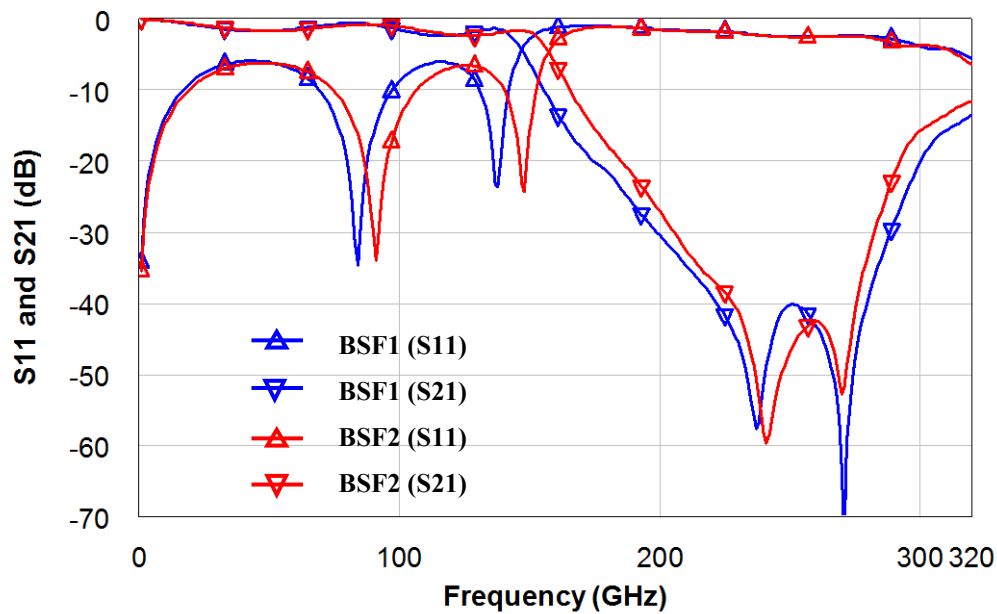


Figure 2.60: Simulated results for 3rd-order quarter-wavelength band-stop filter with a) same 50Ω impedance for all sections (BSF1), and b) various impedances for different sections, 50Ω feed lines, 55Ω stubs and 45Ω connection lines (BSF2)

When further increasing the impedance of the stubs to 94Ω ($45\text{-}5\text{-}45\mu\text{m}$), while keeping the impedance of connecting lines as before, not only there is no significant performance improvement (Figure 2.60), but the filter begins to show very poor roll-off characteristics at the upper cut-off frequency. This poor performance is due to the poor performance of the high/low impedance CPW transmission line. Many different structures using different impedances ratios were simulated and no significant improvement was ever observed for this filter.

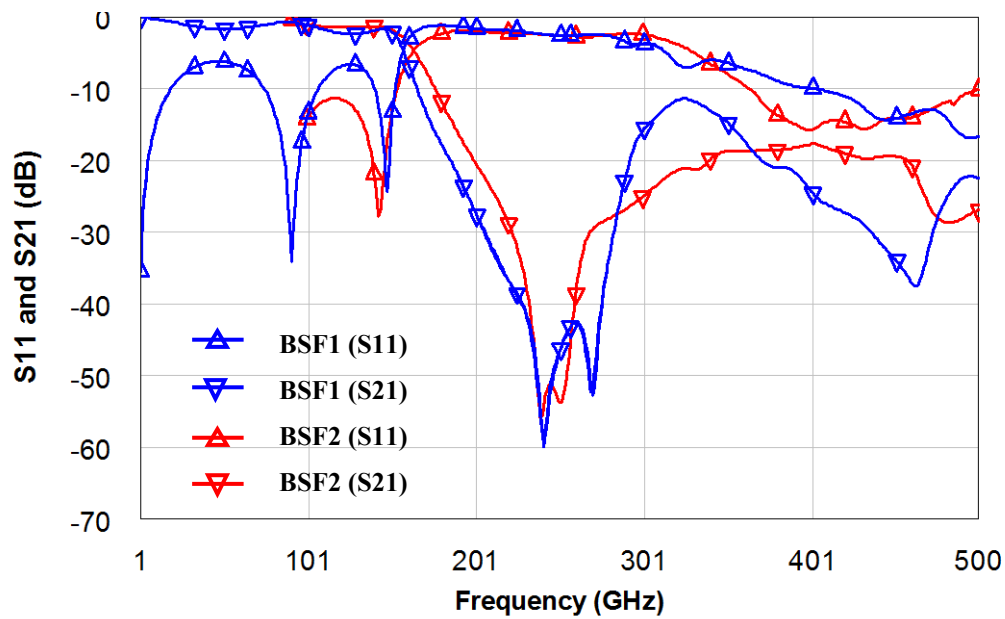


Figure 2.61: Simulated results for 3rd-order quarter-wavelength band-stop filter with a) same 50Ω impedance for all sections (BSF1), and b) various impedances for different sections, 50Ω feed and connection lines and 94Ω stubs (BSF2).

Since using double open stubs decreases the overall impedance of the section, a 3-rd order bandstop filter was designed with single open stubs to keep the impedance of the stubs high. By designing in this manner, the 3dB-bandwidth of the filter was decreased significantly. However, the filter shows very high return loss which increases with frequency and a lower insertion loss. Figure 2.62 compares the bandstop filter implemented with single and double open stubs. Both filters use 50Ω transmission lines in the feed, stub and connecting sections.

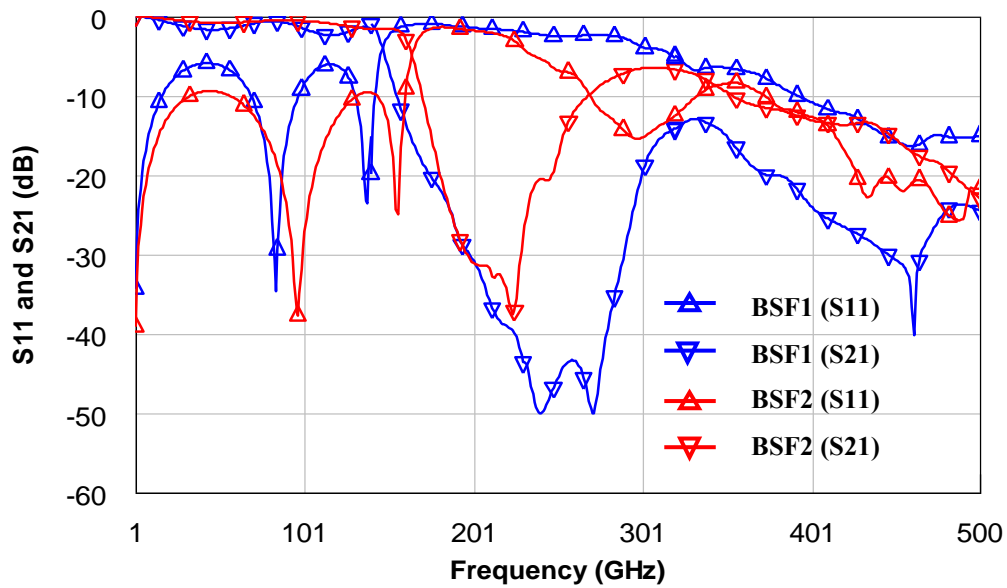


Figure 2.62: Simulated CPW band-stop filter implemented by double open-circuited stubs (BSF1) and Single open-circuited stubs (BSF2)

In addition, by varying the impedances of the stub section and connecting lines, further reductions in terms of bandwidth can be achieved, Fig.2.62. However, in all cases, the CPW band-stop filters suffer from a very poor roll-off characteristics at the upper portion of the stop-band.

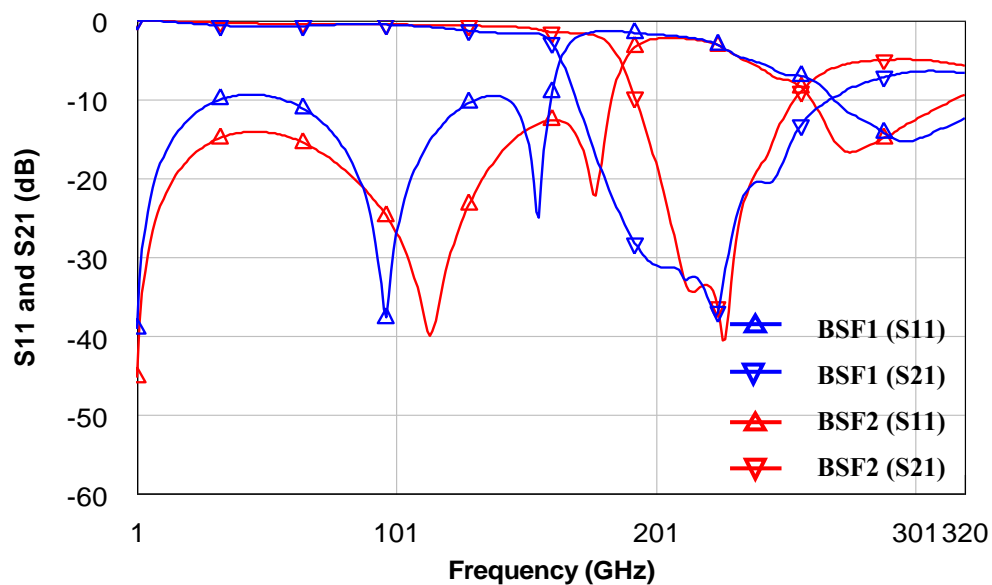


Figure 2.63: Simulated results for band-stop filter using single open stubs with a) same 50Ω impedance for all sections (BSF1), and b) various impedances for different sections, 50Ω feed and connection lines and 94Ω stubs (BSF2).

To further investigate the performance of the band-stop filter using CPW transmission line, another band-stop structure is considered. This structure implements the band-stop filter by using a combination of short and open quarter-wavelength stubs which are connected together by quarter-wavelength transmission lines. This filter has band-stop characteristics at $\omega_0, 2\omega_0, \dots, N\omega_0$. This is due to the fact that at each frequency corresponding to multiples of 90° , at least one of the stubs is a short circuit. Since they are in parallel the result is a short circuit and a null in the transmission every 90° . By using this structure, an improved performance for the filter with much narrower 3-dB bandwidth than the double open stub filter was achieved, Figure 2.64.

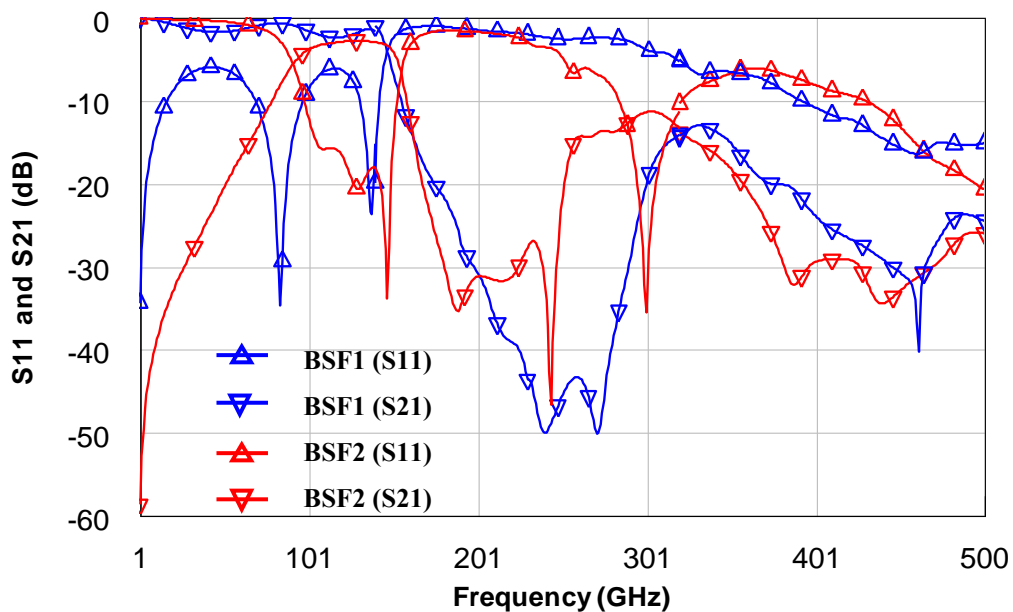


Figure 2.64: Simulated results for 3rd-order quarter-wavelength band-stop filter with two parallel open stubs at each junction (BSF1), and b) a parallel short and open stubs at each junction (BSF2)

However a comparison of this structure with the single open stub band-stop filter shows no improvement in the filter performance by using the new structure.

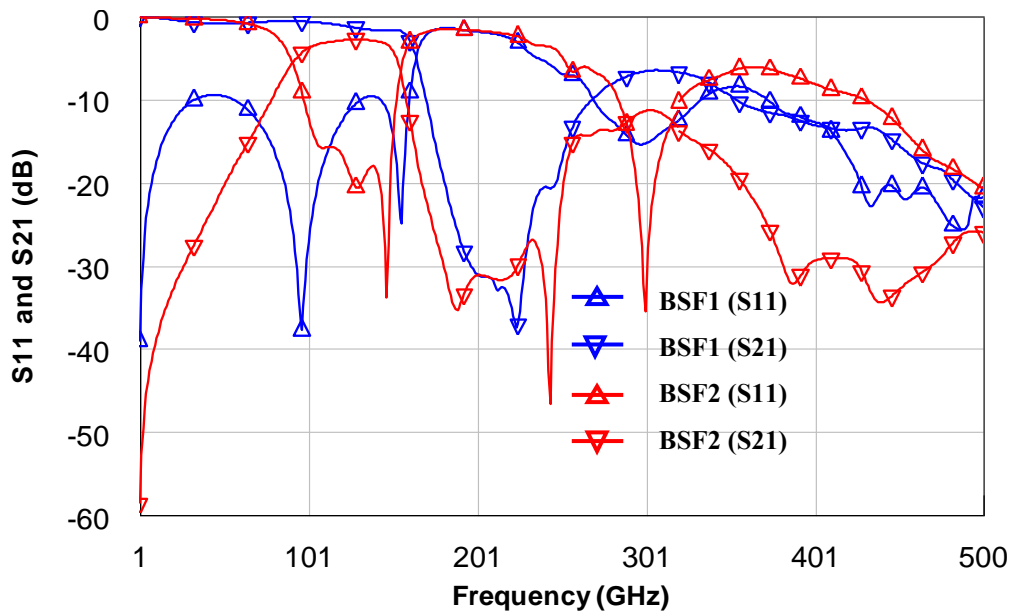


Figure 2.65: Simulated results for 3rd-order quarter-wavelength band-stop filter with single open stubs at each junction (BSF1), and b) a parallel short and open stubs at each junction (BSF2)

Further investigation shows that using high impedance line for the open stubs and low impedances for short circuit stubs, with the feeds and connecting lines set to 50Ω , can reduce the bandwidth whilst increasing the out of band insertion loss, Figure 2.66.

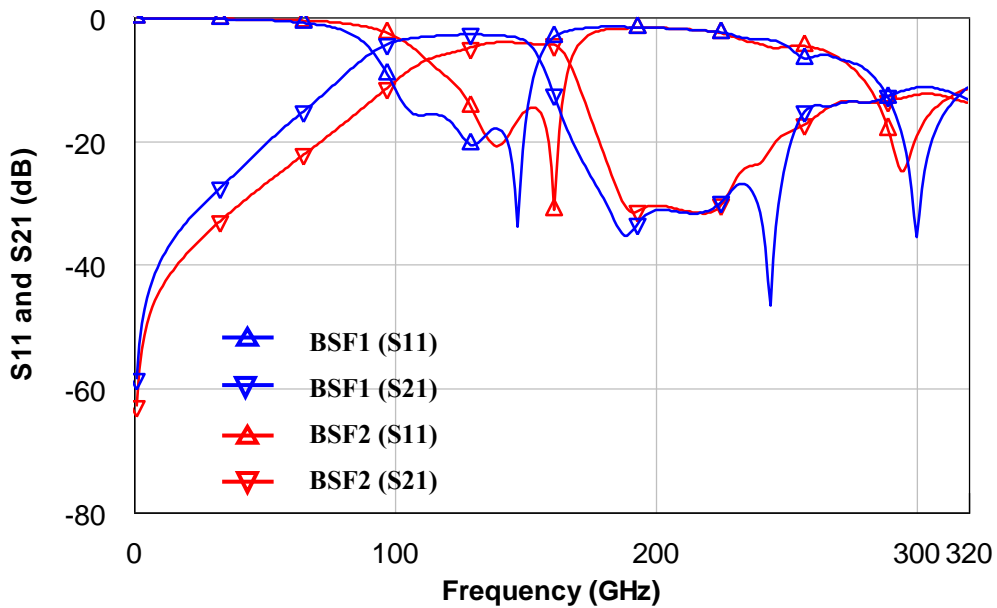


Figure 2.66: Simulated results for band-stop filter using short and open stubs with a) same 50Ω impedance for all sections (BSF1), and b) various impedances for different sections, 50Ω feed lines, 45Ω short circuit stubs and 55Ω open circuit stubs (BSF2).

The very poor performance of CPW structures at frequencies above 200GHz can be clearly seen in the filter performances presented. It can be seen in Figure 2.66 that due to the lossy behaviour of the structure, the insertion loss in the upper pass-band is large compared with the lower pass-band. This gets more severe in the case of high impedance lines as the lines are intrinsically more lossy.

It can be seen that all of the CPW band-stop filters mentioned above exhibit very poor upper roll-off characteristics and very high insertion loss above the stop-band. However, the simulation results for the same filter structure on air substrates do not show this cut-off effect. In fact, the conclusion of detailed simulations in this section illustrates that this poor roll-off characteristics observed for the band-stop filter is due to the poor performance of the CPW structure on GaAs substrate at these high frequencies.

The lossy behaviour of the CPW transmission line does not allow the insertion loss of the filter to return to same level as it was before the stop-band and results in a poor upper roll-off and high out of band insertion loss for the band-stop filter.

2.7 Summary

The performance of coplanar waveguide, CPW, has been investigated up to 320GHz on semi-insulating GaAs substrate and shows very high insertion loss and poor roll-off characteristics at frequencies around 240GHz and above. The problems that CPW transmission line faces in real circuit design along with some suggestions to overcome these have been discussed in some detail. The results show that a new variation of CPW line is desirable for mm-wave applications - one which is greater isolated from the substrate and therefore avoids the high dielectric-related loss at high frequencies and which offers a simple fabrication process. In addition, the performance of some

elementary passive components for MMIC design such as resonators and filters implemented by the CPW structure was investigated. It was observed that in most cases, based on both theory and practice, low loss transmission line at high and low impedances is required in order to achieve a high-Q passive network. This cannot be obtained using conventional Coplanar Waveguide structure. A new transmission line which shows low insertion loss at the impedance extremes is required to implement high-Q passive networks at high frequencies.

In order to fulfil these requirements, the elevated CPW structure has been chosen as an alternative to ordinary CPW transmission line. The following chapters describe the fabrication, design, simulation and measurement of transmission lines and some passive circuit components implemented with various elevated CPW structures.

Chapter 3

Fabrication of Elevated Structures

3-1 Introduction

This chapter presents details of the air-bridge process used to fabricate the elevated CPW structures. First, an overview of the process flow is given, followed by a more detailed analysis of the processes used. Along with the explanation of each step in the common fabrication recipe used in JWNC fabrication centre, the limitations and challenges in using that recipe for our structures and the major developments in improving that recipe to create novel air-bridge structures, are presented.

3-2 Overview of the process flow

Figure 3.1 gives a block-diagram of the main steps of the airbridge process used to fabricate the elevated CPW structures. This is a general process flow for the airbridge technology regardless of material or geometry. However, details such as exposure dose and time, layer thickness and developing recipes are material and geometry dependent. These are explained in detail below based on our structure requirements.

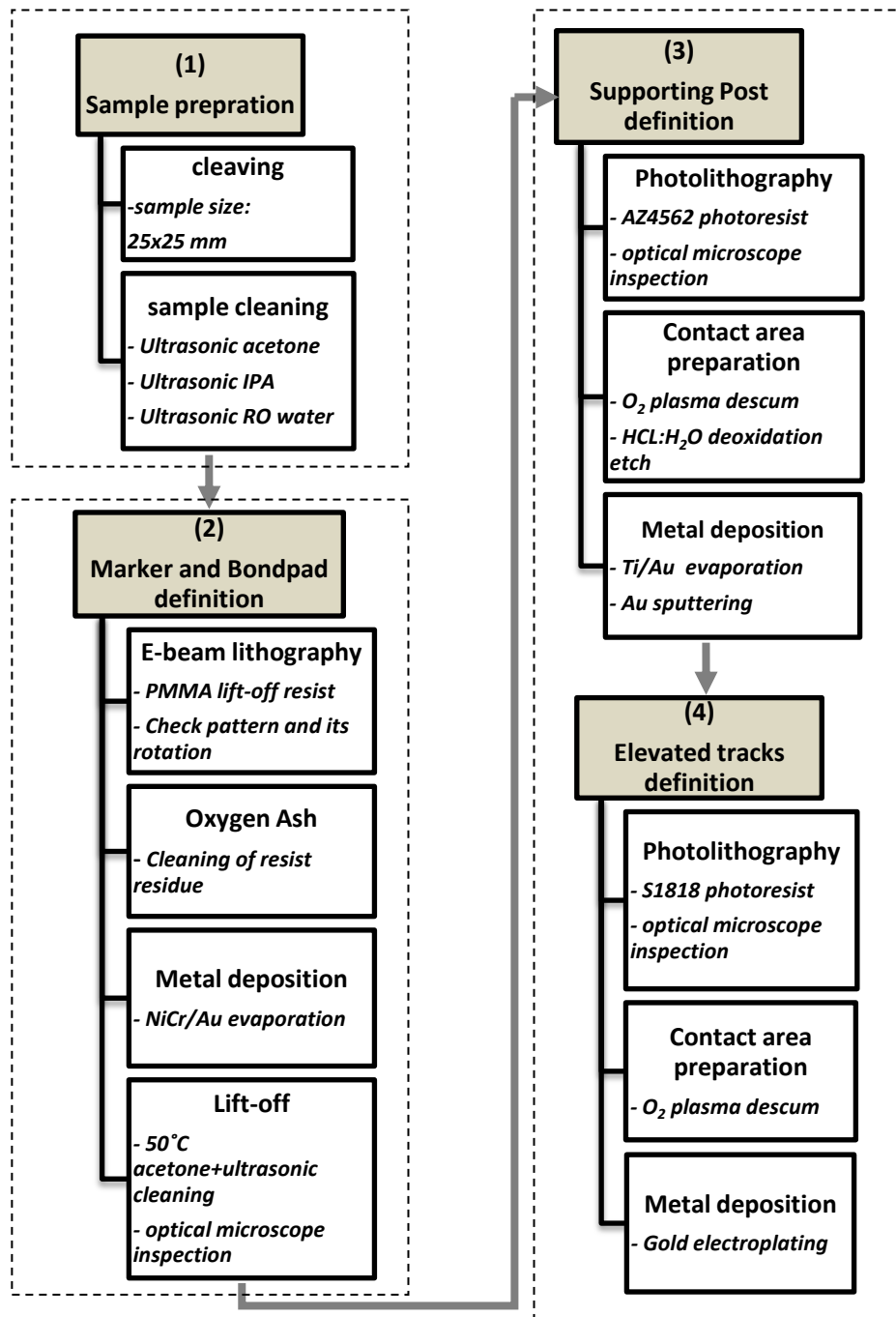


Figure 3.1: General process flow of the fabrication steps required to form elevated passive structures.

As can be seen in block diagram, the general fabrication process can be divided into four main stages. The first stage concerns preparation of the sample and is common to almost every fabrication process. The second stage concerns the formation of markers and bondpad layers. In our structures, these are the areas which are in direct contact with the substrate and include alignment marks, RF positioning marks, conventional CPW sections, transitions from CPW to the elevated parts and underbridges at elevated junctions. The third and fourth stages in the diagram concern the formation of the elevated sections including the supporting posts and elevated tracks.

A detailed explanation of each above-mentioned fabrication stages is given below.

3-3 Sample preparation

Semi-insulating GaAs wafers with a dielectric constant of 12.9 and a thickness of approximately 600 μm are used as the substrate. Gallium Arsenide is the preferred choice of substrate in millimetre and sub-millimetre circuits due to its high electron mobility (required for high frequency response), its sufficiently large bandgap (to reduce current leakage) and its mature and cost-effective fabrication process. The combination of these features makes GaAs an attractive candidate for high frequency circuits compared with other III/IV semiconductor materials. Wafers are usually chosen with a thickness of 600 μm to provide a substrate which is effectively infinitely thick for devices and components at millimetre and sub-millimetre wave frequencies. Substrate thinning can be done before or after fabrication if required.

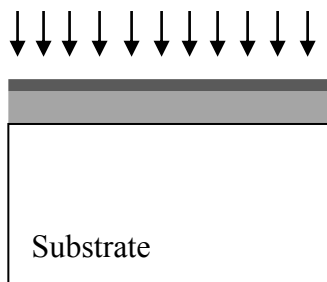
Prior to any processing, wafers are chemically cleaned using a standard cleaning procedure to remove particulate matter on the surface as well as any traces of organic, ionic, and metallic impurities. This is done by immersing the wafers in acetone and

placed in an ultrasonic bath followed by isopropyl alcohol (IPA), each for 5 minutes. An extra 5 minutes of ultrasonic bath cleaning with reverse osmosis water (RO-water) is then used. Next, a nitrogen gun is used to blow the remaining water off the sample surface. Since the absorbed water on the sample surface can decrease the resist adhesion, a further bake is done in a 120°C oven or on a hot plate to dehydrate the wafer.

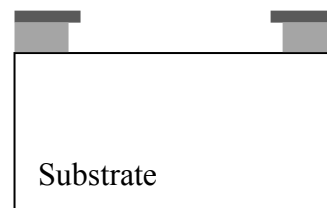
3-4 Markers and Bondpad definition

After sample preparation, we can divide the fabrication process of our devices into two major stages. The first stage is to form the markers and bondpad layers and the second stage is to define the elevated parts of the structures. The fabrication steps of the first stage (forming markers and bondpad layers) are sketched in Figure 3.2 and explained in detail below.

- High molecular weight resist
- Low molecular weight resist
- Metal



1) Forming mask for markers and bondpad layers:
Spinning e-beam resist, baking, E-beam Exposure



2) Resist development in IPA:H₂O
(2:1)
Oxygen Ash

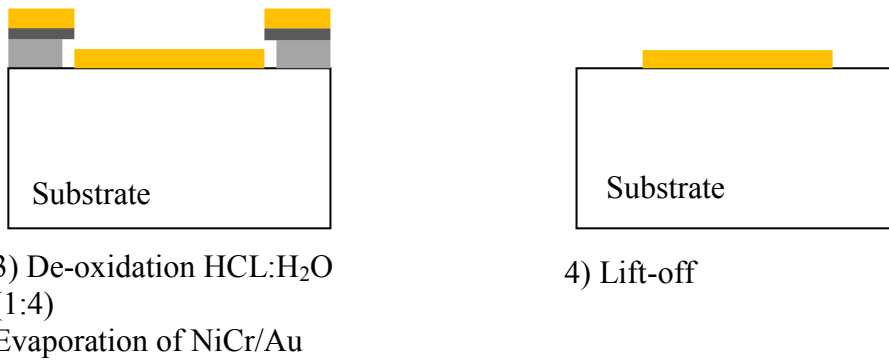


Figure 3.2: Fabrication steps (1-4) of markers and bondpad layers

The marker layer includes the registration marks used for alignment purposes during fabrication process and the RF positioning marks used for measurement purposes. The registration marks are required for the fabrication of circuits which consist of more than one level of lithography. The alignment markers used in this work are squares of various sizes positioned at each corner of a cell or the chip. Fig.3.3 shows an example of our alignment marks for one cell. RF positioning marks are used to provide a known distance from the probe tips to the measured device during the S-Parameter measurement process, Fig.3.4. The defined distance from the probe tips to the device under test is important to provide reliable measurement repeatability.

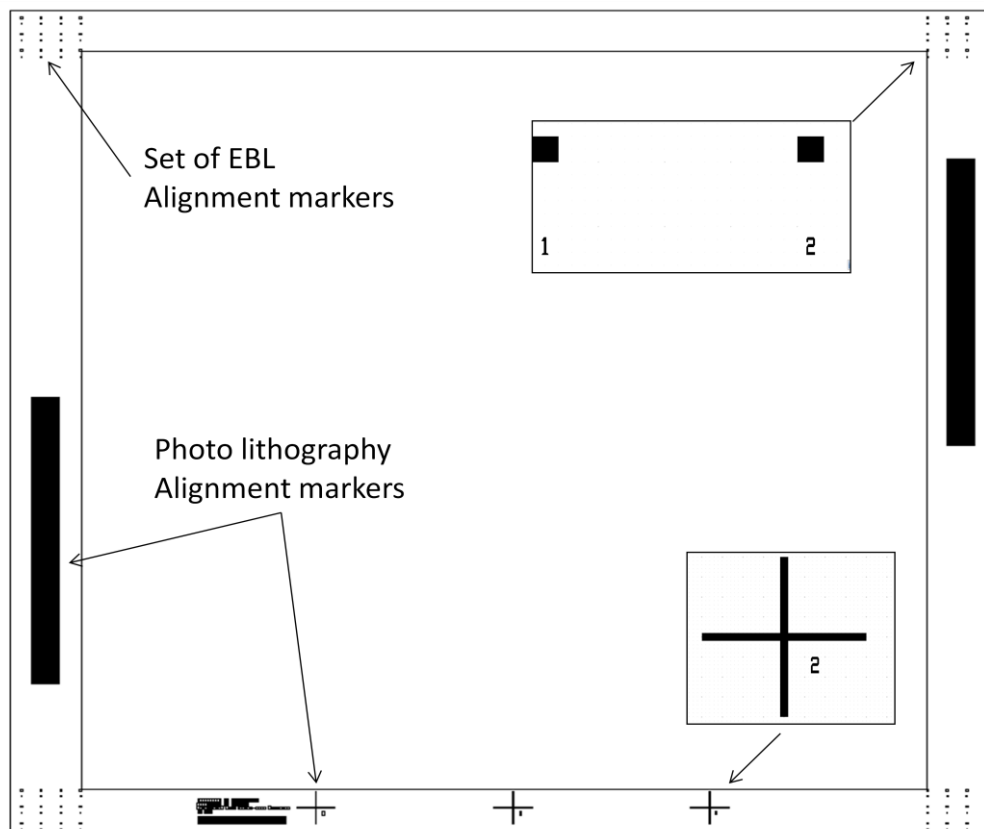


Figure 3.3: Layout of alignment markers

The marker layer, including registration and RF positioning marks, consists of metallisation and lift off of NiCr/Au (50nm/50nm). NiCr is used to provide good adhesion at the substrate interface and gold is used to provide the contrast for the e-beam automatic alignment system.

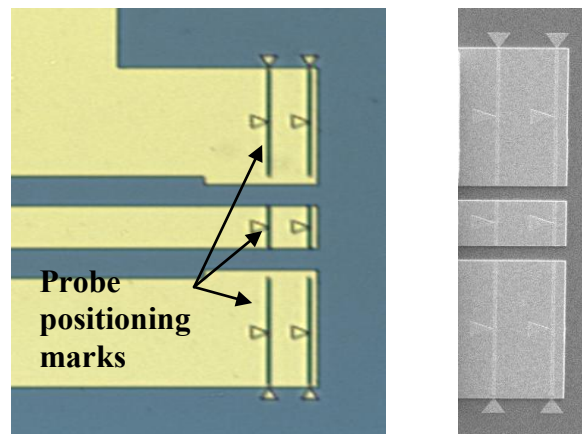


Figure 3.4: Optical and SEM pictures of the structure with probe positioning marks

The bondpad layer includes the parts of structures resting directly on the substrate such as conventional CPW lines and structures, and transitions from conventional to elevated structures and underbridges at the elevated junctions. This layer is achieved by metallisation and lift off of 50nm NiCr followed by 1.2 μm of gold. NiCr is used to enhance the adhesion of the structures to the substrate and Au is used due to its relatively good conductivity and also because it does not oxidise. The thickness of gold, 1.2 μm , is chosen to be more than 5 times the skin depth at the desired frequency range in order to minimise the conductor losses [126].

The fabrication processes involved in forming the marker and bondpad layers are very similar and include: resist coating and development, e-beam lithography, metal evaporation and lift-off - which will now be explained in detail.

3-4-1 Resist coating and development

Pattern transfer from the designed layout to the substrate, in this stage, is done using Electron Beam Lithography (EBL), using the very high resolution positive tone resist, poly-methyl methacrylate (PMMA). PMMA with two different molecular weights of

345k (referred to as 2041) and 90k (referred to as 2010) are the standard PMMA used in JWNC [127] with ethyl lactate used as a solvent.

In the fabrication of marker and bondpad layers, the bi-layer resist strategy is used to provide an undercut resist profile which supports reliable lift-off. An undercut resist profile is required to avoid coating the resist sidewalls during the metal deposition and produce good lift-off, Fig.3.5. Therefore, first the resist with lower molecular weight and high concentration, PMMA 2010, is spun on the substrate followed by the spinning of the high molecular weight resist with lower concentration, PMMA 2041.

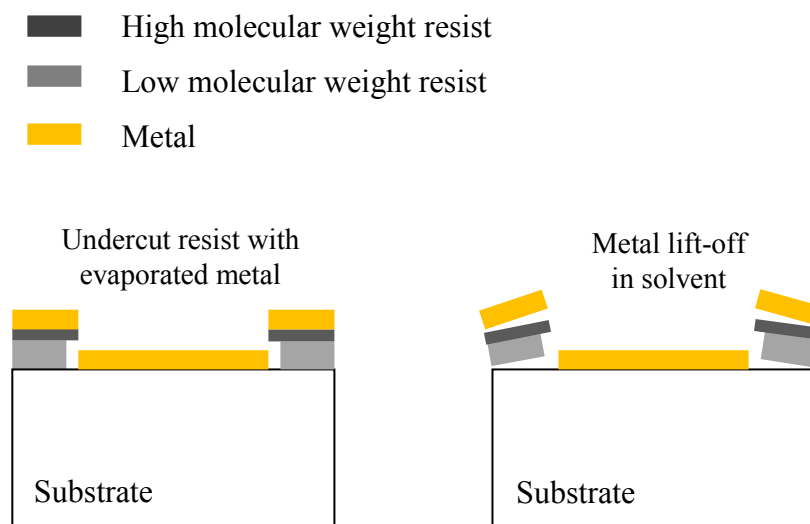


Figure 3.5: Schematic of metal lift-off with undercut resist profile

The other consideration in this stage is the resist thickness. In general, the thickness of the coated resist is determined by the spinning speed and also the concentration of the dissolved resist in solvent [128]. Table 3.1 shows the thicknesses which can be achieved by spinning different PMMA resists used in this work with a speed of 5000r.p.m for 60seconds.

Table 3.1: Experimental thickness achieved for PMMA resists used in this work

Resist Type	Thickness (nm)
	Spun at 5000 r.p.m for 60sec
2.5 % PMMA 2010	30
4 % PMMA 2041	100
12 % PMMA 2010	720
15 % PMMA 2010	1450

The numbers in the table are derived from experimentally spinning the utilised PMMA with a fixed speed and for a fixed time and from measuring the thickness using a surface profilometer -*Veeco Dektak* in JWNC - after development. The Dektak uses a diamond tipped probe to carry out contact profilometry whereby it scans across a surface and measures vertical displacement with the results displayed on a PC.

The resist thickness should be chosen to be higher than the metal thickness in order to provide better lift-off. The metallisation thickness of marker layers is around 100nm. Therefore, the resist for this layer is provided by first spinning 12% PMMA 2010 for 60sec, followed by 4% PMMA 2041 for 60sec both spun with the speed of 5000 r.p.m. The total thickness of this resist layer is approximately 800nm, which is enough to support good lift-off. In the case of the bond-pad layer, due to the higher required metallisation thickness (around 1200nm), the bottom layer resist is 15% PMMA 2010 spun with 3000 r.p.m for 60sec and top layer is 4% PMMA 2040 both spun with the speed of 5000 r.p.m for 30sec. This provides a total resist thickness of more than 1.5 μ m. In both cases, marker and bondpad layer, the sample is baked at 120 $^{\circ}$ c for 60min after

spinning the first resist and is then baked in a 180°C for 120min after spinning the second resist layer. This is to drive off the solvent from the resist film.

To develop the resist after exposure, the standard 2:1 IPA:MIBK (methyl isobutyl ketone) developer is used for 2mins at 23°C followed by 60sec IPA. After using the developer, a barrel asher is used in order to remove any residual resist scum in the developed area. The barrel asher generates low power oxygen ions which etch the undeveloped resist at an insignificant rate, but are aggressive enough to remove the scum from the developed area.

3-4-2 Electron-Beam Lithography

Electron-Beam Lithography (EBL) is used for transferring the pattern to the resist coated semiconductor during the fabrication of marker and bond-pad layers. Electron beam lithography uses a focused beam of electrons to write patterns directly onto the sample and unlike photolithography, there is no need for a mask in this system. The main advantages of electron beam lithography are ultra high resolution, highly automated and precisely controlled operation, alignment accuracy, and accessibility to the designed pattern for modifications or correction of the faults during the fabrication between different levels. EBL used throughout this project for the fabrication of all levels except for the airbridge level, where the need for thick resist during the fabrication of elevated parts, makes photolithography more suitable. The photolithography process steps will be discussed when considering the fabrication stage of elevated parts in section 3-5. The electron beam lithography in this work is carried out using a Vistec VB6-UHREWF (Ultra High Resolution Extremely Wide Field) machine. In order to transfer the pattern to the substrate through this machine, first the

layout created using ADS software is exported to the GDSII file format. The Computer Aided Transformation Software (CATS) is then used to fracture the pattern and the final layout is generated in Belle software with a given substrate size, resolution, dose and beam size. [129, 130]. Then the job is submitted to the JWNC staff and the pattern is transferred to the resist coated substrate using VB6 machine.

3-4-3 Metallisation and lift-off

Metallisation in the fabrication of the marker and bond-pad layers is done using electron-beam evaporation where an electron flux generated by a high voltage applied between a thermionic emission filament and a crucible is used to heat the source material to be deposited. The metallisation takes place in a vacuum chamber.

Plassys (MEB 400S and MEB 550S) evaporation systems are employed to deposit NiCr and Au on our samples during the fabrication of markers and bond-pad layers. Prior to metallisation, de-oxidation of the samples is done using 1 HCL: 4H₂O to remove any possible oxide layer formed on top of the semiconductor. This is to optimise the resistance between metal and semiconductor material since this oxide layer presents a barrier to the electrons as they pass from metal to semiconductor and should be removed.

The metallisation step in both marker and bond-pad fabrication is followed by 'lift-off' which is used to remove the resist mask and unwanted metal. For lift-off to be successful, an undercut profile in the resist is required which, as mentioned before, can be obtained by using a bi-layer resist strategy, Fig.3.5. The ledges in the undercut profile prevent the sidewall of the resist from being coated during evaporation and

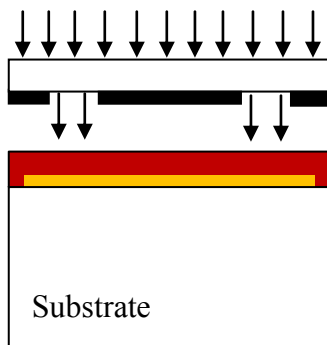
therefore allow reliable metal lift-off. The metal is lifted-off along with unexposed resists by immersing the sample in warm acetone at 50°C.

3-5 Definition of elevated structures

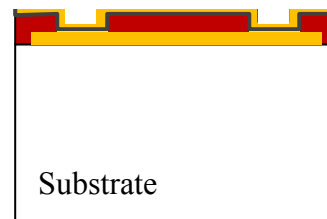
After fabrication of the markers and bond-pad layers, the elevated structures are formed. In this stage, we utilise a standard air-bridge process which is used in the JWNC fabrication centre [131]. Modifications and development to the standard recipe was required due to our novel structure requirements. The standard air-bridge fabrication process is sketched in Figure 3.6.

 AZ4562 Photoresist
 S1818 Photoresist

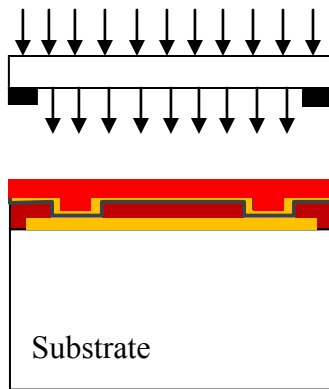
 Au
 Titanium



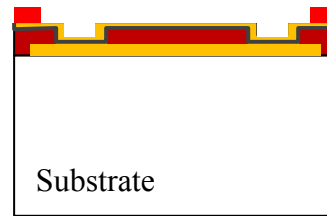
1) Forming mask for Supporting posts:
 Spinning photoresist, baking, UV Exposure



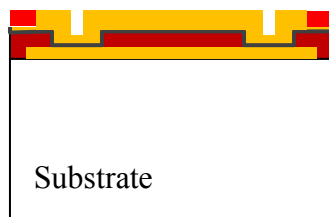
2) Resist Development in AZ400K:H₂O (4:1)
 De-oxidation in HCL:H₂O(1:4)
 Seed-layer: Evaporation of Ti/Au(50nm/10nm) followed by sputtering Au(40nm)



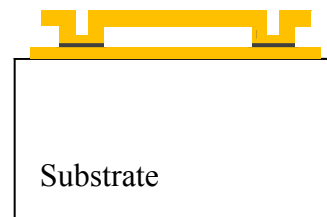
3) Forming mask for elevated tracks:
Spinning S1818 photoresist,
Baking, UV Exposure



4) Resist Development in
Microposist:H₂O (1:1),
O₂ Ash in dry etch machine



5) Forming the elevated parts:
Electroplating ~2 μ m gold
(20 min, 50°C, 100rpm)



6) Lifting-off the photoresist
and etching Ti/Au seed layer

Figure 3.6: Fabrication steps (1-6) of airbridge process

The air-bridge fabrication process includes the fabrication of supporting posts (steps:1-2) and elevated traces (steps:3-6). The complete fabrication process of the elevated parts consists of: resist coating and development, photolithography, metallisation (e-beam evaporation, sputtering and electroplating) and etching.

3-5-1 Photolithography

Photolithography is used to transfer the pattern onto the substrate during the air-bridge fabrication process. This is because of the use of thick resist (6-13 μm) to support the high elevation in our structures and because the large feature sizes of the air-bridges does not require e-beam lithography. UV photolithography is able to transfer the pattern to the semiconductor substrate by a single exposure over a large area and therefore it is fast and cheap compared with e-beam lithography. Two levels of photolithography are used in our process - in the fabrication of supporting posts (level 1) and in the fabrication of the elevated traces (level 2). The required mask for each level is prepared using e-beam lithography. The procedure for the design and job submission of the masks is similar to that explained in the e-beam section. The technical staff of the JWNC prepare the masks by coating a quartz mask with chrome and spinning the e-beam resist on top of the chrome. After exposure and development, the chrome is etched away using a chemical wet etch and the remaining resist is removed using a barrel asher- leaving the original pattern transferred onto the chrome. Multiple copies of the chrome master are then made using photolithography. Apart from the structure pattern, each mask also contains a series of alignment marks which are used to align the sample with respect to the mask. After alignment, the sample is brought into contact with the mask and exposed to UV light using a Karl Suss MA6 mask aligner machine.

The exposure dose and time need to be calibrated. In the standard air-bridge process, with a resist thickness of almost 6 μm and supporting posts of minimum 15 \times 22 μm size, the supporting posts (first level) are exposed to UV light for 15sec and then the elevated tracks (second level) for 15sec. However, when smaller supporting post sizes and/or thicker resists are used (to achieve higher elevation), the process needs to be

modified. To this end, a set of experiments were done to optimise the exposure and developing process for the fabrication of the elevated structures with smaller supporting posts and higher elevations. It was found that the exposure time can be increased to values as high as 80-100secs when the AZ4562 is used without causing overexposure. This, otherwise, increases the yield when smaller posts sizes are used. Therefore, during the fabrication of our structures, to achieve small supporting posts, i.e. $7 \times 7\mu\text{m}$, with a resist thickness of around $6\mu\text{m}$, it was found that the exposure time needs to be increased to 85sec for the first level. Also, in the case of using thicker resist ($12\text{-}13\mu\text{m}$), the exposure time at the first photolithography level need to be changed to 30sec for usual post sizes (minimum of $14 \times 22\mu\text{m}$) and 100sec for small post sizes (minimum of $10 \times 10\mu\text{m}$).

In the second fabrication level of the air-bridge process (forming elevated tracks), the standard exposure time of 15sec is used for resist with $6\mu\text{m}$ thickness while it was found that this value should be increased to 20secs when a thicker resist of $12\text{-}13\mu\text{m}$ is used.

These changes, along with the development optimisations, which will be explained in the next section, resulted in the successful fabrication of elevated structures with smaller supporting posts and/or higher elevations. Decreasing the size of supporting posts and increasing the elevation height led to significant performance enhancements in our fabricated circuit components and provided useful data in the characterisation of our structures. Fig.3.9 (e) shows a fabricated structure with an elevation of $6\mu\text{m}$ and post sizes of $7 \times 7\mu\text{m}$.

3-5-2 Photoresist and development

In our photolithography process, AZ4562 and S1818 photoresists are used for different lithographic levels. In the elevated structures, the final elevation height is mainly determined by the thickness of the photoresist used in the fabrication process for the supporting posts, and the type of photoresist chosen is based on the required elevation.

Elevated structures with elevation heights of 2 μm , 6 μm and 13 μm were required, and process optimisation was needed in resist coating and development to achieve these elevations.

In the standard air-bridge process, AZ4562 is spun at 4000 rpm for 30secs in the fabrication of supporting posts, Fig.3.6 (step:1), followed by baking at 90°C for 30 mins to evaporate the solvent. This provides a resist thickness and elevation height of around 6 μm . In general, the AZ4562 can support a thickness range 5.06-8.77 μm [132] by controlling the spinning speed. In order to achieve elevations as high as 13 μm , two layers of AZ4562 resist are spun. After spinning the first AZ layer with a speed of 4000rpm for 30sec, the sample is baked in a 55°C oven for 20mins. This baking time is found to be critical in order to prevent the structure from reshaping when it goes through the other baking processes in the following stages. After baking the first layer, a second layer of AZ resist is spun with the same recipe followed by baking at 90°C for 30mins. Using this process, a final resist thickness of 12.5-13 μm can be achieved.

In order to fabricate structures with elevation heights as low as 2 μm , S1818 photoresist is used in forming the supporting posts. S1818 can provide thicknesses of almost 2 μm when spun at 3000 rpm for 30secs. The resist is then baked in a 90°C oven for 15 mins to evaporate the solvent.

After exposure of the photoresist in the first level (fabrication of supporting posts), the AZ45642 resist is developed using 1AZ400K: 4H₂O followed by rinsing in RO water. Development time for one layer AZ resist is 2.5mins and for the sample using two layers of AZ resist is 5mins. In the case of using S1818 at this level, 1Microposit:1H₂O is used as developer with development time of 1mins. The sample is always checked during the development process and further development is done if required. The development process is followed by 2mins oxygen ash in a dry etch machine to remove any resist scum. Fig.3.7 shows the successful development of the post sections with a resist thickness of 13 μ m and supporting posts with minimum size of 10 \times 10 μ m.

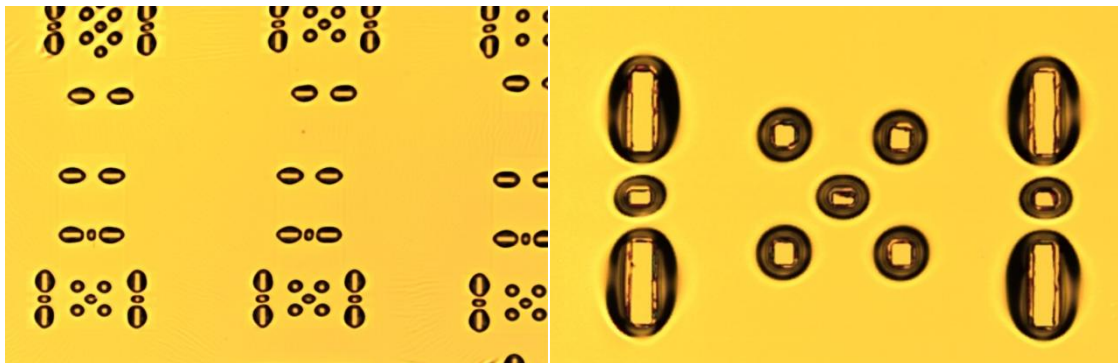


Figure 3.7: Developed holes with minimum size of 10 \times 10 μ m on 13 μ thick resist to form supporting posts in elevated structures

In the second level of the air-bridge fabrication process (fabrication of elevated traces), Fig.3.6 (step:3), S1818 is used as photoresist. The resist is spun for 30sec with a speed of 3000rpm to provide 2 μ m thickness. After exposure, the resist is developed in 1Microposit:1H₂O for 3mins. In the whole of the air-bridge process, this part of the fabrication is found to be the most critical, and the limiting factor in reducing the size of the supporting posts and/or increasing the elevation height. This is because, in order to

provide good adhesion for the metal deposited in the following fabrication step to the substrate and to form strong supporting posts, the spun S1818 resist should be perfectly removed from the bottom of the holes opened for the supporting posts. To achieve this, when small supporting posts or higher resist thickness is used, an increase in exposure dose/time or development time is required which can lead to overdevelopment of the elevated parts. After considerable process optimisation, the smallest post size we could reliably fabricate was $7 \times 7 \mu\text{m}$ at an elevation of $6 \mu\text{m}$ and $10 \times 10 \mu\text{m}$ at an elevation of $13 \mu\text{m}$. It should be mentioned that the final elevated structure with these sizes of supporting posts are not very strong mechanically.

3-5-3 Metallisation

During the air-bridge fabrication process, three methods of metallisation are utilised to shape the elevated sections. These are: evaporating, Fig.3.6 (step:2), sputtering, Fig.3.6 (step:2), and electroplating, Fig.3.6 (step:5).

In the fabrication of the supporting posts, a seed layer is formed to support the electrical contact for the subsequent electroplating process in the fabrication of the elevated tracks. This seed layer is formed by first evaporating a 50nm of Titanium to increase the adhesion of airbridge contacts, followed by a 10nm layer of Au to prevent the Titanium from oxidising. Plassys MEB 450 Electron Beam Evaporator (*Plassys I*) and a Plassys MEB 550S (*Plassys II*) are used for metal evaporation. To complete the seed layer, 50nm of Au is sputtered to the sample. The sputtering technique is used to achieve better coating of the walls of the small holes used to form supporting posts and provide better contact for the next metallisation step. Sputtering is carried out using Plassys MP900S.

Finally, to form the elevated tracks, electroplating is used. Electroplating is usually used to produce a very thick layer of metal when large process variations can be tolerated. Although very high resolution cannot be achieved by using a plating process, it offers a formation of a metal layer in a particularly cost-effective manner.

An electrical current is used to deposit the desired material from a metal salt solution and coat a conductive surface with a thin layer of the material. During the electroplating process, our sample is mounted on a copper plate using wax while the electrical connection to the plate is achieved using silver paint. The sample is immersed in the electroplating solution which is stirred with a stirrer paddle. During the process, the solution is placed in a water bath at 50°C. The sample is negatively biased by a d.c power supply with its current set using the following equation [131]

$$\text{Plating current (mA)} = [\text{Sample holder area} - \text{sample area}](\text{mm}^2) \times 0.013$$

Applying the calculated current for 20mins, results in 2µm electroplated gold. A thickness of 2 µm is used to ensure optimum metal thickness (more than 5times the skin-depth for the whole frequency range of interest) for our structures to keep the conductor loss at minimum and also to reasonably fill the supporting posts for good mechanical strength. However, as can be seen in Fig.3.9 (b), using this metallisation thickness, compared with the elevation height of 6µm or 13µm, completely filled supporting posts cannot be achieved and posts in the final structure include small holes. The fabrication flow is as shown in Fig. 3.6 if the posts are not required to be completely filled. If the holes are required to be filled, additional fabrication steps are required and the fabrication steps from 6 to 9 can be followed, Fig 3.8.

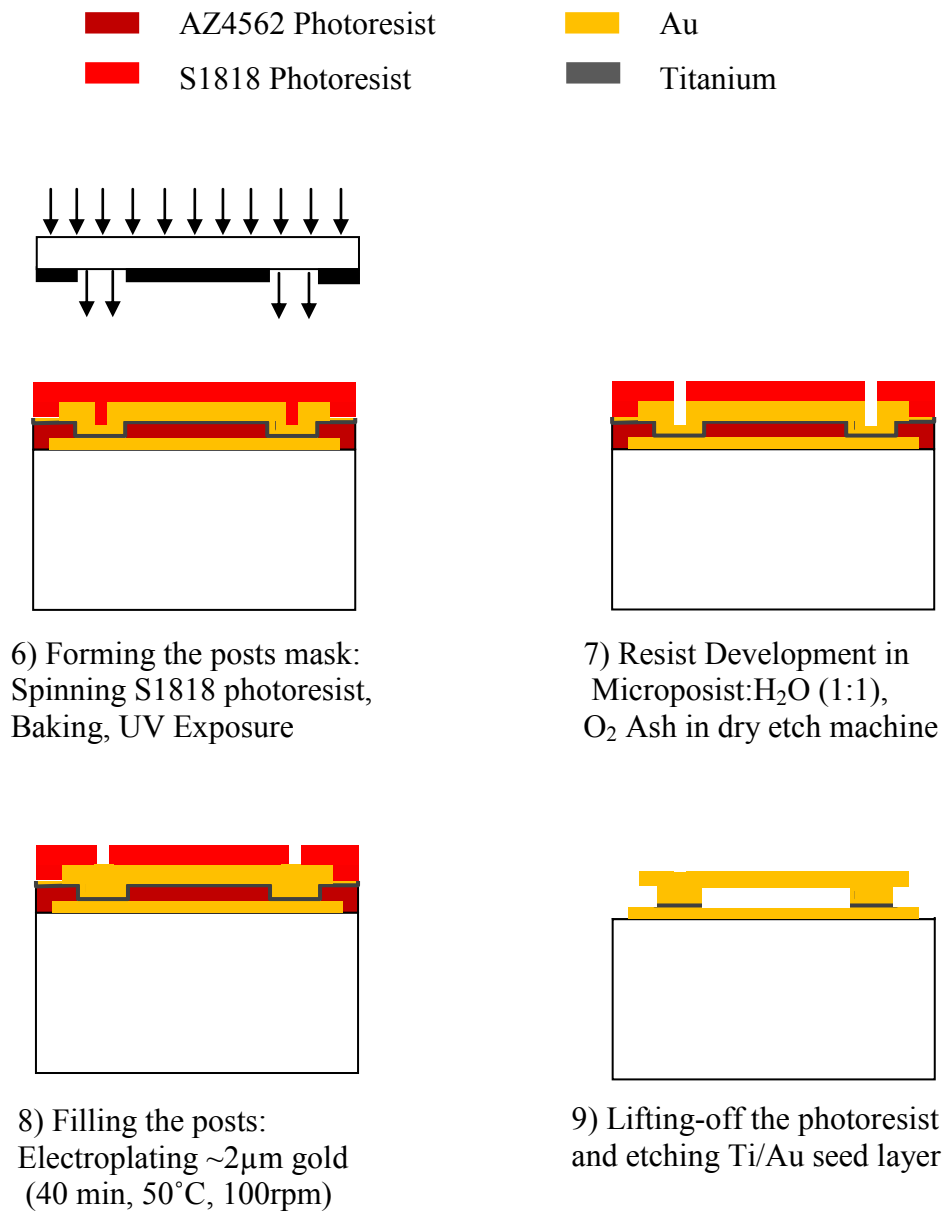


Figure 3.8: Continued fabrication steps of Fig.3.6, (6-9) when the supporting posts need to be filled.

After electroplating, only remaining process steps are to remove the unwanted masks and layers. Flood exposure and development in 1:1 Microposit:H₂O is done to remove the top photo-resist layer. In subsequent stages, etching is used to remove the seed layer. The gold etcher is used for 10sec to remove the gold and 4:1 buffered HF is utilized for

30sec or more to etch the titanium away. This is a critical stage since any remaining gold or titanium can make the next stage in the process fail and also extra gold etching can remove some amount of gold from the elevated parts. For the final step, the AZ photo-resist layer is washed out using flood exposure and development. The full recipe of the fabrication process for 6 μm and 13 μm elevated structures are given in Appendix1. Fig.3.9 (a-f) shows micrographs of some of the fabricated elevated structures in this work from different angles.

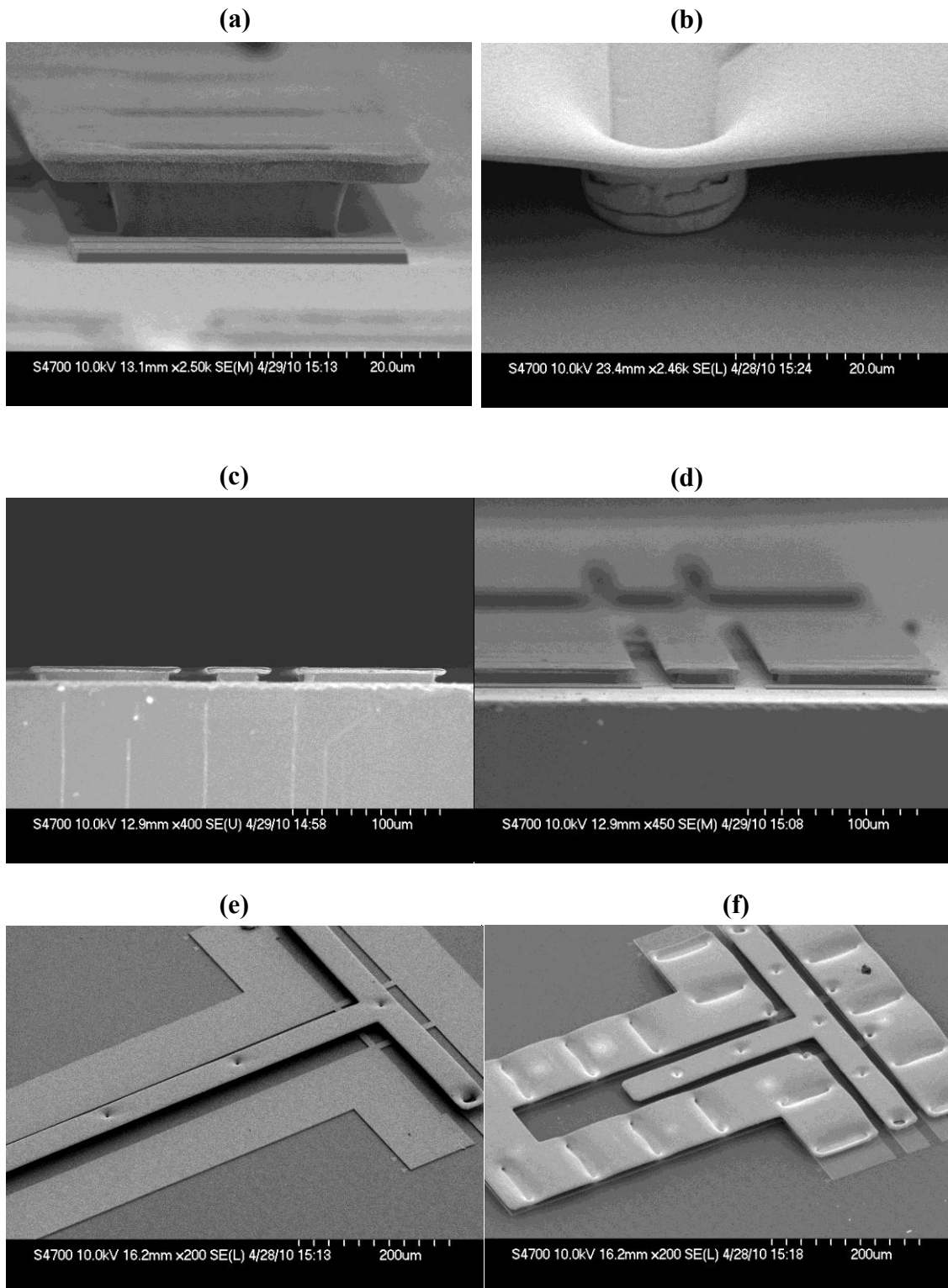


Figure 3.9: Fabricated elevated structures at: a and b) post section, c and d) cross-section, e and f) angled view.

3-6 Summary

The general fabrication principle of elevated CPW structures using air-bridge process as applied to the work in this project has been presented and discussed. The process flow of the air bridge process is presented and discussed in details. Work was undertaken to optimise the general airbridge fabrication process used in JWNC in order to achieve elevated structures with small supporting posts and/or high elevations. The limitations to achieve this is discussed and the development process is presented. Using developed recipe, structures with elevations as high as $13\mu\text{m}$ (compared with usual $6\mu\text{m}$ elevations) and supporting posts as small as $10 \times 10\mu\text{m}$ (compared with usual $14 \times 21\mu\text{m}$ post size) were fabricated for this work.

Chapter4

All-elevated Coplanar Waveguide

4-1 Introduction to Elevated CPW structures

This chapter presents a comprehensive study of a transmission line, which shows a good potential for high frequency applications, called the elevated coplanar waveguide. Elevated CPW structures, which use airbridge technology to elevate the CPW traces above the substrate, were initially proposed to overcome the problem of high losses that are found in conventional CPW implementations of extremely low and extremely high impedance lines [93]-[95]. Due to its structure, the elevated CPW transmission line seems to be a very attractive candidate for sub-Millimetre wave I.C interconnects and passive networks [20], [58]-[60]. A lower effective dielectric constant (compared to conventional CPW lines) can be obtained by use of this structure as most of the electric field is contained within the air gap between the substrate and elevated trace(s) and in the air immediately above these traces. This, in general, results in lower loss through the line and higher Q distributed networks. In fact, the parameters of an elevated CPW line depend less strongly on the substrate thickness than do non-elevated CPW lines as the electric field weakly penetrates the substrate. It is through this phenomenon that the benefits of elevated CPW are achieved as the signal is, to some extent, isolated from the

lossy semiconducting substrate. This can be clearly seen in Figure 4.1 which shows a cross-sectional view of the electric field in CPW (a) and elevated CPW (b) transmission lines. Fig.4.1(b) shows that most of the electromagnetic field in elevated-CPW structure is confined in the lossless air layer and only weakly penetrates the semiconductor substrate. Compare this with conventional CPW structure, Fig.4.1(a), which shows an electric field distributed evenly between the air and dielectric regions.

Another characteristic of elevated CPW lines is that, compared with CPW, a relatively wide signal trace can be used to form a high impedance line. This is due to the fact that, as will be discussed in the next section, the characteristic impedance of elevated CPW structures is defined by the elevation height as well as the ratio between the centre conductor and slots of the CPW structure. This allows us to increase the impedance by increasing the elevation height without extreme reduction in centre conductor width. Therefore, high impedance elevated CPW transmission lines typically exhibit lower conductive loss compared with high impedance CPW lines.

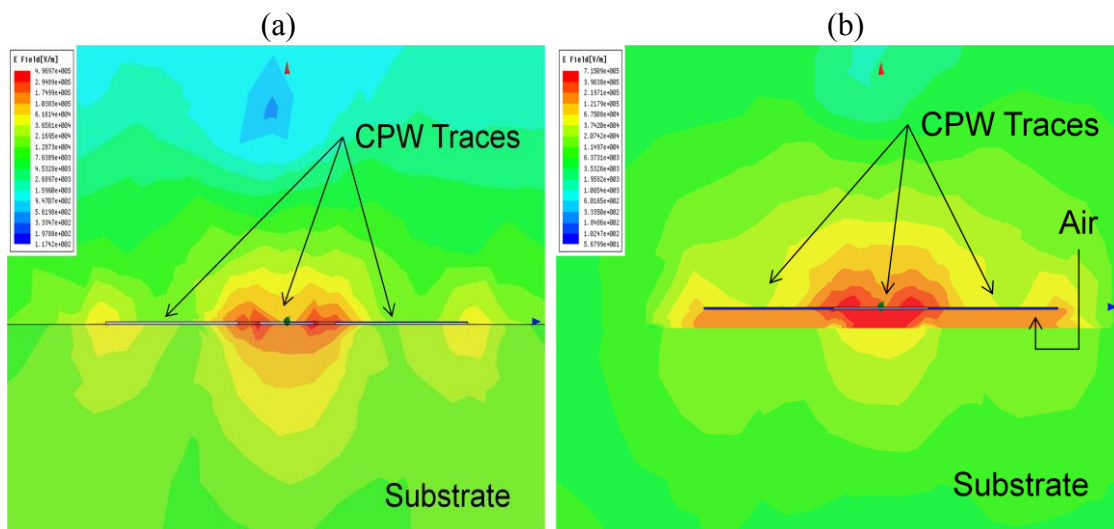


Figure 4.1: Profile of electric-field distribution modelled for (a) CPW line directly on the substrate and (b) CPW line 5µm elevated above the substrate.

Despite the potential of the elevated CPW line, this structure, prior to the work in this thesis, had not been investigated for its performances at sub mm-wave frequencies and for mid range characteristic impedances.

Different structures for this kind of transmission medium are possible and some of them have been suggested before, such as elevated centre conductor, elevated centre and ground conductors, and overlapped structures [58]-[60], [93]-[95], [133]-[134]. In this work, we first consider three different configurations of elevated CPW structures for the study of their high frequency performance. Figure 4.2 shows the cross sectional view of these three configurations which are here named: all-elevated CPW (a), signal-elevated CPW(b) and ground-elevated CPW(c) structures.

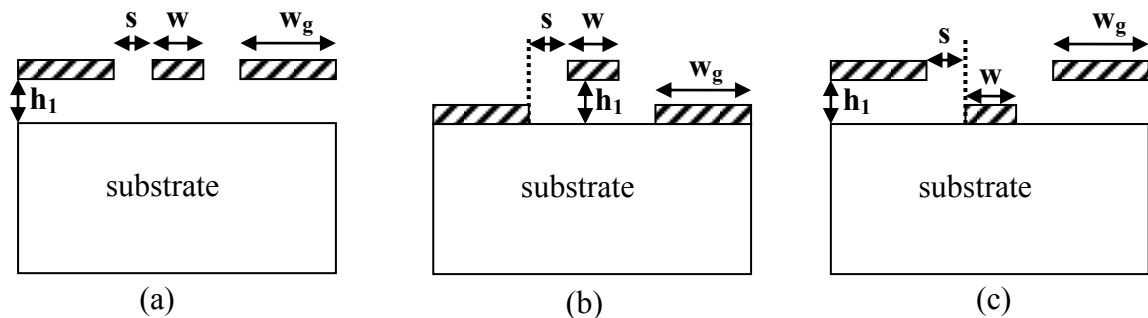


Figure 4.2: Elevated CPW structure with (a) all traces elevated (b) signal trace elevated, and (c) ground traces elevated.

A series of transmission lines with the three above-mentioned geometries were designed, fabricated and measured. All-elevated(a) and signal-elevated (b) structures have previously been investigated. However, the ground-elevated (c) structure is here investigated - to the best of the author's knowledge - for the first time. In all three cases, this work presents the first measurements up to a frequency of 320GHz. The calibration method and measurement procedure is explained in detail in section 4.3. The lines have identical designed geometries with 2.136mm length and the following dimensions:

$W=36\mu\text{m}$, $S=20\mu\text{m}$, $W_g=100\mu\text{m}$. The lateral dimensions of 20-36-20(μm) was chosen as a starting point in order to achieve a line with a characteristic impedance close to 50Ω . Lateral dimensions of 25-36-25(μm), provides a 50Ω conventional CPW line. Since it was expected that elevated CPW structures would have a higher characteristic impedance than conventional CPW, smaller gaps were considered in the initial design to compensate.

However, due to the fabrication tolerances in airbridge technology, the fabricated dimensions of the lines are subject to small changes specific to each structure. The magnitude of the variation also increases as the elevation increases - i.e. the fabrication process is prone to greater variation between the designed and actual fabricated structure for high elevations. The fabrication process for the elevated CPW structures was explained in detail in Chapter 3. At an elevation of $6\mu\text{m}$, the fabricated dimensions of the all-elevated CPW line is found to be (15-41-15) μm and is (17.5-41-17.5) μm for signal-elevated CPW line and (17.5-36-17.5) μm for ground-elevated CPW line. A general view of the lines' performance can be achieved by looking at the measurement results for the mentioned lines shown in Figure 4.3. A more detailed investigation of elevated CPW performance will be given later in this chapter.

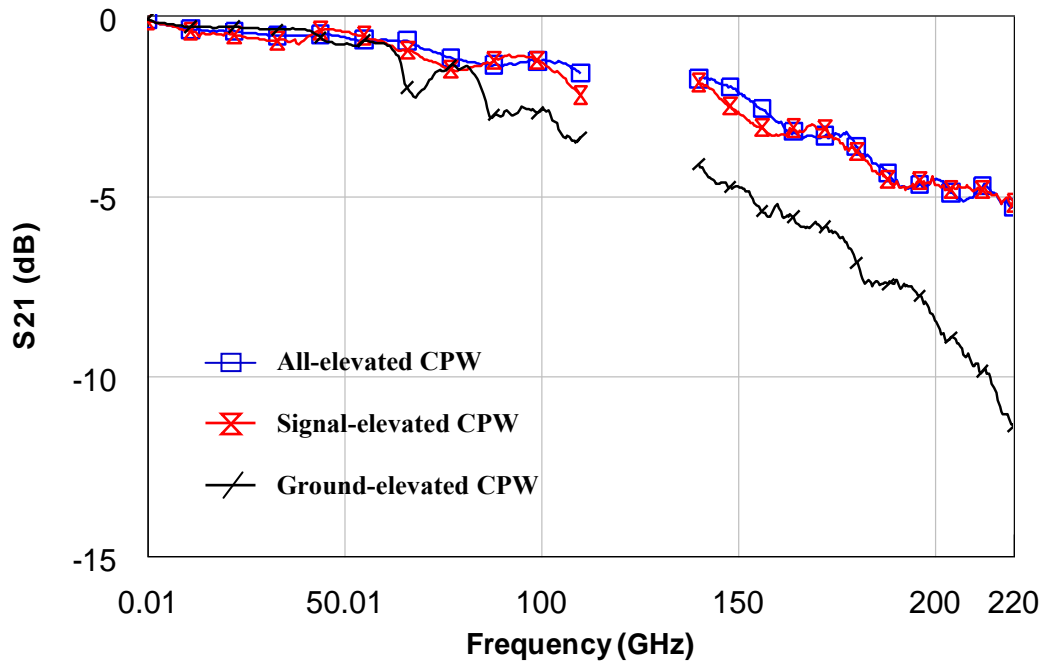


Figure 4.3: Measured S-parameters of elevated CPW with 3 different configurations: all-elevated CPW, signal-elevated CPW and ground-elevated CPW

The chart reveals that elevating all traces leads to slightly lower losses than the signal elevated line, Fig.4.3, whilst both lines are found to have lower insertion losses than the ground elevated CPW line. To remove the effect of characteristic impedance discrepancies, these elevated transmission lines are compared in terms of loss factor in Figure 4.4.

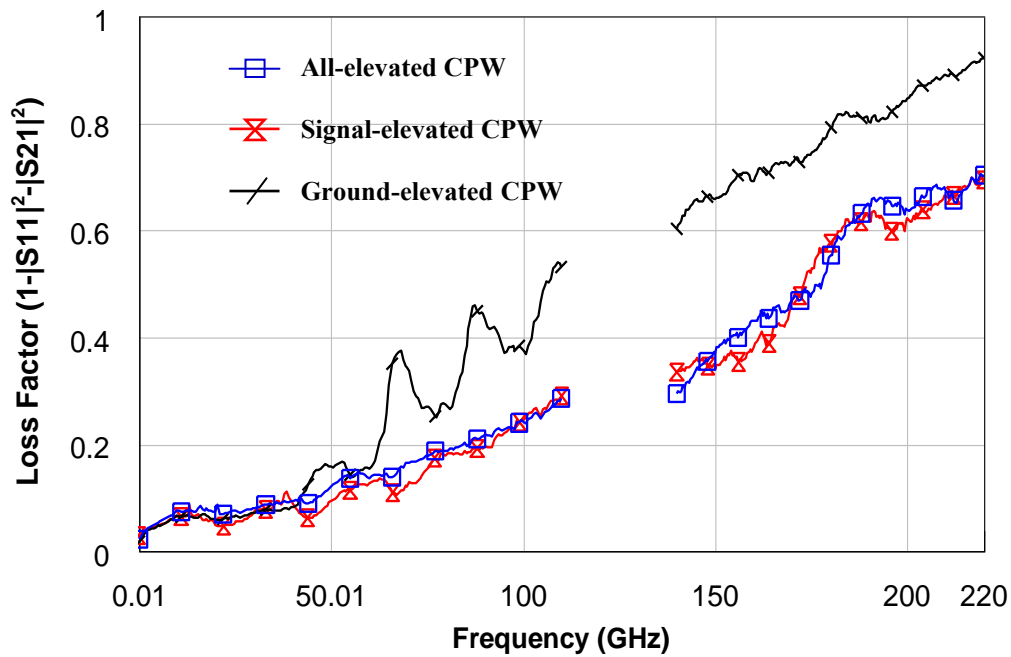


Figure 4.4: Measured loss-factor of all-elevated, signal-elevated and ground-elevated CPW structures.

Similar results, in terms of loss factor, can be observed for the first two types of elevated structure. However, the ground-elevated CPW shows resonances at frequencies above 50GHz and a very high loss factor when the frequency enters the G-band.

Due to the good performance of all-elevated and signal-elevated CPW transmission lines compared to ground-elevated CPW, these two structures were picked for further investigations. This chapter will be continued with a detailed investigation into the all-elevated CPW passive structures. A treatment of Signal-elevated CPW transmission line and associated passive circuit components will be deferred to the next Chapter.

In order to have a comprehensive study of all-elevated CPW transmission media, first the quasi static parameters including propagation constant and characteristic impedance of the line are derived in section 2 using conformal mapping techniques. In the 3rd section, the performance of the all-elevated CPW transmission line is presented up to 320GHz and compared with the conventional CPW transmission media. Furthermore, the response of matching networks which feature all-elevated structures are compared with equivalent geometries utilising conventional CPW (section 4). Due to the good results achieved for elevated CPW matching stubs, several band-pass and band-stop filters were designed, fabricated and measured up to 320GHz and their performance was also compared with CPW counterparts in section 5.

4-2 All-elevated CPW (ECPW) Analysis

All of the previously reported works on elevated CPW structures use either EM or experimental approaches for finding the characteristic impedance and effective permittivity. However, to aid physical insight and line synthesis, accurate analysis formulae are needed in order to determine a transmission line's characteristic impedance and effective dielectric constant. Therefore, in this section a semi-empirical quasi static analysis of the all elevated CPW transmission line is described. As previously mentioned in Chapter 2, the conformal mapping technique has been used to analyse various transmission lines commonly found in RF and microwave circuits. It provides a relatively simple and accurate approach for extracting the closed-form equations for the transmission line parameters. However, a full-wave analysis is required to obtain the information regarding frequency dependence of the characteristic impedance of elevated CPW transmission line. In general, the static parameters are easier to obtain than their

dynamic counterparts but, strictly speaking, such results are valid only at dc. In practice, however, the static parameters can be used in the analysis and design of microwave components and circuits even when the operating frequency is quite high, perhaps more than 18GHz or so, and still good results can be achieved [111].

In this section, the analysis is based on the conformal mapping of the dc fields in the physical z -plane to a parallel plate capacitor configuration in the w -plane via CPW on an infinitely thick substrate in the t -plane.

4-2-1 The structure of all-elevated CPW

A cross section of the elevated CPW structure is shown in Figure 4.5.

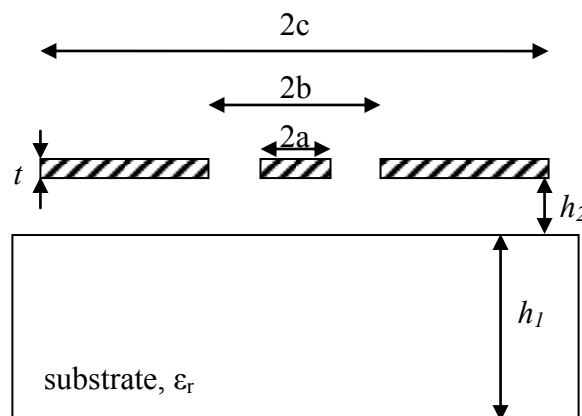


Figure 4.5: Cross section of an elevated CPW line

The elevated CPW line is suspended, in air, above a substrate and is supported by posts at the beginning and end of the line. The width of the signal line is $2a$ and the gap is given by $(b-a)$. The width of the ground planes are given by $(c-b)$, the substrate height is h_1 and the air gap between the substrate and the bottom of the conductors is h_2 . The finite thicknesses of the conductors and of the substrate layer are also taken into account and are denoted by t and h_1 respectively. In practice, the supporting posts are placed

periodically to provide the mechanical strength when the longer line is required. Figure 4.6 shows an angled elevated CPW transmission line resting on supporting posts.

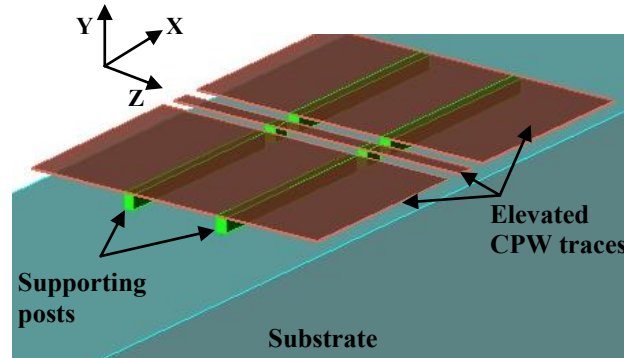


Figure 4.6: Angled 3-D conceptual view of a section of an all-elevated CPW line resting on posts.

Looking at the structure, it can be seen that the elevated CPW transmission line, unlike conventional CPW, is non-uniform in the z -direction i.e. direction of propagation. As will be discussed later in this section, the transmission line in this case can be approximated as cascaded CPW/Elevated CPW sections. However, in order to analyse the complete elevated CPW transmission line, it is first required to analyse the elevated section and then consider the effect of supporting posts. This analysis is presented in the following subsection.

4-2-2 Analysis in terms of capacitances for finite substrate height and finite conductor thickness

As mentioned previously in chapter 2, the transmission line's parameters can be obtained by calculating the total capacitance of the line. The total capacitance of the line, with and without dielectric, can be broken down into a number of discrete partial capacitances. After finding these partial capacitances, the total capacitance of the line

can be calculated with and without dielectric layers. It should be mentioned here that, due to the geometry of elevated CPW line, the 'conventional' partial capacitance analysis cannot be used here and needs to be modified. Typically, in layered structures, the familiar 'parallel partial capacitance' approach is employed for layers ordered in terms of decreasing permittivity i.e. [102]. In contrast, in the elevated CPW structure, dielectric layers are ordered in terms of increasing permittivity underneath the CPW traces. This type of configuration has been shown [135, 136] to need a 'series partial capacitance' approach. However, the series partial capacitance approach is applicable only to structures with infinite CPW ground planes. At relatively narrow ground widths, this approach can significantly underestimate the characteristic impedance and overestimate the effective dielectric constant. As an alternative, the problem is formulated here in terms of parallel partial capacitances but to match experiment the mapping function transforming between physical and t-planes is empirically modified to become a particular function of the substrate dielectric and geometrical parameters. The agreement thus obtained between calculated and experimentally derived results is extremely close. The discrete capacitances used for calculating the elevated CPW parameters are shown in Fig.4.7. Because of the symmetrical configuration of transmission line, only half of the structure is shown.

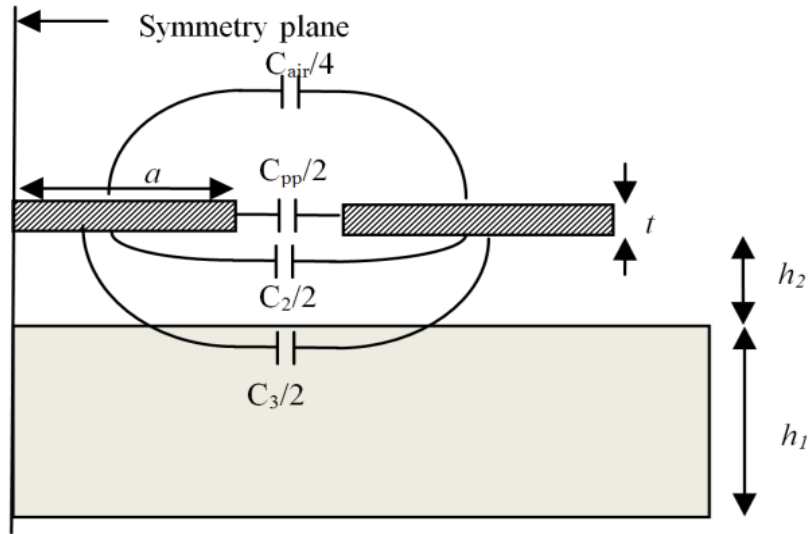


Figure 4.7: One half of all-elevated CPW cross section with various discrete capacitances [137]

With reference to Fig.4.7, C_{air} is the total capacitance between the signal strip and ground planes when there are no dielectrics present. This capacitance is a function of a , b and c only. C_{pp} represents the parallel plate capacitance formed by the signal and ground traces in the presence of finite conductor thickness. C_2 is the capacitance formed by the signal and ground traces over the height h_2 . C_3 is the capacitance between signal and ground traces over the height (h_2+h_1) .

The capacitance of the structure with all dielectric material replaced with air, C_{air} , is first calculated.

$$C_{air} = 4 \varepsilon_0 \frac{K(k_1)}{K(k_1')} \quad (4.1)$$

$K(k_1)$ and $K(k_1')$ are a complete elliptical integral of the first kind and its complement respectively. The modulus, k_1 , is given by

$$k_1 = \frac{a}{b} \sqrt{\frac{1-\frac{b^2}{c^2}}{1-\frac{a^2}{c^2}}} \quad (4.2)$$

and the complementary modulus is

$$k_1' = \sqrt{1 - k_1^2} \quad (4.3)$$

The parallel plate capacitance is

$$C_{pp} = 2\varepsilon_0 \frac{t}{b-a} \quad (4.4)$$

The 'air-gap' capacitance is calculated from

$$C_2 = 2\varepsilon_0 \frac{K(k_2)}{K(k_2')} \quad (4.5)$$

and k_2 is given by

$$k_2 = \frac{\sinh(x a)}{\sinh(x b)} \sqrt{\frac{1 - \frac{\sinh^2(x b)}{\sinh^2(x c)}}{1 - \frac{\sinh^2(x a)}{\sinh^2(x c)}}} \quad (4.6)$$

x is

$$x = \frac{\pi \sqrt{\left(\frac{\varepsilon_r - 2}{23} h_2 + 0.176t + 0.5a\right) \frac{1 - \frac{a}{2b}}{\varepsilon_r - \frac{a}{2b}}}}{\sqrt{2b} h_2} \quad (4.7)$$

The 'standard' modulus for C_2 can be obtained by substituting $x = \pi/(2h_2)$.

C_3 , the capacitance between the bottom faces of the conductors over the area occupied by the air gap plus dielectric when the dielectric is replaced with air, is given by

$$C_3 = 2\varepsilon_0 \frac{K(k_3)}{K(k_3')} \quad (4.8)$$

The modulus, k_3 , is given by substituting $x = \pi/(2(h_1 + h_2))$ in (4.7). The total capacitance of the line with dielectric is calculated according to

$$C_{tot} = C_{air} + C_{pp} + C_3(\varepsilon_r - 1) + C_2(1 - \varepsilon_r) \quad (4.9)$$

(4.9) shows that the total capacitance can be calculated by summing the air capacitance, the parallel plate capacitance, the capacitance of the substrate plus air gap regions when they are occupied by an homogenous dielectric layer, subtracting the air capacitance over the same region, adding the air capacitance of the air gap layer (this has been

subtracted by the $-C_2$ term) and finally subtracting the air gap capacitance with dielectric replacing air (this 'fictitious' value has been 'added' by the $C_2\varepsilon_r$ term).

The total capacitance of the line with dielectrics removed is given by

$$C_{totair} = C_{air} + C_{pp} \quad (4.10)$$

The effective dielectric constant is

$$\varepsilon_{eff} = \frac{C_{tot}}{C_{totair}} \quad (4.11)$$

and the characteristic impedance is

$$Z_0 = \frac{1}{c\sqrt{C_{tot}C_{totair}}} \quad (4.12)$$

c is the speed of light.

Figure 4.8 shows the plot of characteristic impedance calculated by varying the signal trace, $2a$, between $20\mu\text{m}$ and $160\mu\text{m}$ for three elevation of 2 , 8 and $14\mu\text{m}$. The constant values of $20\mu\text{m}$ for gap width($b - a$), $100\mu\text{m}$ for ground widths and $2\mu\text{m}$ for conductor thickness were considered. The substrate with dielectric constant of 12.9 (GaAs) and thickness of $600\mu\text{m}$ was taken into account for all cases.

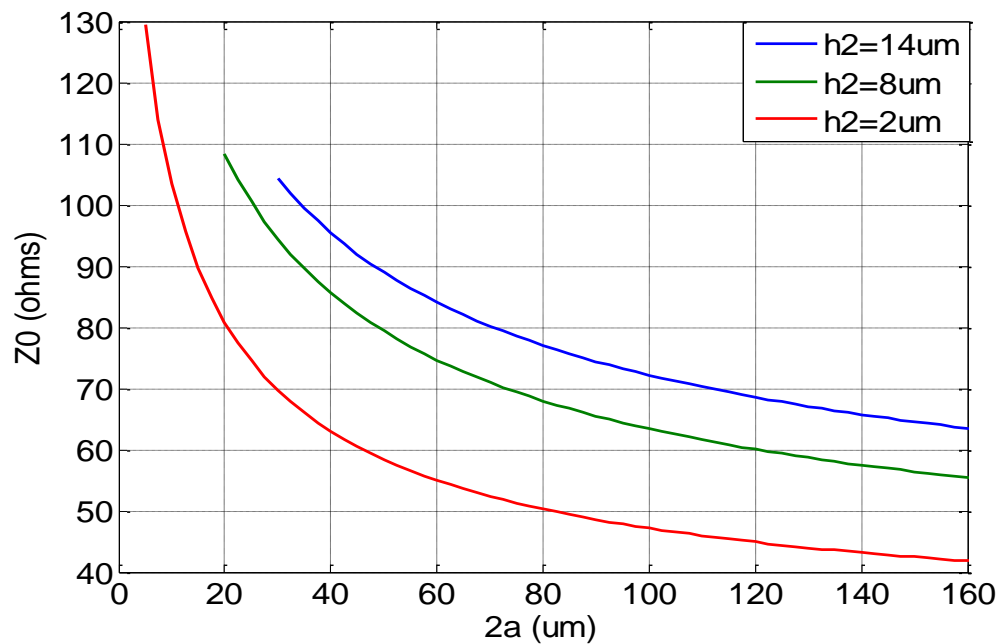


Figure 4.8: Calculated characteristic impedance of all-elevated CPW from (4.12) for varying $2a$, $b=2a+20$, $c=b+100$, $h=2,8$ and 14 . All dimensions are in micron.

It can be seen that by increasing the elevation height, whilst keeping other parameters constant, the characteristic impedance increases. For instance, the line with $60\mu\text{m}$ signal width exhibits a change in characteristic impedance from 55 to 85Ω when the elevation changes from 2 to $14\mu\text{m}$ with otherwise fixed geometries. The graph also shows that high characteristic impedances are possible at low elevations i.e. a 100Ω line can be achieved with lateral dimensions of $30\text{-}10\text{-}30\mu\text{m}$ at $2\mu\text{m}$ elevation. Low elevations, compared with higher elevations, are advantageous in terms of the mechanical stability. From the fabrication point of view, narrower signal traces, i.e. $10\mu\text{m}$, are possible with lower elevations than with high elevations. However, the characteristic impedance is more sensitive to geometry changes at low elevations. For example, by changing the signal width from 15 to $20\mu\text{m}$ with otherwise fixed geometries and with an elevation of $2\mu\text{m}$, the characteristic impedance changes from ~ 90 to 80Ω , Fig.4.8. Therefore, to take advantage of the possibility of combining low elevations with high characteristic

impedance, a tight control over the line dimensions is required during the fabrication process.

The effect of finite metallisation thickness is to decrease the characteristic impedance. This is because of the increase in parallel plate capacitance and the total capacitance of the line as a result. For instance, the characteristic impedance of an elevated CPW line with dimensions (20-60-20) μm and an 8 μm elevation reduces from 78 to 74.6 Ω by increasing the metal thickness from 0.002 to 2 μm . The effect of the finite thickness is more pronounced for relatively small signal widths since in this case the parallel plate capacitance accounts for a greater proportion of total capacitance. In the above example, by considering 20 μm for signal width, the impedance decreases from 115 to 108 Ω by increasing the metal thickness from 0.002 to 2 μm .

Also, the effect of finite substrate thickness is to increase the characteristic impedance as a result of smaller total capacitance with dielectric present. However, in this particular example, the effect of substrate thickness is negligible compare to the effect of finite metallisation thickness.

The effective permittivity calculating from (4.11) is plotted in Fig.4.9 for the same range of values as in Fig.4.8.

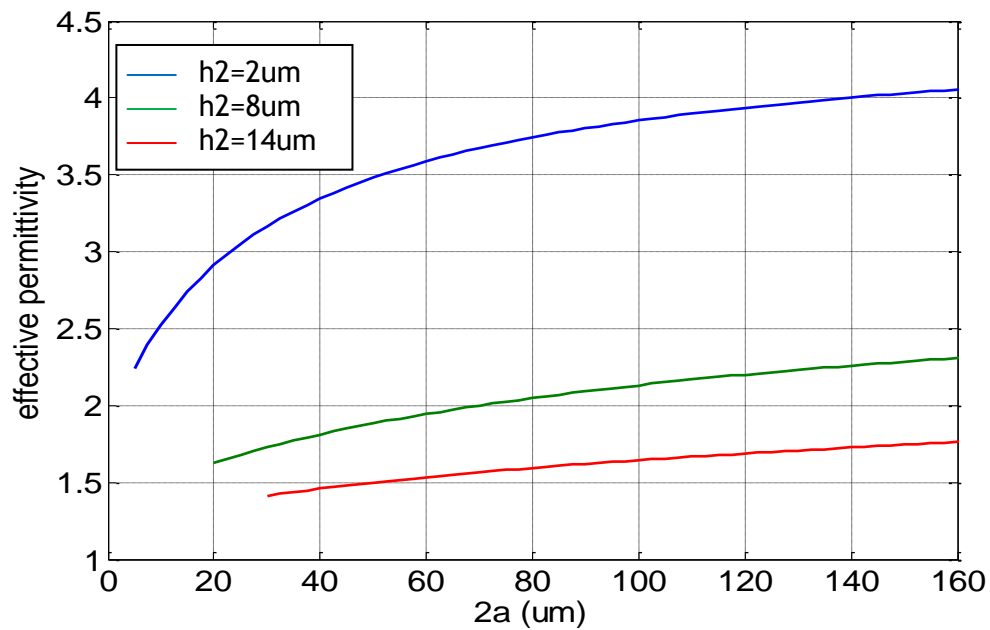


Figure 4.9: Calculated effective permittivity of all-elevated CPW from (4.11) for varying $2a$, $b=2a+20$, $c=b+100$, $h=2,8$ and 14 . All dimensions are in micron.

It can be seen that the effective permittivity decreases to values close to one by increasing the elevation height. Also, by increasing the signal width, the effective permittivity increases. For example, the increase of 1.8 to 2.25 is observed for effective permittivity by increasing the signal width from 40 to 140 μm at the elevation of 8 μm .

This is because by increasing the signal width, the more elongated electric field lines penetrate the substrate more deeply resulting in an increase in effective permittivity.

4-2-3 Comparison between the empirical approach and previously reported series capacitance approach

The empirical approach reported here is accurate for conditions satisfying $\frac{2a}{h_2} > 2$. The CPW on multilayer substrate was analysed previously by Ghione, *et al* [135] for the layers ordered in terms of increasing the permittivity underneath the CPW traces. The authors used the series partial capacitance approach to analyse the mentioned transmission line. The method reported only holds for CPW with infinite ground planes and gives highly accurate results under these conditions. In the case of CPW with finite extent ground planes, the series partial capacitance approach for the ratios of $\frac{2a}{h_2} < 2$ gives more accurate results than the empirical approach and is recommended. However for the ratios of $\frac{2a}{h_2} > 2$, the empirical approach gives more accurate results. This condition was determined by carefully comparing simulation data with the results calculating from the empirical method for various a, b and c and with the results calculated from the method in [135]. Comparison between the results based on these two methods is made in Fig.4.10. For all the numerical values in this figure, the condition $\frac{2a}{h_2} > 2$ is satisfied.

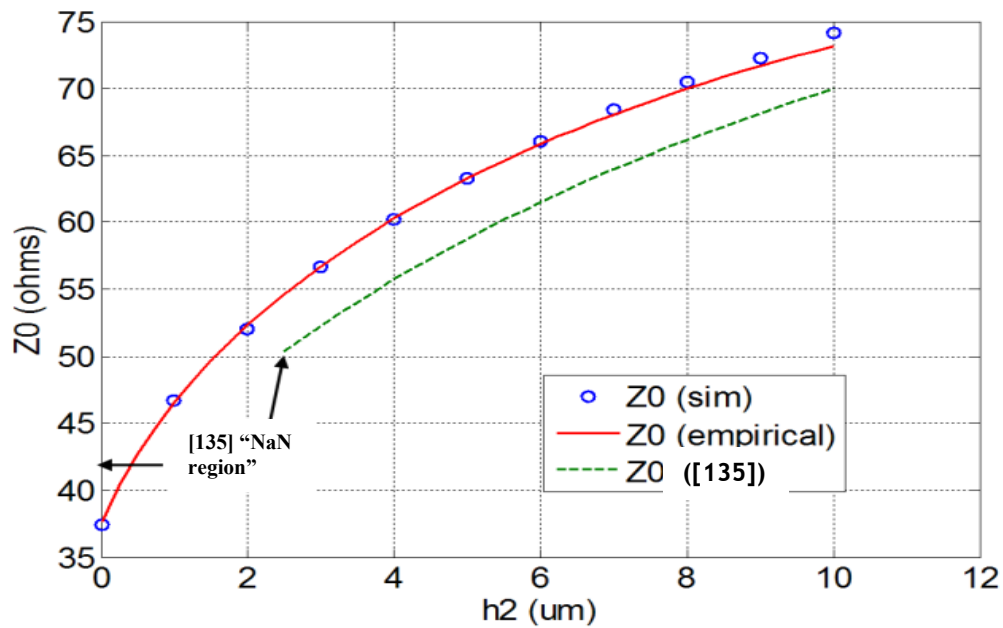


Figure 4.10: Characteristic impedance obtained for ECPW line by simulation, calculation from empirical approach (4.12) and calculation from [135]

It can be seen that series partial capacitance method slightly underestimates the characteristic impedance. This situation is reversed when $\frac{2a}{h_2} < 2$. The region marked

"NaN" (Not a Number) means that for the values of h_2 from 0 to approximately $2.5\mu\text{m}$, an undefined numerical result was returned since the ratio $K(k_2)/K(k'_2)$ tends to

infinity as the modulus, k_2 , approaches 1. Increasing the precision of the calculation would allow $K(k_2)/K(k'_2)$ to be computed for values of elliptic modulus increasingly close to 1. Also, developing a specific approximation, e.g., based on the formulae in

[138] could solve this problem. For values of $\frac{2a}{h_2}$ close to 2, the results calculated from

the empirical and series capacitance methods are in close agreement.

Looking from the practical point of view, the fabrication technique of standard MMIC compatible airbridge process dictates the upper and lower limits on the elevation height to be around $14\mu\text{m}$ and $2\mu\text{m}$, respectively. At and above $14\mu\text{m}$, the elevated lines are

very fragile and subject to the mechanical failure. At and below $2\mu\text{m}$, although the elevated lines have good mechanical strength, the characteristic impedance is very sensitive to even very small variations in elevation. Extremely precise elevation height is very difficult to achieve by using standard airbridge fabrication process.

Also, in order to approximate the practical upper-bound limit on the value of $2a$, the measurement and fabrication limitations needs to be considered. In the measurement process of most microwave and millimetre-wave components, probes with $50\text{-}100\mu\text{m}$ pitch are commonly used. If we assume the value for $2a$ to be less than two times of the size of the probe pitch, and also consider that the minimum fabricated gap for elevated structure is around $5\mu\text{m}$, the quantity of $2a$ is unlikely to exceed $180\mu\text{m}$. And the gap, $b - a$, is unlikely to exceed $90\mu\text{m}$. As for the lowest bound, the minimum trace width we fabricated with reasonable mechanical strength was around $8\mu\text{m}$. However, at $14\mu\text{m}$ elevation it is almost impossible to fabricate the $8\mu\text{m}$ trace and a more reasonable value at this elevation is around $20\mu\text{m}$.

Considering the limitation given for the previously discussed techniques, for example at the elevation of $14\mu\text{m}$, the empirical approach is suggested to use for $2a > 28\mu\text{m}$ and for $20\mu\text{m} < 2a < 28\mu\text{m}$, the analytical technique presented in [135] is recommended.

4-2-4 Comparison between theory, simulation and measurement for elevated CPW

To demonstrate the accuracy of the developed equations, the calculated data are compared with simulation and measurement results. Structures with various geometries over practical range of a , b and c were considered in this comparison. To obtain the simulation data, the Momentum planar RF solver is used. Figure 4.11 shows the

calculated and simulated results for various elevation heights from 0 to $14\mu\text{m}$. The signal width, $2a$, is considered to have a constant value of $40\mu\text{m}$ and data is obtained for gap widths, $b - a$, smaller, equal and larger than the signal width.

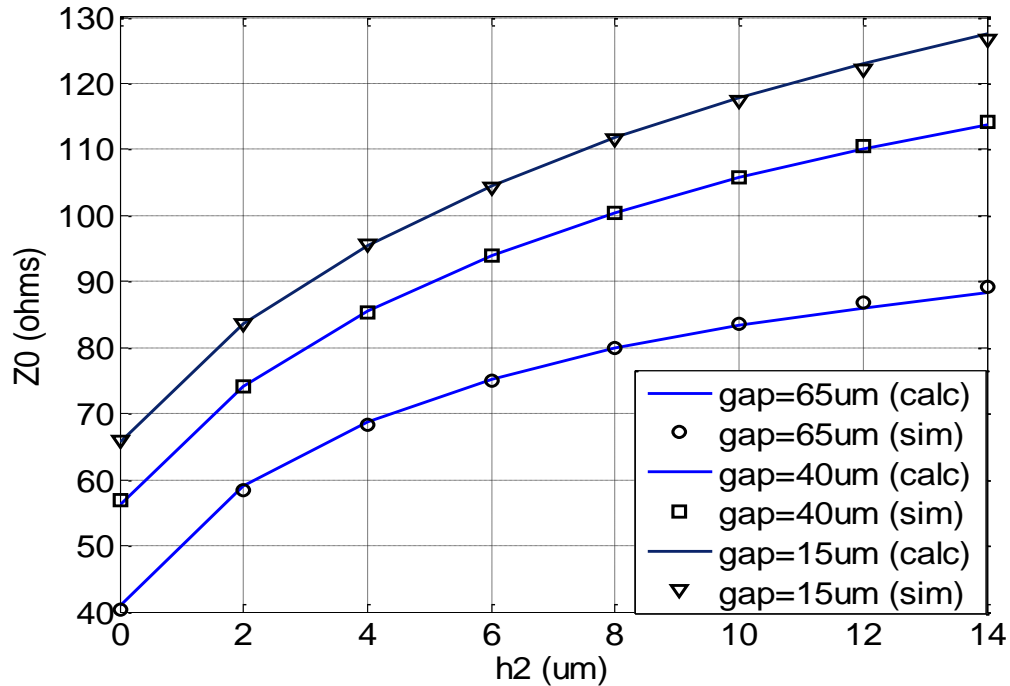


Figure 4.11: Comparison between modelled and calculated characteristic impedances for $2a=40\mu\text{m}$, $b=40+(15, 40 \text{ and } 65)\mu\text{m}$, $c=b+100\mu\text{m}$ and varying air gap thickness, h_2 . conductor thickness, t , is $2\mu\text{m}$ and substrate is GaAs with $600\mu\text{m}$ thickness.

It can be seen that excellent agreement between the calculated and simulated data is achieved here. Similar agreement was observed for widely varying geometries. In all cases sufficiently fine meshing is used in the simulations to ensure convergence.

Also to ensure the validity of calculated and simulated results, several structures with various geometries were fabricated and measured. The structures were inspected during and after fabrication using atomic force microscope, AFM, and optical microscopes to obtain accurate dimensions with $\sim 0.5\mu\text{m}$ tolerance. On-wafer measurement of the structures were done using an Agilent VNA network analyser from calibrated from 10MHz to 110GHz. The machine was calibrated using SOLT calibration technique.

Probes with 100 μm pitch were used during the measurement and also to minimize the feed effect, double set of posts were fabricated close enough, with 15-20 μm distance, to provide mechanical strength for probing on top of the elevated lines. Some of the measurement results are given in table 4.1 along with the calculated and simulated data. The results are for two different elevations of 2 μm and 10 μm which are near the low and high end of fabrication capabilities.

Table 4.1: Comparison between simulated, calculated and measured characteristic impedance of ECPW line for various geometries.

Width (μm)	Gap (μm)	h_2 (μm)	Z_0 (ohms) (4.12)	Z_0 (ohms) Meas.	Error% Meas& Calc	Z_0 (ohms) Sim.	Error% Sim& Calc
85	30	10	76.9	80	0.031	76.2	0.007
50	40	10	98	100.4	0.024	97.3	0.007
50	5	10	57.8	55.2	0.026	57.8	0
20	55	2	101.4	101.7	0.003	101.2	0.002
55	45	2	68.4	68.9	0.005	68.6	0.002
55	15	2	53.11	52.9	0.002	54.2	0.010

The table shows very good agreement of the measurement results with calculated and modelled data with error percentage less than 0.03% for whole range. The small discrepancies between the measured and calculated data can be due to the errors in the measurement of line dimensions and fabrication tolerances which causes non uniformities in the widths and gaps along the line.

To calculate the characteristic impedance of the lines from measurement results, the S-parameter block containing the line data is first connected to the short and open circuits.

The input impedance of each circuit is then measured and the characteristic impedance of the line is achieved by calculating the square root of the product of these input impedances. The concept of this method is explained in more detail as follows:

Considering the equivalent circuit of the transmission line, Fig.4.12, the characteristic impedance of a transmission line can be calculated using [29]

$$Z_0 = \sqrt{\frac{R+j\omega L}{G+j\omega C}} \quad (4.13)$$

where R is the conductor resistivity , G is the substrate conductance, L and C are the inductance and capacitance of the line per unit length, respectively.

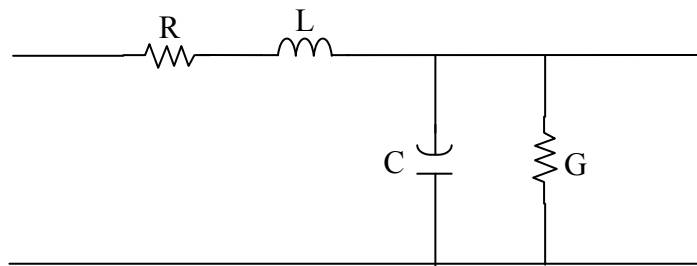


Figure 4.12: Equivalent circuit model of the transmission line [29]

In the transmission line's equivalent circuit, if we ignore the CPW trace resistivity and substrate conductance, R and G, the open circuited transmission line will have a predominantly capacitive input impedance and the short circuited line will have a prevalently inductive input impedance. Considering this, the open-circuited line can be viewed as a series capacitance between a port and ground and short-circuited line as a series inductance between the port and ground. Therefore the line capacitance and inductance can be written as

$$C_{line} = \frac{1}{2\pi f Z_{inoc}} \quad (4.14)$$

$$L_{line} = \frac{Z_{in sc}}{2\pi f} \quad (4.15)$$

where Z_{inoc} and $Z_{in sc}$ refer to the input impedances of open-circuited and short-circuited lines, respectively. They are, in fact, the input impedances of the two port blocks which are open or short circuited at the other port.

Placing (4.14) and (4.15) in the general equation of transmission line (4.13), we have

$$Z_0 = \sqrt{Z_{inoc}Z_{in sc}} \quad (4.16)$$

When applied to the uniform transmission line in the direction of propagation, the calculated characteristic impedance is independent of length since any parasitic inductance, for example due to physical length, appearing in the input impedance of the open circuit is cancelled by a proportional capacitive term in the input impedance of the short circuit. The validity of this equation is checked by using calculated results for simulated S-parameter data of CPW lines with various physical lengths and comparing the results with known accurate expressions of ideal CPW. The agreement in this case is near exact. The results achieved using this method are also compared with the method suggested in [139] for extracting the transmission line parameters from S-parameter data and near exact agreement is observed. However, when this method is applied to the non-uniform transmission line, in this case the elevated line, the derived characteristic impedance clearly has frequency dependence i.e. dispersion and at high frequencies, resonance. This will be discussed in next section. The characteristic impedances in table 4.1 were extracted below 10GHz on the flattest part of the extraction curve for each particular line.

4-2-5 Analysis of frequency dependent effects arising from CPW feed/post section/elevated section discontinuities

In real world, the elevated CPW transmission lines need to be connected to the CPW line on substrate so they can be connected to transistors and/or passive components. The connection between the CPW on the substrate and elevated CPW is via posts. These supporting posts also need to be placed along the elevated line to provide the necessary mechanical strength. Figure 4.13 shows an angled view of the elevated CPW line with CPW feeds and also posts along the line.

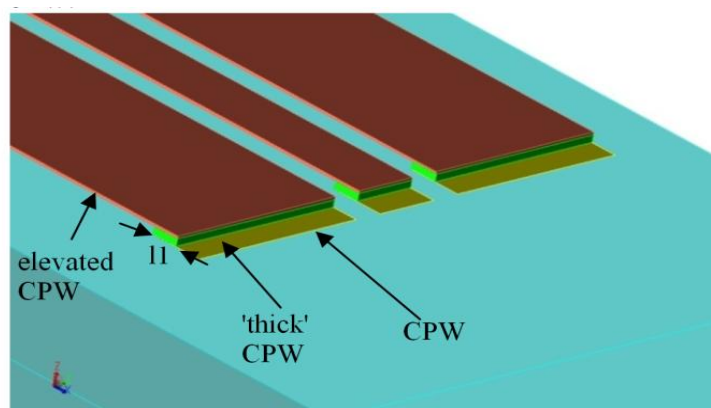


Figure 4.13: Diagram of CPW/ECPW transition feeds

It can be seen that elevated CPW line is non-uniform in the direction of propagation, z , and can be considered as cascaded CPW with various thickness and elevated CPW sections. The CPW sections are the transition feeds with metallisation thickness of t_1 and the posts with metallisation thickness of $(t + h_2)$ where t is the thickness and h_2 is the height of the elevated parts. Therefore, the formed compound transmission line will have a characteristic impedance different from the elevated line and this should be considered in the design of elevated transmission line. To calculate the characteristic impedance of this composite line, one possible approach is to analyse each section in isolation and then calculate the overall cascaded response. The CPW and thick CPW

parameters can be calculated from [98] with t_1 and t set to appropriate values. The elevated CPW part can be analysed as discussed. After analysing each section, the frequency dependant characteristic impedance of the composed line can be calculated from

$$Z_{inx} = Z_{0x} \frac{Z_{Ly} + jZ_{0x} \tan \left[\frac{\frac{2\pi}{c}}{f \sqrt{\epsilon_{effx}}} l_x \right]}{Z_{0x} + jZ_{Ly} \tan \left[\frac{\frac{2\pi}{c}}{f \sqrt{\epsilon_{effx}}} l_x \right]} \quad (4.17)$$

Where Z_{0x} and ϵ_{effx} are the parameters of each section with length of l_x and Z_{Ly} is the impedance of the pervious section. After determining these values for each of the distinct sections, to calculate the effective characteristic of the complete line, first Z_{Ly} is set to 0 and ∞ with Z_{0x} , ϵ_{effx} and l_x specified by the feed section parameters. This is to implement the short and open circuit at one port of the transmission line. Secondly, the two resulting input impedances are considered as Z_{Ly} of the second line with Z_{0x} , ϵ_{effx} and l_x specified by the second section. The process continues until the input impedances of the complete line with both short and open circuits connected at the far end are calculated. At the end, (4.16) is used to calculate the effective characteristic impedance of the composed line. The calculated results are then compared with the characteristic impedance calculated by applying (4.16) to measured data.

This comparison is made for a $6\mu\text{m}$ elevated CPW line on GaAs substrate which is broken up with 9 regularly spaced post sections, Figure 4.14. The parameters for the CPW feed sections are $Z_{0x} = 45\Omega$, $\epsilon_{effx} = 6.55$ and $l_x = 10\mu\text{m}$. For the post section they are $Z_{0x} = 41\Omega$, $\epsilon_{effx} = 6.4$ and $l_x = 10\mu\text{m}$. And for the elevated sections they are $Z_{0x} = 77.4\Omega$, $\epsilon_{effx} = 2.1$ and $l_x = 205\mu\text{m}$.

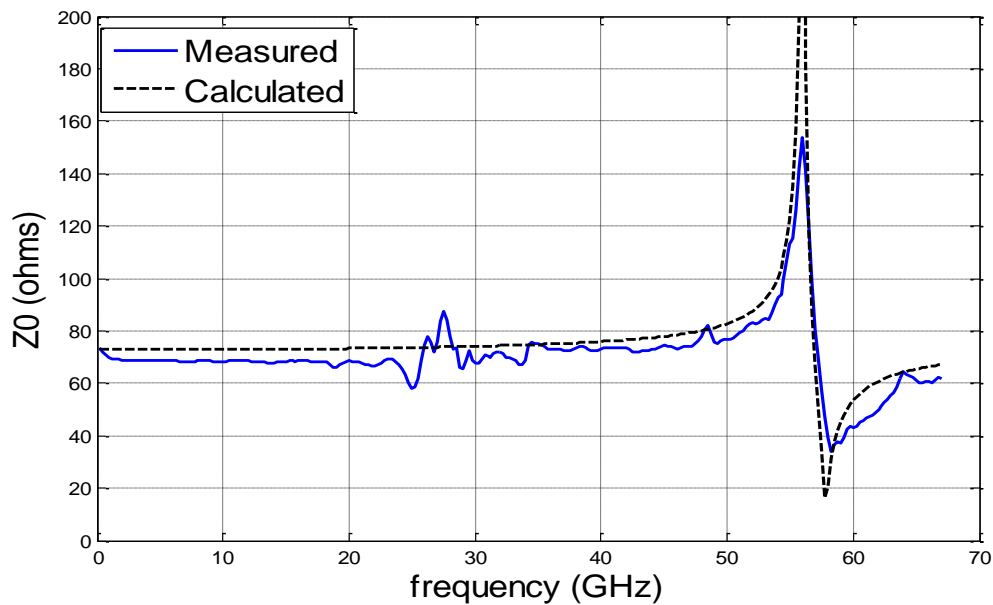


Figure 4.14: Comparison between measured and calculated effective characteristic impedance for the structure with CPW/thick CPW/elevated-CPW sections.

It can be seen that very good agreement is achieved between the measured and calculated characteristic impedance of this relatively complicated structure. A small discrepancy in shape and peak magnitude are mainly due to the assumption of zero CPW trace resistivity in the calculation.

As mentioned before, the observed resonance in the characteristic impedance is due to the effect of post and feed sections and the resulting impedance mismatches. For a given electrical length, the resonance effect is less pronounced for a line with less posts/ longer elevated section and is more pronounced for more posts/ shorter elevated section. In general, it is preferable to have as minimum a number of posts as possible in the

elevated CPW line. This is to minimize the resonance effect as well as reducing the contacts points to the semiconductor substrate and minimizing the unwanted substrate effect as a result. In practice, current fabrication processes allow us to have elevated sections of approximately 1mm at $6\mu\text{m}$ elevation. This maximum elevated length can be varied depending on the elevation height and the size of supporting posts. For example for the same transmission line, when the posts are reduced to 3 sets in the direction of propagation (2 sets of posts to connect the CPW feeds at each end and one set at the middle of the line to support the elevated traces) with elevated sections of $725\mu\text{m}$, the resonance frequency is pushed to higher frequencies by 5GHz. However, it is impossible to completely remove this resonance phenomena since in real situations the minimum 2 sets of supporting posts are necessary to support the elevated tracks at each end. In fact, simulation results for similar elevated line with just two sets of posts at each end of the line ($1460\mu\text{m}$ elevated line) pushes this resonance phenomena to the higher frequencies by 8GHz.

Besides, in order to reduce the impedance mismatch along the line, we can design the CPW sections in a way that they have similar/close impedances to the elevated part. For instant, for a given impedance and fixed $2a$, the CPW feed section can be designed to have larger gap than the ECPW and the CPW post section to have around 35% larger gap than the CPW feeds. In this way the impedance mismatch will be minimized and the characteristic impedance of the composite line will be less dispersive. By simulating the line in Fig.4.14 with feed lines, posts and elevated sections having close or similar impedances, the resonance becomes much less pronounced and finally disappears at the exact impedance match.

4-2-6 Losses in all-elevated CPW

The total loss of a transmission line is the sum of dielectric loss (due to non-zero conductance of the substrate dielectric), conductor loss (due to finite conductivity of the CPW traces) and radiation loss - the latter accounting for all losses not associated with either conductor or dielectric loss. To have a better understanding of the loss mechanism in ECPW, the 2-D plot of total attenuation and substrate loss for different elevation heights and different geometries is given in the following figures. The same process as in CPW case, Chapter 2, is followed to model the losses in all-elevated CPW through a set of 2-D and 3-D simulations.

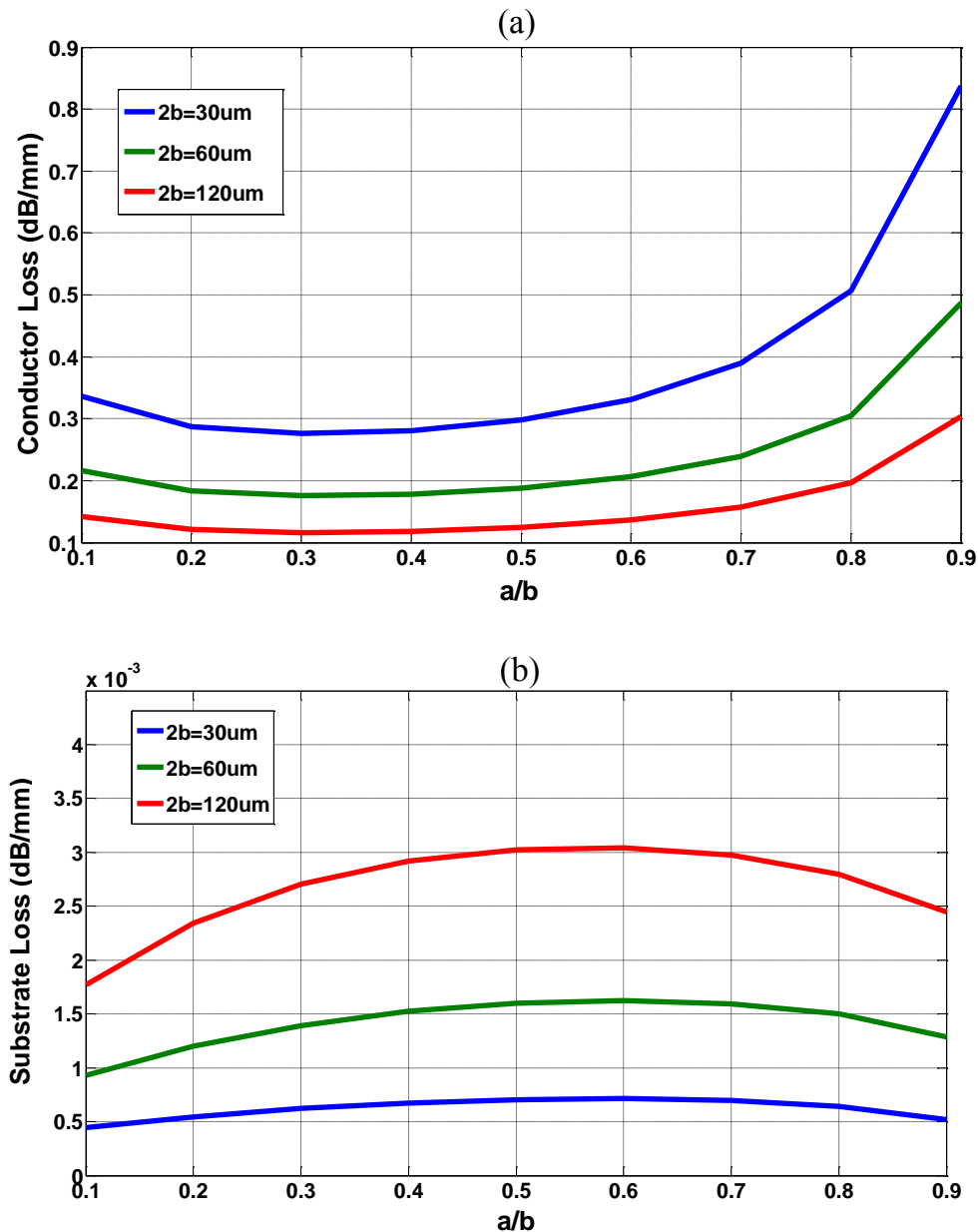


Figure 4.15: Plot of simulated (a) conductor loss and (b) substrate loss of ECPW lines with three different lateral dimensions ($2b$) of 30, 60 and 120 μm for various ratios of signal width to lateral dimensions (a/b).

The results from 2-D simulations of 5 μm elevated ECPW lines at 60GHz with different geometries show that the conductor and substrate loss (without radiation) in all-elevated CPW structure follow the same trend as in the CPW case. As for the CPW transmission line, the conductor loss is the dominant loss for ECPW line at low frequencies and its value is almost half of the conductor loss in an equivalent CPW structure. This can be

explained by the fact that it is mostly the surface of the conductor nearest to the media which is carrying the RF current. Therefore by elevating the signal in the air and disconnecting its bottom surface from the substrate, the resistance in the way of propagating wave will decrease. Also, by elevating the CPW traces, the field concentration and current crowding at the bottom edge of the line will decrease and results in lower conductor loss [95].

Also the substrate loss in an ECPW structure is around 30 times less than the CPW case and the total attenuation (without radiation) of ECPW line is near half the total attenuation in CPW line. This is the great advantage of elevated-CPW over CPW structure.

Also to illustrate the effect of elevation height on the loss performance, ECPW lines with different elevations are compared in terms of their conductor and substrate loss at 60GHz. in Figure 4.16.

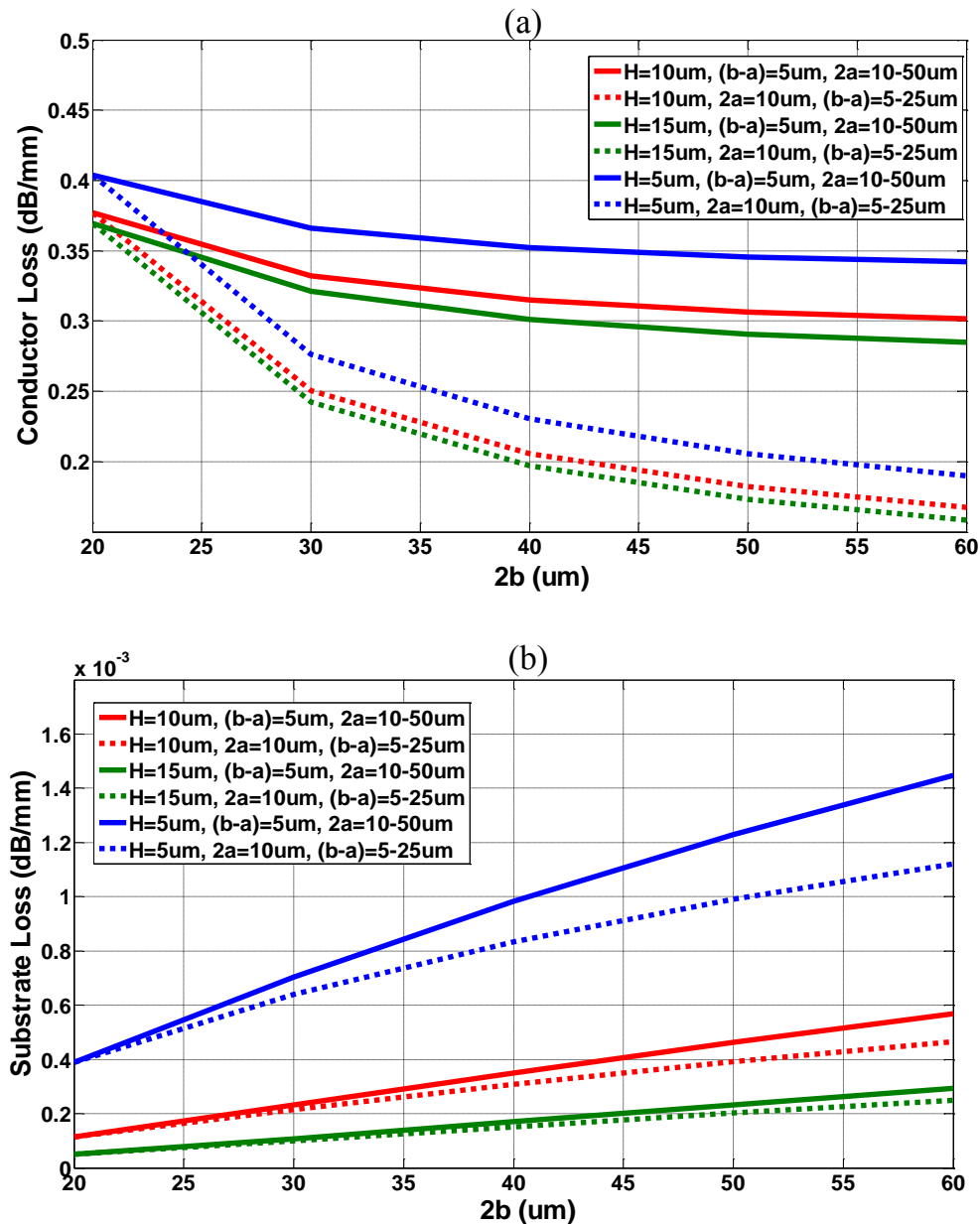


Figure 4.16: Plot of simulated (a) conductor loss and (b) substrate loss of ECPW lines for various lateral dimensions ($2b$) and three elevation heights of 5, 10 and 15 μm . The range of lateral dimensions is maintained by once keeping the signal width constant and varying the gap size and once varying the signal width when the gap size is constant.

The 2-D simulation results show that changing elevation height has a very small effect on the conductor loss whilst, as expected, it has a large effect on the substrate loss. It can be seen in Fig.4.16 that the elevation height has a nonlinear effect on the substrate loss and, for instance, there is a greater decrease in loss by increasing the height from

5 μm to 10 μm than there is increasing the height from 10 μm to 15 μm . Also, as for the CPW case, for a constant lateral dimension, the total loss decreases more significantly by having wider gaps than by wider signal width which means that ECPW lines with lower impedances have higher loss than higher impedance ECPW lines.

Also, to get an idea of the radiation losses in all-elevated CPW structure, the 2-D and 3-D simulation results of ECPW lines with two different lateral dimensions of 30 μm and 120 μm are compared from 1-320GHz, Figure 4.17. The main difference in these two type of simulation is that the 2-D solver does not take into account the radiation from the structure while the 3-D solver does. Therefore, comparing these results, although not exact, gives us a qualitative assessment of the radiation in the structure.

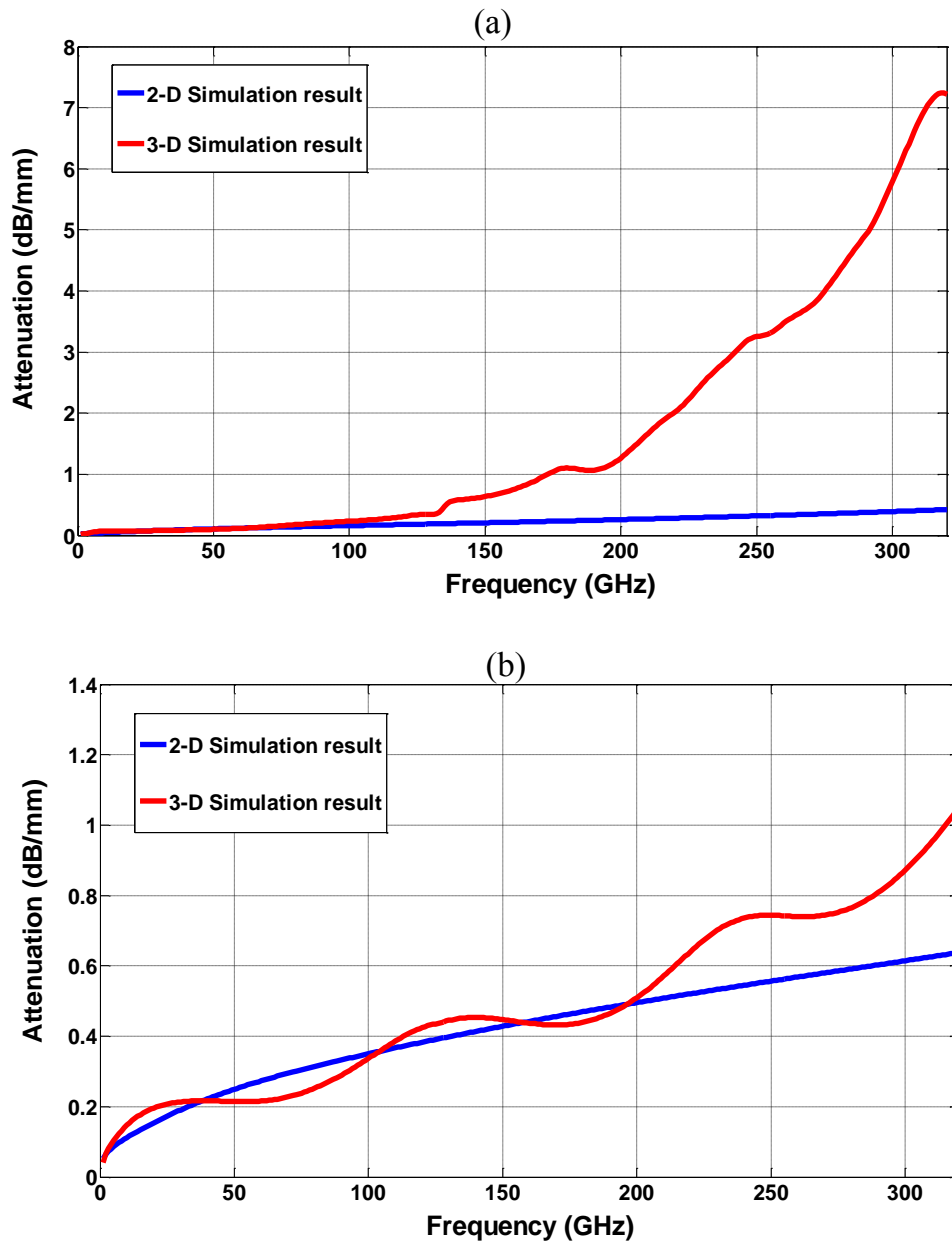


Figure 4.17: 2-D and 3-D Simulation plots of total attenuation of a 5-μm-elevated ECPW line with lateral dimension of (a) 120 μm and (b) 30 μm. Substrate is 600 μm thick.

The figures above show that at lower frequencies, where the conductor loss is the dominant attenuation mechanism and radiation is trivial, the 3-D results follow the results from the 2-D solver. At higher frequencies, when the propagating wave starts to radiate into the substrate, the results diverge. In ECPW line with lateral dimension of 120 μm, the radiation starts at frequencies around 120 GHz and increases with increasing

the frequency. Although this structure shows 2dB less loss at 300GHz than conventional CPW line, the loss can still be as high as 7dB/mm. Fig.4.17(b) shows that by decreasing the lateral dimension to 30 μ m, the radiation loss decreases significantly. However, such a small lateral dimension causes problems because the corresponding signal widths and gap sizes required for typical characteristic impedances are also very small. Such relatively small features are extremely difficult to fabricate because of the imprecise nature of our air-bridge process. The consequence is that the range of characteristic impedances which can actually be fabricated is greatly reduced. These simulation results are for a line width $W = 15\mu\text{m}$ and $S = 7.5\mu\text{m}$ with an elevation height of 5 μ m which are just at the edge of achievable dimensions by today's fabrication techniques. The fabrication yield is not high at these dimensions. Also, a major problem arises when we need to design lines with higher or lower characteristic impedances and, consequently, narrower signal traces or smaller gaps. Therefore, this range of lateral dimensions is not currently practical for all-elevated CPW lines.

Simulating transmission lines with different lateral dimensions shows that elevating the CPW traces in air always improves the line's attenuation and the amount of this improvement depends on the lateral dimension of the line. However, it should be considered that these results are before adding the effect of supporting posts. To have a better understanding of real elevated lines, the attenuation performance of a practical ECPW line is investigated in the following sections. Also, by consideration of the above explanations, the ECPW lateral dimensions are chosen in such a way to yield low attenuation and at the same time fall within the fabrication limitations.

4.3 Modeling and measurement of all-elevated CPW transmission line

This section, shows the performance of all-elevated CPW transmission line which was designed, fabricated and measured at G-band (140-220GHz) and H-band (220-320GHz) frequency ranges and also is compared with a CPW line of the same impedance. The effect of elevation height is examined by fabricating lines with 6 μm and 13 μm elevation heights. The effect of supporting post on the performance of the lines is also investigated by considering varying post sizes and distances.

Measurement of the lines was performed up to 320GHz with measurement and fabrication techniques as described in 2.4.1. Coaxial probes with 100 μm pitch were used for W-band (0.1-110GHz) and waveguide probes with 50 μm pitch were used for G-band (140-220GHz) and H-band (220-320GHz) measurements. The transmission lines were designed so as to support measurement with both 50 μm and 100 μm pitch probes without need of any extra tapered transmission lines. Such transition tapers were observed to have destructive effect on the high frequency performance of the structures and, therefore, should be avoided if at all possible. Two methods were used in the measurement of the elevated structures; once measurement is done on top of the elevated structure by providing two posts close to each other to make a strong landing position. This is to eliminate the effect of the ECPW to CPW transmission. Also, the measurement is carried out for the structures using CPW feeds. These measurement methods are explained in detail in Section 4-3-2.

The structures are simulated using Ansoft HFSSTM, a 3-D full-wave analysis tool. Lumped ports were used and optimised during the simulation in order to apply the excitations. A conductivity of 4.1×10^7 mho is used for gold conductors and GaAs with a

dielectric constant of 12.9 and loss tangent of 0.0016 is used as substrate. The structures were simulated inside a radiation boundary and a perfect-E boundary was applied to act as a reference ground.

4-3-1 All-elevated and Conventional CPW transmission lines

Figure 4.18 shows a micrograph of an all-elevated CPW transmission line. The design dimensions of the line are as follows: $W=35\mu\text{m}$, $S=20\mu\text{m}$ and $W_g=92\mu\text{m}$. However, due to the fabrication process of the airbridge technology, there are always some discrepancies between designed and fabricated dimensions. The fabricated dimensions achieved for the all-elevated line are: $W=41\mu\text{m}$, $S=14.5\mu\text{m}$ and $W_g=97\mu\text{m}$.

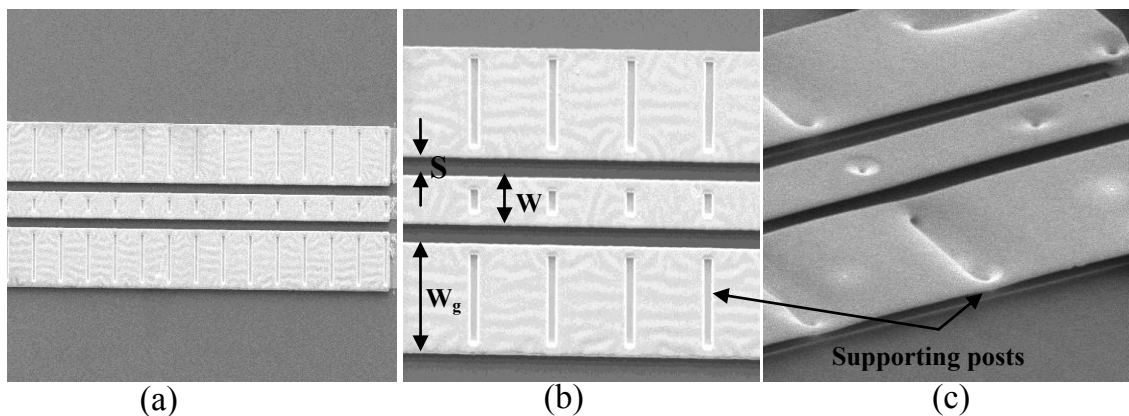


Figure 4.18: Micrograph of an all-elevated CPW transmission line at (a) and (b) top view, (c) angled view.

All-elevated transmission line with the mentioned fabricated dimensions have a characteristic impedance of $\sim 60\Omega$. Therefore, a 60Ω CPW transmission line is required so that a valid comparison can be made with all-elevated CPW line. Two different approaches were used in the design of 60Ω CPW transmission line: first the signal width was considered similar to the ECPW line and the gap width was changed

(increased to $50\mu\text{m}$) to get 60Ω line, CPW1, and second, the gap remained the same size and the signal line width was changed (decreased to $17\mu\text{m}$), CPW2.

The G-band (140-220GHz) performance of the 60Ω CPW and all-elevated CPW transmission lines is compared in Figure 4.19.

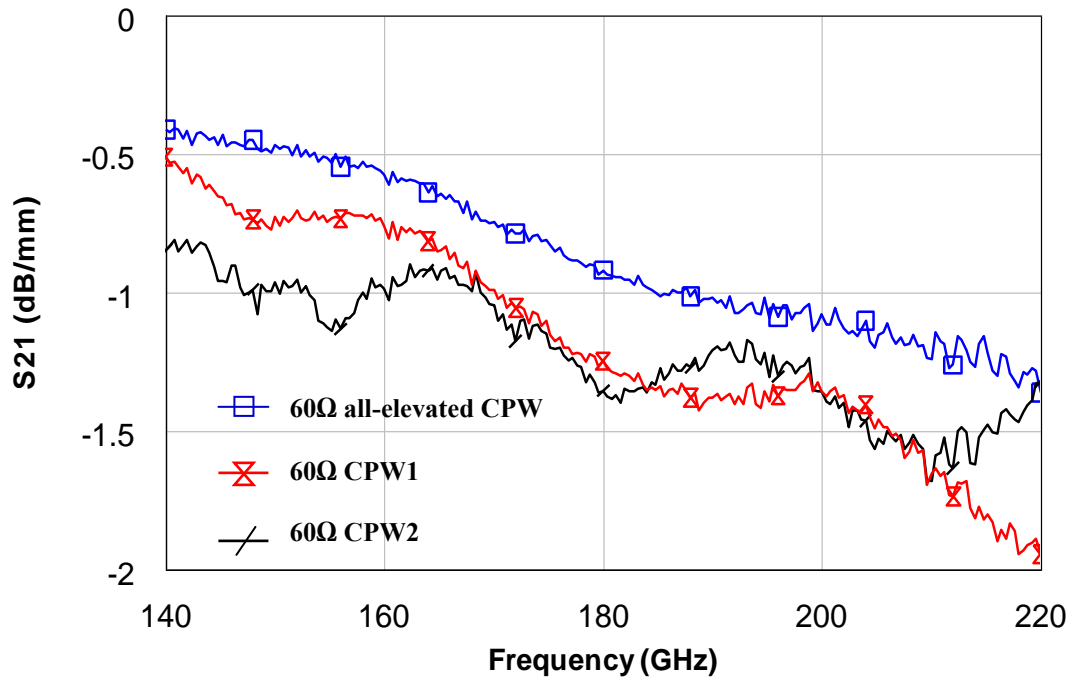


Figure 4.19: Comparison between measured Insertion loss of 60Ω all-elevated and conventional CPW lines. CPW1 has a dimension of: $(50-35-50)\mu\text{m}$ and CPW2 has a dimension of $(25-17-25)$. The designed dimension of ECPW line is $(20-35-20)$ with elevation of $6\mu\text{m}$.

It can be seen that the all-elevated CPW transmission line exhibits better performance than both CPW lines. The insertion loss per unit length of ECPW line is 1.24dB at 210GHz while both CPW lines show 1.63dB loss/mm at the same frequency.

In general, the ECPW line shows an improvement in loss of approximately 0.6dB across most of the measurement range.

A noteworthy observation is that, due to the lower effective permittivity of ECPW compared with CPW, a line of given electrical length will be physically longer when realized in all-elevated CPW than if it is realized in conventional CPW line. This has

many implications: if compactness is the biggest challenge then CPW should be used. The CPW line may offer loss comparable with or better than an elevated line if the line is required to implement a specific phase shift and also that, if a line of fixed physical length is required then the elevated CPW line offers the best performance.

These results show a very good performance for elevated CPW transmission line and the advantages can be achieved over conventional CPW media up to 220GHz. However, when the frequency enters to the H-band (220-320GHz), the performance of the elevated CPW starts to degrade - especially at frequencies around 240GHz- and exhibits higher insertion loss than conventional CPW toward the end of frequency range. Fig.4.20(a) shows the measurement results of the ECPW transmission line along with the simulated data while Fig.4.20(b) compares the measured results of ECPW line with the measured data for CPW transmission line.

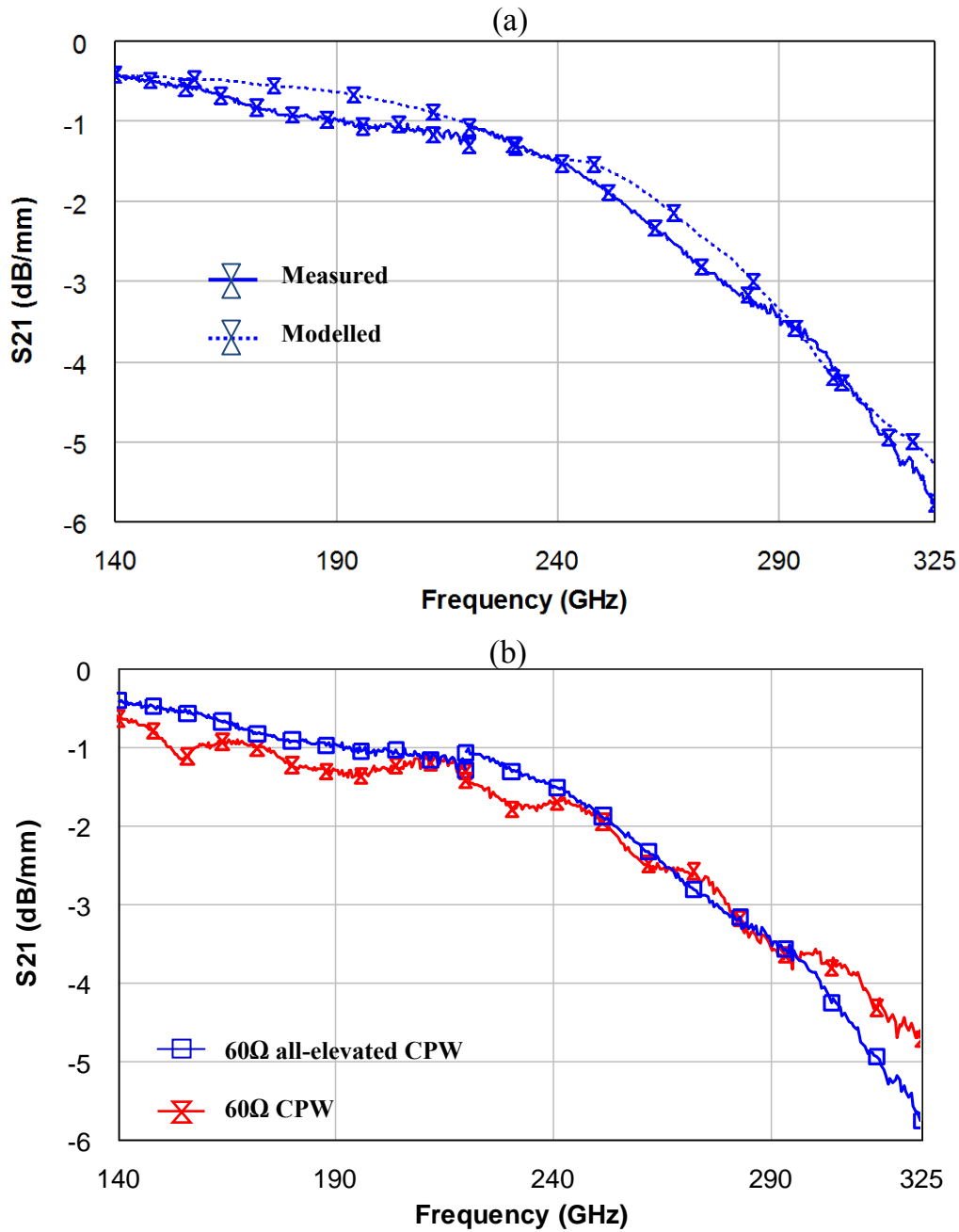


Figure 4.20. (a) Measured and simulated S-parameters for ECPW transmission line, and (b) Comparison between measured insertion loss of 60Ω ECPW and CPW transmission lines at G-band (140-220GHz) and H-band (220-320GHz).

It is shown in Fig.4.20(b) that at 300GHz, the insertion loss for all-elevated CPW line is 5.3dB per unit length compare to 4.5dB for CPW line.

Such results compelled us to investigate the elevated CPW structure in more detail to hopefully determine the source of the performance degradation. In this regard, the effect

of supporting posts, ECPW/CPW transition feeds and elevation height were considered for investigation.

4-3-2 Effect Of CPW/ Elevated CPW Transition Feeds

A critical issue during the measurement process of the elevated CPW lines is probing with microprobes. One way to facilitate on-wafer probing for all-elevated CPW is by connecting the elevated line to CPW feeds directly on the substrate. It was discussed earlier in this chapter that these CPW feeds cause dispersion in the characteristic impedance due to the impedance discontinuity when transitioning from the CPW feed to the elevated line. To investigate the effect of these CPW feeds on the performance of elevated CPW from the insertion loss point of view, two different techniques are used for the probing of elevated CPW. In one, CPW feeds are used and, in the other, probing on the elevated line is facilitated by putting two posts close enough together (a $\sim 20\mu\text{m}$ spacing) to make a stable position for probe landing without damaging the sample.

Fig.4.21 shows micrographs of the two probing structures.

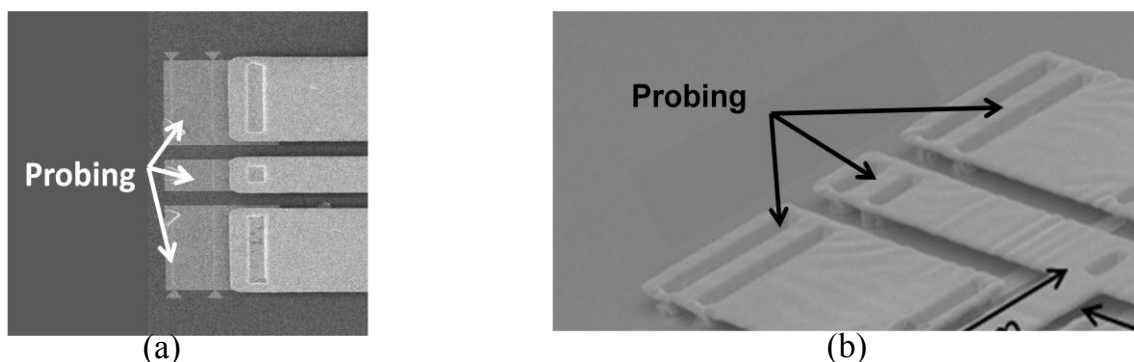


Figure 4.21: Micrograph of two different structures for ECPW probing by (a) using CPW/ECPW transition feeds and (b) using two close supporting posts to facilitate probing on top of elevated lines.

Measurement results for the insertion loss of the elevated line per unit length with and without transmission pads is shown in Figure 4.22.

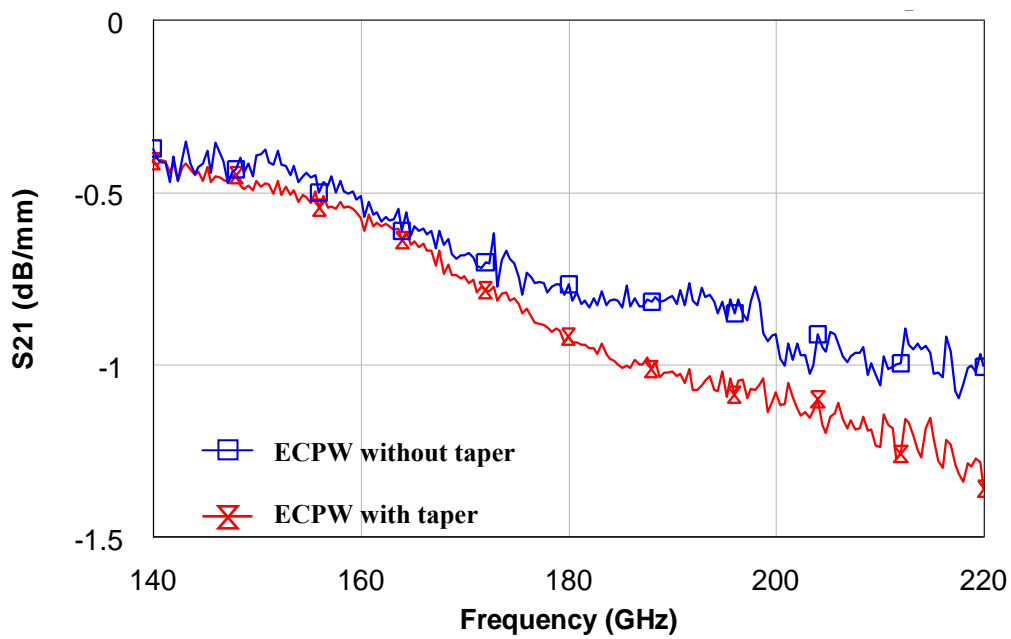


Figure 4.22: Measured insertion loss of ECPW transmission lines with and without CPW/ECPW tapers at G-band (140-220GHz).

As shown in Fig.4.22, at 210GHz, the elevated CPW transmission line without using CPW tapers shows 0.2dB lower loss than the one with tapers. To investigate if these CPW transition feeds are the source of performance degradation for elevated CPW or not, the same measurement techniques are applied to the 220-320GHz frequency band, Fig.4.23.

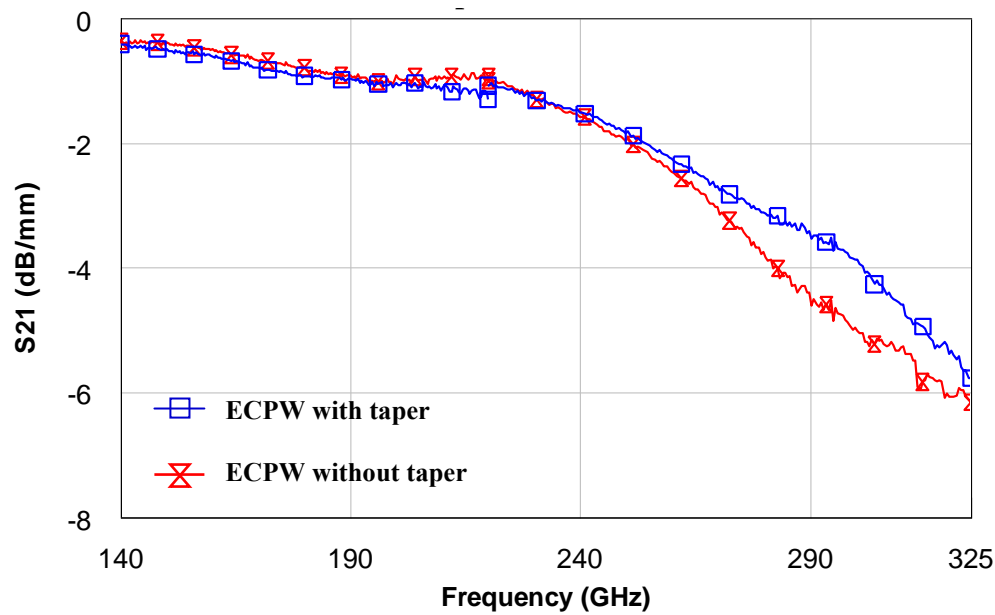


Figure 4.23: Measured insertion loss of ECPW transmission lines with and without CPW/ECPW tapers up to 320GHz.

It can be seen that the measurements of elevated CPW with and without CPW feeds at H-band follow the same overall trend with no significant difference in the magnitude of the transmission coefficient. Therefore, employing a CPW/ECPW transition for measurement purposes can be ruled out as the direct cause of the observed high frequency roll off above 240GHz.

4-3-3 Effect of the size and distance between supporting posts:

Elevated CPW structures utilize supporting posts to elevate the CPW traces above the substrate. The effect of these supporting posts on the characteristic impedance of the elevated lines was shown earlier in section 4-2-5. In this section, we investigate the effect of size and distance of supporting posts on the loss performance of all-elevated CPW transmission line.

Figure 4.24 shows an identical all-elevated CPW line with two different post sizes of $7\mu\text{m}$ and $14\mu\text{m}$ (in the direction of propagation) and also two different post distances of around $100\mu\text{m}$ and $210\mu\text{m}$ at G-band.

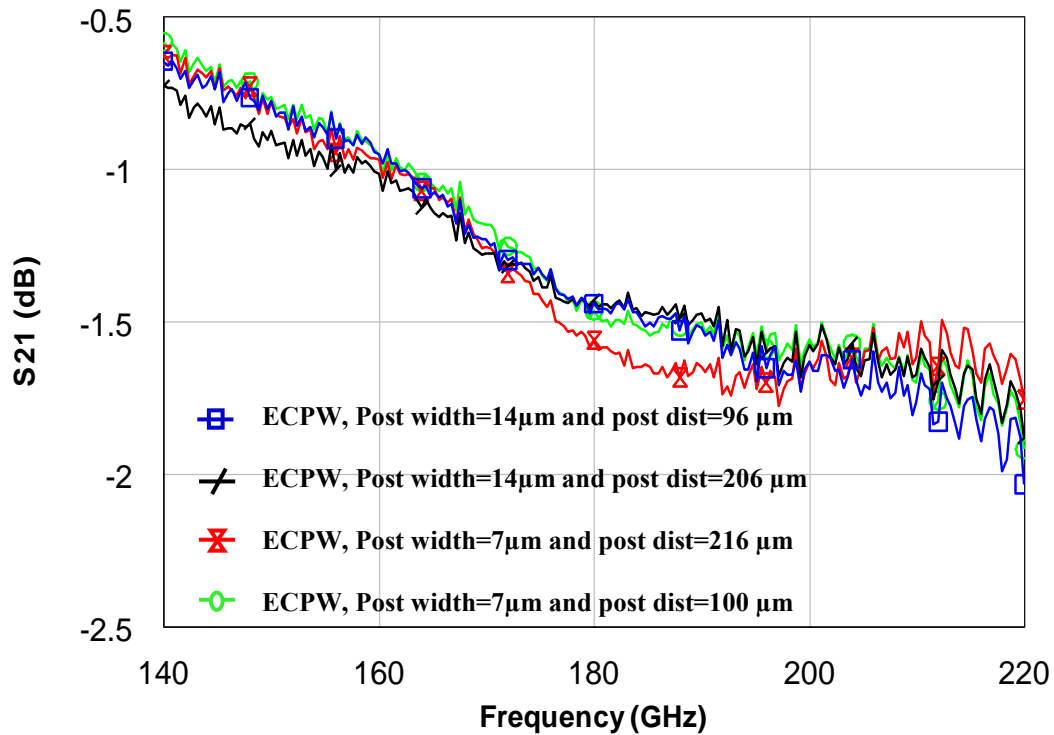


Figure 4.24: Comparison between measured insertion loss of all-elevated CPW transmission lines with different size and distance of supporting posts at G-band(140-220 GHz).

As can be seen in Fig.4.24, although it has a pronounced affect on the characteristic impedance, changing the size of and distance between supporting posts doesn't significantly change the loss characteristic of the elevated CPW lines.

The measurement results of the lines at H-band, Fig.4.25, show the same thing.

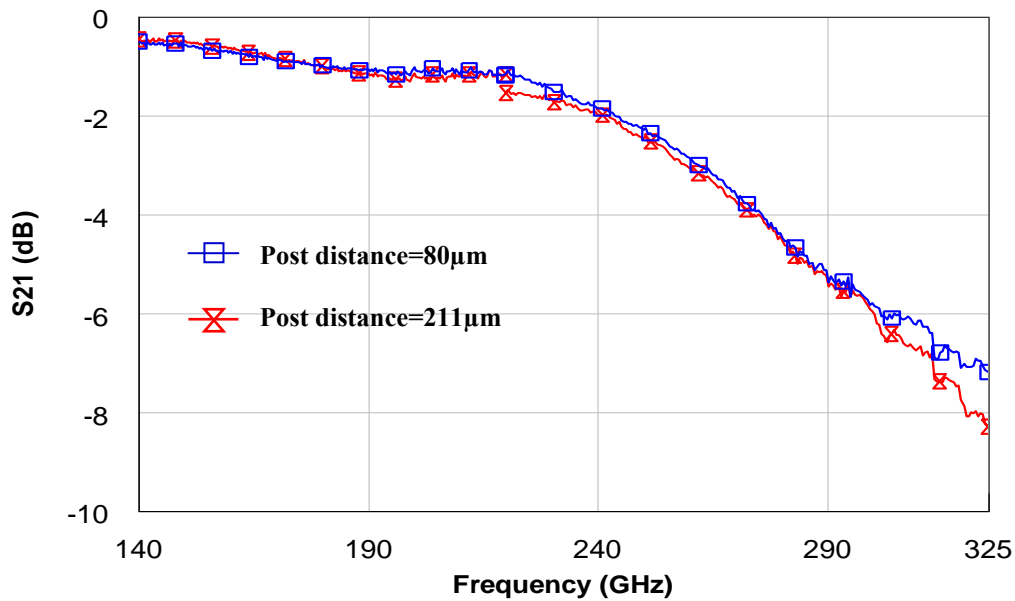


Figure 4.25: Comparison between measured insertion loss of two ECPW transmission lines with different supporting post distances up to 320GHz.

Since changes in the size and number of supporting posts leads to changes in characteristic impedance, a comparison is also made in the form of the loss factor ($1 - |S_{11}|^2 - |S_{21}|^2$) in the following Figure.

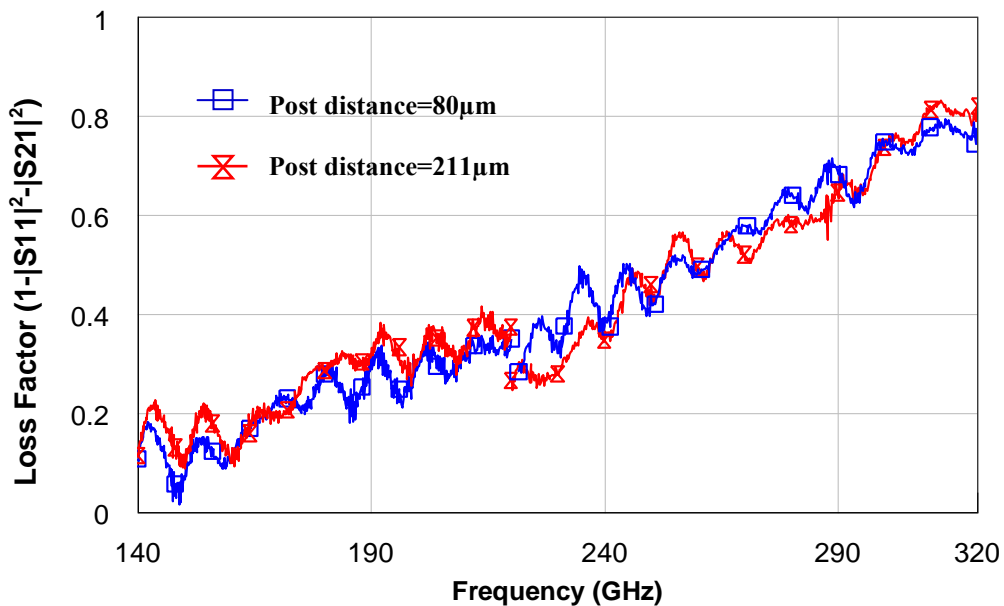


Figure 4.26: Measured loss factor of two ECPW transmission lines with different supporting post distances up to 320GHz.

Figure 4.26 shows very similar results for the loss factor of transmission lines with different numbers of supporting posts. The same applies to the ECPW lines with different size of posts. Therefore, the size and number of supporting posts cannot be the source of performance degradation for elevated CPW lines and employing less posts doesn't necessarily improve the loss behavior of the ECPW line at high frequencies.

As discussed before, the maximum distance of supporting posts is limited to the amount that keeps the elevated sections well in the air without collapsing onto the substrate. It should also be mentioned here that there is a limitation in the minimum size of supporting posts from the fabrication point of view. This becomes more critical as the elevation height increases due to the limitations of the airbridge fabrication process. For example, a minimum post size of $7 \times 7\mu\text{m}$ was achieved for a fabricated line with $6\mu\text{m}$ elevation while it was $10 \times 10\mu\text{m}$ for $13\mu\text{m}$ elevation height - both with reasonable mechanical strength.

4-3-4 Effect of elevation height

As stated earlier, in section 4-2-2, the elevation height is a major factor in determining the characteristic impedance of elevated structures and small changes in elevation height (compared to the signal and gap widths) can lead to significant changes in the line's impedance. We investigated the effect of elevation height, which is achievable from fabrication point of view, on the loss behaviour of all-elevated CPW transmission lines. In this regard, identical transmission lines were designed and fabricated with $6\mu\text{m}$ and $13\mu\text{m}$ elevations. The lines have characteristic impedances of 61Ω and 70Ω for the elevations of $6\mu\text{m}$ and $13\mu\text{m}$, respectively. Due to the difference in characteristic

impedance, looking at the loss factor is a better way of comparing the performance of these two transmission lines, Figure 4.27.

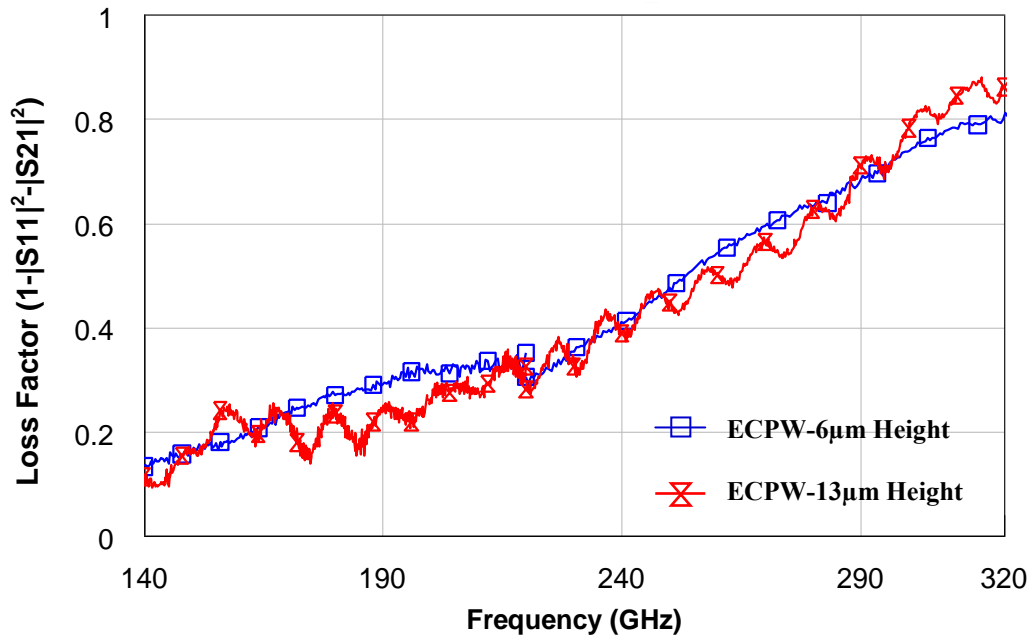


Figure 4.27: Comparison between the measured loss factor of ECPW transmission lines with elevation heights of 6µm and 13µm.

As we can see in Figure 4.27, increasing the elevation height to 13 µm, does not improve the roll-off characteristic of all-elevated CPW TRL and Loss factor of 6µm elevated ECPW line is comparable to the loss factor of 13µm elevated ECPW. The 3-D simulations on this effect shows that, in general, by raising the CPW traces higher above the substrate, one can achieve improved performance in terms of loss. In fact, the loss decreases almost linearly with increasing elevation till around 20µm. This is before considering the effect of CPW/ECPW transitions and supporting posts. From 20µm onward, increasing elevation does not yield significant changes in terms of loss. For example, the loss behaviour of a 30µm elevated line is very similar to one with 50µm elevation. However, after adding the supporting posts and CPW/ECPW transition pads, the loss factor of the higher elevated line becomes comparable to that of lines with

relatively low elevation. For example, we see in Fig.4.27 that the loss factor of $6\mu\text{m}$ and $13\mu\text{m}$ elevated CPW lines are very similar. This can be explained in part by the greater impedance mismatch between the transition pad, post sections and elevated parts for higher elevations which reduces the overall performance of the lines. In this regard, the effect of the CPW/ECPW transition is more pronounced and we can see in Fig.4.28 that with $13\mu\text{m}$ elevation, no significant difference in the loss factor of elevated CPW is observed for lines with differing numbers of posts. This is confirmed with a set of 3-D simulation results.

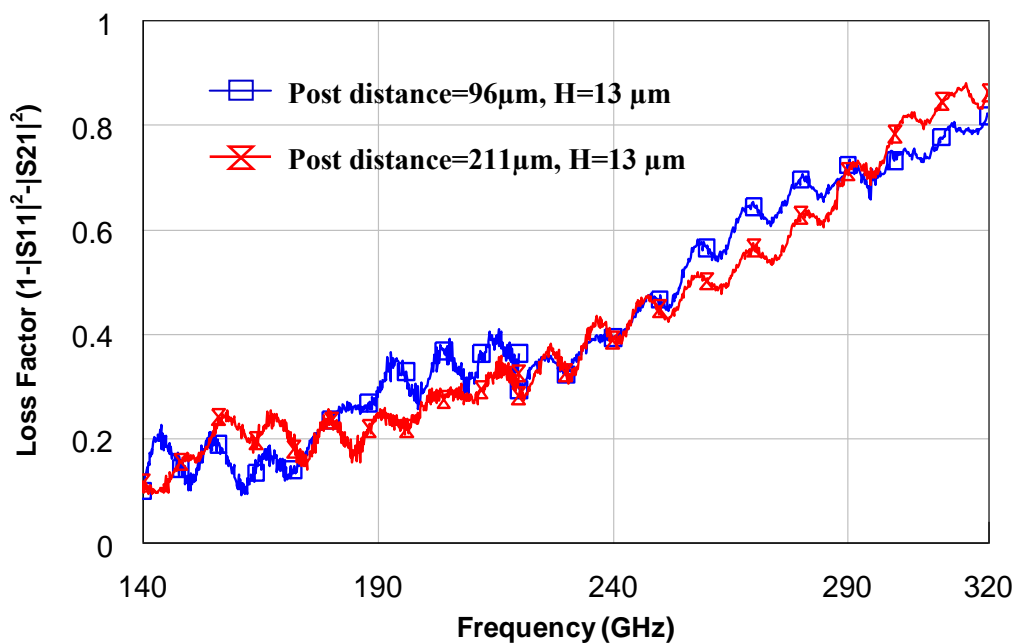


Figure 4.28: Comparison between the measured loss factor of $13\mu\text{m}$ elevated ECPW transmission lines with different supporting post distances.

The high insertion loss of all-elevated CPW at relatively high elevations considered along with simulation results indicates that the elevated CPW structure is not completely isolated from the semiconducting substrate, and hence, it cannot eliminate

the substrate effect completely. Simulation results shows a considerable penetration of the substrate by the electric field for a $5\mu\text{m}$ elevated ECPW line, Figure 4.29.

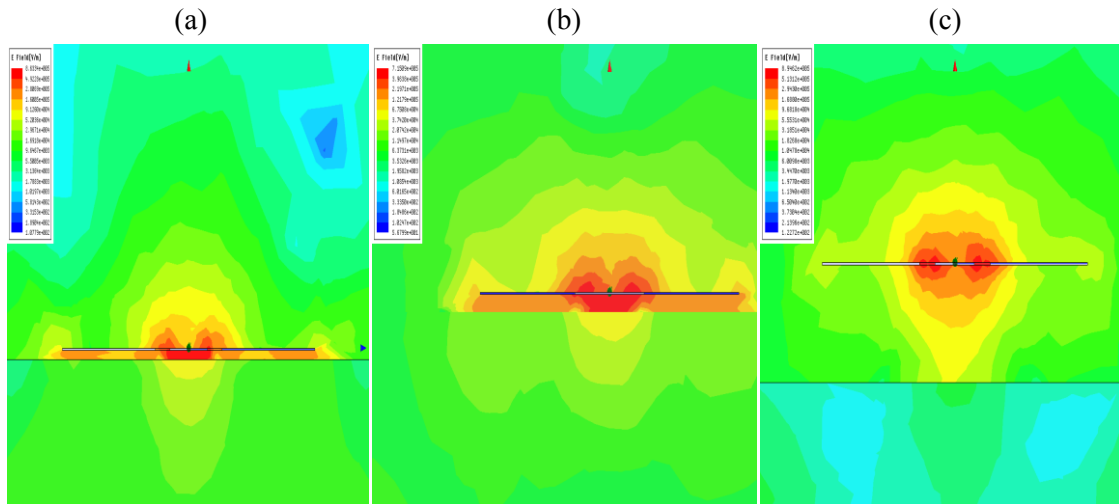


Figure 4.29: Profile of electric-field distribution modelled for ECPW line with (a) $5\mu\text{m}$ elevation, (b) $10\mu\text{m}$ elevation and (c) $70\mu\text{m}$ elevation.

The Figure shows the cross sectional view of the electric field plot of all-elevated CPW structures with (a) $5\mu\text{m}$, (b) $10\mu\text{m}$, and (c) $70\mu\text{m}$ elevation. In fact, simulation results show that an elevation height of almost $70\mu\text{m}$ is required to completely confine the electric field to the air gap and completely isolate the CPW traces from the semiconducting substrate. This elevation height cannot be achieved by today's fabrication processes and considering this limitation, complete isolation of this elevated CPW structure is impossible. To overcome this problem, a novel variation of elevated CPW is considered and will be investigated in Chapter 6.

From the preceding arguments we can conclude that, for all elevated CPW, the dielectric loss due to substrate conductance is, for GaAs substrates at least, negligible in comparison to both conductor losses and radiation losses. The conductor losses are dominant at low frequencies whilst the radiation loss becomes the dominant loss mechanism at sufficiently high frequencies. Simulation data shows that radiation occurs

mainly because of the simple fact of a dielectric substrate being in close proximity to the CPW traces carrying the signal and not because of CPW feeds or supporting posts.

4.4 All-elevated CPW (ECPW) resonators

In this section, two-port elevated CPW networks including open and short circuited stubs are studied. The open and short circuited matching stubs are useful topologies for a variety of circuits and, as was discussed in Chapter 2, it is improbable that you achieve good performance for a short circuit matching stub at high frequencies using a conventional CPW structure. As mentioned earlier, this is due to the high dielectric loss and surface-wave modes which are unavoidable in conventional CPW structures. To overcome the poor performance of CPW short circuited stubs in particular, the elevated CPW structure is proposed as it is surface-wave free and is semi-isolated from the lossy substrate. To examine this, a series of open and short circuited matching stubs were designed and fabricated for different frequencies using the all-elevated CPW structure. The effect of the size and distance between the supporting posts was also investigated. These stubs were designed and fabricated with two different elevations of $6\mu\text{m}$ and $13\mu\text{m}$ to study the effect of elevation height on the stub's performance. At the end, some useful electric characteristics of different elevated CPW structures such as effective permittivity, was extracted by the measurement of open circuit stubs.

4.4.1 Quarter-wavelength ECPW Short-circuited stub

Figure 4.30 shows the micrograph of typical short circuit stub implemented with all-elevated CPW (ECPW).

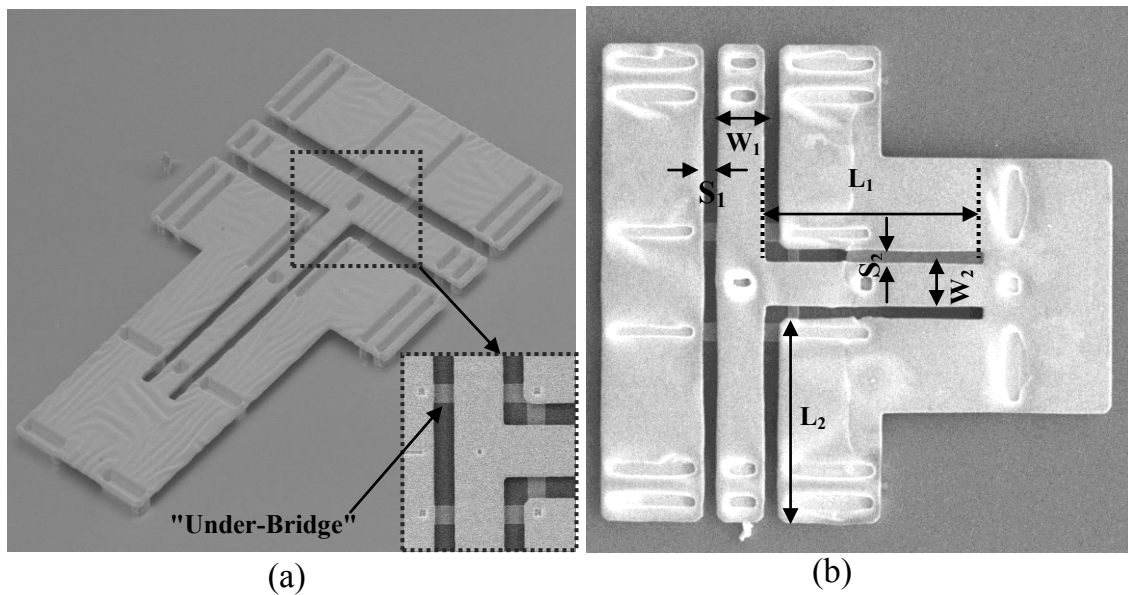


Figure 4.30: Micrograph of a short-circuited ECPW stub at (a) angled and (b) top view. The stub dimensions are $L_2=220$, $S_1=16$, $W_1=41$, $S_2=15.5$ and $W_2=41$. The stub length, L_1 , is 292 for resonator at 160GHz and is 176 for resonator at 240 GHz. All dimensions are in microns.

The designed ECPW line dimensions are: gap width= $20\mu\text{m}$, signal width= $35\mu\text{m}$, ground width= $100\mu\text{m}$ and elevation= 6 and $13\mu\text{m}$. These initial dimensions were chosen as they provide a close to 50Ω transmission line. The gold supporting posts with two different dimensions of $14\times 22\mu\text{m}$ and $7\times 7\mu\text{m}$ (for signal trace) and $14\times 87\mu\text{m}$ and $7\times 87\mu\text{m}$ (for ground planes of ECPW) were used to elevate the CPW traces. Note that, the actual fabricated dimensions are somewhat different from the designed dimensions due to fabrication tolerances. The fabricated dimensions at $6\mu\text{m}$ elevation are gap width= $16\mu\text{m}$, signal width= $40\mu\text{m}$, ground width= $105\mu\text{m}$ and at $13\mu\text{m}$ elevation are 14 , 43 and $107\mu\text{m}$ respectively. To investigate the effect of posts, structures identical in all respects except the number and spacing of posts were designed. The stub lengths for different resonant frequencies are designed based on equations (2.47) and (2.48) by considering an initial effective permittivity of 2.26 (derived from simulation results) for structures with $6\mu\text{m}$ elevation. This leads to a stub length of $292\mu\text{m}$ for the 160GHz resonator and a stub length of $176\mu\text{m}$ for the 240GHz resonator. The initial effective

permittivity for the design of stubs at $13\mu\text{m}$ elevation is considered to be 1.26 which results in a stub length of $846\mu\text{m}$ for the 160GHz resonator and $278\mu\text{m}$ for the 240GHz resonator. Feed lines of length 93deg are connected via a T-junction to the shunt stub. The electrical length of the feed is much shorter than 90° for shorts with $13\mu\text{m}$ elevation and is comparable with, yet shorter than, 90° for shorts with $6\mu\text{m}$ elevation. Ideally, the feeds would be kept much shorter than the stub. However, practical considerations dictate a certain minimum length of feed in order both probe the circuit and maintain appropriate ground plane width.

Another critical factor in the design of CPW short and open-circuited stubs is the excitation of the unwanted slotline mode at the discontinuity. The same problem is observed for the elevated CPW short and open circuit stubs. In conventional CPW circuits, airbridges are used to keep the ground planes at the same potentials at the discontinuity and to therefore suppress the unwanted higher order modes [140], [141]. In the design of elevated CPW stubs, 'underbridges' are used to short out the unwanted higher order slotline modes at the discontinuity. These 'underbridges' consist of traces on the bond pad layer connecting the elevated grounds via airbridge posts, Figure 4.30.

4.1.1.1 Experimental results

Figures 4.31(a) and (b) show simulation and measurement results of all-elevated short circuit matching stubs with $6\mu\text{m}$ elevation for 160GHz and 240GHz, respectively. (The ECPW short circuit designed for G-band has a stub length of $290\mu\text{m}$ and the one designed for H-band has a stub length of $176\mu\text{m}$).

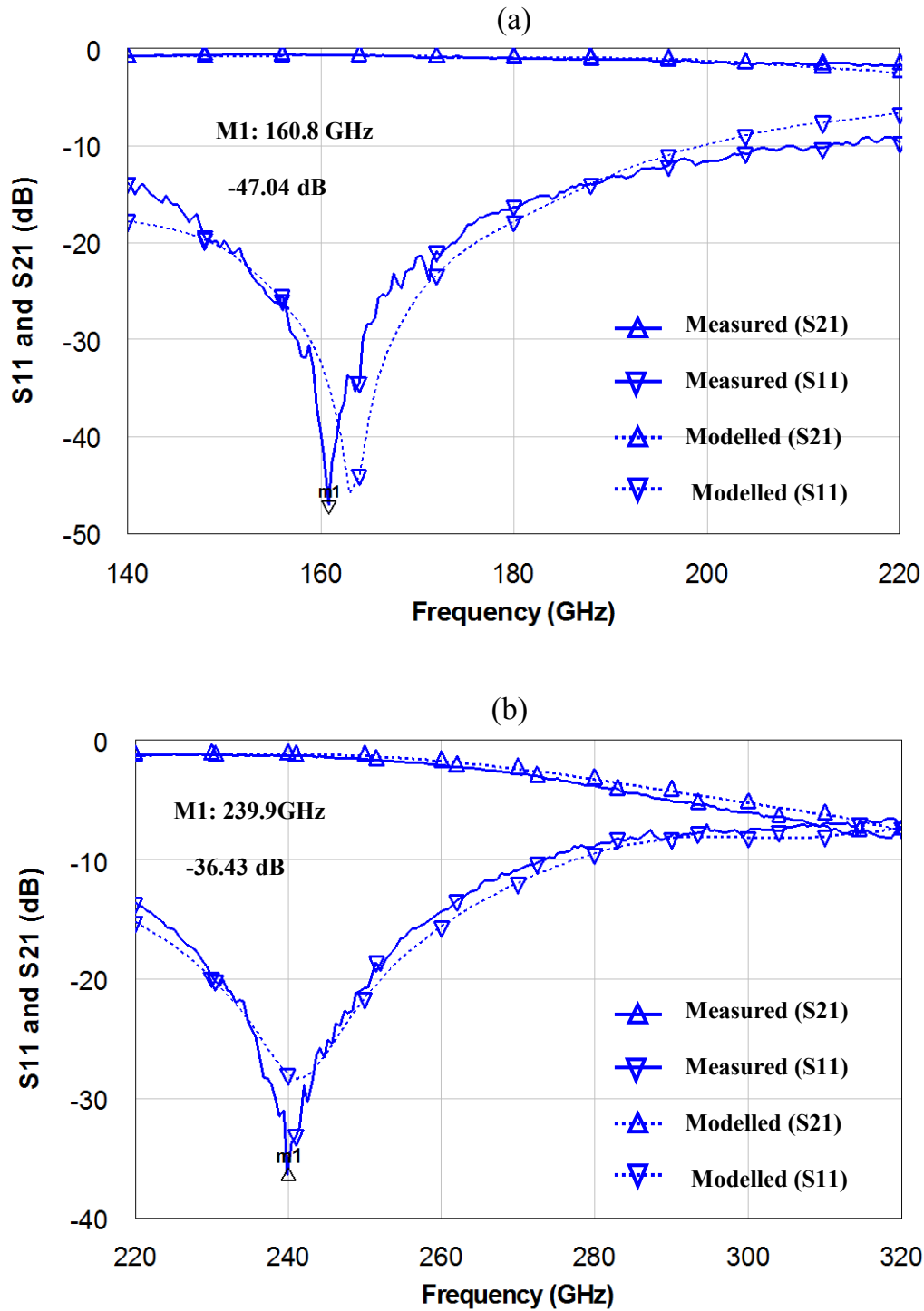


Figure 4.31: Measured and simulated S-parameters for ECPW short-end shunt stub with 6 µm elevation with resonance frequency at (a) 160 GHz and (b) 240 GHz

As can be seen in the above figures, the measurement results are in good agreement with the simulation results and the short circuit matching stub using the all-elevated CPW structure shows impressive performance, with a deep null in the reflection coefficient at the centre frequency and a narrow 3-dB bandwidth for the whole

frequency range. To have a better understanding of the performance improvement which can be achieved using all-elevated CPW, the short circuit stubs are compared with CPW counterparts in the G and H frequency bands in the following Figures.

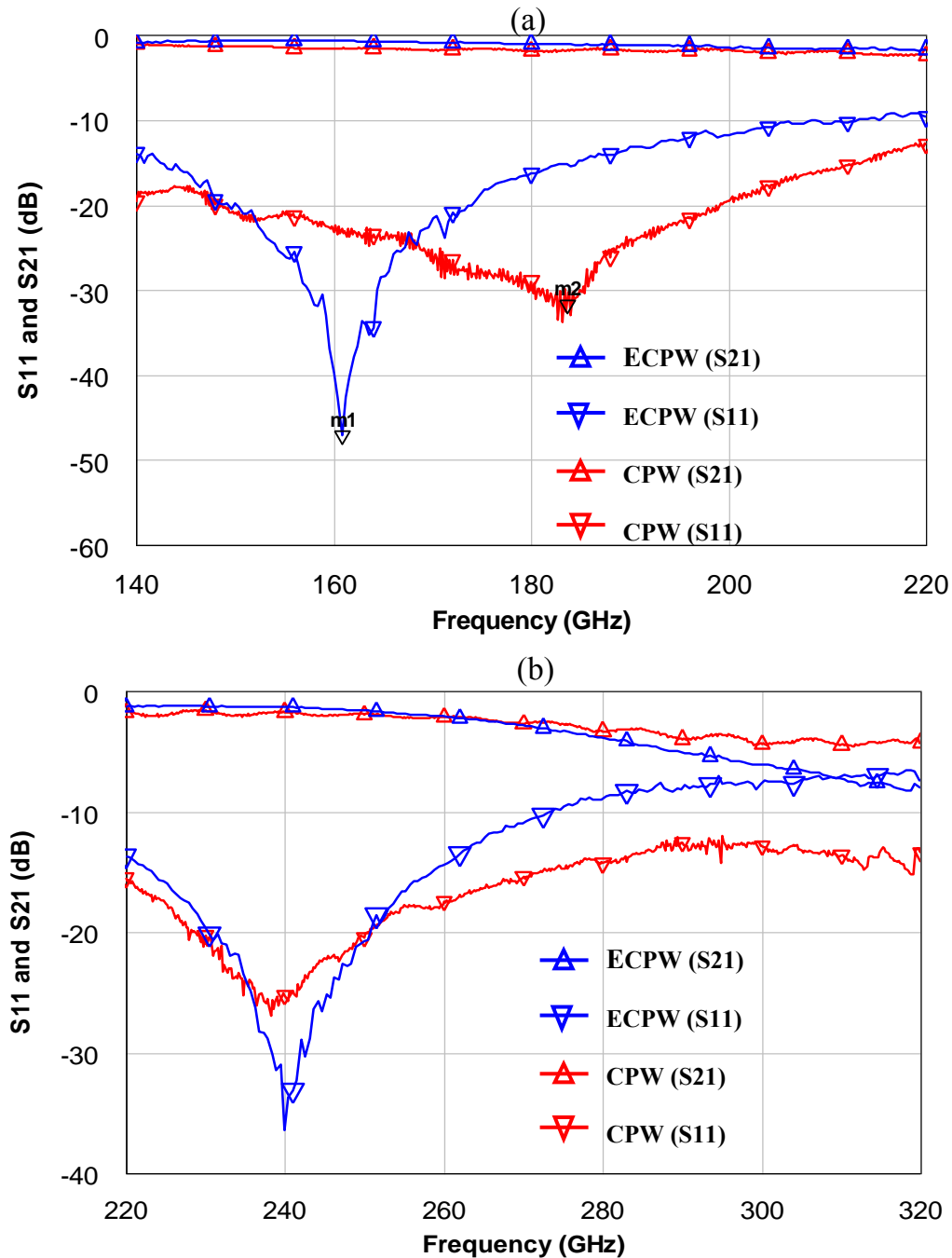


Figure 4.32: Comparison between measured S-parameters for $6\mu\text{m}$ elevated ECPW and conventional CPW short-end shunt stubs at (a) G-band (140-220GHz) and (b) H-band (220-320GHz).

It can be seen from Fig.4.32 that the elevated stub-in comparison with CPW stub-exhibits superior performance with a relatively sharp resonance, with a return loss of -48dB at 160GHz and -36.41dB at 240 GHz. The insertion loss for the all-elevated stub is -0.6dB and -1.3dB at 160 and 240GHz, respectively. Measurement results for short circuit stub using conventional CPW shows -31.6dB return loss and -1.9dB insertion loss at the resonant frequency of 180GHz and -16.7dB and -1.7dB at frequency of 220GHz. The H-band ECPW short stub has a 3dB bandwidth of 195GHz(81% fractional bandwidth) which shows 37% improvement over CPW short stub. This ECPW stub has a loaded quality factor of ~ 1.2 (33.5% better than CPW) and unloaded quality factor of 8.63 which is 50% better than CPW counterpart. The performance enhancement observed in short-circuited stubs by using elevated CPW structure is due to the low loss transmission line with higher isolation from the substrate. Looking at the electric field plot of the ECPW short-circuited stub, we can see less penetration of the field to the substrate at centre frequency compared with the CPW stub, Figure 4.33. This explains the greater isolation of the ECPW structure from the substrate and better performance of the short-circuited stub.

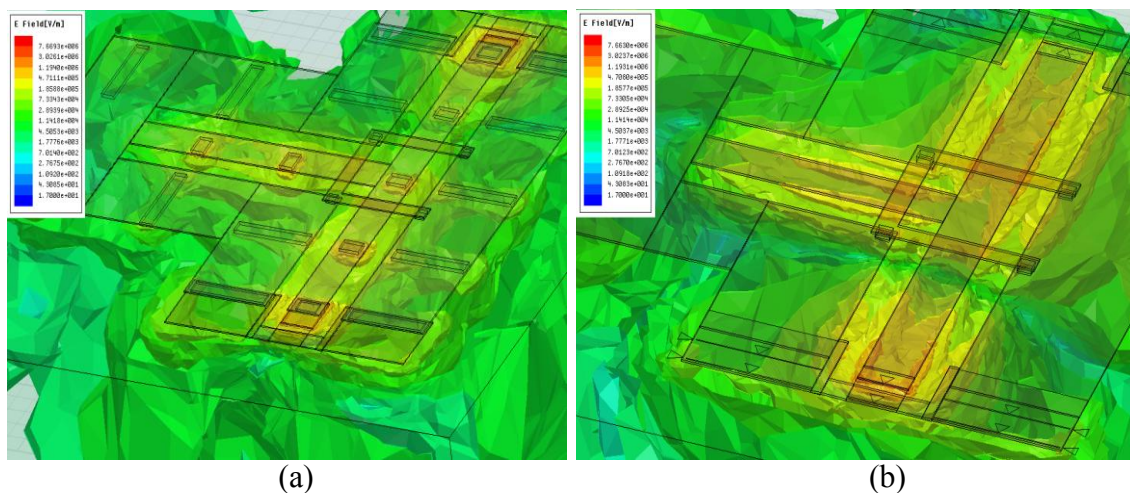


Figure 4.33: The substrate electric field plot of a short-circuited shunt stub with (a) ECPW and (b) CPW structures at the centre frequency of 170 and 165GHz, respectively.

The elevated CPW transmission lines in this particular example have a characteristic impedance of around 65Ω while the impedance is 50Ω in CPW case. An ECPW short-circuited stub implemented with 50Ω lines doesn't show significant changes in overall performance.

Also, as discussed in Chapter 2, one can achieve an optimised short-circuited stub by using higher impedance lines at feeds and lower impedance lines at the stub. By applying this rule to the above-mentioned ECPW short-circuited stub, even better performance is achieved. Fig.4.34 indicates that an ECPW circuit with 100Ω feed lines and 40Ω stub shows much narrower bandwidth compared with the one which exclusively uses 65Ω lines. Also, the use of high and low impedances didn't introduce significant additional loss to the circuit and still provides a close match to 50Ω ($S_{11} = -23\text{dB}$) at resonance. This is an enormous improvement over the conventional CPW short-circuited stub implemented with similar impedances.

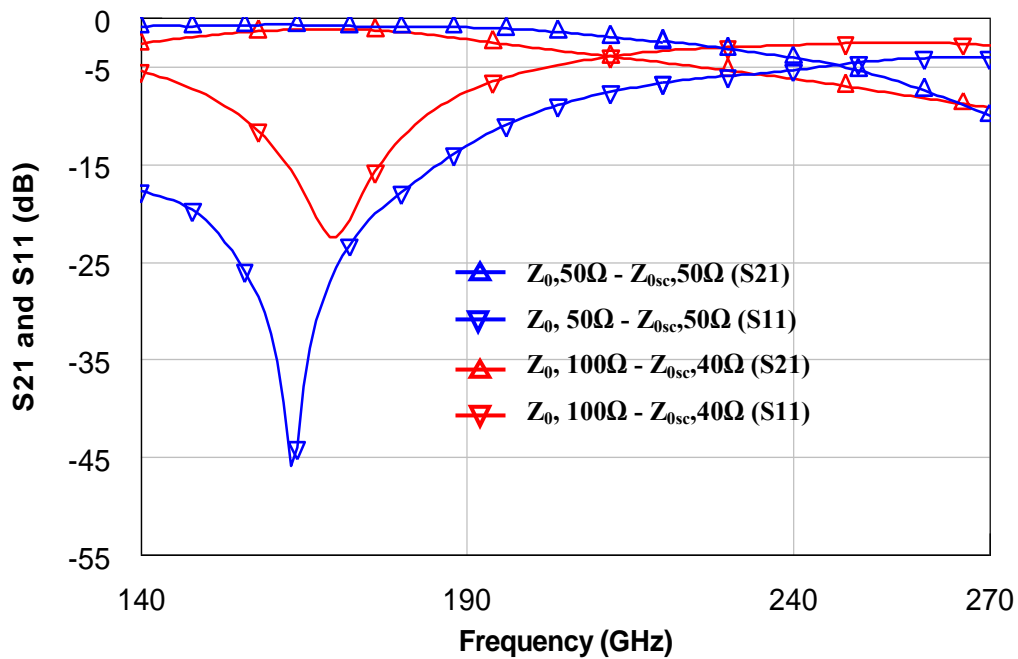


Figure 4.34: Comparison between simulated S-parameters for short-circuited stub designed with all similar impedance lines (50Ω) and the stub designed with various impedance lines (high impedance at feeds and low impedance at stub section).

Achieving very low impedances is more challenging with the ECPW structure and it requires a narrower gap or a wider signal strip than conventional CPW line. As an option, one can use double stubs instead of a single stub. This decreases the overall impedance of the stub and improves the bandwidth. However, by using this method, the in-band loss increases significantly. Therefore, in order to further improve the performance of the elevated CPW short-circuit stubs other methods such as increasing the elevation height and/or decreasing the size and number of supporting posts is suggested. This is explained below.

4.1.1.2 Effect of elevation height

All of the two-port stubs were designed and fabricated with 2 different elevation heights (6μm and 13μm) to investigate the effect of elevation height on the stub performance.

Fig.4.35 shows the measured performance of short circuit stubs using all-elevated CPW line with 6 μm and 13 μm elevation.

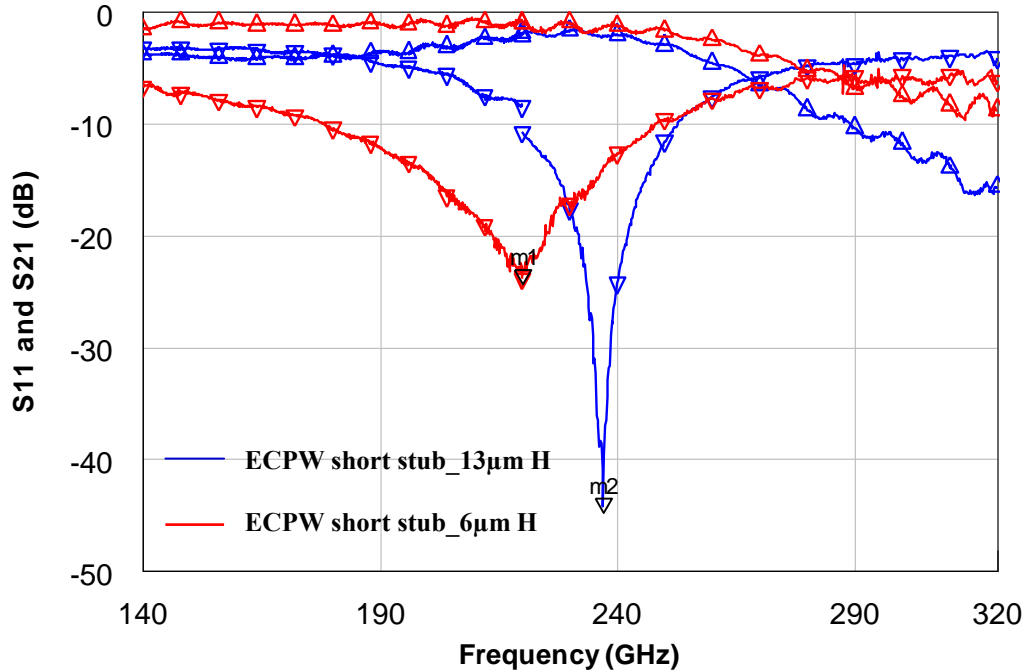


Figure 4.35: Comparison between measured S-parameters of ECPW short-end stubs with 6 μm and 13 μm elevations.

Using higher elevation leads to a lower effective permittivity which shifts the resonance frequency higher for a structure with otherwise fixed geometry. Therefore, the stub with 13 μm elevation is designed to be longer than the stub with 6 μm elevation so that they resonate at a similar frequency. It can be seen that, by using higher elevation, a sharper resonance and narrower impedance bandwidth are achieved. By using higher elevation, the 3dB bandwidth of ECPW short circuited stub is decreased by 122GHz (88%). Also this stub has a Q_L of approximately 3.2 and Q_u of 17.09 which are 75% higher than the Q_L and Q_u of the CPW and 62% higher than Q_L and 50% better than Q_u of the 6 μm elevated ECPW short stub. This is due to the further reduction of the substrate effect by elevating the CPW traces to higher values. By applying the high/low impedance rule the performance of this short-circuited stub can be further improved.

4.1.1.3 Effect of size, number and distance of supporting posts

By investigating different structures, it is found that the size, number and spacing of supporting posts has a critical effect on the characteristic impedance and effective dielectric constant of the elevated CPW lines and, consequently, the performance of the matching stubs. Fig.4.36 compares the performance in terms of S-parameters of two ECPW short circuit stubs with $6\mu\text{m}$ elevation. The only difference between the two resonators is the number of supporting posts.

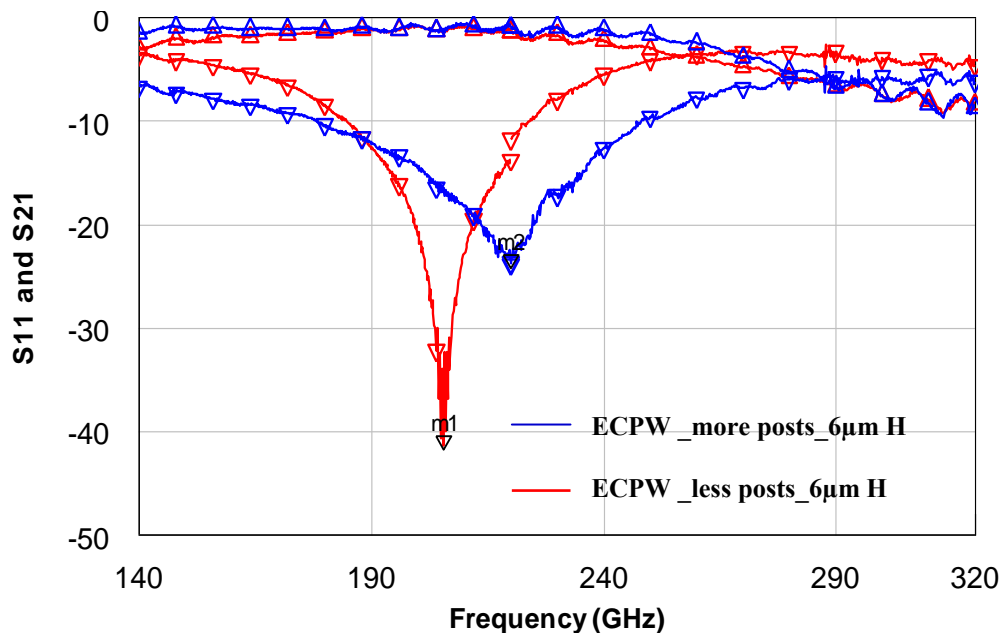


Figure 4.36: Comparison between measured S-parameters of $6\mu\text{m}$ elevated CPW short-end stubs with different number of supporting posts.

It can be seen that using less posts results in a significant improvement in the performance of ECPW short-circuited matching network. The resonance frequencies of both stubs are near to 213GHz.

A more detailed investigation into this effect reveals that increasing the elevation height is not the only way of improving the performance of ECPW short circuit stubs. By proper design in terms of line geometry, post size and number and distance between

posts, one can achieve a high performance and narrow bandwidth short circuit stub with relatively low elevation. Fig.4.37 compares the ECPW short circuit stub with 13 μm elevation and one with 6 μm elevation and less supporting posts. Compared with high elevations, lower elevations are advantageous in terms of yield, fabrication complexity and mechanical strength.

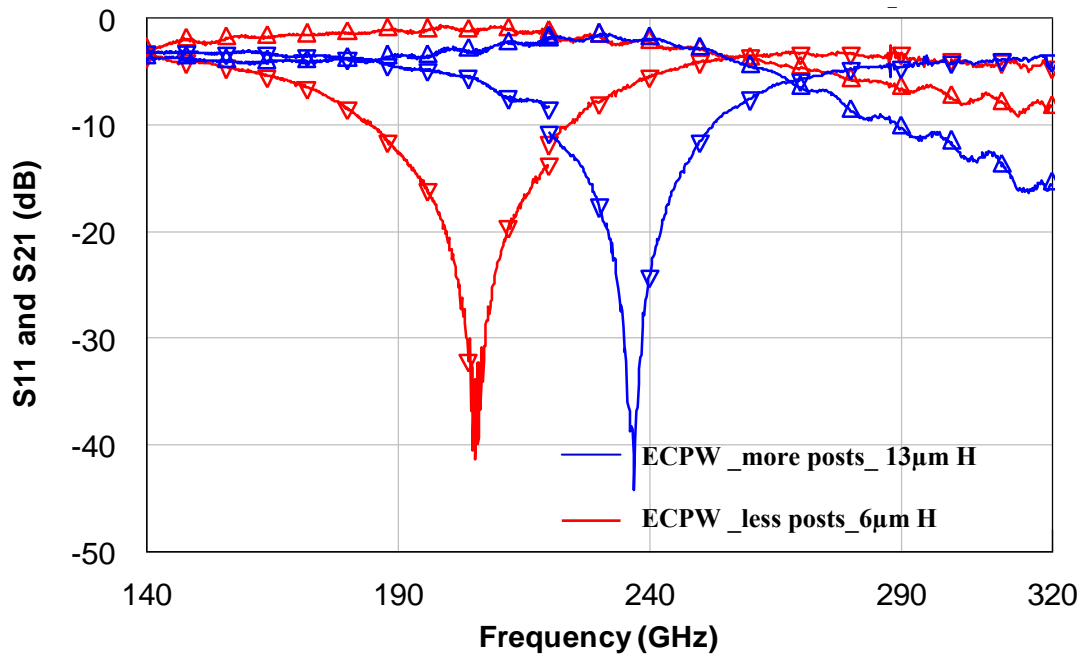


Figure 4.37: Comparison between measured S-parameters of ECPW short-end shunt stubs with 6 μm and 13 μm elevation heights.

4.4.2 Quarter-wavelength ECPW open-circuited stub

Figure 4.38 shows a micrograph of an open circuit matching stub which uses an all-elevated CPW structure.

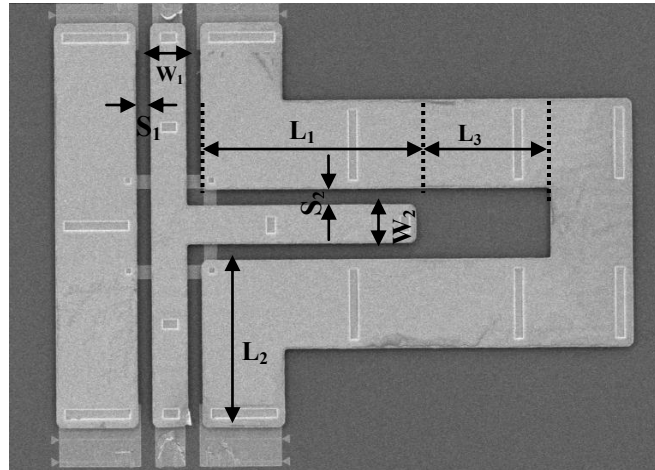


Figure 4.38: Micrograph of a open-circuited ECPW shunt stub. The stub dimensions are $L_2=220$, $L_3=150$, $S_1=16$, $W_1=41$, $S_2=15.5$ and $W_2=41$. The stub length, L_1 , is 292 for stub designed for 160GHz and is 180 for stub at 240 GHz. All dimensions are in microns.

The same dimensions as for short circuit stubs, section 4.4.1, was considered for the design of the open circuited stubs. The end gap was considered to be more than $[2 \times (W+2S)]$ in order to minimize the contribution of the end-effect [124].

Figure 4.39 shows the simulation and measurement results of an open circuit stub using all-elevated CPW structure.

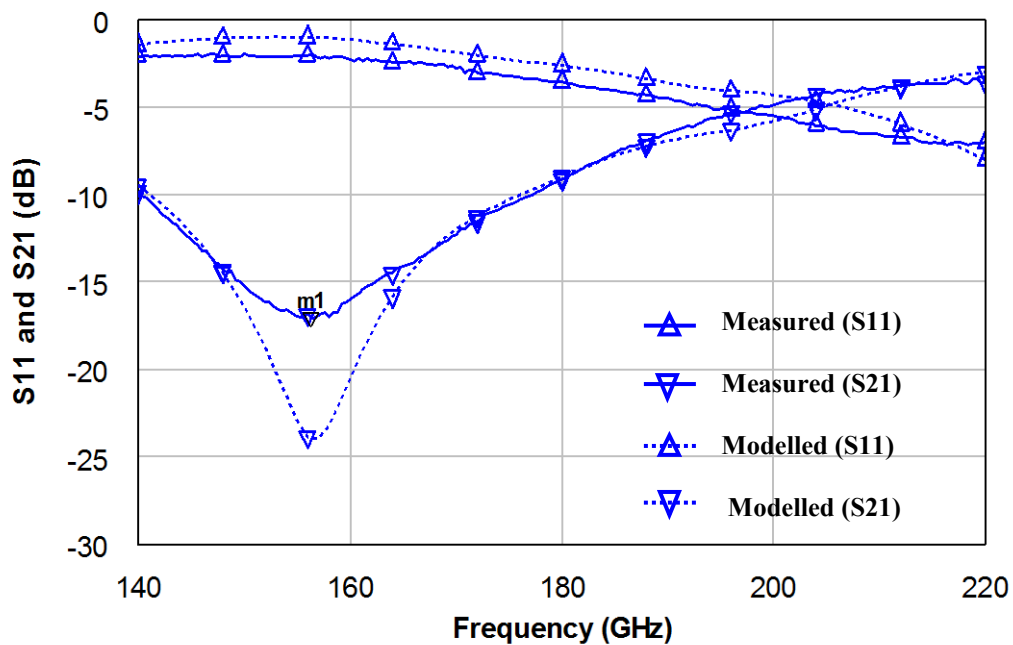


Figure 4.39: Measured and simulated S-parameters for ECPW open-end shunt stub with 6 μ m elevation.

Figure 4.39 shows a good agreement between measurement and simulation results for ECPW open stub. It was shown in Chapter 2 that CPW open circuit stubs using conventional CPW transmission lines show good performance between 140-220 GHz [50] and reasonable performance up to 320GHz. The performance enhancement of the open stub by using ECPW structure compared with CPW structure, is not as significant as short-circuited stub. The 3dB fractional bandwidth of the G-band open stub decreased by 10% by using ECPW structure than CPW one and also the loaded quality factor (Q_L) of open stub increased from 1.7 for CPW to 2.2 for ECPW (by 22%). This ECPW open stub also has an unloaded quality factor (Q_u) of 11.9 which is 27% better than CPW counterpart. This is shown in Fig4.40(a) and (b) which compare the results of open stubs using conventional and all-elevated CPW structures designed for G and H frequency bands, respectively. The impedance of the CPW lines are 50Ω and is around 65Ω for the ECPW lines- these latter have an elevation of about $6\mu\text{m}$.

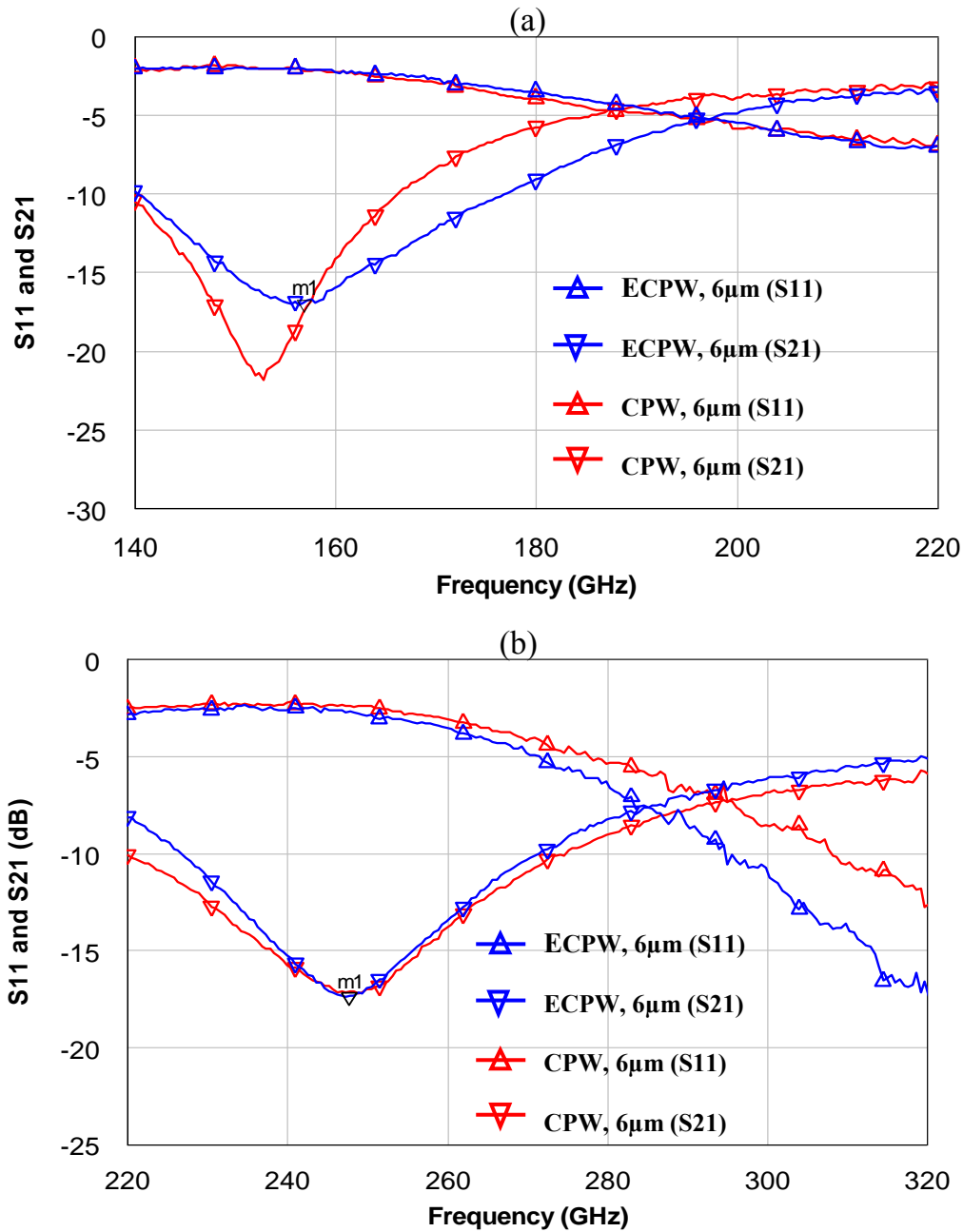


Figure 4.40: Comparison between measured S-parameters for 6 μm -elevated ECPW and conventional CPW open-end shunt stubs at (a) G-band (140-220GHz) and (b) H-band (220-320GHz).

An ECPW open-circuited stub implemented with 50 Ω elevated CPW line didn't show any significant difference in performance to the stub implemented with 65 Ω line.

It was discussed in Chapter 2 that increasing the impedance at the stub and decreasing the impedance at the feed lines results in a higher quality factor for the open-circuited

stub. Also, it was shown that applying this rule to conventional CPW open-stubs results in a very poor performance due to the high loss of CPW transmission line at low and high impedances. However, when this rule is applied to the ECPW open-circuited stub, much narrower bandwidths are achieved but with the in-band loss increased. Despite the increased in-band return loss, the elevated CPW open-circuited stub shows superior performance to the open-circuited stub which uses conventional CPW with the same impedances. This is shown in Figure 4.41. The figure shows that, by doubling the stub impedance to 100Ω and halving the feed impedance to 25Ω , the bandwidth decreases from 64GHz to 28GHz and the return loss increases from 1.02dB to 2.3dB at the centre frequency. When the same rule is applied to the CPW open circuit stub, the bandwidth decreases from 51GHz (33%) to 10GHz (7%) and the return loss increases from 1dB to 5.1dB at the centre frequency.

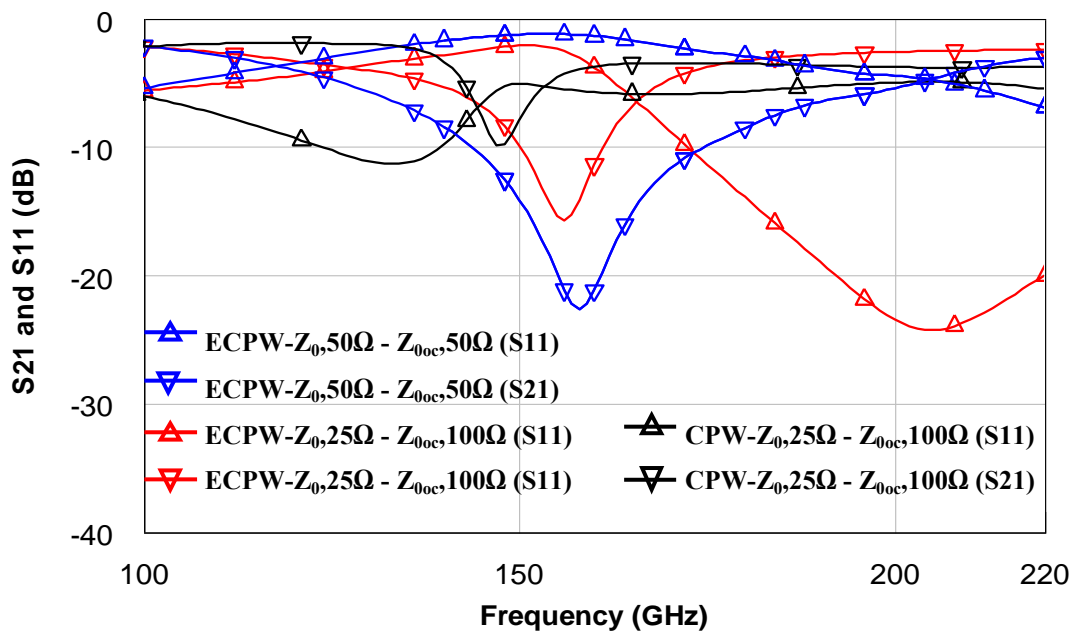


Figure 4.41: Comparison between simulated S-parameters for ECPW open-circuited stub with all 50Ω lines, various impedance lines and CPW with various impedance lines (low impedance feeds and high impedance stubs)

One important note relevant to the design of open-circuited stubs is that using a double open stub - which is common in the circuit designs with CPW structure - not only doesn't improve the performance of the network but actually degrades the performance and should be avoided, Figure 4.42.

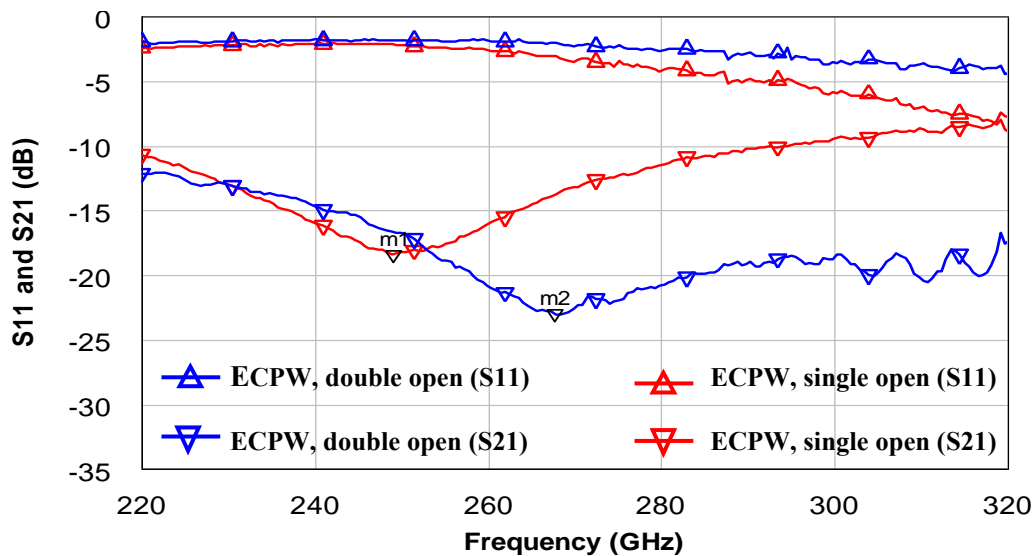


Figure 4.42: Comparison between measured S-parameters of double and single open-end ECPW shunt stubs. (m1: -18.37dB @ 249GHz, m2: -22.95dB @ 267.6GHz) The performance degradation is due to the lower effective impedance seen at the junction of the two stubs.

The effect of other elevated CPW parameters such as elevation height and supporting posts on the performance of the open-circuited stub is now investigated.

4.4.3 Effect of elevation height

Increasing the elevation height from $6\mu\text{m}$ to $13\mu\text{m}$ results in a shift in resonance frequency due to the changes in effective permittivity but doesn't yield any improvement in terms of the bandwidth or impedance match at the centre frequency. Figure 4.43 shows the measured results for two open stub structures identical in every respect except for a difference in elevation height.

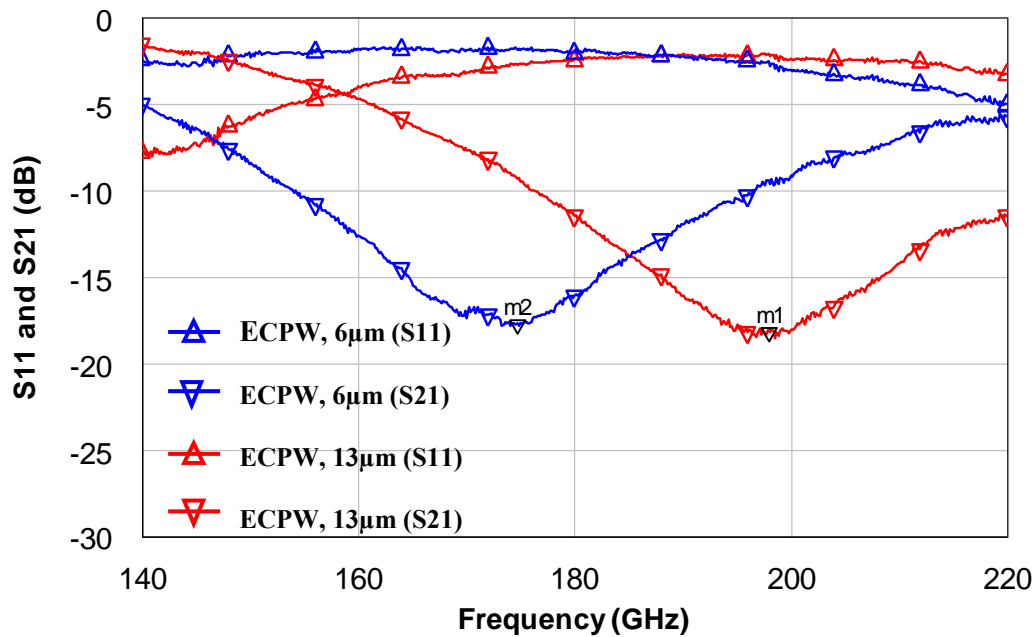


Figure 4.43: Comparison between measured S-parameters of open-end ECPW shunt stubs with $6\mu\text{m}$ and $13\mu\text{m}$ elevation heights. (m1: $-17.72\text{ dB @ }174.6\text{GHz}$, m2: $-18.8\text{dB @ }197.83\text{GHz}$)

The same result is observed with the effect of the size of and distance between the supporting posts - again the only difference being a shift in the resonance frequency and no improvement in the performance of the network.

4.5 All-elevated CPW quarter-wavelength resonator filter

High-Q band-pass and band-stop filters with sharp roll-off characteristics are useful passive elements in MMIC design which cannot be easily designed at frequencies above 110GHz . As we showed in Chapter 2, using conventional CPW does not result in good performance for band-pass and band-stop filters at G and H-band frequencies. To investigate the use of elevated CPW traces, the same band-pass and band-stop filters are designed using all-elevated CPW. This section looks at the performance of the elevated CPW filters up to a maximum frequency of 320GHz .

4.5.1 Quarter-wavelength ECPW Band-pass filter

Figure 4.44 shows a micrograph of an all-elevated 3rd order quarter-wavelength shunt stub band-pass filter. This filter structure can be simply constructed by connecting three double-stub short circuit matching networks in series. Due to the superior performance the elevated CPW short circuit stub showed over conventional CPW, this filter is expected to exhibit a superior performance to the filter of section 2.6.1.

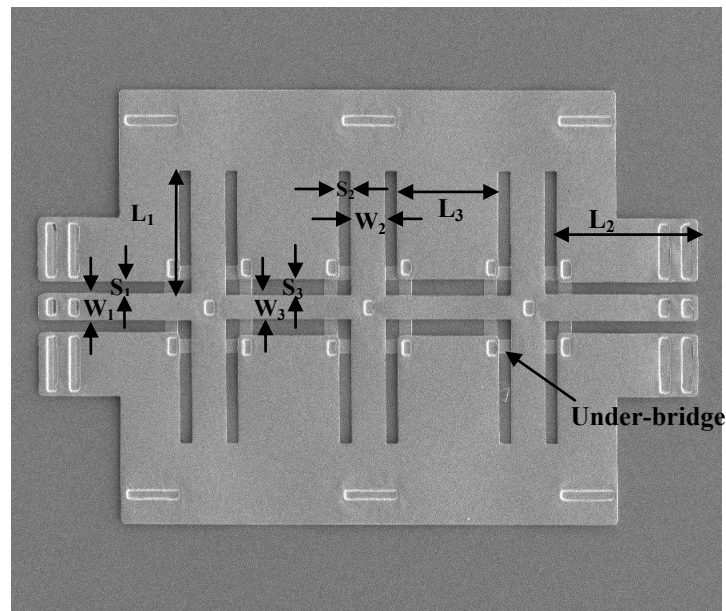


Figure 4.44: micrograph of the 3rd order quarter-wavelength band-pass ECPW Filter. The filter dimensions are $L_1=190$, $L_2=171$, $S_1=20$, $S_2=18.5$, $S_3=26$, $W_1= 41$, $W_2= 54$, $W_3= 35$. All dimensions are in microns.

It was shown in Chapter 2 that a CPW 3rd-order quarter-wavelength shunt stub band-pass filter designed for a centre frequency of 220GHz, has a high insertion loss in the pass band as well as a slow cut-off. A broad 3-dB bandwidth of 103GHz (45%) and high insertion loss of 6.99dB at the center frequency was observed for this filter. Designing this filter with all-elevated CPW structure, significantly improves the performance.

Fig.4.45 gives the measurement and simulation results for the band-pass filter implemented with ECPW at $6\mu\text{m}$ elevation. The results are in good agreement with the modeled data. The CPW/ECPW transition feeds were used for the filter measurements.

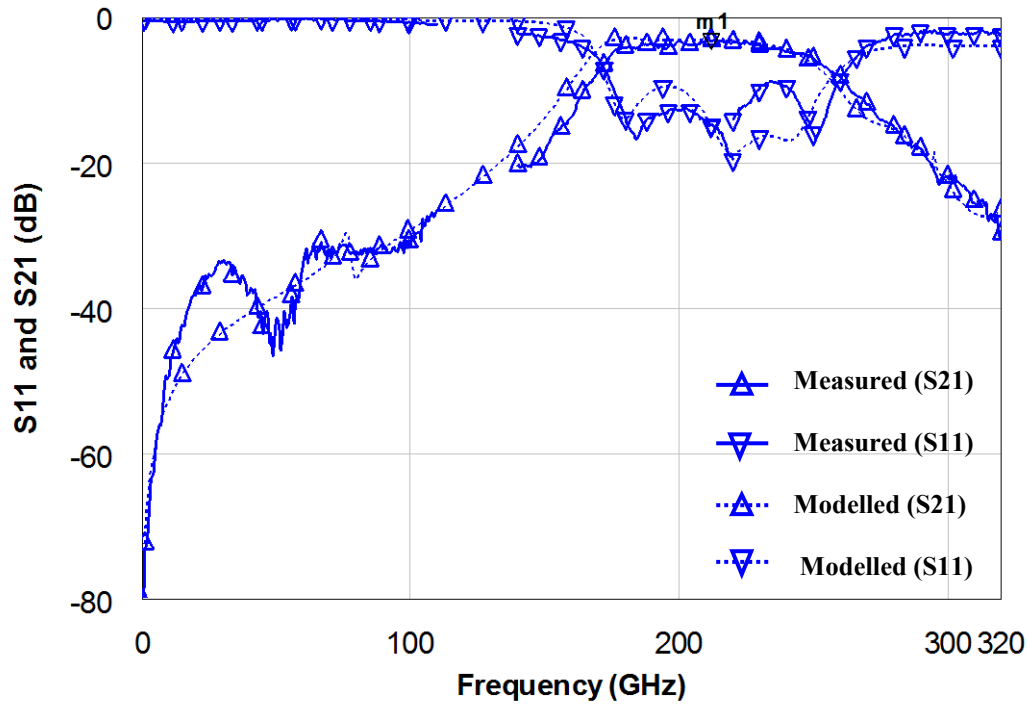


Figure 4.45: Measured and simulated S-parameters for a 3rd order ECPW band-pass filter with elevation height of $6\mu\text{m}$. (m1: -2.89dB @ 211.4 GHz)

The elevated CPW filter shows a 78GHz 3dB -bandwidth (36%) with a centre frequency of 211GHz . The measurement results are compared with the results for a CPW band-pass filter in Fig.4.46.

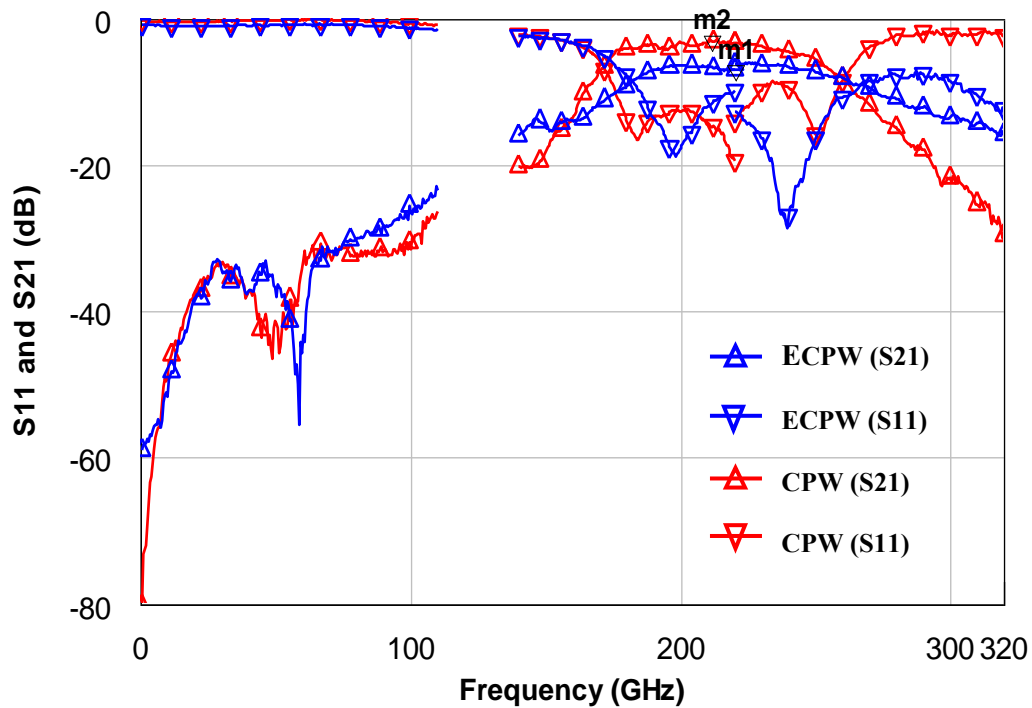


Figure 4.46: Comparison between measured S-parameters for $6\mu\text{m}$ -elevated ECPW and conventional CPW bandpass filters with centre frequency of 240GHz. (m1: -6.998dB @220GHz , m2: -2.89dB @ 211.4 GHz)

Looking at Fig.4.46, we can see that, by using elevated CPW, the insertion loss is decreased to 2.895dB at the centre frequency (compared with 6.99dB for CPW filter). It can also be seen that the high frequency roll-off of the ECPW filter is much steeper than that of the CPW filter. The result shows a narrowing in bandwidth of 25GHz (8%) and generally improved performance for the ECPW filter.

Looking at the electric field distribution of the filters will give us a better understanding of the performance improvement of the filter when using the all elevated structure rather than conventional CPW transmission.

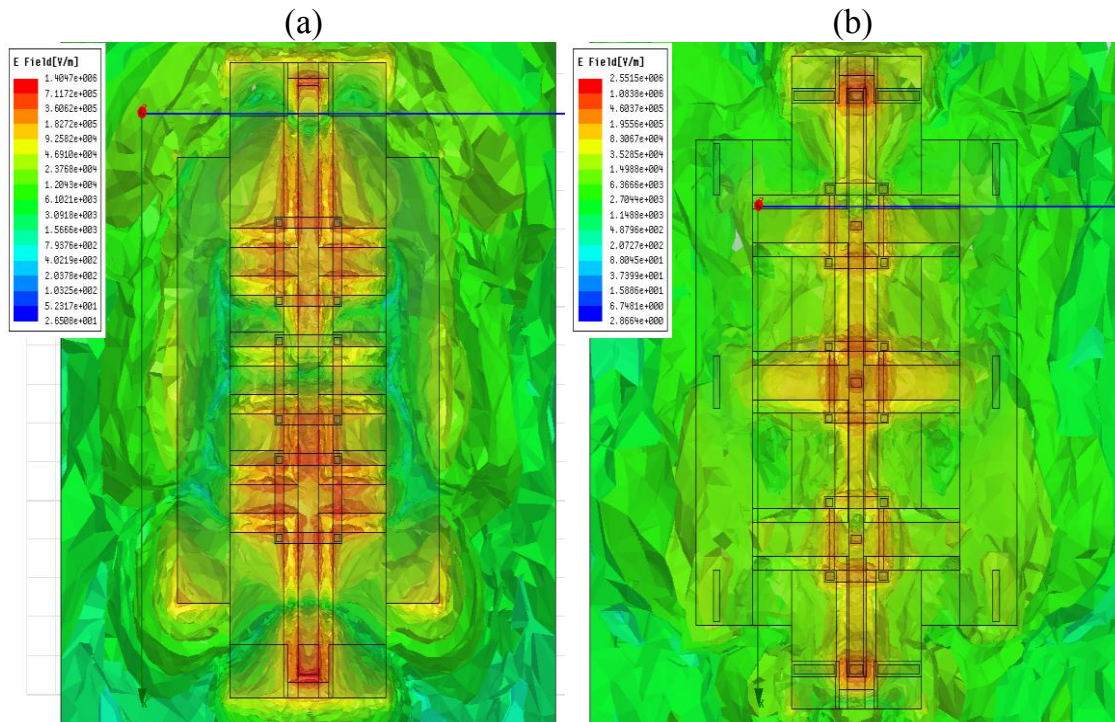


Figure 4.47: Top view of electric-field distribution in the substrate modelled for (a) CPW and (b) ECPW band-pass filters at the centre frequency.

Figure 4.47 shows the top view of the electric field plot, in the substrate, at the centre frequency for CPW and all-elevated 3rd order band-pass filters. Lower electric field penetration of the substrate is observed for the elevated structure, resulting in better in-band performance.

From basic transmission line theory, optimum performance for this filter structure can be obtained using high characteristic impedances for the connecting lines and low impedances for the stubs. This rule was considered in the design of the elevated CPW filter. However, the corresponding CPW filter makes use only of 50Ω lines for the entire structure. It was shown in Chapter 2 that designing a conventional CPW band-pass filter by applying this rule, improves the 3dB bandwidth but increases the in-band loss. This, as discussed earlier, is due to the increased CPW loss at impedance extremes which is not the case in the elevated CPW structure. Fig.4.48 shows a comparison

between the simulation results for an elevated CPW filter and for a conventional CPW band-pass filter designed with the same impedances as elevated lines.

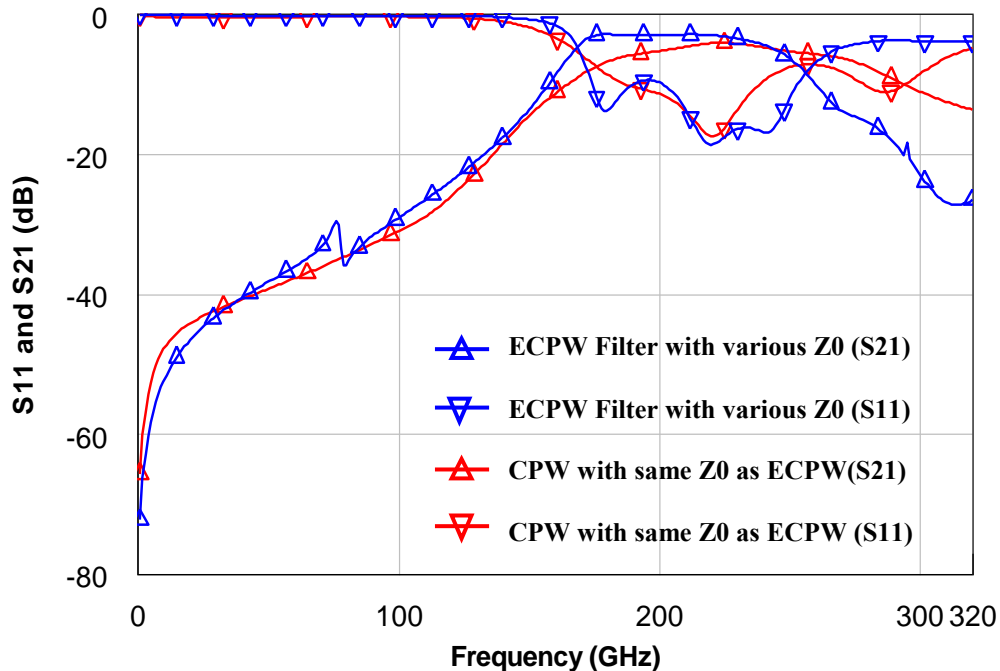


Figure 4.48: Comparison between simulated S-parameters for ECPW and CPW band-pass filters designed with identical high impedance connecting lines and low impedance stubs.

The CPW filter implemented with the same impedances as the elevated CPW lines, not only shows no improvement in performance compared with the 50 Ω CPW filter, but also shows a degradation in the filter's functionality. This example shows the advantage of elevated CPW structure when used to form high and low impedance transmission lines i.e. they exhibit lower loss than CPW lines and, hence, it is easier to achieve higher-Q passive networks.

4.5.1.1 Effect of elevation height on the filter performance

The all-elevated CPW 3rd-order quarter wavelength filter was also designed and fabricated with 13 μm elevation. The measurement and modeling results of this filter are shown in Figure 4.49. Results for the filter with 6 μm elevation is shown in Fig.4.50.

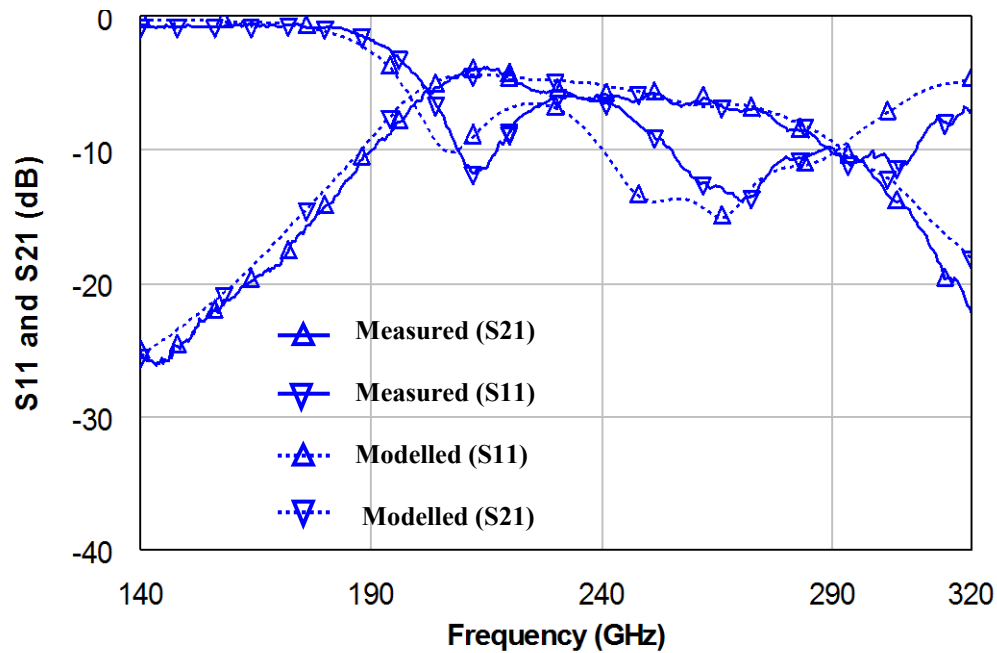


Figure 4.49: Measured and simulated S-parameters for a 3rd order ECPW band-pass filter with elevation height of $13\mu\text{m}$.

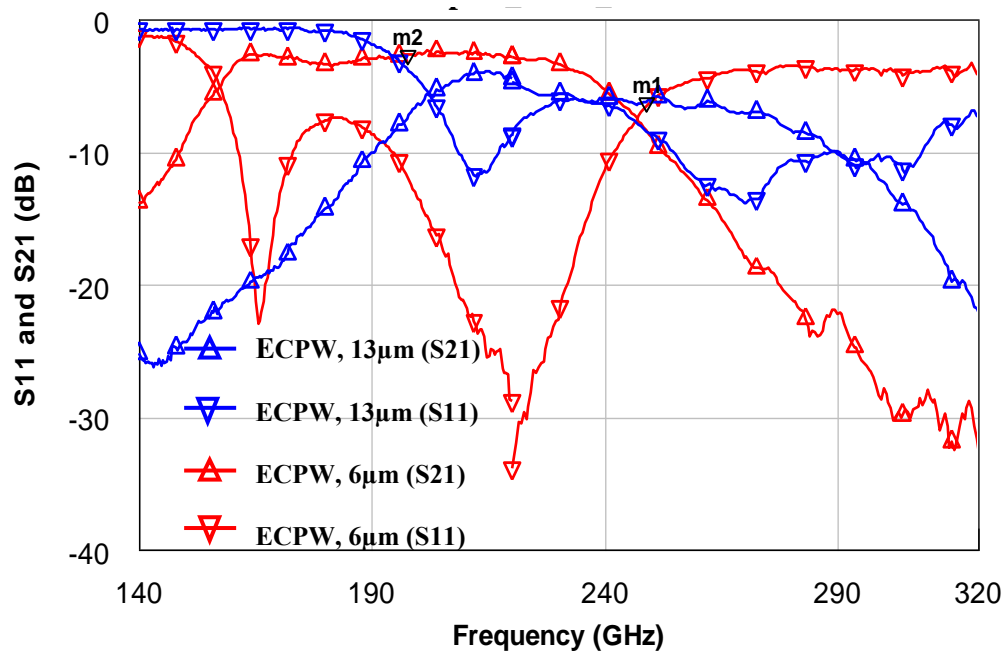


Figure 4.50: Comparison between measured S-parameters of 3rd-order bandpass ECPW filters with $6\mu\text{m}$ and $13\mu\text{m}$ elevation heights. (m1: -6.198dB @ 248.8GHz , m2: -2.63dB @ 197.6GHz)

As expected, increasing the elevation height -with otherwise fixed geometries- shifts the resonance frequency higher due to the reduction of the effective permittivity. It can be

seen that the center frequency of the filter shift to frequencies around 245GHz where the performance of elevated CPW transmission line starts to degrade. The 13 μ m elevated CPW filter then shows worse performance than the 6 μ m elevated counterpart. This can be explained by the fact that in order to achieve a high performance bandpass filter in this topology, low impedance transmission lines are required to implement the stub sections. Increasing the elevation height to 13 μ m by keeping the other geometries fixed, increases the impedance of the line and degrades the performance of the band-pass filter as a result. Also, increasing the elevation height in this particular example pushed the center frequency to around 245GHz which is the frequency at which the performance of ECPW line starts to degrade sharply.

The 3rd order quarter-wavelength, 13 μ m elevation, all-elevated filter is also compared with a CPW counterpart and, as we can see in Fig.4.51, it shows improved performance with respect to the filter making use of conventional CPW- although, this improvement is not significant.

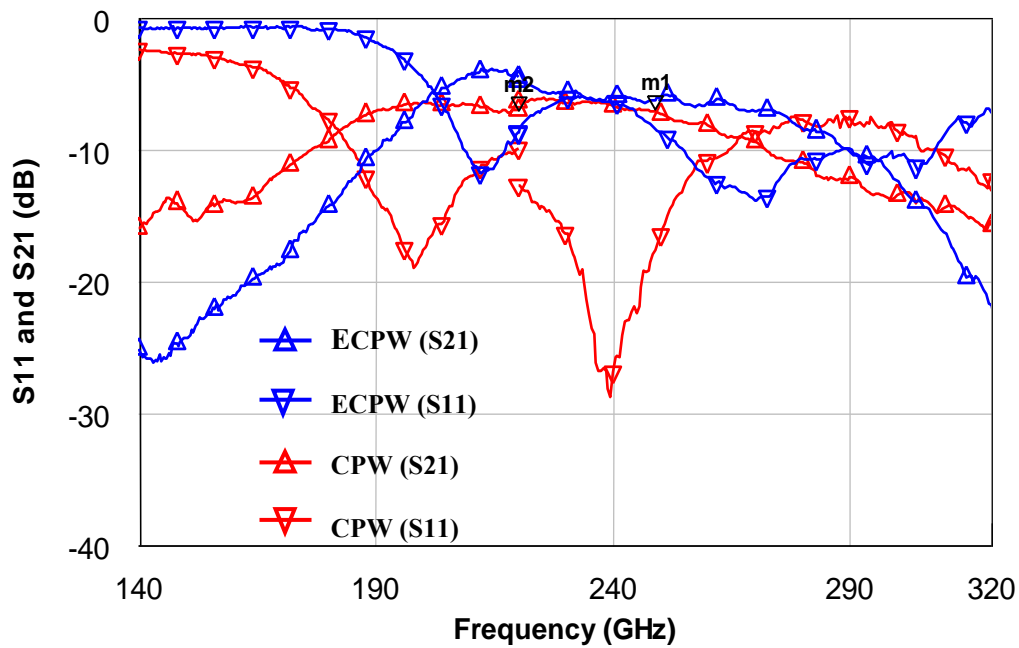


Figure 4.51: Comparison between measured S-parameters of a $13\mu\text{m}$ -elevated ECPW and conventional CPW bandpass filters.

It should be considered that, in this example, the ECPW line has much higher impedance than the CPW line. The CPW filter designed in the same impedance range shows significantly worse performance than this particular all-elevated CPW filter.

4.4.2 Quarter-wavelength ECPW Band-Stop filter

By cascading multiple open circuited shunt stubs, it is quite simple to realize a band-stop filter with high in-band insertion loss and low return loss. A third order quarter wavelength band-stop filter is designed and fabricated using a all-elevated CPW structure.

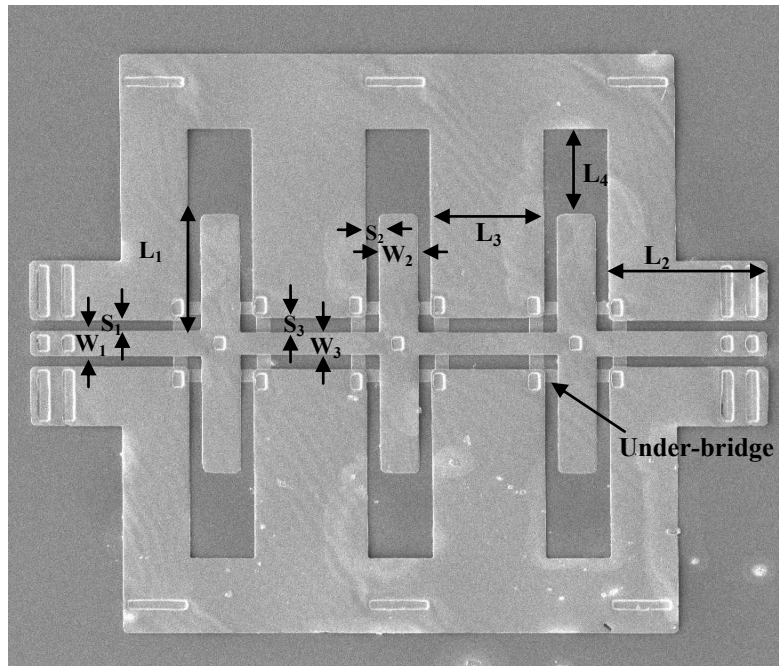


Figure 4.52: Micrograph the 3rd order quarter-wavelength ECPW band-stop Filter. The filter dimensions are $L_1=190$, $L_2=171$, $L_4=150$, $S_1=20$, $S_2=18.5$, $S_3=26$, $W_1=41$, $W_2=54$, $W_3=35$. All dimensions are in microns.

The measurement results along with the simulation data for this filter is shown in Fig.4.53.

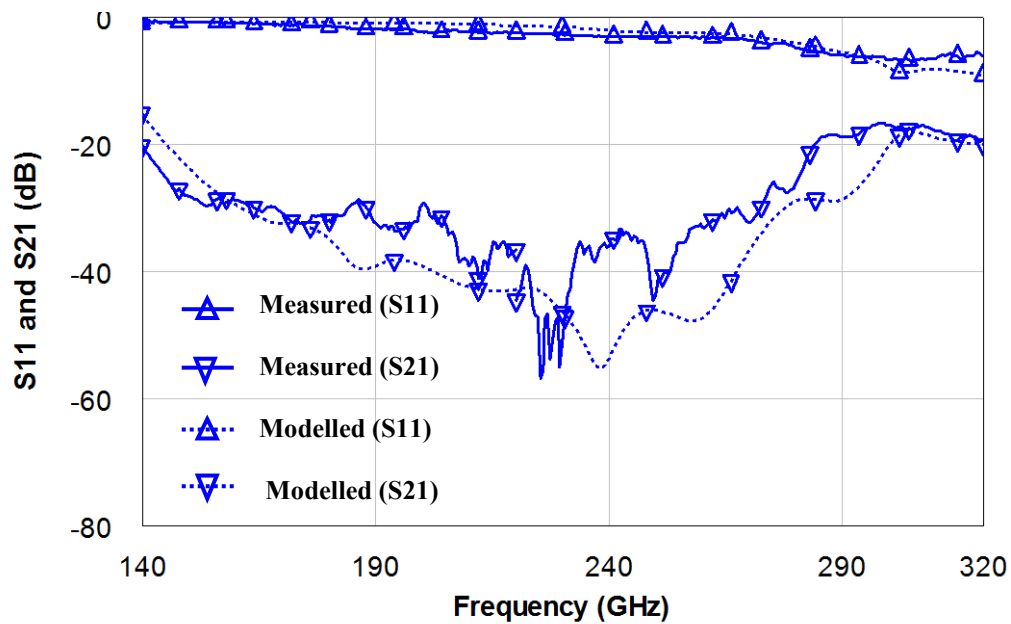


Figure 4.53: Measured and simulated S-parameters for a 3rd order ECPW band-stop filter with elevation height of $6\mu\text{m}$.

The results achieved for this filter are compared with the results of CPW band-stop filter in Fig.4.54.

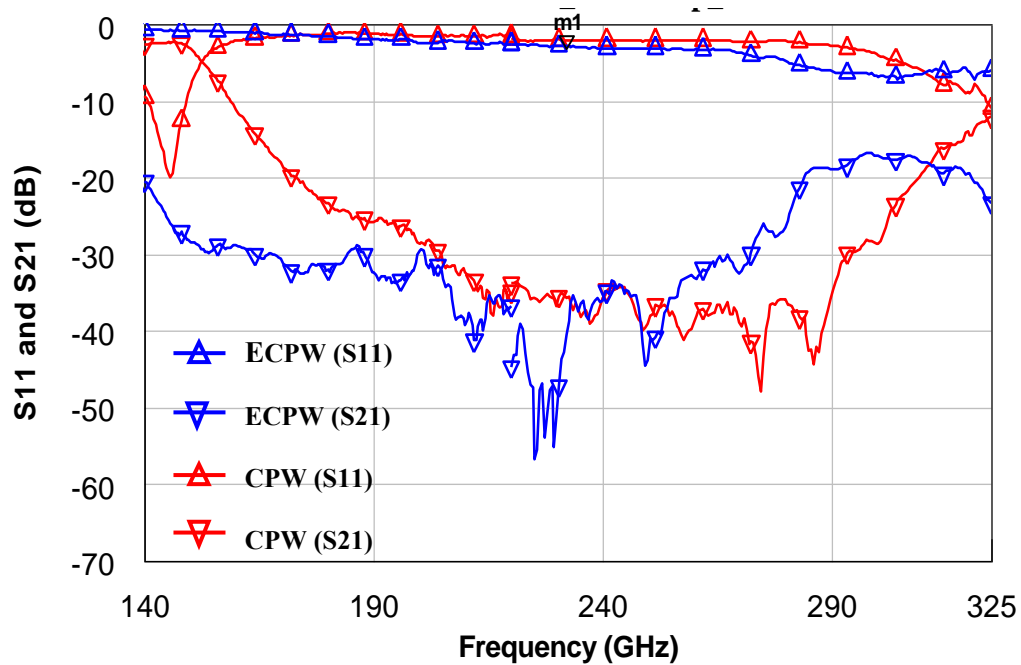


Figure 4.54: Comparison between measured S-parameters of $6\mu\text{m}$ -elevated ECPW and conventional CPW band-stop filters. ($m1 = -1.99\text{dB}$ @ 232GHz)

It can be clearly seen that this filter structure doesn't exhibit desirable performance characteristics. This filter has dimensions similar to the dimensions of the band-pass filter and consists of low impedance lines for the stubs and high impedance connecting lines (although only a small variation between the low and high characteristic impedances is used). However, from the rule described in chapter 2, in order to achieve good performance, high impedance lines are required for the stubs and low characteristic impedances for the connecting lines. By reordering the characteristic impedances of the stubs and connecting lines, the ECPW band-stop filter gives better performance, Figure 4.55.

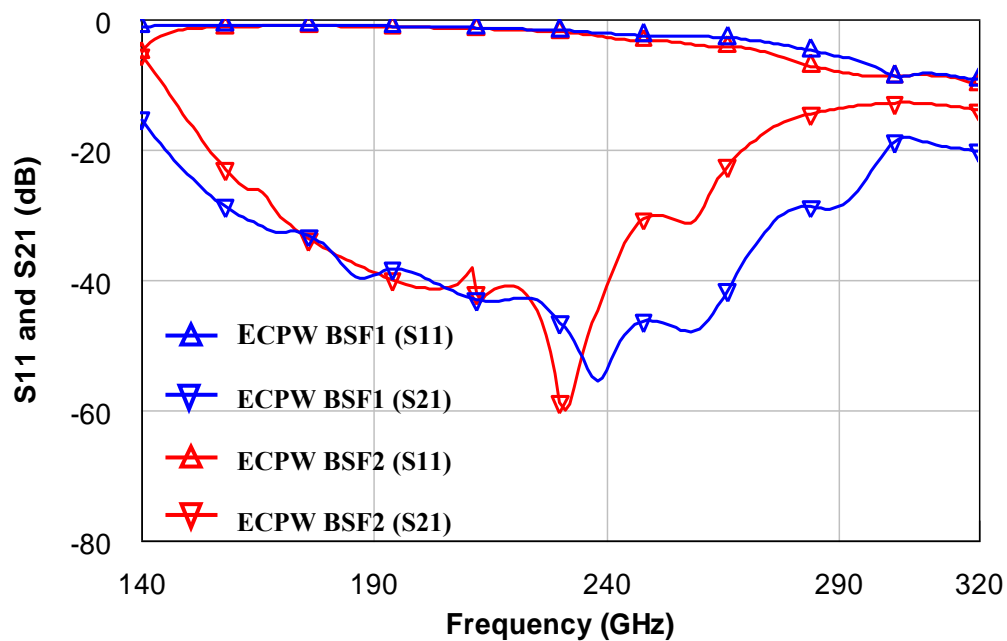


Figure 4.55: Comparison between simulated S-parameters for band-stop filter with centre frequency of 220GHz high impedance connecting lines and low impedance stubs (BSF1) and filter with low impedance connecting lines and high impedance stubs (BSF2).

Looking at Fig.4.55 shows that although the performance of double stub band-stop filter improved by applying the optimizations, still, a very wide bandwidth is observed for this structure. This is because of using the double open stubs which are in parallel at each junction and this causes the overall impedance of the stubs to become lower. Therefore, in the design of band-stop filters with narrow band width, the use of double open stubs should be prohibited. Also, by using the higher value impedances at the stub and lower values in the feed lines of a 3-rd order band-stop filter with single opens, further improvement in performance can be achieved. Fig.4.56 shows the results of the band-stop filter in above example compared with the results of the optimized filter with single open stubs and optimised impedances.

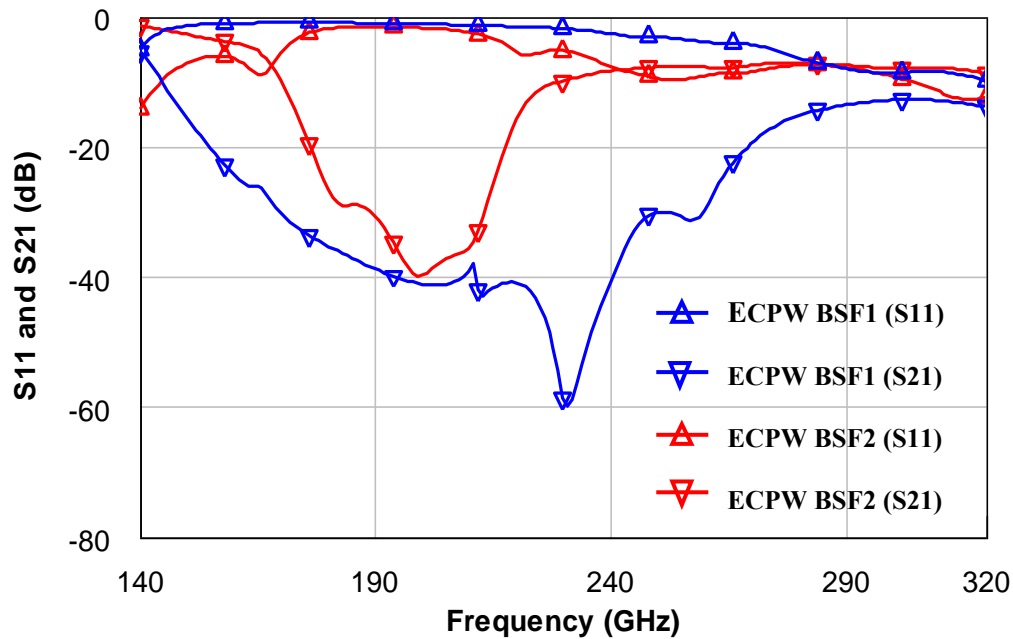


Figure 4.56: Comparison between simulated S-parameters for band-stop filter using double open stubs (BSF1) and single open stubs (BSF2).

It can be seen that a great improvement is obtained in the performance of band-stop filter resulting in narrower bandwidth without significant increase in the return loss. It was shown in Chapter 2, that by applying the same topology and dimensions to CPW band-stop filter, a reduction in bandwidth was achieved while the in-band loss was increased dramatically. This example shows the advantage that using ECPW to implement high and low characteristic impedances offers over CPW implementations when a narrow band /low loss band-stop filter at sub-mm wave frequencies is required. Another topology which is offered in Chapter 2 and which uses a combination of quarter-wavelength open and short-circuited stubs to implement the band-stop filter is also designed with a ECPW structure. In the design of this filter, high impedances are used for open-circuited stubs and short-circuited stubs are implemented using low impedances. Figure 4.57 shows the results achieved for a band-stop filter designed with

this topology and compares it with the results of the band-stop filter with single open stubs.

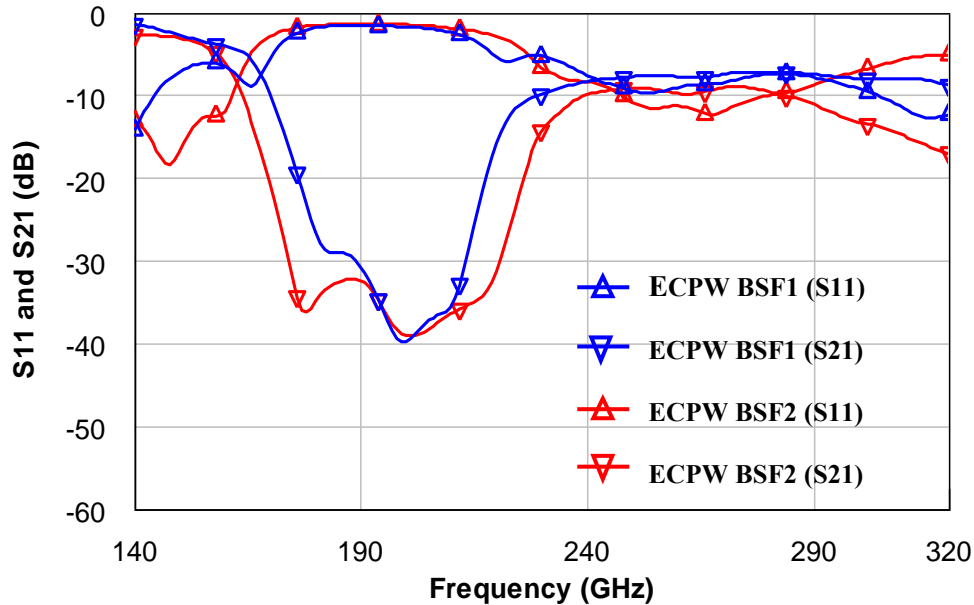


Figure 4.57: Comparison between simulated S-parameters for band-stop filter using single open stubs (BSF1) and band-stop filter utilising combination of short and open stubs (BSF2).

We see from Fig.4.57 that employing the combinations of open and short-circuited stubs in implementing the band-stop filter results in a more satisfactory response than with the use of double open stubs. However, BSF with this topology shows very similar results to the one implemented using single open stubs. The BSF with single open stub is advantageous in term of compactness since it takes up less space on the wafer.

In general, compared with the results in Chapter 2 for the CPW BSF, all of the band-stop filters with ECPW structures show superior performance to their CPW counterparts in terms of roll-off characteristics and in-band return loss. As an example, Fig.4.58 compares the CPW and ECPW band-stop filters which use the open/ short topology.

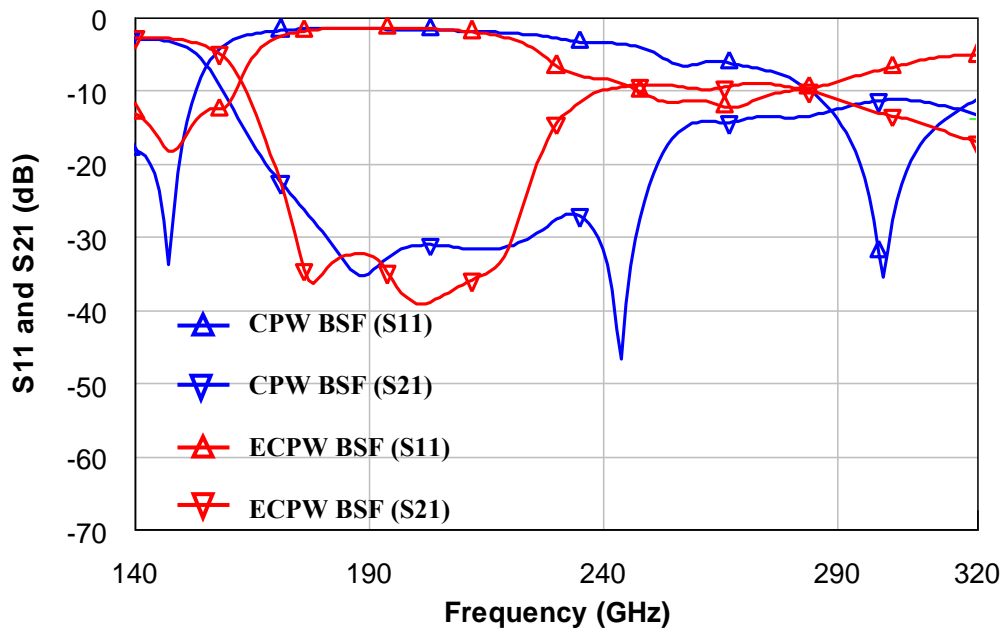


Figure 4.58: Comparison between simulated S-parameters for ECPW and CPW band-stop filters utilising short/open topology.

4.5 Summary

The elevated coplanar waveguide is investigated in this chapter by considering its potential in implementing a low loss transmission line for sub-millimeter wave applications while only requiring a relatively simple fabrication process. Different forms of elevated CPW structures are introduced and their high frequency performance is compared. The structure with all of the CPW traces elevated above the substrate, all-elevated CPW, is investigated in detail. First the quasi-static analysis of the line is performed using conformal mapping techniques to enable calculation of the characteristic impedance and effective permittivity. The all-elevated CPW line is also analysed in terms of its attenuation at low and high frequencies via a series of 2-D and 3-D simulations and the results are compared with those for a conventional CPW line. It is observed in static simulations that, by elevating the CPW traces above the substrate,

both conductor and dielectric losses of the line will decrease by half and by 30 times compared to a CPW line, respectively. However, the 3-D simulation results of the ECPW line still show high attenuation of this line at high frequencies starting around 120GHz and increasing with frequency to the value ~ 7 dB at 320GHz for the line with lateral dimension of $120\mu\text{m}$. This attenuation results from the non-complete isolation of the elevated CPW traces from the substrate-resulting in energy radiated into the substrate. It is also shown that, by decreasing the lateral dimensions of the ECPW line, e.g. from $120\mu\text{m}$ to $30\mu\text{m}$, one can reduce the attenuation in ECPW line by 6dB at 320GHz, at the expense of less freedom in the design dimensions and poorer yield. To investigate the performance of the ECPW line in real life, a set of ECPW lines are designed, fabricated and measured. The results of an ECPW line with lateral dimensions which provide reasonable loss and which are able to be fabricated, is presented and also compared with CPW results. It is observed that, at lower frequencies, ECPW shows slightly lower loss than CPW (e.g. 0.4dB/mm lower at 140GHz). However, the attenuation of these two lines becomes similar - 2dB/mm at 250GHz. In order to investigate the source of the losses and improve the roll-off observed in ECPW line performance, the effect of different parameters are investigated. It is shown that changing the size, distance and number of supporting posts and also changing the elevation height cannot improve the high levels of radiation of the wave into the substrate and a structure which is completely isolated from the substrate is required to remove this roll-off effect.

The performance of the all-elevated CPW structure in implementing passive components is investigated by design and fabrication of a set of ECPW matching networks and filters. In this regard, short and open-circuited matching stubs operating at

G and H-band frequency ranges were designed, fabricated, measured and compared with the CPW counterparts. It is observed that the ECPW short circuit stub shows superior performance to the CPW short stub with 1.3dB improvement in insertion loss at 140GHz and 0.5dB at 240GHz. Also, a reduction in bandwidth and better matching to 50Ω at the centre frequency is achieved for the ECPW short circuit stub compared with the CPW equivalent. The ECPW short circuited stub shows 37% improvement in 3dB fractional bandwidth and 33% higher loaded and 50% higher unloaded quality factors than CPW counterpart. Also, the performance of ECPW short-circuited stubs is investigated in detail through looking at the effect of transition to CPW feeds, elevation height and size and number of supporting posts. It is observed that at the elevation of $13\mu\text{m}$, ECPW short stub shows 75% higher loaded and unloaded quality factor than CPW short circuit stub. The elevated CPW open circuited stub is investigated in the same manner. Although the performance enhancement of ECPW open circuit stub compared with CPW open is not as significant as short circuit stub, it still shows 10% improvement in fractional bandwidth and 22-25% in quality factor. At the end, the results of the quarter-wave length band-pass and band-stop filters using ECPW structure are presented. The ECPW band-pass filter is shown to have a significant performance improvement with a 4dB reduction of in-band losses. It also exhibits a narrower bandwidth than the CPW counterpart (by 9%). Also, the advantages which can be enjoyed by using all-elevated structures, in preference to conventional CPW structures, when implementing band-stop filters is discussed.

It is in the implementation of high-Q passive networks, matching stubs and filters that the main advantage of the elevated CPW structure becomes apparent. While CPW structures cannot support low loss coupled with high/low impedance extremes – which

are vital to increase the quality factor of the stubs and filters – elevated CPW structures offer low loss even at extremes of characteristic impedance and higher Q networks follow as a result. It should be mentioned though, that, while achieving high impedances is very easy in the elevated structures so far detailed, implementing low impedances is more challenging.

Although using all-elevated CPW is advantageous compared with conventional CPW in many cases, it is still not an ideal transmission media for submillimeter wave structures due to its tendency to radiate at sufficiently high frequencies. Due to the high penetration of the field by the substrate at high frequencies, a structure with more complete isolation from the substrate is desired for sub-millimeter wave applications.

Chapter 5

Study of Signal-Elevated Coplanar Waveguide Structures

5-1 Signal-elevated CPW (SECPW) transmission line

Some of the possible configurations for elevated CPW structures were shown in Chapter 4. One of the elevated structures which shows good potential for high frequency MMIC applications, as was shown in last chapter, is signal-elevated CPW (SECPW). A brief explanation of the quasi-static analysis of SECPW line with detailed investigation into the performance of SECPW transmission lines at submillimeter-wave frequencies is presented in this chapter. Also, the performance of some passive networks, including short-circuited and open-circuited matching networks, using signal-elevated CPW is shown. The effect of supporting posts and elevation height is also examined. A comparison between signal-elevated CPW structures and conventional as well as the all-elevated CPW is given for each of the lines and matching networks.

5-1-1 SECPW Analysis

Signal-elevated CPW line can be achieved by elevating the CPW signal trace above the substrate using air-bridge technology and keeping the ground traces in contact with the substrate. Signal-elevated CPW on GaAs substrates is presented in [134] along with an accompanying 2D-FDTD analysis. This work shows the reduced attenuation of these lines compared with their CPW counterparts. In [48] it was shown that high impedance/low loss lines on silicon substrates can be achieved using signal-elevated CPW. However no mathematical analysis was reported on the parameters of this line; such as characteristic impedance and effective permittivity. Doing the quasi-static analysis for signal-elevated CPW is not as straightforward as the analysis for all-elevated CPW lines which was presented in chapter 4. The problem is the large number of unknowns to be solved during the mapping process - the so called 'parameter problem'. Closed form expressions for the t-plane variables are not obtainable and instead an iterative process - e.g. Broyden's (Newton's method generalised to multiple variables) method - must be used to find the mapped constants. Therefore, in order to investigate signal-elevated CPW lines, we carried out a set of 2-D simulations to extract each line's parameters of interest. Figure 5.1 shows the cross section of a signal-elevated CPW structure.

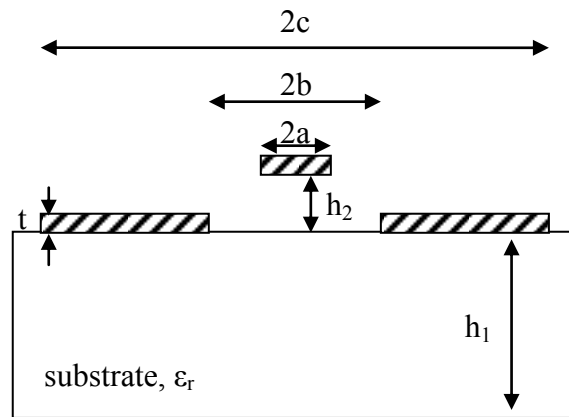


Figure 5.1: Cross section of a signal-elevated CPW line

The width of the signal line is $2a$ and the gap $(b-a)$. The width of the ground planes are $(c-b)$ and the elevation height, is h_2 . The substrate thickness is h_1 and the finite thickness, t , of the conductors is also taken into account.

Fig.5.2 plots the simulated characteristic impedance varying the signal trace, $2a$, between $20\mu\text{m}$ and $160\mu\text{m}$ for three different elevations of $2\mu\text{m}$, $8\mu\text{m}$ and $14\mu\text{m}$. Constant values of $20\mu\text{m}$ for gap width $(b - a)$, $100\mu\text{m}$ for the ground widths and $2\mu\text{m}$ for the conductor thickness were considered. A substrate with dielectric constant of 12.9(GaAs) and thickness of $600\mu\text{m}$ was used in all cases. The geometries in this plot are the same as the ones in the plot for all-elevated CPW, Chapter 4, Fig 4.15 , so as to allow direct comparison.

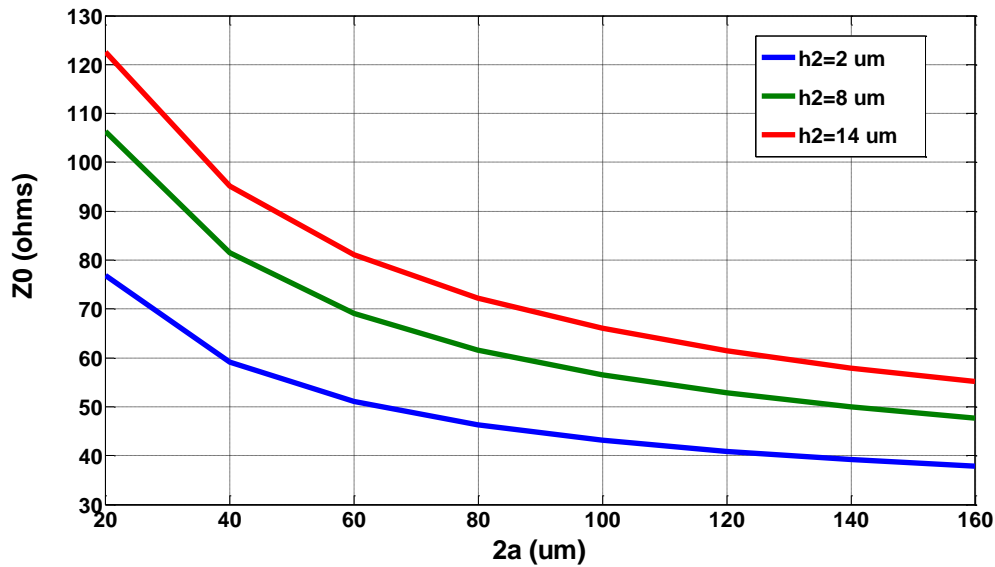


Figure 5.2: Simulated characteristic impedance of signal-elevated CPW for varying $2a$, $b=2a+20$, $c=b+100$, $h=2,8$ and 14 . All dimensions are in micron

It can be seen that the characteristic impedance of the SECPW line increases by elevating the signal trace to higher values although this change is not linear and depends on the lateral dimension of the line. Also, high characteristic impedances are possible at low elevations (which is advantageous for fabrication yield). Comparing these results with the values for all-elevated CPW line shows that signal-elevated CPW, in general, has lower impedance than the all-elevated CPW. However, the difference between the impedances is not linear with respect to trace width. For example, the difference between the impedance of SECPW and ECPW line with $2a = 40\mu m$ at an elevation of $14\mu m$ is 1Ω while it is 5Ω at the same elevation for $2a = 160\mu m$.

A plot of the effective permittivity of signal-elevated CPW lines with the same dimensions as in Fig.5.2 is shown in Figure 5.3.

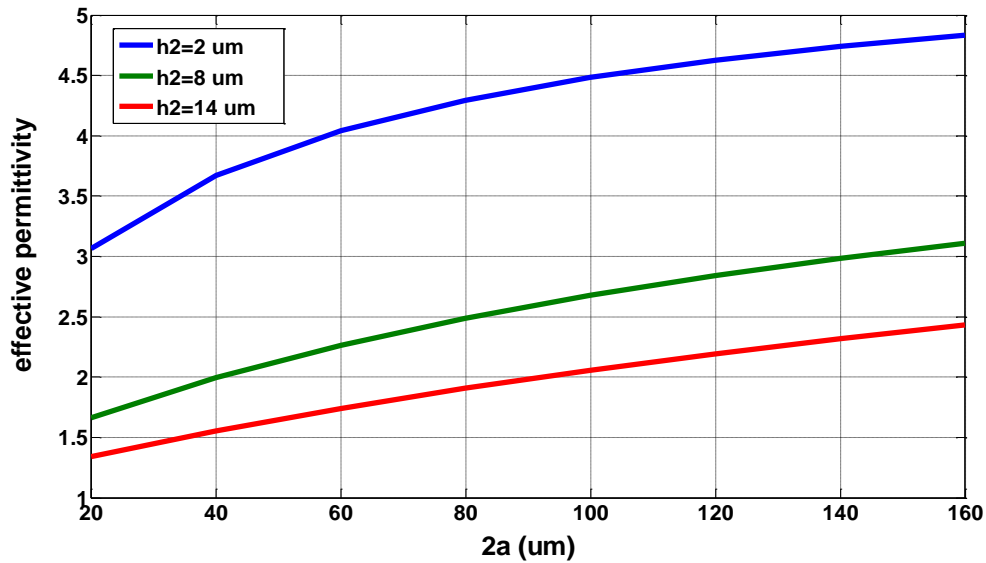


Figure 5.3: Simulated effective permittivity of signal-elevated CPW from for varying $2a$, $b=2a+20$, $c=b+100$, $h_2=2,8$ and 14 . All dimensions are in micron

The graph illustrates that the effective permittivity of signal-elevated CPW lines decreases with increasing elevation height. An effective permittivity close to one can be achieved for some geometries i.e for lines with an elevation of $14\mu\text{m}$ and a narrow signal width of $20\mu\text{m}$ or less. As we expect, the effective permittivity of signal-elevated CPW is higher (around 0.5) than the all-elevated CPW line. This is because of the greater isolation of the all-elevated CPW from the substrate compared with signal-elevated CPW.

5-1-2 Losses in signal-elevated CPW

As for the other types of transmission lines, the total attenuation in SECPW consists of conductor, dielectric and radiation losses. Using the same technique as for ECPW noted in section 4.2.6, a set of 2-D and 3-D simulations were carried out to extract the losses in signal-elevated CPW lines. In the following Figures, Fig.5.4(a) and (b), the conductor

and substrate losses of SECPW are plotted for the ratio of signal width, $2a$, to the lateral dimension, $2b$. The lateral dimensions are kept to be $30\mu\text{m}$, $60\mu\text{m}$ and $120\mu\text{m}$ and the signal width is increased from 10% to 90% of these values.

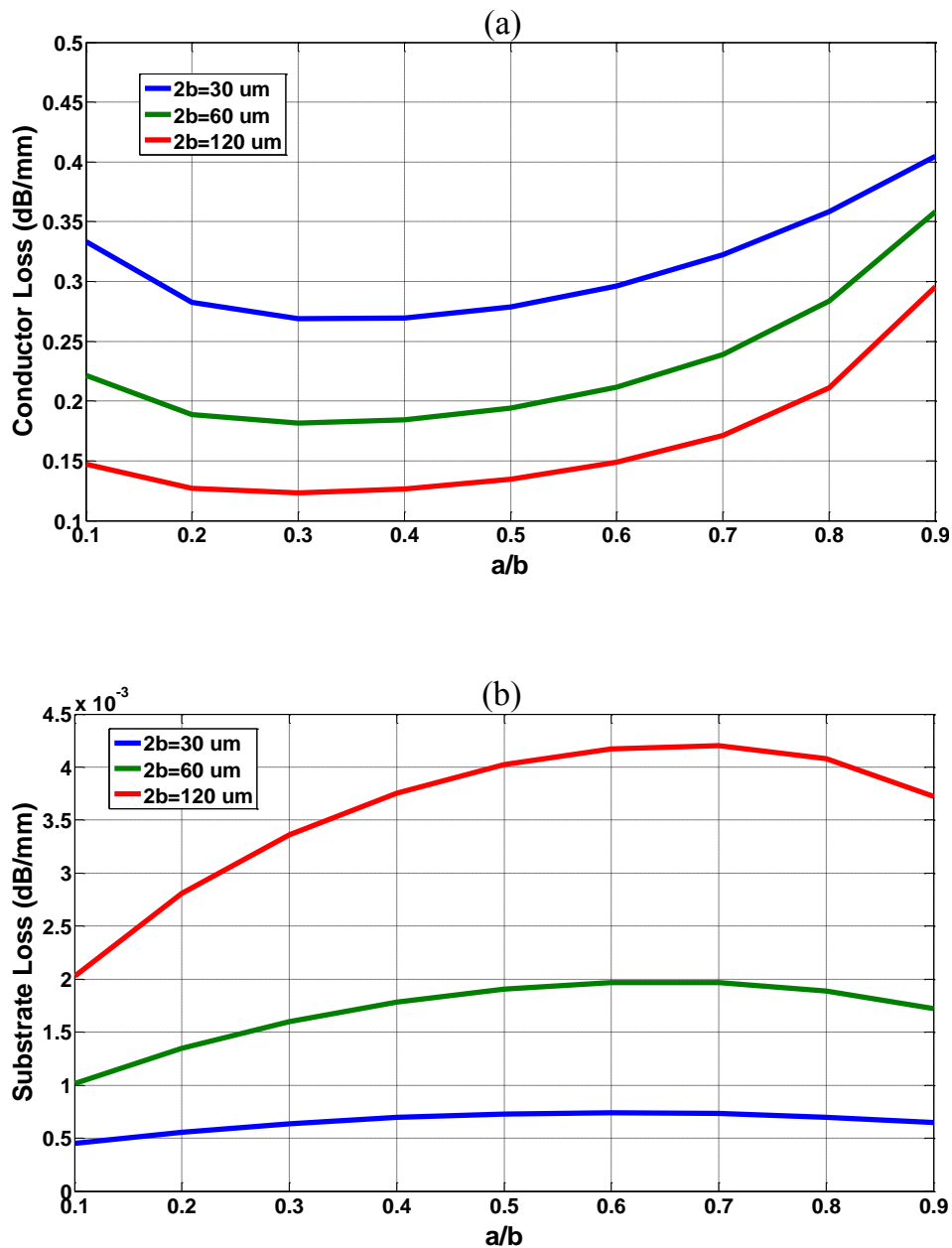


Figure 5.4: Plot of simulated (a) conductor loss and (b) substrate loss of SECPW lines with three different lateral dimensions ($2b$) of $30\mu\text{m}$, $60\mu\text{m}$ and $120\mu\text{m}$ for various ratios of signal width to lateral dimensions (a/b).

It can be seen that, as with the other transmission lines, the conductor loss is dominant at low frequencies and increases when the line has narrow signal traces or small gaps. Compared with the ECPW line, conductor loss in SECPW line is very similar at small and medium ratios of a/b where the lines have wide or medium gap width. However, when the ratio increases and the lines have small gaps, the conductor loss in signal-elevated line is almost half the values in the all-elevated structure. This is because in SECPW lines, the signal and ground traces are not parallel to each other and therefore with small gaps the high current density at the edges of conductors is not as large as with CPW and ECPW lines. This results in lower attenuation for low impedance transmission lines implemented with a SECPW structure. However, having lower conductor loss in low impedance SECPW lines is only advantageous at low frequencies where the conductor loss is dominant. As the frequency increases and radiation becomes a major source of attenuation, this becomes less advantageous. In terms of substrate loss (without radiation), SECPW lines show slightly higher values, around 0.5×10^{-3} dB/mm, than the ECPW lines. This is because of the higher isolation from the substrate in all-elevated CPW structures than the signal-elevated ones.

The effect of elevation height on the loss parameters of SECPW lines is shown in Fig.5.5.

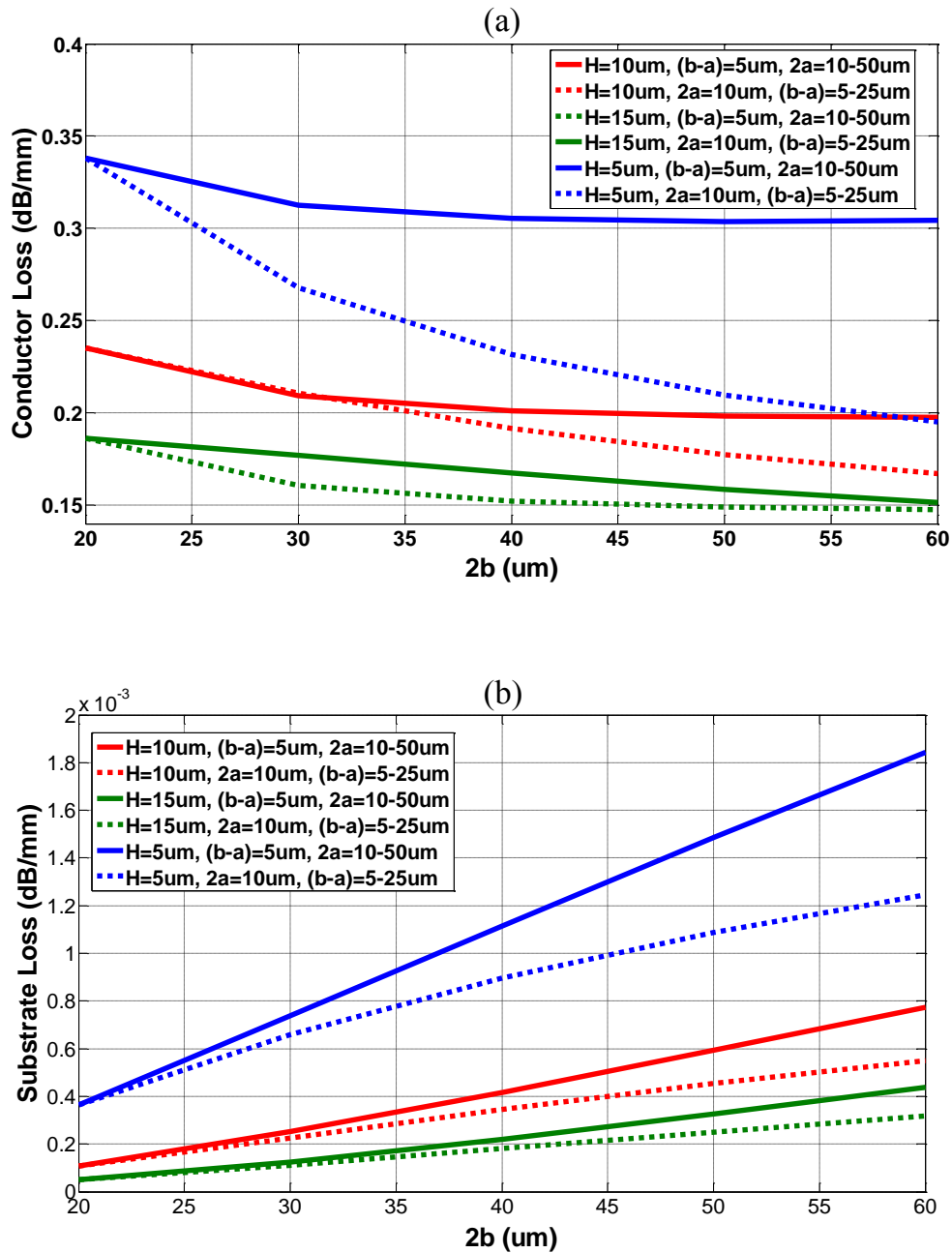


Figure 5.5: Plot of simulated (a) conductor loss and (b) substrate loss of SECPW lines for various lateral dimensions ($2b$) and three elevation height of 5, 10 and $15\mu\text{m}$. The range of lateral dimensions is maintained by once keeping the signal width constant and varying the gap size and once varying the signal width when the gap size is constant.

In the above Figures, the conductor and substrate (without radiation) losses are plotted for different lateral dimensions, ($2b$), firstly by keeping the signal width constant and changing the gap size, and then by keeping the gap width constant and changing the

signal width. The data is plotted for three different elevations of 5, 10 and 14 μm . It can be seen in Fig.5.5 that, perhaps surprisingly, the conductor loss of a signal-elevated CPW line is strongly affected by the amount of elevation of the signal trace. At 5 μm elevation, the conductor loss is very close to that of all-elevated line. However, unlike ECPW, when the elevation increases to 10 μm , the conductor loss decreases significantly and it reaches values close to half at the elevation of 15 μm compared with 5 μm elevation. Also, at higher elevations, for a constant lateral dimension, there is no significant difference in terms of conductor loss between having larger signal width or smaller gaps. In contrast, for all-elevated CPW at constant lateral dimension, it is always the case that smaller widths and larger gaps show lower losses than wider signal traces and smaller gaps. This can be explained by the fact that by increasing the elevation height, the signal trace becomes more isolated from the ground traces and the edge current density becomes minimal.

In terms of substrate loss (without radiation), the SECPW lines follow the same trend as the ECPW case by having values slightly higher than the all-elevated structures.

In order to investigate radiation losses in SECPW, 2-D and 3-D simulation results are compared in the same manner as explained for CPW in chapter 2, and ECPW in chapter 4. The line dimensions are the same as for the CPW and ECPW examples, Fig.2.16 and Fig.4.17, with lateral dimensions of 120 μm and 30 μm .

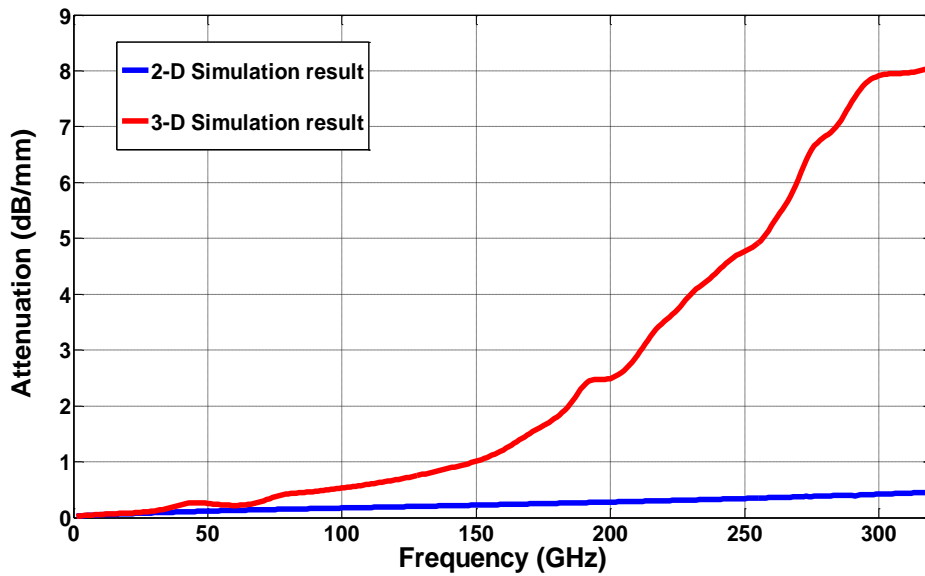


Figure 5.6: 2-D and 3-D Simulation plots of total attenuation of a $5\mu\text{m}$ -elevated SECPW line with lateral dimension of $120\mu\text{m}$.

Figure 5.6 shows that, for a lateral dimension of $120\mu\text{m}$, radiation in signal-elevated CPW starts from frequencies around 70GHz while it is above 100GHz in ECPW and CPW structures. As with CPW and ECPW structures, the radiation losses increase significantly as frequency increases. At 300GHz , the total attenuation of the SECPW line, from 3-D simulation, is almost 1dB/mm lower than the CPW line and 1dB/mm higher than the ECPW structure. This is due to the greater isolation of SECPW from the substrate, compared with the CPW line, and lower isolation compared with the ECPW line. By decreasing the lateral dimension of SECPW line to $30\mu\text{m}$, as in the CPW and ECPW cases, the total attenuation of the line decreases significantly, Figure 5.7.

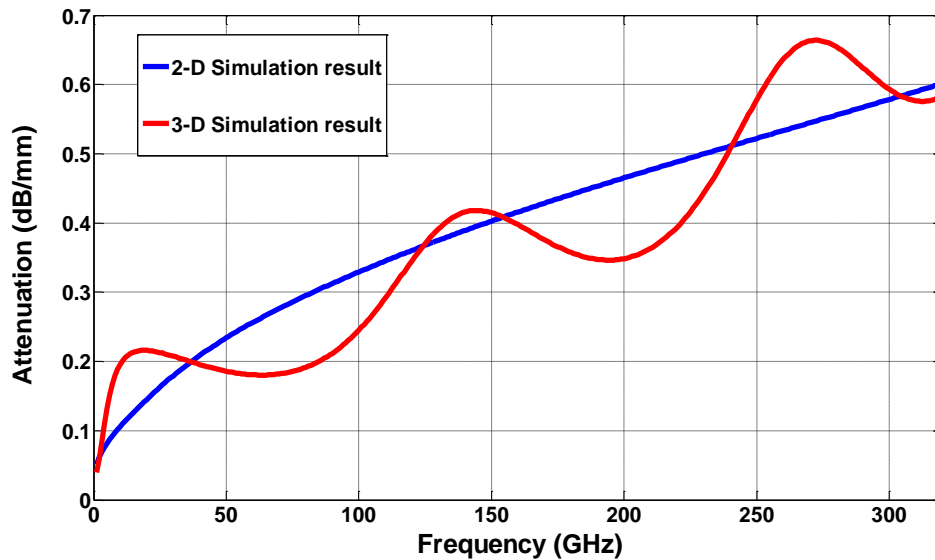


Figure 5.7: 2-D and 3-D Simulation plots of total attenuation of a 5 μm -elevated SECPW line with lateral dimension of 30 μm .

The attenuation of the line with these dimensions is similar to the ECPW line. The same discussion as for ECPW, section 4.2.6, in terms of the fabrication limitations and these small ranges of dimensions applies to the SECPW line. The only difference is the fact that, due to its structure, very small gap widths- even negative gaps- are possible for SECPW lines. This makes the low impedance/low loss transmission lines easier to achieve with SECPW lines. However, having a negative gap makes the integration of SECPW lines with other parts of the circuit (i.e. with the CPW feed of the active devices) hard to achieve. Also, the fabrication limitations still apply to the narrow signal traces. Therefore, as with the ECPW case, SECPW lines with fabricable dimensions are chosen for investigation into their high frequency performance.

5-1-3 Signal-elevated, all-elevated and conventional CPW transmission lines

A micrograph of signal-elevated CPW transmission line is shown in Figure 5.8.

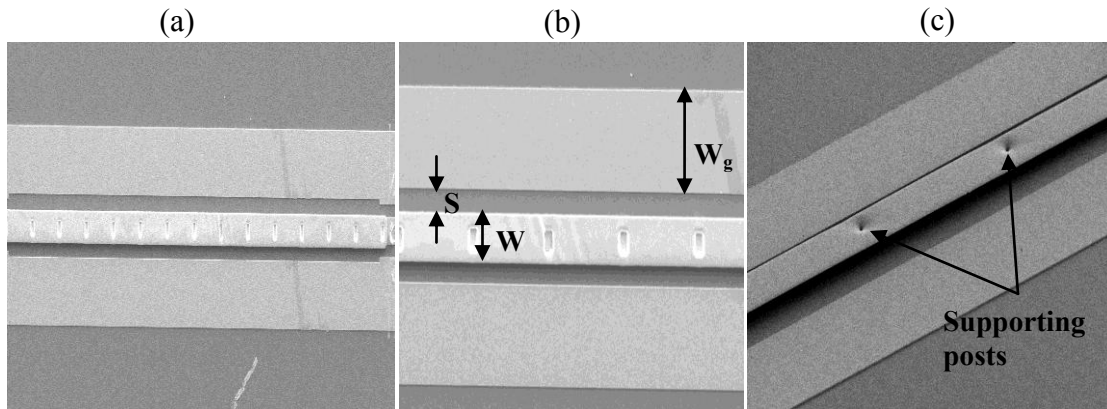


Figure 5.8: Micrograph of a signal-elevated CPW transmission line at (a) and (b) top view, (c) angled view.

In this chapter, a set of signal-elevated CPW lines with various dimensions is designed, fabricated and their high frequency performance is measured up to 320GHz for first time. Also, by developing the fabrication process, as explained in Chapter 3, structures with 13 μm elevation was fabricated. Similar to all-elevated CPW transmission lines, dimensions of the elevated parts of the fabricated line are subject to small variations due to the fabrication tolerances. Measurement results up to 320GHz for a signal-elevated transmission line are first compared with the results for the all-elevated CPW structure in Fig. 5.9. Both lines have the same design dimensions: $W=36\mu\text{m}$, $S=20\mu\text{m}$ and $W_g=90\mu\text{m}$ but their fabricated dimensions slightly differ due to the structural differences. The fabricated dimensions of the SECPW line are 17.5-41-17.5(μm) and are 15-41-15(μm) for the ECPW line. As with the ECPW lines, these initial dimensions were considered in the design of SECPW line as it was expected to give a close to 50 Ω transmission line at 6 μm elevation height.

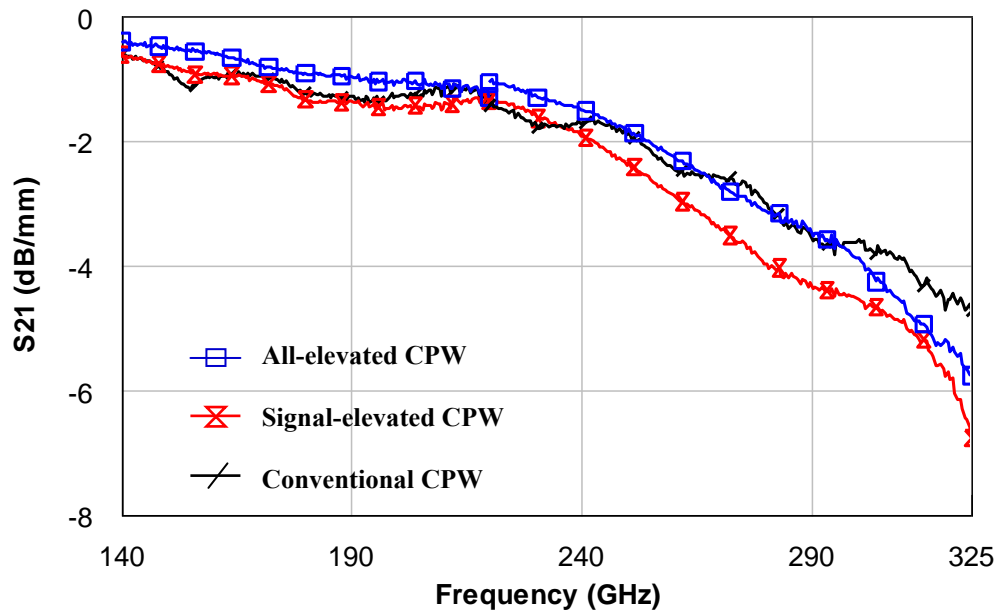


Figure 5.9: Comparison between measured S-parameters of signal-elevated, all-elevated and conventional CPW transmission lines. The elevation height for elevated structures is $6\mu\text{m}$.

The plot reveals that signal and all-elevated CPW transmission lines with similar dimensions have very similar performances up to 320GHz at an elevation of $6\mu\text{m}$.

Since the signal-elevated CPW structure has a higher effective permittivity than the all-elevated CPW line, it offers a lower characteristic impedance for identical dimensions. To eliminate the effect of the impedance discrepancy, the signal elevated CPW line is compared with the all-elevated and conventional CPW lines in terms of the loss factor, in Figure 5.10.

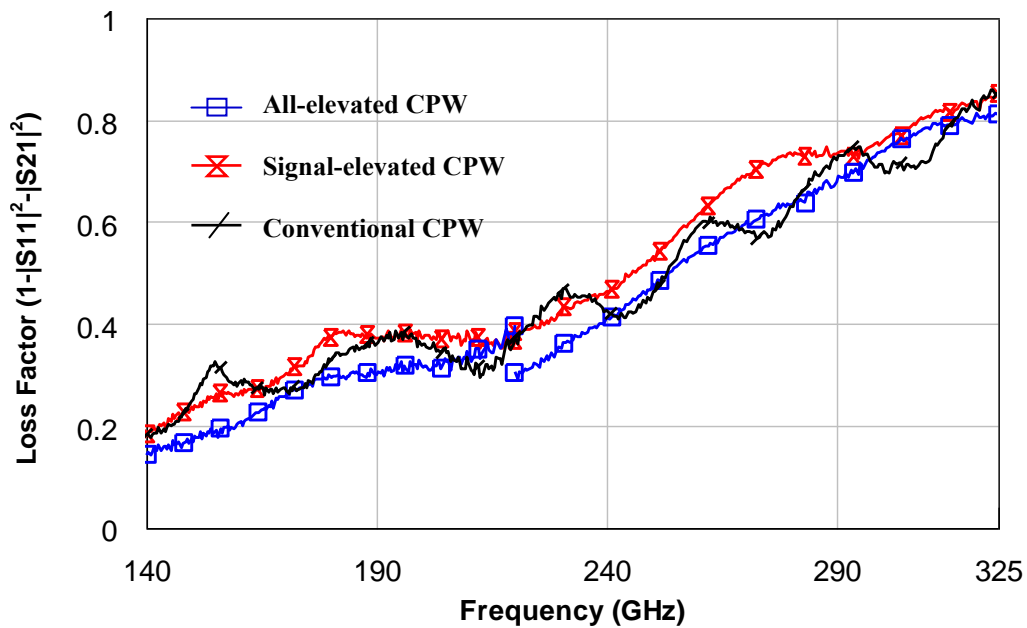


Figure 5.10: Measured loss factor of signal-elevated, all-elevated and conventional CPW transmission lines. The elevation height for elevated structures is $6\mu\text{m}$.

As can be clearly seen in above Figure, signal-elevated CPW also shows performance degradation and comparable loss factor with CPW when the frequency enters the H-band (220-320 GHz) i.e. at 320GHz, the loss factor is 0.8 for SECPW and CPW lines. Also, signal-elevated CPW shows a slightly higher, ~ 0.05 , loss factor than the all-elevated CPW structure for the whole frequency range.

Elevating all of the traces leads to slightly lower losses ($\sim 0.5\text{dB}$) than the signal elevated line but from the fabrication point of view, elevated CPW structure with just the signal line elevated is a simpler fabrication process. In general, the all-elevated line offers a lower effective dielectric constant than the signal-elevated line and can therefore support higher impedances with lower loss than the signal elevated line. However, a line of given electrical length will be longer when realised in all-elevated CPW than if it is in signal elevated line. The performance of signal-elevated, all-

elevated and conventional CPW lines are also compared in terms of loss per wavelength in Fig. 5.11.

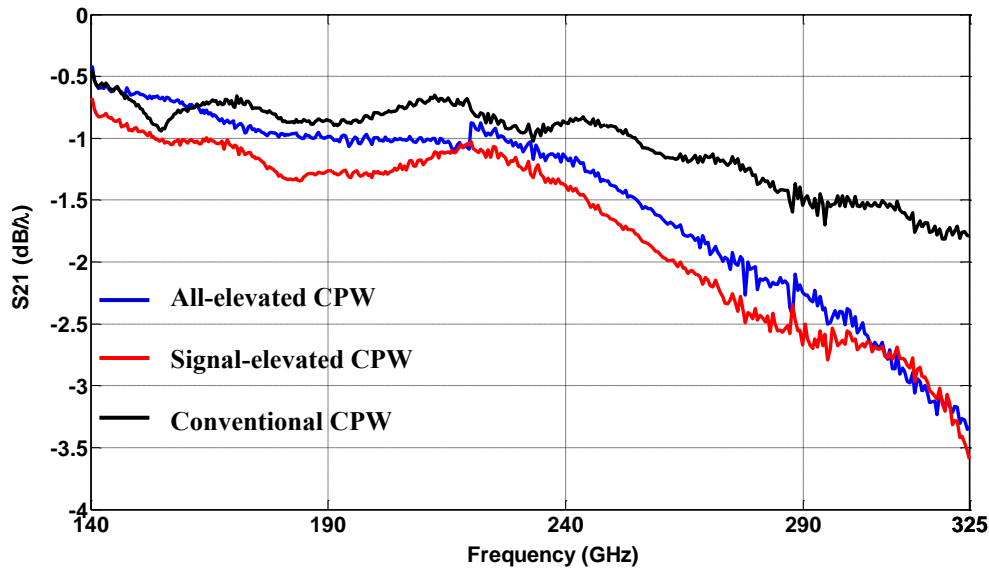


Figure 5.11: Measured insertion loss of signal-elevated, all-elevated and conventional CPW transmission lines per unit wavelength.

As can be seen in figure 5.11, due to the higher effective permittivity and shorter wavelength, CPW line has lower insertion loss per wavelength compared with signal and all-elevated CPW lines and it is recommended in applications where a fixed physical length of line is required.

5-1-4 Effect of size and distance of supporting posts

As mentioned earlier, all of the elevated CPW structures make use of supporting posts to elevate the CPW traces above the substrate. As with all-elevated CPW line, the size and number of these supporting posts has a role in determining the characteristic impedance of a signal-elevated CPW transmission line. By comparing the measurement results of otherwise identical transmission lines, where the only difference is the number

and size of the supporting posts, the effect of this element on the loss performance of signal-elevated CPW is investigated.

Figure 5.12 shows two signal-elevated CPW lines, for two different post sizes of $7\mu\text{m}$ and $14\mu\text{m}$ (in the direction of propagation) and also two different post distances of around $100\mu\text{m}$ and $210\mu\text{m}$.

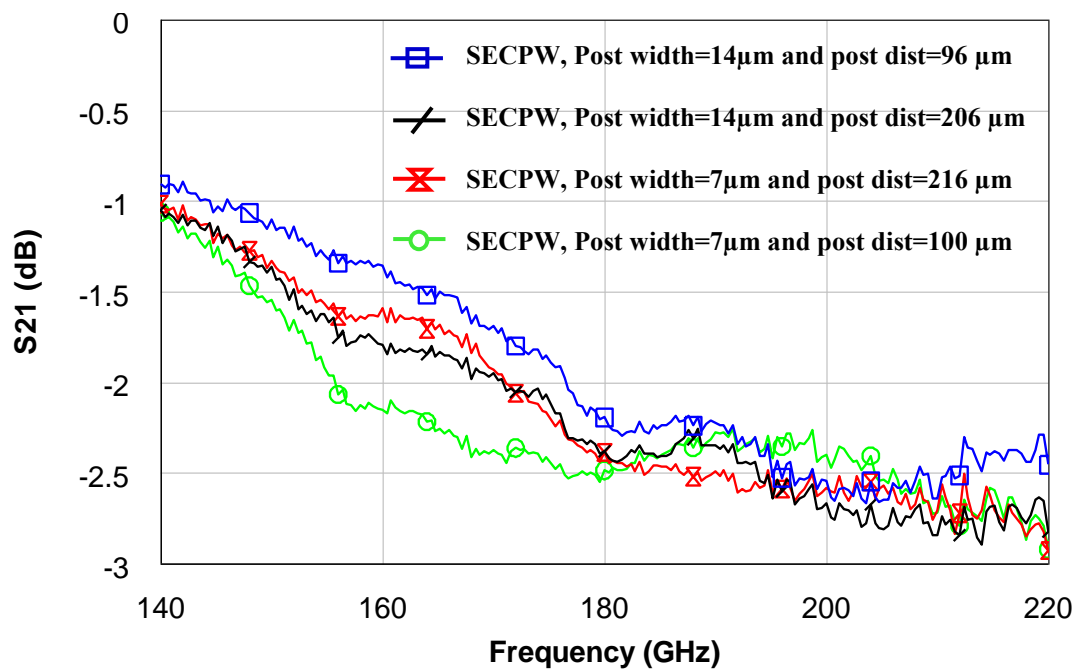


Figure 5.12: Comparison between measured insertion loss of signal-elevated CPW transmission lines with different size and distance of supporting posts at G-band(140-220 GHz).

As can be seen in Fig.5.12, similar results to those obtained as for all-elevated CPW line are obtained for signal elevated CPW transmission lines: changing the size and number of the supporting posts doesn't have a significant effect on loss. Although the size and number of the supporting posts is less critical in changing the characteristic impedance of signal elevated CPW than all-elevated CPW, the performance of the SECPW lines with different numbers of supporting post were compared in terms of loss factor up to 320GHz to eliminate the effect of impedance discrepancy.

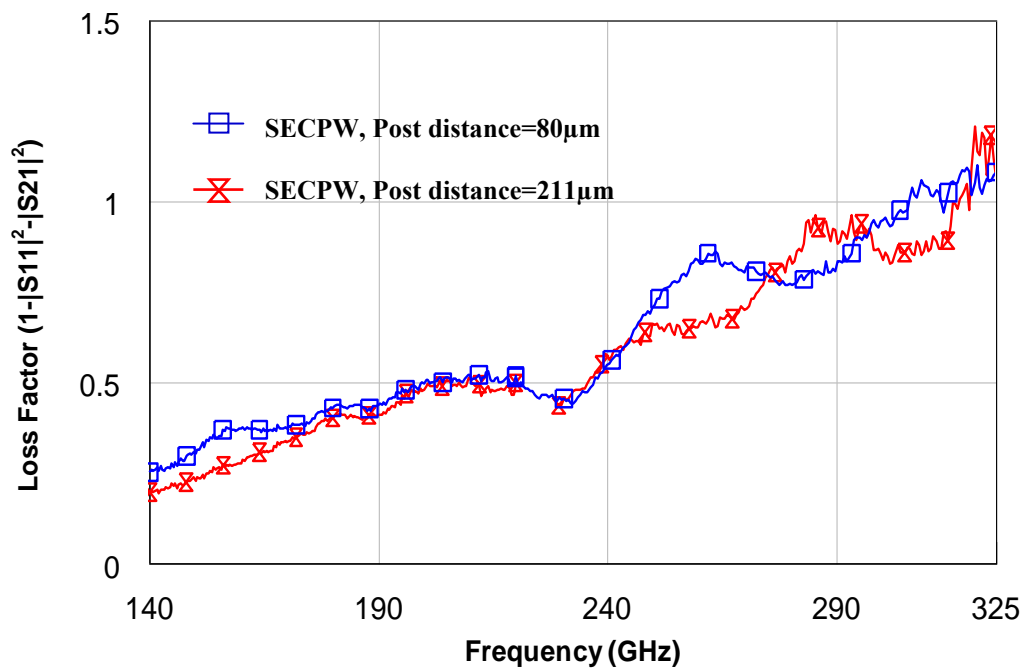


Figure 5.13: Measured loss factor of two SECPW transmission lines with different supporting post distances up to 325GHz.

As can be seen, increasing the post distance by almost three times, results in little change in loss for the signal-elevated line. The same result applies to post size.

5-1-5 Effect of elevation height

It was discussed in Chapter 4 that elevation height is a major factor in determining the characteristic impedance of all-elevated structures and small changes in elevation height (compared to the signal and gap widths) can lead to the significant changes in a line's impedance. The effect of elevation height on determining the impedance of a signal-elevated line, is there, but is not as significant as in the all-elevated CPW case. This can be seen from the analysis given in section 5-1-2 and also by looking at the return loss of the signal elevated CPW line with 6 and 13μm elevation height in Figure 5.14.

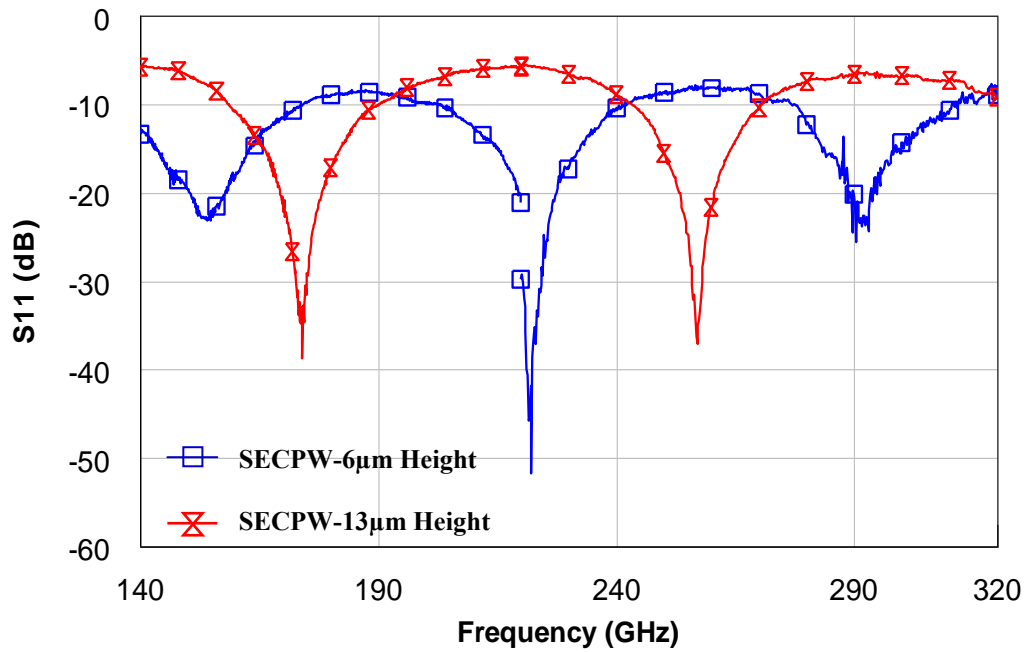


Figure 5.14: Comparison between measured reflection coefficient of SECPW transmission lines with elevation heights of 6µm and 13µm.

The line with 6µm elevation has a characteristic impedance of 51Ω and this impedance increases to 59Ω by increasing the elevation height to 13µm.

Therefore, in order to investigate the effect of elevation height on the loss behavior, the loss factor of signal-elevated CPW lines with 6 and 13µm elevations are compared in Fig.5.15.

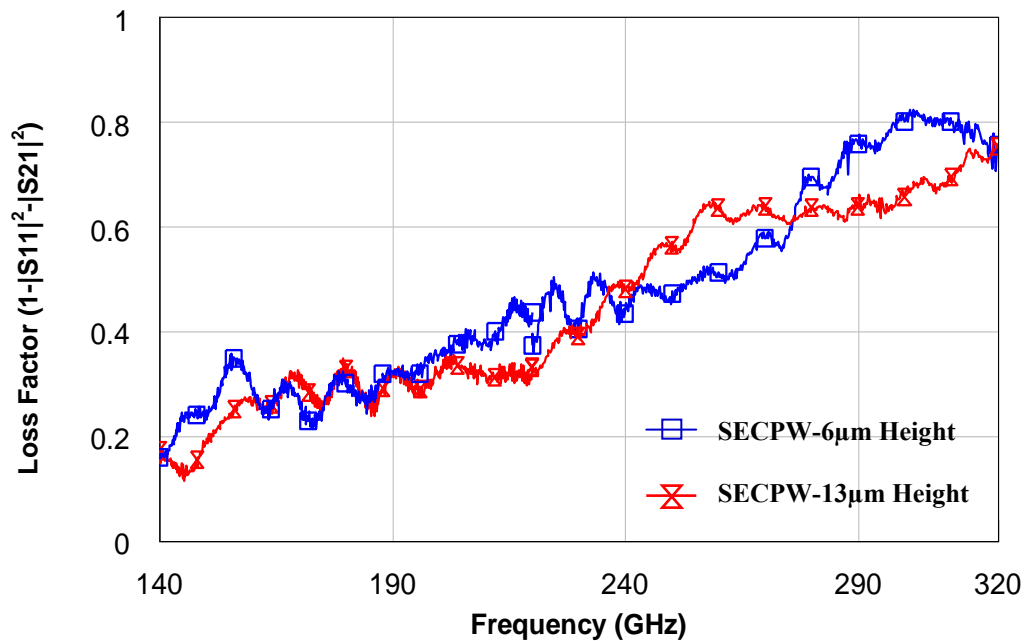


Figure 5.15: Comparison between the measured loss factor of SECPW transmission lines with elevation heights of 6µm and 13µm.

Fig.5.15 reveals that similar results can be achieved for signal-elevated CPW lines with 6 and 13µm elevation and even doubling the elevation height cannot make significant improvement in the loss performance of this transmission media. In fact, simulation results show that an elevation of around 90µm is required for SECPW structure to completely isolate the signal trace from the substrate, whilst the maximum elevation height that can be achieved in practice is approximately 13µm due to the limitations of air-bridge technology.

For further investigation, after increasing the elevation height to 13µm, the effect of supporting posts was also investigated. Figure 5.16 shows the loss factor of all-elevated CPW line with two different post distances at 13µm elevation.

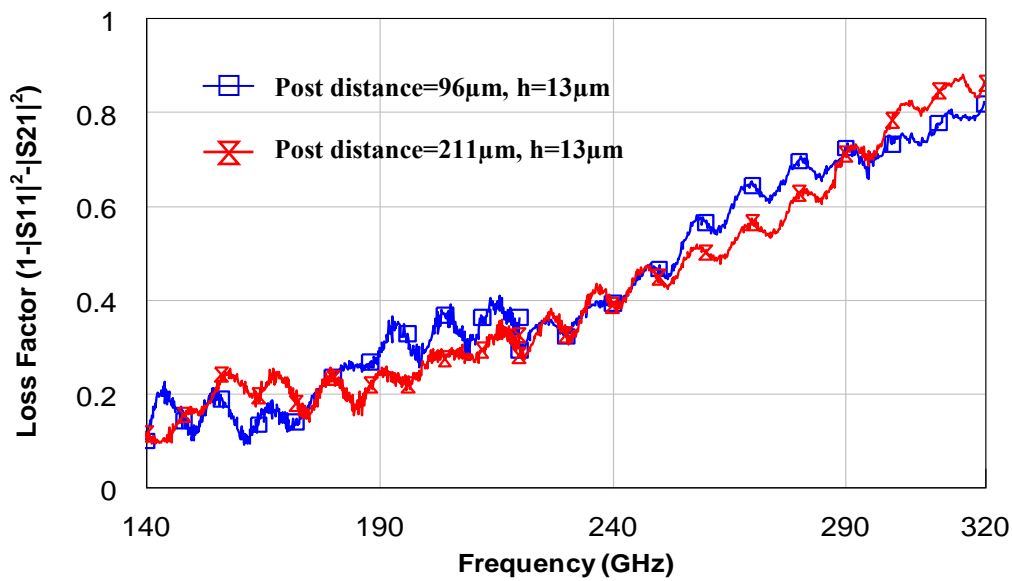


Figure 5.16: Comparison between measured loss factor of 13 μm -elevated SECPW transmission lines with different supporting post distances.

Figure 5.16 shows that at the elevation of 13 μm , almost doubling the number of supporting posts is not effecting the loss performance of the SECPW line. This is a good indication for designers that a higher density of supporting posts can be used to increase the mechanical strength of the line without introducing additional losses.

Finally, the signal-elevated CPW is compared with the all-elevated configuration at an elevation height of 13 μm and with conventional CPW line in Figure 5.17.

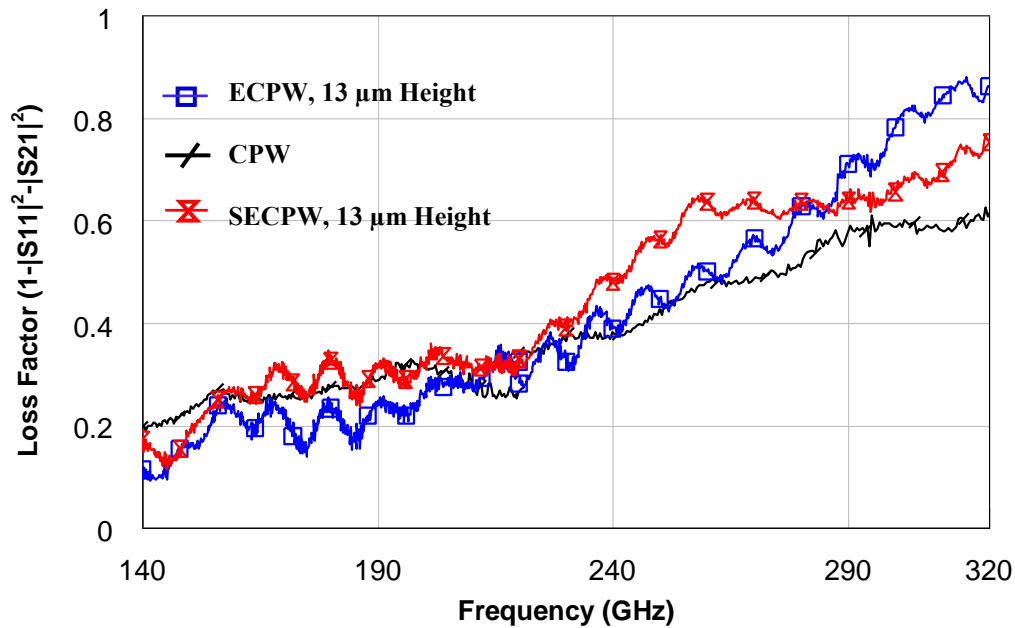


Figure 5.17: Comparison between measured loss factor of 13 μm -elevated ECPW and SECPW transmission lines with conventional CPW line.

Figures 5.10 and 5.17 show that signal-elevated CPW has slightly higher loss factors than all-elevated CPW at 6 μm elevation. When the elevation height is increased to 13 μm , it has comparable performance with the ECPW structure. This can be explained by the fact that at the elevation of 13 μm , the SECPW structure has much lower conductor loss than the ECPW structure, whilst this difference is not as pronounced in 6 μm elevation height (section 5.1.2). While the signal and ground traces in the ECPW structure are parallel – regardless of elevation height – in the SECPW structure increasing the elevation height further separates the conductor traces. As explained in 5.1.2, This reduces the conductor loss of the SECPW line by reducing the current density at the edges of signal and ground traces. This can explain why, although the SECPW line is not as isolated as ECPW from the substrate, at the elevation of 13 μm , their performance is comparable. This, and also the results in Fig.5.17, indicates that higher elevations should be used to achieve good performance for signal-elevated CPW

line. However, in general, like the all-elevated CPW structure, increasing the elevation height up to $13\mu\text{m}$ does not improve the roll-off characteristics observed in the performance of signal-elevated line.

5-2 Signal-elevated CPW (SECPW) resonators

To investigate the performance of the SECPW structure in more detail, a series of open and short-circuited SECPW stubs were designed and fabricated at different resonant frequencies in the G and H-band. The SECPW stubs are compared with their all-elevated and conventional CPW counterparts and the effect of size and distance of posts, as well as elevation height, on the stubs' performance is examined. The effective permittivity of various elevated CPW structures are extracted from the measurement of open-circuited stubs.

5-2-1 Quarter-wavelength SECPW short-circuited stub

Figure 5.18 shows the micrograph of the signal-elevated CPW short-circuited matching stub.

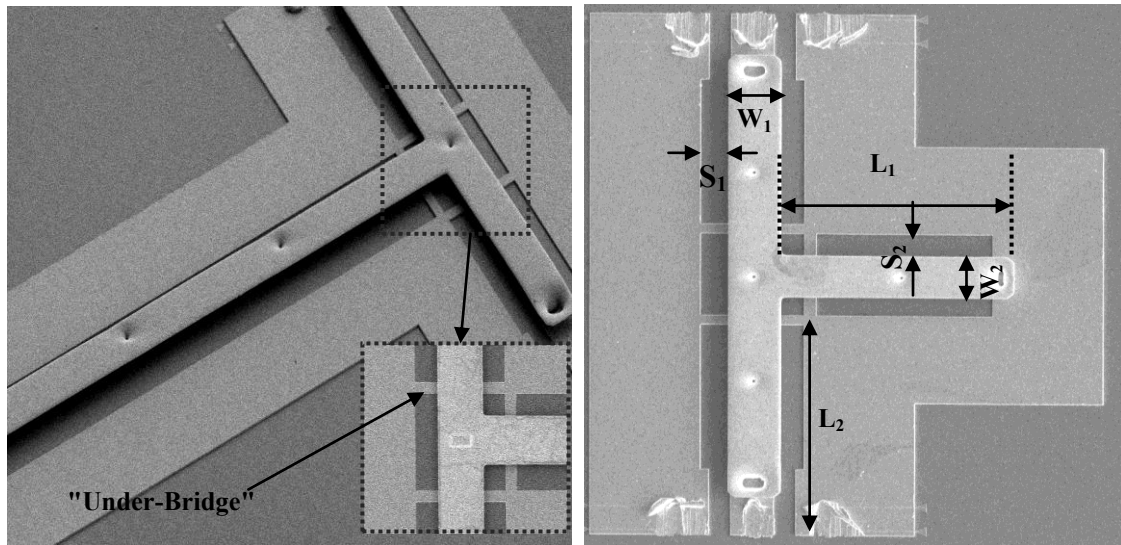


Figure 5.18: Micrograph of a short-circuited SECPW stub at (a) angled and (b) top view. The stub dimensions are $L_2=220$, $S_1=17.5$, $W_1=41$, $S_2=17.5$ and $W_2=41$. The stub length, L_1 , is 280 for stub designed for 172GHz and is 185 for stub at 240 GHz. All dimensions are in microns.

The designed short circuited stub here has dimensions of $W=36\mu\text{m}$, $S=25\mu\text{m}$ and $W_g=90\mu\text{m}$ and the final fabricated dimensions are $W=41\mu\text{m}$, $S=17.5\mu\text{m}$ and $W_g=90\mu\text{m}$. Similar to all-elevated CPW matching stubs, "underbridges" are used on the bondpad layer to suppress the slot line mode at the junctions, Figure 5.18.

Measurement and simulation results for the SECPW short circuit stubs designed for G-band and H-band are shown in following figures for first time.

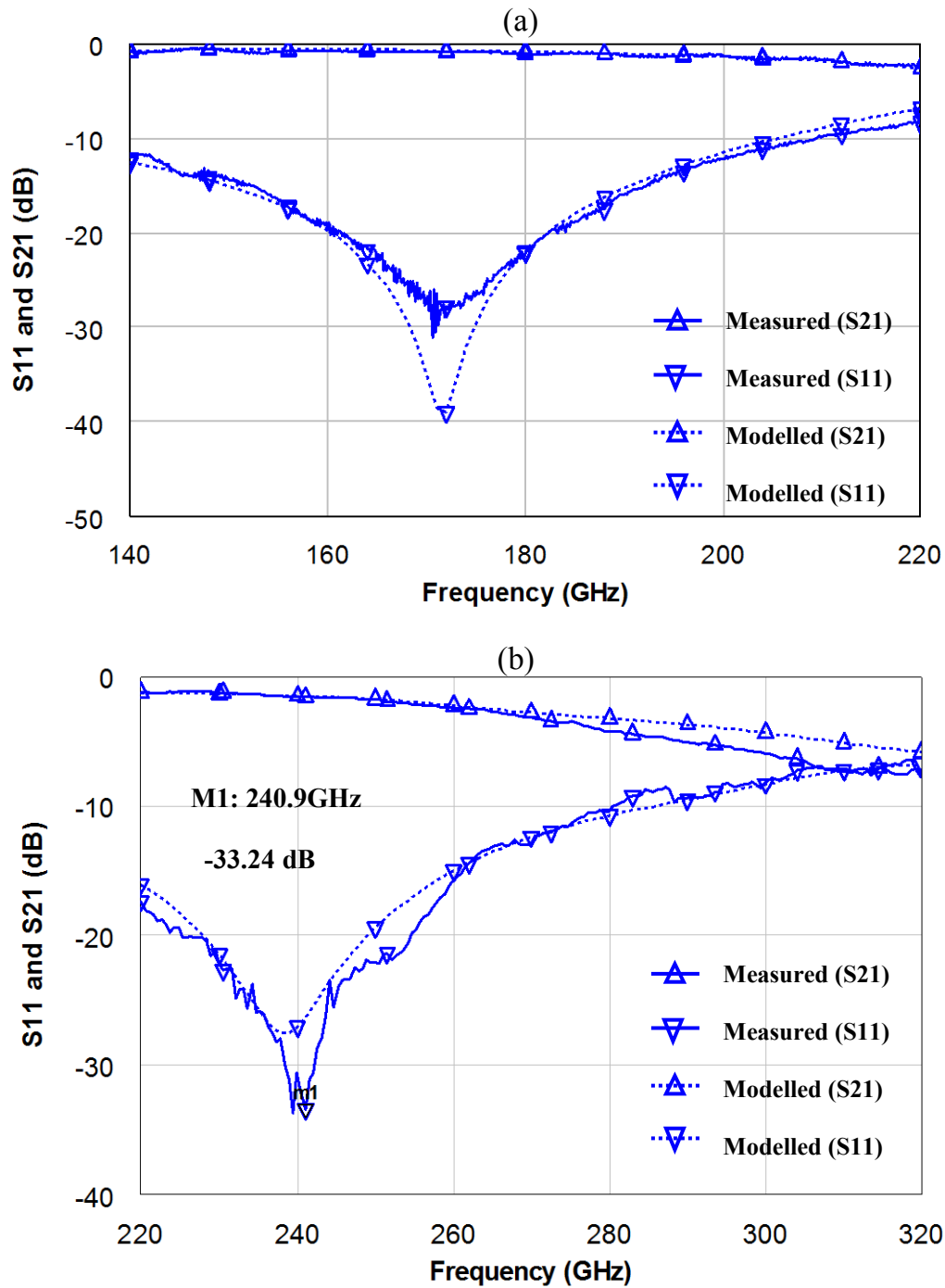


Figure 5.19: Measured and simulated S-parameters for SECPW short-end shunt stub with 6µm elevation with resonance frequency at (a)160GHz and (b)240GHz

An assumed effective permittivity of 2.26 was considered in the design equations (2.47) and (2.48) to calculate the stub-length at an elevation of 6µm. The designed stub for the G-band has a length of 278µm and a length of 184µm for the H-band. The connected feed lines have a length of 224µm. Figures 5.19(a) and (b) show the excellent

agreement between measurement and simulation results for the SECPW short-circuited stubs. The performance of SECPW short stub is compared with other structures in the following section.

5-2-1-1 Effect of different configurations

The performance of the signal-elevated CPW short circuit stub with 6 μm elevation is compared with the all-elevated and conventional CPW short circuit stubs with similar resonance frequencies.

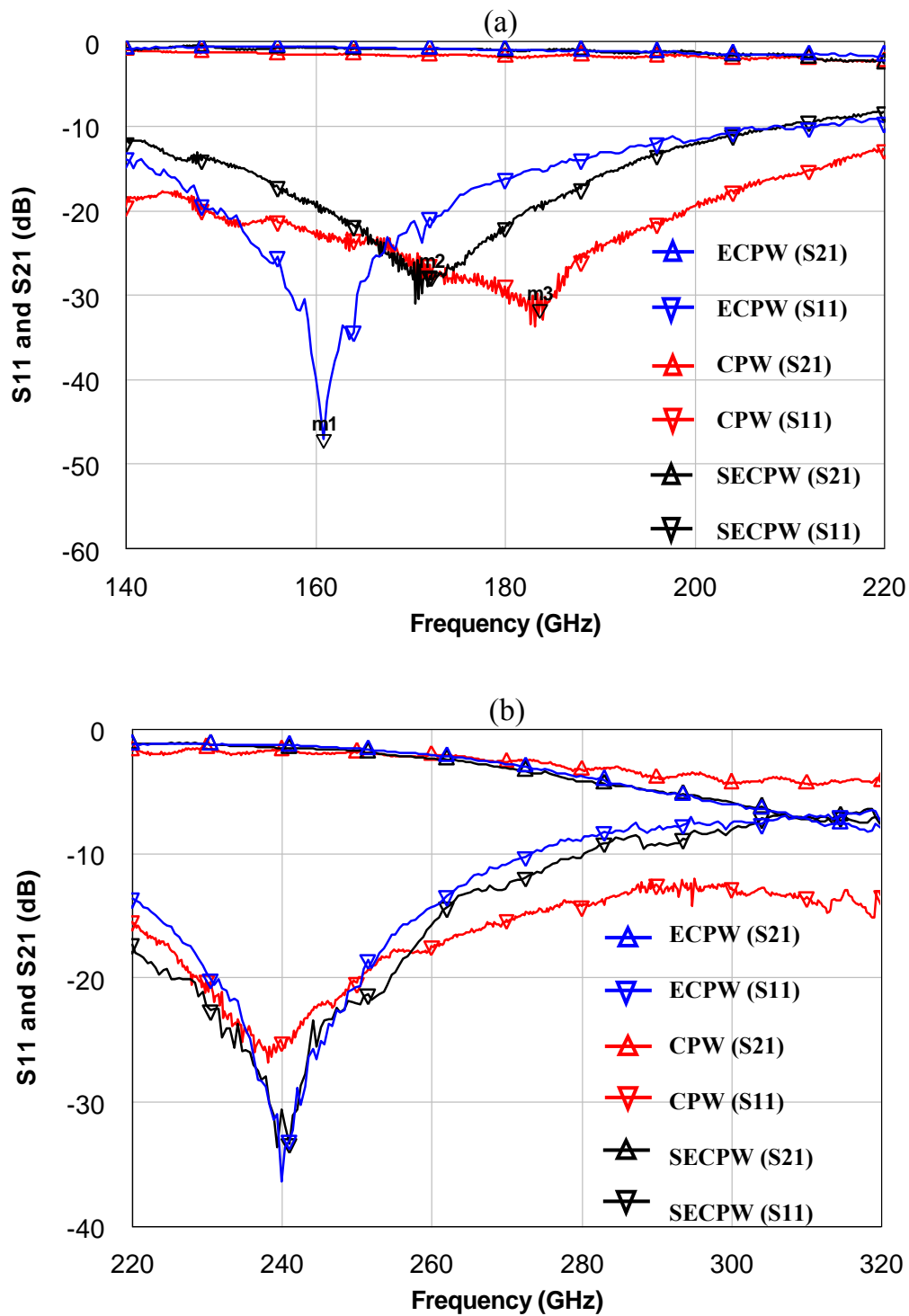


Figure 5.20: Comparison between measured S-parameters of SECPW, ECPW and conventional CPW short-circuited stubs at (a) G-band (140-220GHz) and (b) H-band (220-320GHz). The elevation height for elevated structures is $6\mu\text{m}$.

As can be seen, the short circuit matching stub using a signal-elevated CPW structure has comparable performance to the all-elevated CPW stub and better performance than

the conventional CPW structure over the whole frequency range. The signal elevated CPW short circuit stub has 0.1dB less in-band insertion loss at G-band frequency and a narrower bandwidth than the CPW short-circuit stub. At the H-band frequency range, the SECPW short-circuited stub shows 0.4dB lower loss than the CPW stub at a centre frequency of 240GHz and has a narrower bandwidth. This stub has a 3dB bandwidth of 227GHz (94%) which is by 24% narrower than the CPW short stub. Also the G-band SECPW short stub has a loaded quality factor of 1.05 and unloaded quality factor of 7.05, which shows a 27% and 39.5% improvement over Q_L and Q_u of the CPW stub, respectively. The substrate electric field plot of the SECPW short-circuited stub is compared with its CPW counterpart in Fig.5.21.

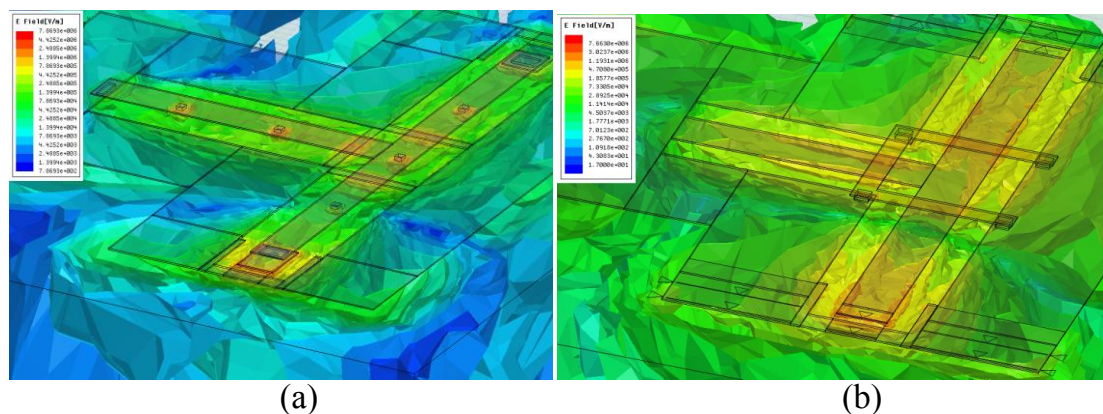


Figure 5.21: The substrate electric field plot of a short-circuited (a)SECPW, (b)CPW shunt stub at the centre frequency of 170 and 165GHz, respectively.

The electric field plot of the SECPW short-circuited stub clearly shows less penetration of the field to the substrate and higher substrate isolation compared with the CPW structure. In fact, the maximum leakage of energy to the substrate for SECPW structure is through the supporting posts, which are in a direct contact with the substrate. This higher substrate- isolation explains the improved performance of SECPW short-circuited stub over its CPW counterpart.

5-2-1-3 Effect of elevation height

To investigate the effect of elevation height on the performance of signal-elevated CPW short circuit stubs, the elevation height was increased to $13\mu\text{m}$ and the stub length was increased to $830\mu\text{m}$ to achieve a similar resonant frequency. A comparison between SECPW short circuit stubs with 6 and $13\mu\text{m}$ elevation is shown in Figure 5.22.

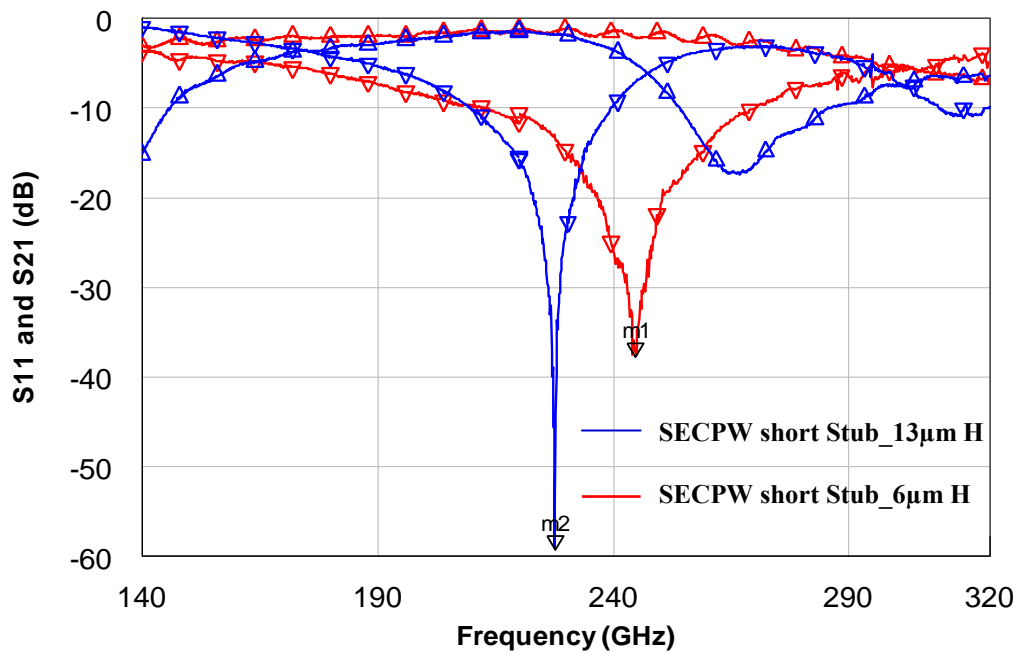


Figure 5.22: Comparison between measured S-parameters of SECPW short-end stubs with $6\mu\text{m}$ and $13\mu\text{m}$ elevations. (m1: $-36.77\text{dB}@242\text{GHz}$, m2: $-58.22\text{dB}@227.5\text{GHz}$)

These results reveal that, for optimum performance, the signal elevated short circuit stub should use a high elevation (e.g. $13\mu\text{m}$) for signal trace. Increasing the elevation height of this particular signal elevated stub from 6 to $13\mu\text{m}$ improves the bandwidth performance of the stub significantly (from 227GHz to 76GHz). Also the loaded quality factor of the stub increases from 1.05 to 3.1 and the unloaded quality factor raises from 7.053 to 17.83 . This stub shows superior performance compared with the CPW short-circuited stub by an 85% decrease in bandwidth and $73\text{-}76\%$ improvement in quality

factor. This performance improvement can be explained by the higher isolation of the signal trace from the substrate and the resulting reduced substrate effect.

In order to observe the effect of different elevated configurations, the results of the 13 μm height signal-elevated CPW short circuit stub is compared with the all-elevated counterpart in Figure 5.23.

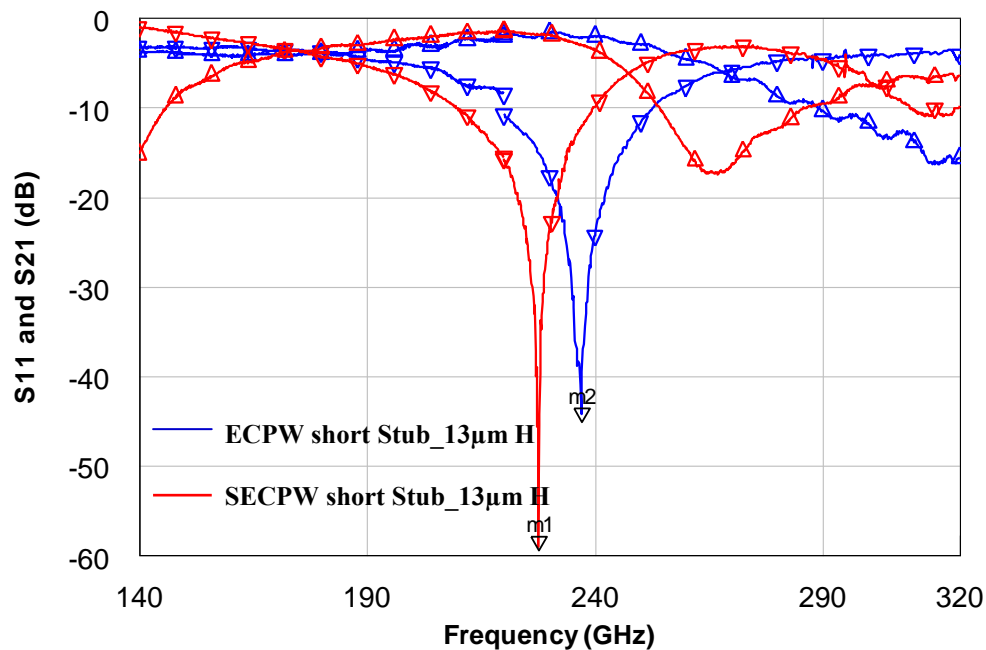


Figure 5.23: Comparison between measured S-parameters of SECPW and ECPW short-end stubs with 13 μm elevations. (m2: -58.22dB@ 227.5GHz, m2: -44.04dB@237GHz)

Comparing all-elevated and signal-elevated CPW short circuit stubs with 13 μm elevation height, shows that similar performance in terms of bandwidth can be achieved. Considering the greater fabrication complexity and variability of the all elevated CPW, signal elevated CPW is the preferred transmission line structure for high millimeter wave frequency regimes.

5-2-1-4 Effect of Size, Number and Distance of Supporting Posts

It was shown in Chapter 4 that the size and number of supporting posts plays an important role in determining the performance of the all-elevated matching stubs. The

same experiment is now done to investigate the effect of supporting posts on the performance of signal-elevated short circuit stubs.

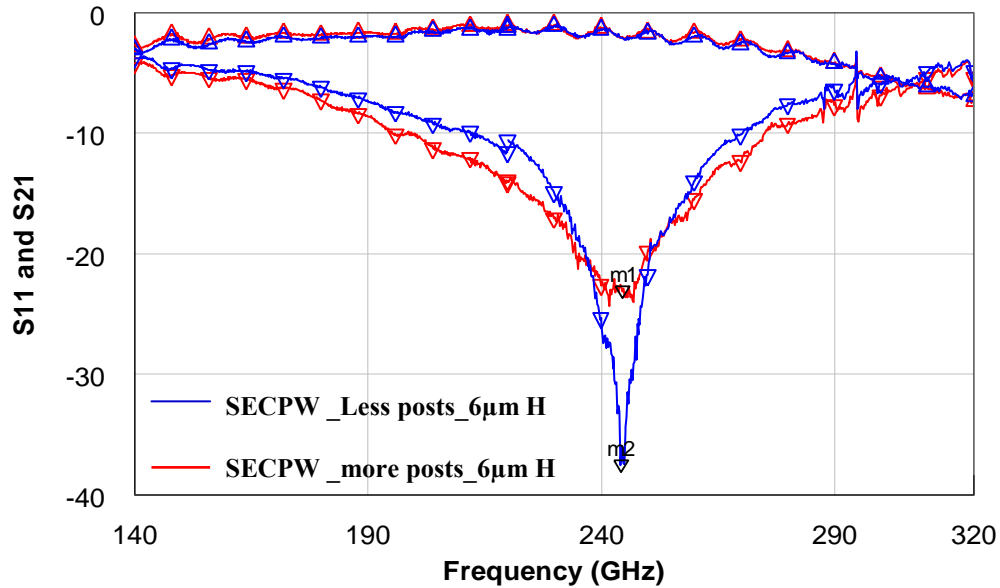


Figure 5.24: Comparison between measures S-parameters of $6\mu\text{m}$ -elevated SECPW short-circuited stubs with different number of supporting posts. (m1: -23.05dB , m2: -37.46dB)

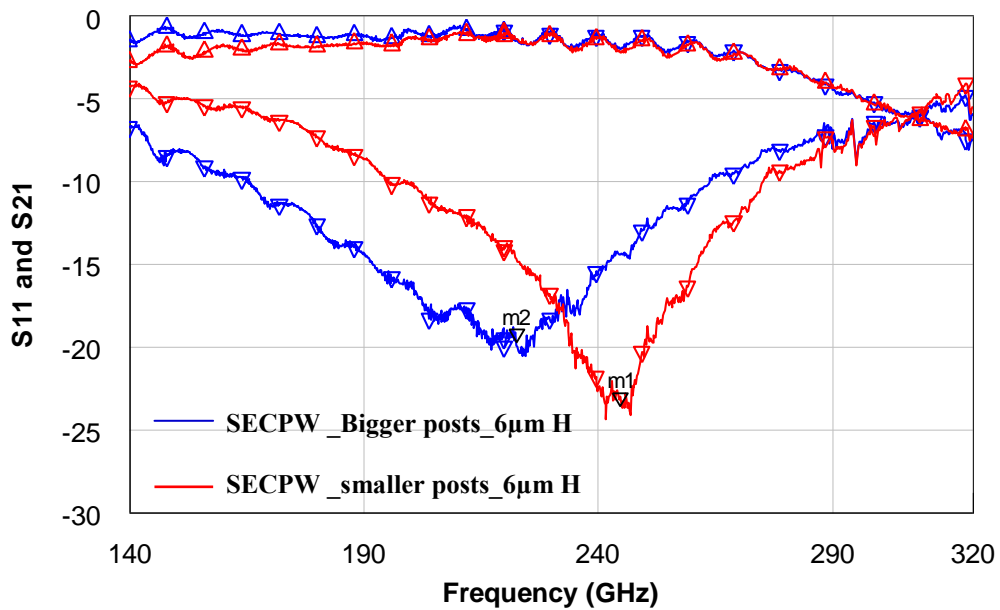


Figure 5.25: Comparison between measures S-parameters of $6\mu\text{m}$ -elevated SECPW short-circuited stubs with different size of supporting posts. (m1: -23.05dB , m2: -19.9dB)

Similar to the all-elevated CPW short circuit stubs, performance improvement can be achieved for the $6\mu\text{m}$ signal-elevated CPW short circuit stub by keeping the elevation height constant and reducing the number and size of the supporting posts.

A detailed investigation into the performance of signal-elevated CPW stubs shows that comparable results to the all-elevated stubs can be achieved, especially at higher elevations (e.g. $13\mu\text{m}$). Due to the simpler elevated structure, the signal-elevated CPW is less subject to fabrication errors and is therefore the preferred structure. Also, it is shown that increasing the elevation height is not the only way of improving the performance of SECPW short circuit stubs. By proper design in terms of line geometry, post size and number of and distance between posts, one can achieve a high performance and narrow bandwidth short circuit stub with relatively low elevation. Compared with high elevations, lower elevations are advantageous in terms of yield, fabrication complexity and mechanical strength.

5-2-2 Quarter-wavelength SECPW open-circuited stub

Figure 5.26 shows the micrograph of the open circuit matching stubs using a signal-elevated CPW structure.

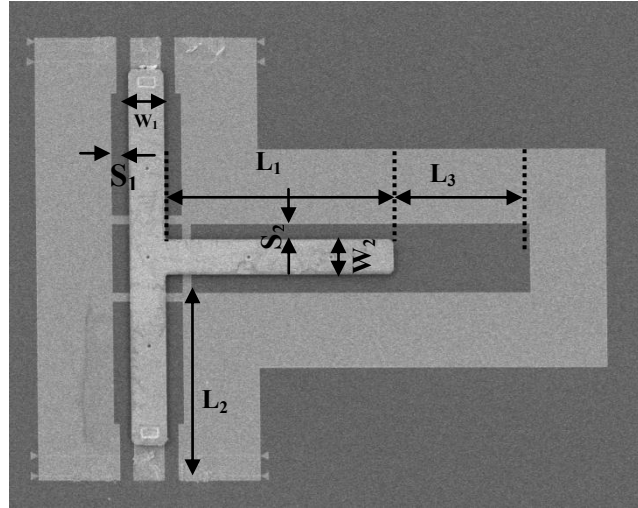


Figure 5.26: Micrograph of a open-circuited SECPW shunt stub. The stub dimensions are $L_2=220$, $L_3=150$, $S_1=17.5$, $W_1=41$, $S_2=17.5$ and $W_2=41$. The stub length, L_1 , is 280 for stub designed for 172GHz and is 185 for stub at 240 GHz. All dimensions are in microns.

The same dimensions as used for the short circuit stubs (see §5-2-1), are considered for the design of the open circuit stubs. The end gap was designed to be more than $[2 \times (W + 2S)]$ in order to minimize the end-effect [124]. Figure 5.27 shows the simulation and measurement results for an open circuit stub using the signal-elevated CPW structure at a resonant frequency of 152GHz. The measurement results are in very good agreement with simulation.

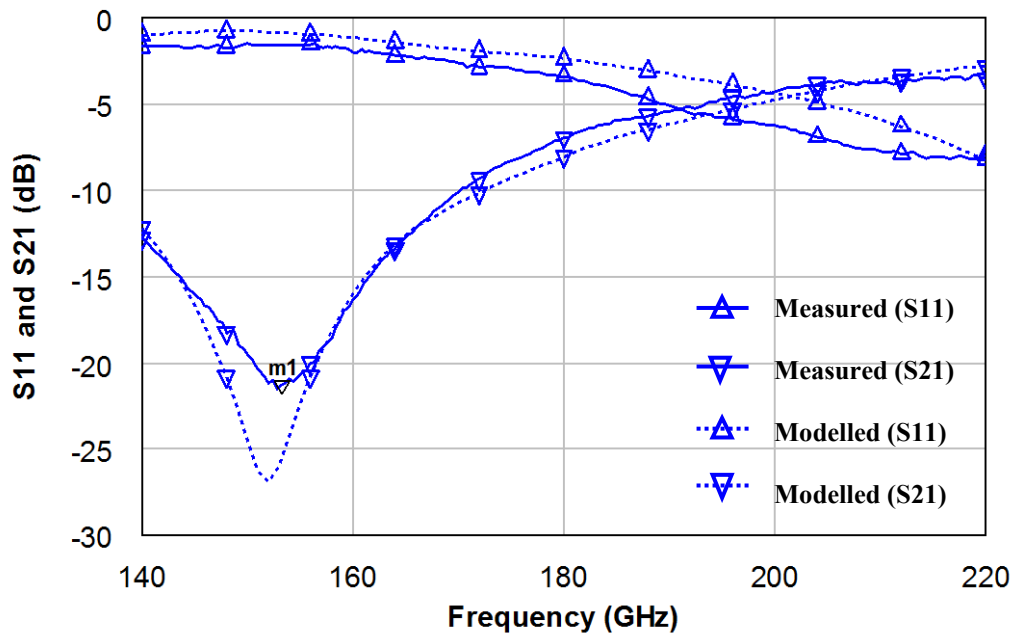


Figure 5.27: Measured and simulated S-parameters for SECPW open-end shunt stub with 6 μ m elevation.

This G-band SECPW open stub has a 3dB fractional bandwidth of 46% , loaded quality factor of 2.1 and unloaded quality factor of 12.48.

5-2-2-1 Effect of different configuration

The SECPW open stub is compared with conventional CPW and all-elevated open stubs in this section. To investigate the effect of elevating the signal trace 6 μ m above the substrate, the SECPW open stub is first compared with its conventional CPW counterpart in Figure 5.28.

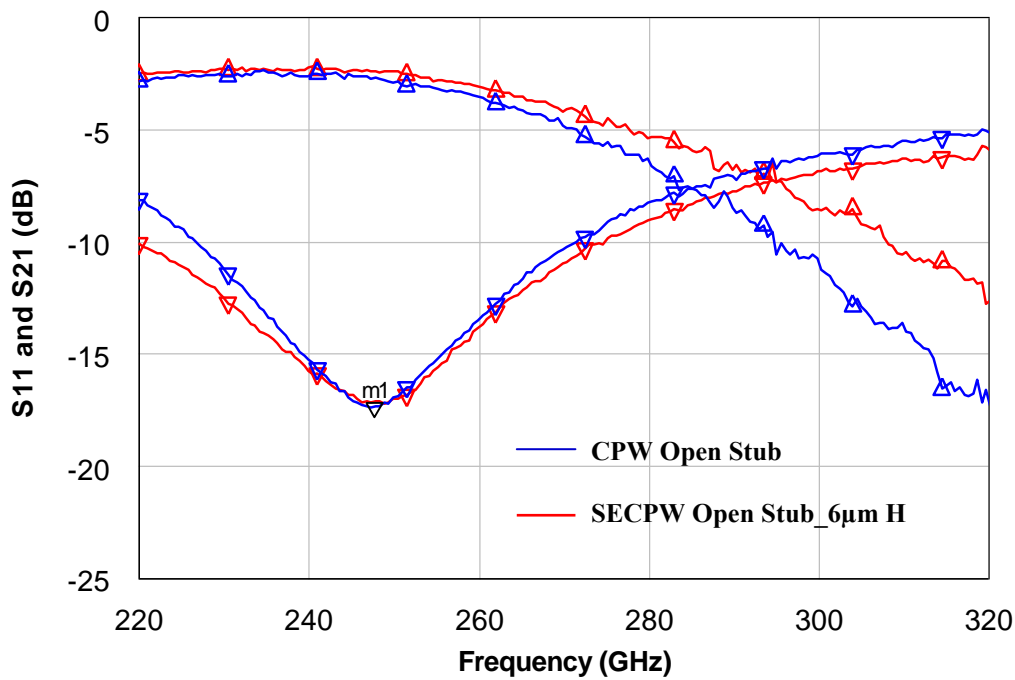


Figure 5.28: Comparison between measured S-parameters for 6 μ m-elevated SECPW and conventional CPW open-end shunt stubs

It can be seen that no significant improvement can be obtained by using signal-elevated structure over conventional CPW structure. However, compared with the CPW open circuited stub, the SECPW open stub still shows 8% less fractional bandwidth and an improvement in the loaded and unloaded quality factor of 19% and 35.2%, respectively.

In this particular example, all of the CPW and SECPW lines are 50 Ω and, as discussed earlier, high impedance transmission lines should be used in the stubs to improve the Q-factor of the open stub. Further improvement in the bandwidth of the open stub can be achieved by using low impedance feed lines. This is shown in Figure 5.29.

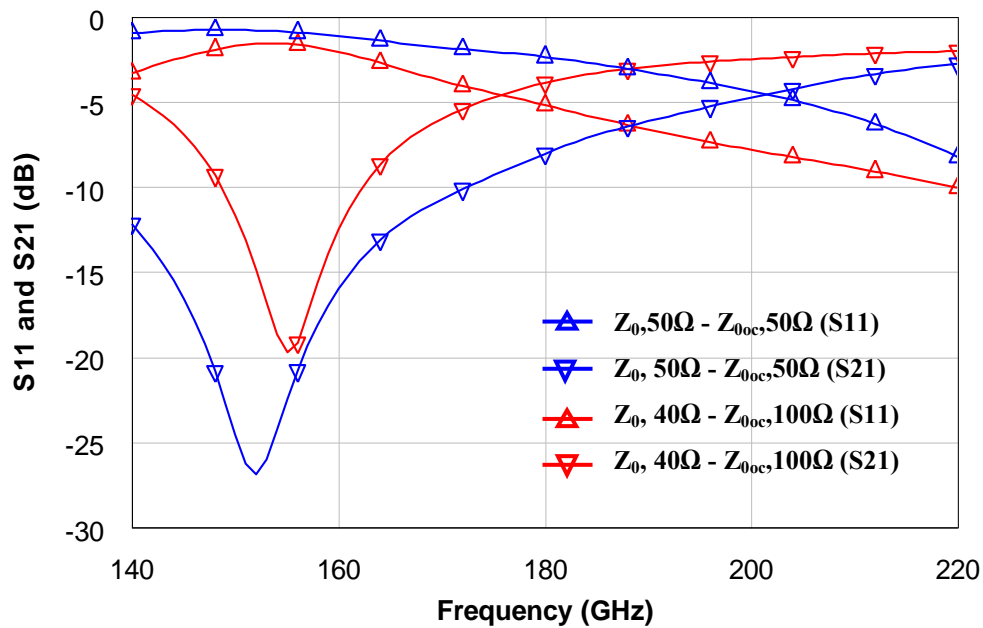


Figure 5.29: Comparison between simulated S-parameters for SECPW open-circuited stubs implemented with all 50 Ω lines and various impedance lines. (Low impedance feeds and high impedance stubs)

However, it can be seen that the narrower bandwidth is at the expense of increased in-band return loss (0.7dB in this example). Still, compared with a CPW stub using the same characteristic impedances, the SECPW open stub exhibits superior performance.

To compare the performance of open-circuited stubs with different elevated configurations, the performance of the SECPW open stub is compared with the all-elevated CPW open stub with 6 μm elevation in Figure 5.30.

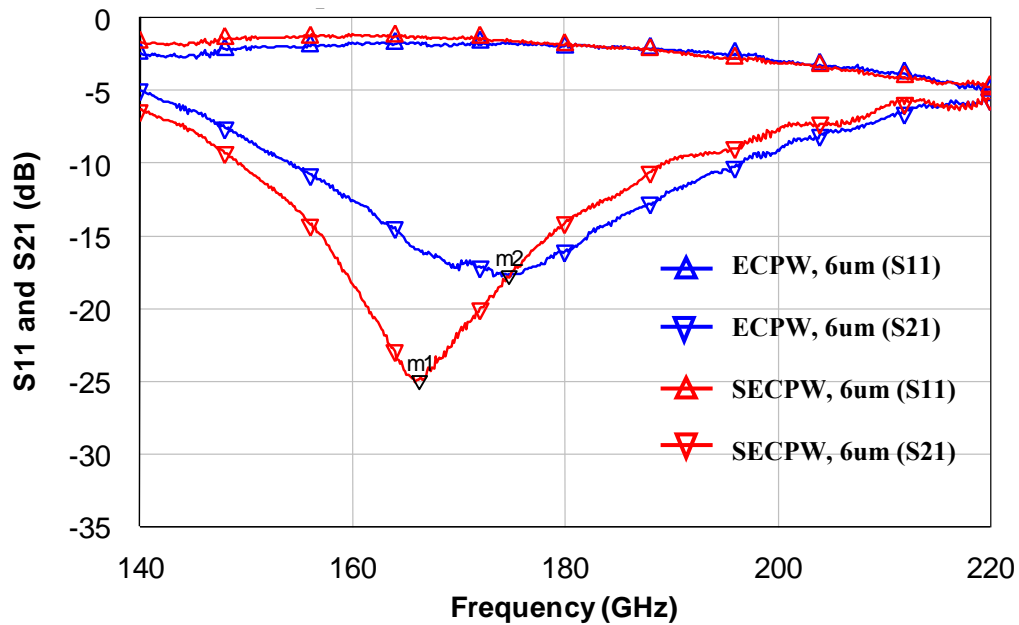


Figure 5.30: Comparison between measured S-parameters for 6µm-elevated SECPW and ECPW open-end shunt stubs. (m1: -24.96dB @166.16GHz, m2: -17.72dB @ 176.4 GHz)

This Figure shows that slightly better performance for the open stub using signal-elevated CPW is achieved than the all-elevated stub with similar dimensions. These results are prior to any optimisation of the open-circuit stubs. Figure 5.31 compares the performance of the open-circuited stubs with CPW, ECPW and SECPW all applied with the same high impedance stubs and low impedance feeds.

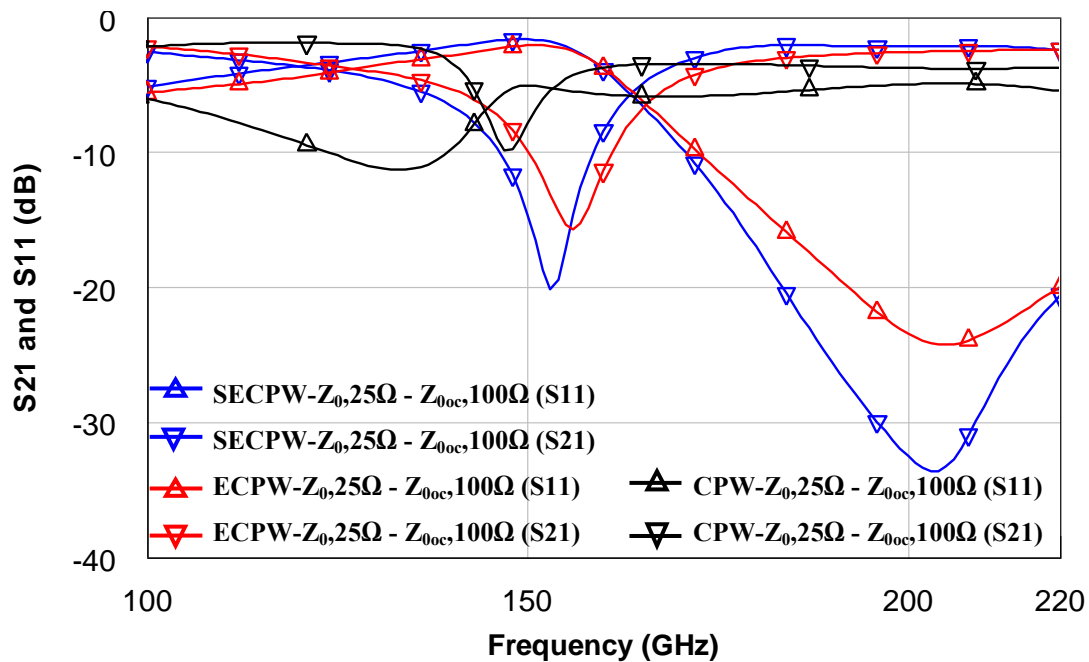


Figure 5.31: Comparison between simulated S-parameters for SECPW, ECPW and CPW open-circuited stubs implied with various impedance lines (Low impedance feeds and high impedance stubs)

In the above Figure, all of the open-circuited stubs with different structures are implemented by considering 25Ω impedance at feed lines and 100Ω impedance at the stub. It can be seen that the SECPW open stub shows slightly better performance than the ECPW open with the same impedances. The bandwidth in both cases is similar but the SECPW open shows 0.4dB less loss at the centre frequency. Both SECPW and ECPW open stubs show superior performance to the CPW open stub implemented with the same impedances.

Besides the advantages in the use of elevated CPW structures in implementing open-circuited stubs over CPW structures, measurements of these structures provides useful data on the electrical characteristics of the transmission media and provides greater insight into the behaviour of the short circuit stubs. Basic transmission line theory indicates that the resonant frequency of an open circuit is dictated by the electrical

length of the stub and the end effect capacitance only and not on the feed length. In table 5.1 we infer the effective dielectric constant of various signal and all elevated structures. These results were obtained by optically measuring the dimensions of each stub, removing the effect of the effective length extension obtained from the equations in (2.49) and then calculating the effective dielectric constant from the resonance frequency.

Table 5.1: Table showing the extracted effective permittivities for various signal and all-elevated open circuit resonators. The CPW ground width is $100\mu\text{m}$.

No	Line	Elevation (μm)	Post Size (μm)	No. of stub posts	L (μm)	ϵ_{eff}	W (μm)	S (μm)
1	SECPW	6	21x12	1	262.2	2.8	46.5	23.3
2	SECPW	13	3.3x3.3	2	278	1.60547	47.5	18.8
3	SECPW	6	19x13.7	2	264.4	2.9855	46.67	19
4	ECPW	6	23x12.4	1	278	2.512	45.3	19.5
5	ECPW	13	22x13	1	272.2	2.111	51	16.67
6	ECPW	13	17.7x10	2	276.7	1.96837	49.78	19
7	CPW	-	-	-	180	6.945	36	25

It can be seen that the lowest effective dielectric constant is achieved by the signal elevated CPW line with fewest posts and an elevation of $13\mu\text{m}$ (row 2). However, for a set geometry, an all elevated line yields a slightly lower effective permittivity than does a signal elevated line. It can also be seen (i.e. from rows 5 and 6) that a greater number of posts and larger post size can significantly increase the effective dielectric constant of an elevated line. We can also see (from rows 4 and 5) that, for a more or less fixed

geometry, increasing the elevation height can greatly decrease the effective dielectric constant. Comparison of the last row and any of the other rows gives an indication of the reduction in effective dielectric constant possible when the CPW traces are elevated above the substrate.

5-3 Summary

Another configuration of elevated CPW line, achieved by elevating only the signal trace above the substrate (SECPW), was investigated in this chapter, considering both its low and high frequency performance. The characteristic impedances of SECPW lines (extracted from 2-D simulations) are slightly lower than for the comparable ECPW lines considered in Chapter4. In general, lower impedances are more easily implemented using SECPW than with ECPW due to the easier fabrication of small gaps. Due to the lower substrate isolation of SECPW, its effective permittivity is slightly (around 0.5) higher than ECPW.

A loss analysis of SECPW lines was performed by 2-D and 3-D simulation. The static results shows that, depending on the lateral dimensions of the line, SECPW has 2-4 times less conductor loss and 4-30 times less substrate loss than conventional CPW transmission lines. However, the results from the 3-D simulations shows that, as with CPW and ECPW structures, the attenuation of the SECPW structure increases significantly at higher frequencies, i.e to around 8dB at 320GHz for the line with 120 μ m lateral dimension. In fact, comparing the 2-D and 3-D simulation results reveals that radiation starts earlier in frequency than the CPW and ECPW lines and continues with frequency. For a similar geometry, the attenuation of the SECPW line without

supporting posts or CPW/SECPW transitions at 300GHz is by 1dB more than for ECPW but still less than for CPW. Similarly to the CPW and ECPW lines, the total radiation of SECPW line decreases as its lateral dimensions are reduced. For example, by reducing the lateral dimension of SECPW line from 120 μ m to 30 μ m, the loss reduces from 8 to 0.6dB at 320GHz. Compared with ECPW structures, smaller lateral dimensions are easier to achieve in SECPW lines due to it being easier to fabricate smaller gaps.

The measurement results, up to 320GHz, on fabricated SECPW lines with around 55 Ω impedance were presented. It was observed that no significant improvement could be achieved by using SECPW instead of CPW at mid-range impedances. SECPW still suffers from the high amounts of radiation (6dB/mm at 320GHz) due to non-complete isolation of the CPW traces from the substrate. An investigation into the effect of size and number of supporting posts as well as the elevation height shows that no particular change in the roll-off characteristics of the SECPW line can be achieved by using higher elevations and/or lower number and size of supporting posts.

Short-circuited quarter-wavelength matching stubs implemented using signal elevated CPW has also been presented in this chapter. Signal-elevated CPW short circuit stubs show better performance with 24% lower fractional bandwidth and 27% and 39.5% improvement in loaded and unloaded quality factors than CPW counterparts. However, to obtain the maximum advantage for short circuit stubs, elevations as high as 13 μ m should be used. For example, by increasing the elevation height from 6 to 13 μ m, a reduction of 1dB in the centre frequency insertion loss and a reduction of 85% in fractional bandwidth and improvement in quality factor by 73-76% can be achieved for

SECPW short circuit stub compared with CPW equivalents. On the other hand, by comparing different SECPW short circuit stubs with the only difference being in the number and size of posts, the significant effect of these supporting posts became clear and it is found that by keeping the size and number of posts minimum, one can improve the performance of SECPW short stub even at lower elevations. This is an important fact as lower elevations are advantageous in terms of yield and mechanical strength compared with the higher elevations.

The open circuited stubs using the SECPW structure at different elevations is also presented. As with the all-elevated CPW the main advantage of the SECPW structure becomes clearer in achieving high-Q passive networks when high and low impedances with low loss are required.

Chapter 6

Elevated-Grounded Coplanar Waveguide Structures

6-1 Introduction to elevated-grounded CPW structure

As observed in the preceding chapters, achieving a low-loss, MMIC compatible, transmission line can be a challenge at sub-millimetre wave frequencies. In Chapter 2, we investigated the performance of the most popular transmission line, CPW, at frequencies up to 320GHz. We observed problems with the CPW structure in its implementation of basic circuits at mm-wave frequencies, such as the short circuited stub which can exhibit ill-defined reflection coefficient curves, and also with band-pass filters which show high insertion loss and wide bandwidth - possibly due to the generation of surface waves. These problems are compounded by high insertion losses at frequencies above 200GHz and the related difficulty of achieving wide impedance ranges for transmission lines. Elevated CPW, which first was proposed as a means to overcome the problem of implementing high impedance CPW transmission lines [93]-[95], was chosen for further investigation due to its potential to provide a surface wave free transmission line. The behaviour of different elevated CPW structures was

investigated in Chapters 4 and 5. A low dielectric constant and partial isolation from the semiconducting substrate can be achieved using ECPW and SECPW. However, the performance of ECPW and SECPW lines was observed to degrade rapidly at frequencies above approximately 240GHz (depending on the lateral dimensions), possibly due to non-complete isolation of the CPW traces from the substrate as we noted considerable penetration of the substrate by the electric field. To overcome this problem, a new variant of elevated CPW (referred to as EGCPW) is presented for the first time [142]. In this novel structure, a ground plane is placed on top of the substrate to provide near-complete isolation of the elevated CPW traces from the substrate. Electrical isolation of the signal trace from the bottom ground is achieved by the use of supporting posts in physical contact with the substrate via exposed rectangular areas in the lower ground plane (bond pad) layer. In fact, these are the only areas in which the line has direct physical contact with the substrate and in which dielectric loss is likely to be significant. This new structure provides a transmission line with much reduced dielectric loss and with very low loss per unit length in the 0 to 320GHz frequency range.

This chapter first presents, in section 1, an approximate synthesis technique for the elevated grounded CPW (EGCPW) portion of the line by building on previously established conformal mapping results. Also a new analysis for the post sections of this structure is presented based on conformal mapping techniques. The feed/post/line combinations in real EGCPW structures can be approximated as cascaded transmission lines with different characteristic impedances and effective dielectric constants [137]. The 2nd section investigates the losses in EGCPW structures via sets of 2-D and 3-D simulations and compares them with conventional and previously discussed elevated

CPW structures. In the third section, we present measured and simulated data for the typical insertion losses exhibited by the new structure and, for comparison purposes, the losses associated with CPW. The chapter continues, in section 4, with the measured and modelled performance of several EGCPW circuit components i.e. short and open-circuited quarter-wavelength resonators. In section 5, band-pass and band-stop filters making use of the novel elevated grounded CPW structure are presented. All of these components are designed and fabricated with both $6\mu\text{m}$ and $13\mu\text{m}$ elevation heights and a comparison is given for each component in order to illustrate the effect of elevation height. CPW counterparts of all the circuits are also measured and their performance compared with that of the circuits implemented using the new transmission line topology. To our knowledge, this is the first time that elevated-grounded CPW is introduced and the first time that detailed design, analysis, modelling, fabrication and measurement up to 320GHz has been carried out for this structure.

6-2 Elevated-grounded CPW (EGCPW) analysis

6-2-1 The structure of elevated-grounded CPW

Figure 6.1 shows an example of an elevated grounded CPW transmission line, along with its supporting posts and CPW feed sections. The CPW traces are suspended in the air above the substrate, post sections are used to connect the elevated traces to CPW feed lines, and there is one supporting post section in the middle of the line which is in physical contact with the substrate via a gap in the lower ground plane.

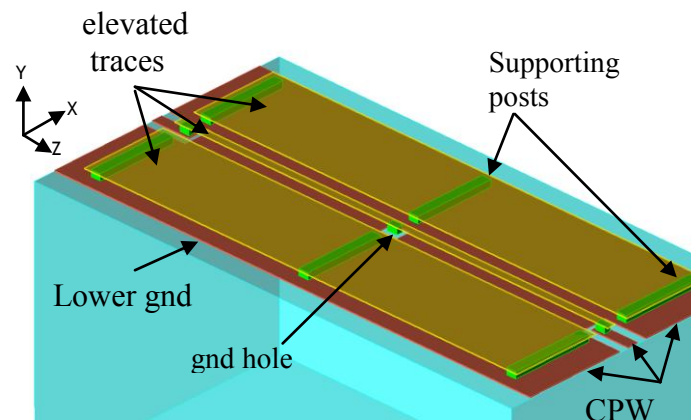


Figure 6.1: Angled 3-D conceptual view of a section of an elevated-grounded CPW line resting on posts and fed by CPW

In a similar fashion to the all-elevated CPW structure, the elevated and post sections can be analyzed separately and at the end the composite characteristic impedance of the line can be achieved by cascading these sections. The cross section of the elevated part of the line is simplified as shown in Fig.6.2. The CPW ground planes are assumed to be infinite in extent and the line is assumed to extend to infinity in the z - direction. The assumption of CPW ground planes of infinite extent yields accurate analysis results as long as the ground plane width does not become comparable with the quantity $2b$.

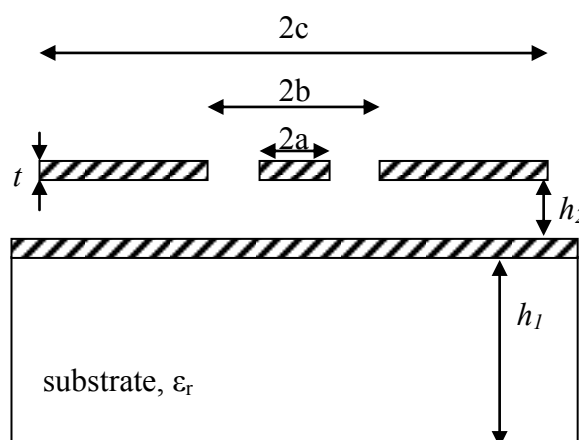


Figure 6.2: Cross section of an elevated-grounded CPW line

6-2-2 Synthesis of thick elevated-grounded CPW resting on dielectric substrate

The elevated grounded structure is essentially conductor-backed CPW with air as a substrate - see Fig.6.2. The quasi-TEM analysis of this structure has been reported by Ghione *et al.* [135]. However, the utility of this analysis is limited when the elevation is equal to or less than the gap width. The assumption of magnetic walls in the CPW slots is no longer valid as the top face of the CPW signal line couples to the ground plane beneath. In order to synthesize a elevated grounded CPW line with a specified capacitance, we consider three different ranges of parameter values:

$$(b - a) < h_2 \quad \text{conductor backed CPW}$$

$$h_2 < (b - a) < 5h_2 \quad \text{combination of microstrip and conductor backed CPW}$$

$$(b - a) > 5h_2 \quad \text{microstrip}$$

When $(b - a) < h_2$, the line can be synthesized by first finding the total line capacitance corresponding to the required characteristic impedance:

$$C_t = \frac{1}{c Z_0} \quad (6.1)$$

in which c is the speed of light in a vacuum. Next, we express the total line capacitance in terms of the contribution of the upper and lower half planes and an extra term representing the parallel plate capacitance between the signal and ground conductors formed by the finite metallization thickness. This is equivalent to introducing magnetic walls linking the top and bottom faces of the signal and ground lines. This simplifying assumption introduces some error into the computation but, in the range of practical line geometries, as will be shown, this error is relatively small. Specifically, the upper and

lower half plane capacitances are expressed in terms of elliptical integrals with modulus

equal to $\frac{\text{Tanh}\left(\frac{\pi a}{2h}\right)}{\text{Tanh}\left(\frac{\pi b}{2h}\right)}$ and $\frac{a}{b}$ respectively. The parallel plate term is proportional to $\frac{t}{b-a}$

We now use the approximations [138] for K/K' when $0.707 < k < 1$ and when $0 < k < 0.707$ for the lower and upper half plane respectively and apply the Newton-Raphson method to obtain an iteration equation for b in terms of a and h :

$$b_{n+1} = b_n - \frac{\frac{t}{b_n - a} + \frac{\pi}{\ln(f)} + \frac{\ln(f_1) - C_t}{\pi} - \frac{C_t}{2\epsilon_0}}{\frac{\sinh\left(\frac{a\pi}{h}\right)}{h(\cosh\left(\frac{a\pi}{h}\right) - \cosh\left(\frac{b_n\pi}{h}\right))} - \frac{2\pi}{\sqrt{1 - \frac{a^2}{b_n^2} b_n \ln(f)^2}} - \frac{t}{(a - b_n)^2}} \quad (6.2)$$

with

$$f = \frac{-4a^2 + 8\left(1 + \sqrt{1 - \frac{a^2}{b_n^2}}\right)b_n^2}{a^2} \quad (6.3)$$

$$f_1 = -4\text{csch}\left(\frac{(a - b_n)\pi}{2h}\right) \sinh\left(\frac{(a + b_n)\pi}{2h}\right) \quad (6.4)$$

An initial value of $b=1.5a$ yields, in most cases, accurate results for b in two to four iterations. When $(b - a) > 5h$, microstrip synthesis equations can be used [143]. However, when $h < b - a < 5h$ - the condition satisfied by a large range of practical EGCPW geometries - using either of the above set of equations leads to large errors. In this case, for synthesis purposes, the total capacitance can be approximated as a combination of the above analyses - essentially grounded CPW empirically modified to

reflect the coupling between the top face of the signal line and the bottom ground plane.

The total line capacitance is now:

$$C_t = C_1 + (C_{ms} - C_2) + 0.9\epsilon_0 \frac{2a}{h} + C_{pp} \quad (6.5)$$

With the microstrip capacitance denoted C_{ms} and with C_1 and C_2 being the CPW and conductor backed CPW half plane capacitances respectively. The utility of separating the analysis into the three sets of simple equations is that an exact quasi-static solution of the structure involving multiple unknowns (the parameter problem) is avoided and yet accuracy good enough for design work is achieved. C_{ms} includes the effect of metallization thickness and can be calculated as per [144]. In a similar way to that used in deriving (6.2)-(6.4), we can obtain an iteration equation for b with assumed values of a , h and Z_0 . The equation is:

$$b_{n+1} = b_n - \frac{2\epsilon_0 \frac{\pi}{\ln(f)} - 0.63662\epsilon_0 \frac{\ln(f)}{\pi} - C_t + C_{ms} + 0.9\epsilon_0 \frac{2a}{h}}{2\epsilon_0 \left(\frac{-\coth\left(\frac{(a-b_n)\pi}{2h}\right) - \coth\left(\frac{(a+b_n)\pi}{2h}\right)}{2h} - \frac{2\pi}{\sqrt{1 - \frac{a^2}{b_n^2} b_n \ln(f)^2}} \right)} \quad (6.6)$$

With ($h=h_2$ =elevation height at all above equations).

Table 6.1 shows the desired characteristic impedance, the corresponding calculated dimensions and the impedance obtained from simulation results of a line with these dimensions. The results show that the synthesis formulae yield results with less than 1.9% error for the whole of the considered range.

Table 6.1: Comparison between calculated and simulated characteristic impedance for various geometries

a (μm)	t (μm)	h_2 (μm)	b (μm)	Calc. Z_0 (Ω)	Sim. Z_0 (Ω)
5	2	5	6.74	50	49.295
10	2	7	14.4	75	74.31
10	3	10	14.64	60	58.87
5	1	2	9.28	45	44.79
10	2	4	18.55	45	44.81
10	2	8	25.5	70	70.54

Good agreement between the simulated and calculated results is obtained using the above equations. The simulated characteristic impedance of EGCPW line for various geometries is plotted in Figure 6.3.

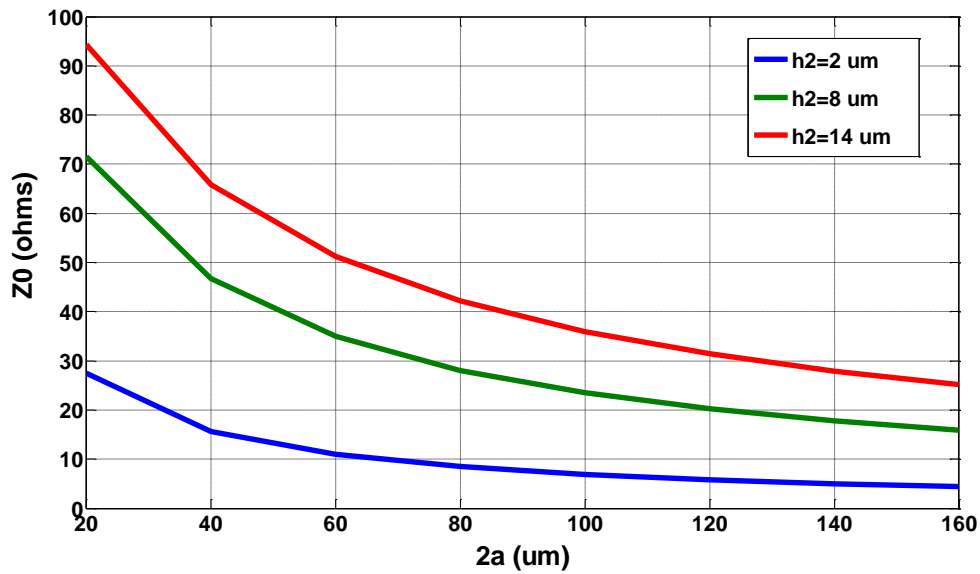


Figure 6.3: Simulated characteristic impedance of elevated-grounded CPW for varying $2a$, $b=2a+20$, $c=b+100$, $h=2, 8$ and 14 . All dimensions are in microns.

Figure 6.3 shows the characteristic impedance of EGCPW lines for various signal widths, $2a$, in the range 20 to 160 μm for three different elevations of 2, 8 and 14 μm . The gap width, $(b-a)$ has a constant value of 20 μm and the conductor thickness is set to be 2 μm for elevated traces and bottom ground. The substrate is GaAs with dielectric constant of 12.9 and 600 μm thickness. It can be seen that high characteristic impedances can be achieved by either increasing the elevation height, narrowing the signal trace, or by a combination of both. The figure shows that the EGCPW line can cover a wide range of impedances as low as 5 Ω and as high as 95 Ω . This is a great advantage of the EGCPW structure over the other elevated structures which tend only to support higher impedances with reasonable dimensions with extremely low impedances associated with often impractical geometries. For instance, in order to achieve a line with 25 Ω impedance, all-elevated CPW has a dimension of around 3-100-3 (μm) and SECPW has a dimension of 5-95-5 (μm) at 2 μm elevation. This causes problems due to the fabrication limitations and also excessive loss due to the high current density at

small gaps. In contrast, an EGCPW line with the reasonable dimensions 20-25-20 (μm) and an elevation height of $2\mu\text{m}$ yields a characteristic impedance of 25Ω . By keeping these dimensions constant and increasing the elevation height impedances as high as 68Ω and 90Ω can easily be achieved at elevations of $8\mu\text{m}$ and $14\mu\text{m}$, respectively.

Fig.6.4 shows a plot of the effective permittivity of EGCPW lines for the same range of geometries as in Figure 6.3.

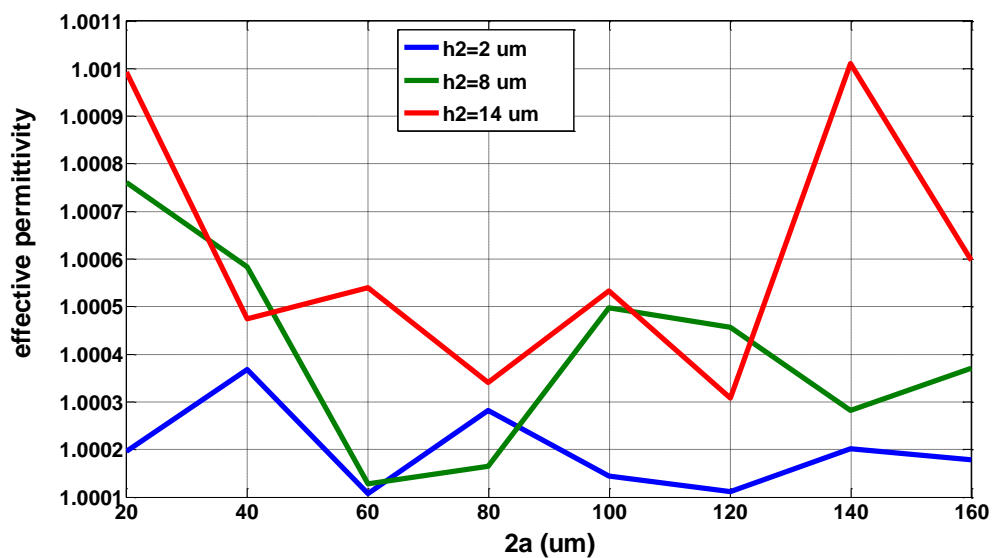


Figure 6.4: Simulated effective permittivity of elevated-grounded CPW for varying $2a$, $b=2a+20$, $c=b+100$, $h=2, 8$ and 14 . All dimensions are in microns.

The Fig illustrates a great advantage of the elevated-grounded CPW structure - that of providing an effective permittivity of one independent of the line geometries and particular nature of the carrier substrate.

In Fig.6.5, the characteristic impedance of EGCPW line for three different gap sizes - 15, 40 and $65\mu\text{m}$ -which are smaller, equal and larger than the constant signal width, $2a$, of the line are presented. The impedances are plotted against elevation height in the range $2\text{-}14\mu\text{m}$.

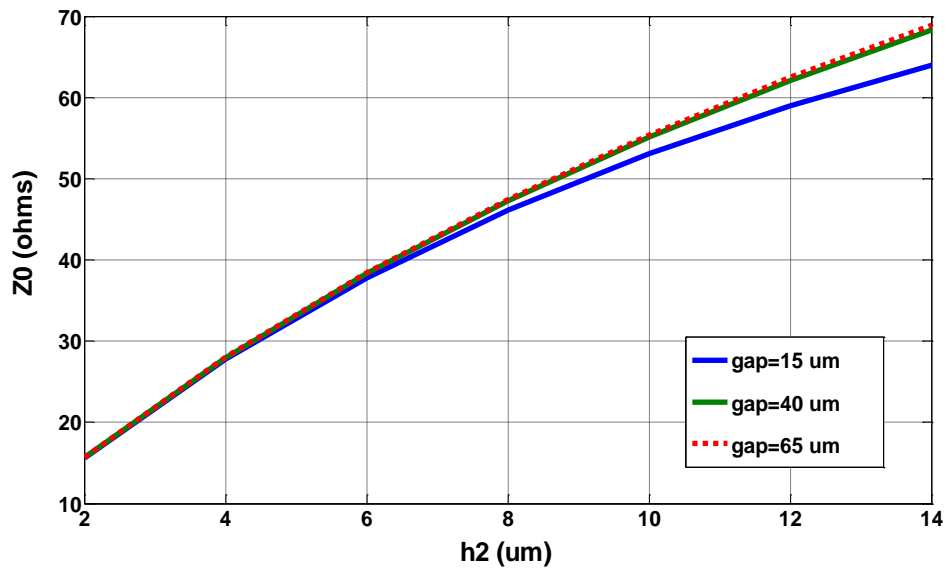


Figure 6.5: Simulated characteristic impedance of elevated-grounded CPW for varying elevation height (h_2), $2a=40$, $b=2a+(15,40 \text{ and } 65)$ and $c=b+100$. All dimensions are in micron.

We can see in Fig.6.5 that the gap width has a trivial effect on determining the characteristic impedance of the EGCPW line. This is a great advantage of EGCPW lines in terms of loss at low impedances and means that a narrow gap is not required to implement a low impedance EGCPW lines. As discussed previously, small gaps are very effective in increasing the conductor loss of coplanar waveguide structures, both conventional and elevated, and result in high loss for low impedance transmission lines. This problem can be overcome by using EGCPW as small gaps are not required in the design of low impedance lines. A plot of effective permittivity for the same dimensions as in Fig.6.5, shows an invariant value of one.

6-2-3 Analysis of thick elevated-grounded CPW resting on dielectric substrate with the gap in bottom ground

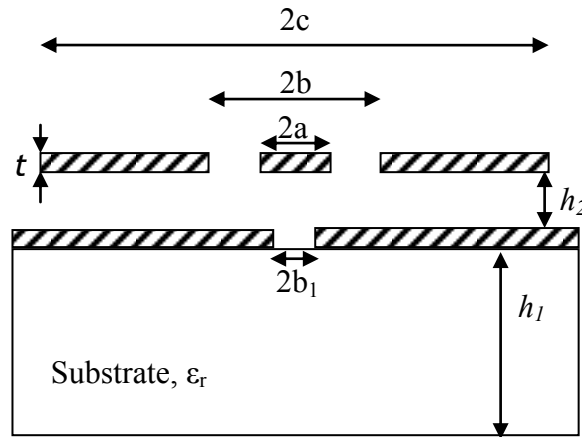


Figure 6.6: Cross section of a elevated-grounded CPW section with gap on the lower ground

A cross section of the part of the line which forms the transition between the elevated section and the section in which the signal line comes into physical contact with the substrate is shown in Figure 6.6. Here, we assume magnetic walls in the slots of the CPW and use Fig.6.7 to formulate the mapping function. The points in the intermediate t -plane and final t' are shown along with the relevant points in the z -plane.

The mapping function relating t and z -planes is

$$z = \frac{h}{t_{b1}\pi} \left(2\sqrt{t+1} + t_{b1} \log \left(\frac{1+\sqrt{t+1}}{-1+\sqrt{t+1}} \right) \right) \quad (6.7)$$

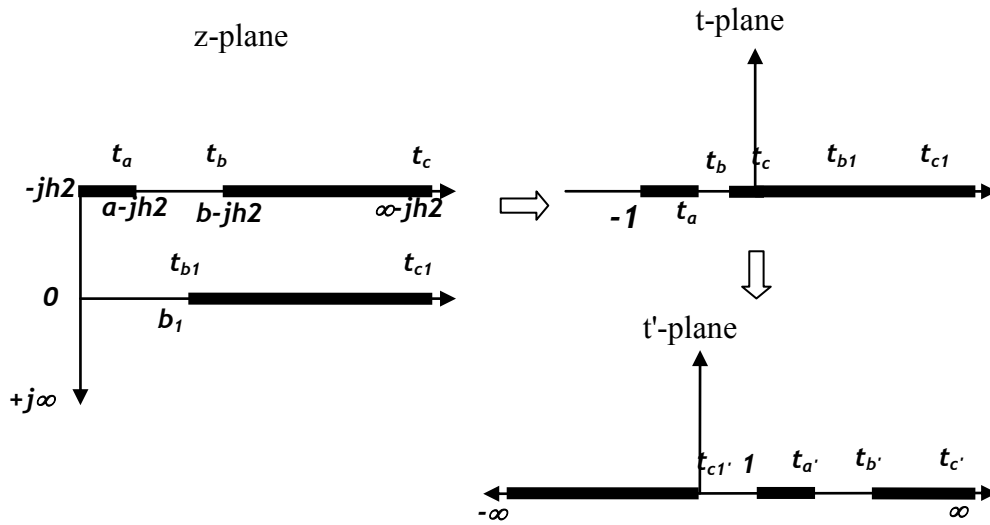


Figure 6.7: Mapping between physical (z) plane, intermediate t -plane and final t' plane for the intermediate post section

Setting $t = t_{b1}$, (6.7) involves only one unknown and allows us to numerically search for the value of t_{b1} which yields the known value of b on the left hand side. Once t_{b1} is known, left and right hand sides of the mapping function can be equated for each of the required z -plane points and the root of the equation solved using a suitable algorithm.

With the t -plane points known, we further transform according to $t' = -\frac{1}{t}$. The elliptic modulus is now

$$k = \sqrt{\frac{\frac{t_{a'}-1}{t_{a'}+1}}{\frac{t_{b'}-1}{t_{b'}+1}}} \quad (6.8)$$

The resulting capacitance we denote C_3 .

Finally, we use the series capacitance techniques in [135, 136] to find the total substrate capacitance for two layered substrates ordered in terms of decreasing permittivity as follows

$$C_4 = \frac{\frac{\epsilon_r}{\epsilon_r - 1} C_2 \epsilon_r C_3}{\frac{\epsilon_r}{\epsilon_r - 1} C_2 + \epsilon_r C_3} \quad (6.9)$$

The total line capacitance can be written

$$C_{t1} = C_4 + C_1 + 2\epsilon_0 \frac{t}{b-a} \quad (6.10)$$

6-2-4 Analysis of post section

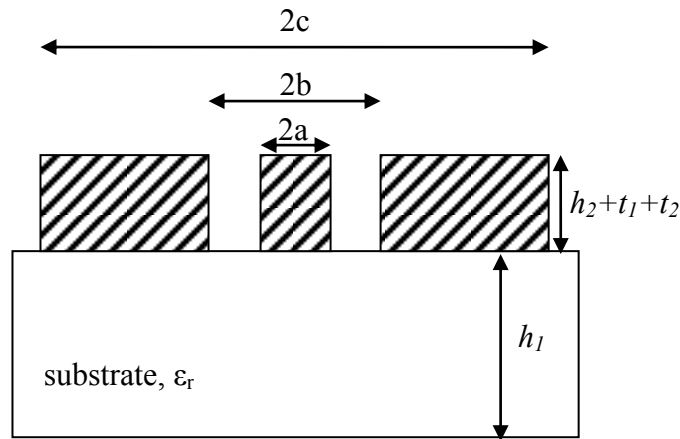


Figure 6.8: Cross section of EGCPW post section

The cross section of the region of the line in which the signal trace comes into contact with the substrate can be considered as CPW with thick metallization. With reference to Fig.6.8, the capacitance of this section can be approximated as the sum of the lower and upper CPW half plane capacitance and a parallel plate capacitance term proportional to $(h_2 + t_1 + t_2)/(b - a)$. Where t_1 and t_2 refer to the metallization thickness of the bond pad and airbridge layers respectively.

6-2-5 Quasi-static characteristics of composite line

Fig.6.9 shows the results of a cascaded transmission line analysis when applied to a line characterized by a A/B/C/D/C/B/C/D/C/B/A geometry where A=CPW feed, B=post section, C=grounded CPW with gap in the ground plane and D=elevated grounded CPW. In this particular case, the parameters for the CPW section are $\epsilon_{\text{eff}}=6.186$, $Z_0=42.23\Omega$, $l=20\mu\text{m}$. For the post section they are $\epsilon_{\text{eff}}=5.1318$, $Z_0=36.93\Omega$, $l=22\mu\text{m}$. For the elevated section with gap on the lower ground, they are $\epsilon_{\text{eff}}=1.155$, $Z_0=104.387\Omega$, $l=10\mu\text{m}$ and for the elevated section they are $\epsilon_{\text{eff}}=1$, $Z_0=87.7\Omega$, $l=468\mu\text{m}$. This particular geometry is chosen simply because it reflects a practical, unoptimised, and easily fabricated structure. Also shown are the results obtained from full wave solver Ansoft's HFSSTM. All results assume infinite conductivity and zero dielectric loss.

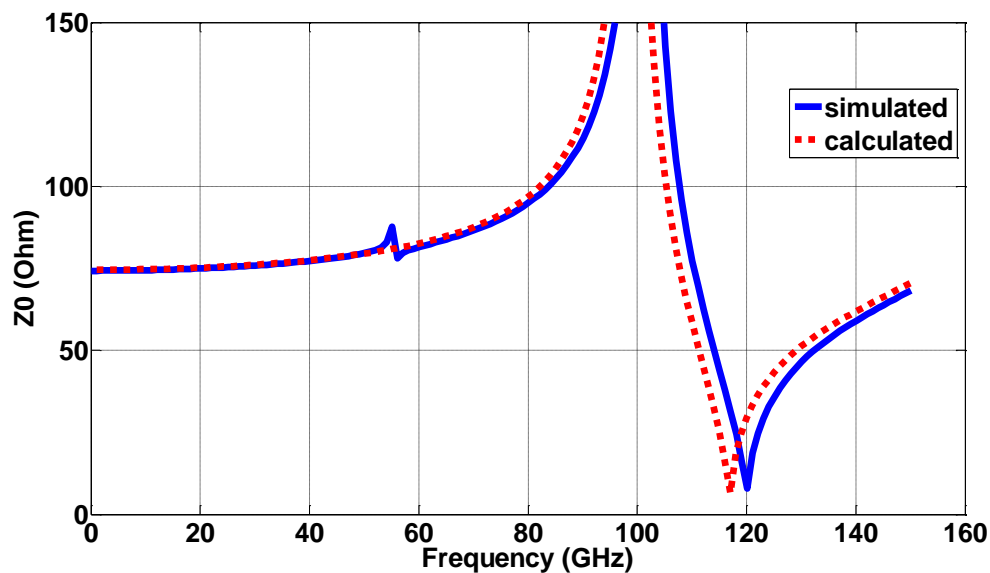


Figure 6.9: Comparison between simulated and calculated frequency dependent characteristic impedance for seven section EGCPW line

It can be seen that the low frequency impedance is computed almost exactly whilst the high frequency dispersion is accurately modelled up to about 140GHz in this particular

case. A full wave analysis is required above this frequency to accurately compute the dispersion relation. Nevertheless, a quasi static analysis is useful in designing the post sections in order to reduce the effects of impedance mismatch in the line. Analyses for EGCPW lines with varying geometries show similarly good agreement between simulation and calculation results.

6-2-6 Losses in elevated-grounded CPW lines

As with previously discussed transmission lines and their associated chapters, the losses of elevated-grounded CPW are now analyzed in this section using a set of 2-D and 3-D simulations. Fig.6.10 shows the conductor loss of EGCPW lines for various geometries. The loss is plotted for the same dimensions as for the CPW, ECPW and SECPW cases in order to allow direct comparison of the losses between these structures. First, the conductor loss is plotted for different lateral dimensions, ($2b$) and also different ratios of signal width to the lateral dimensions of EGCPW, a/b .

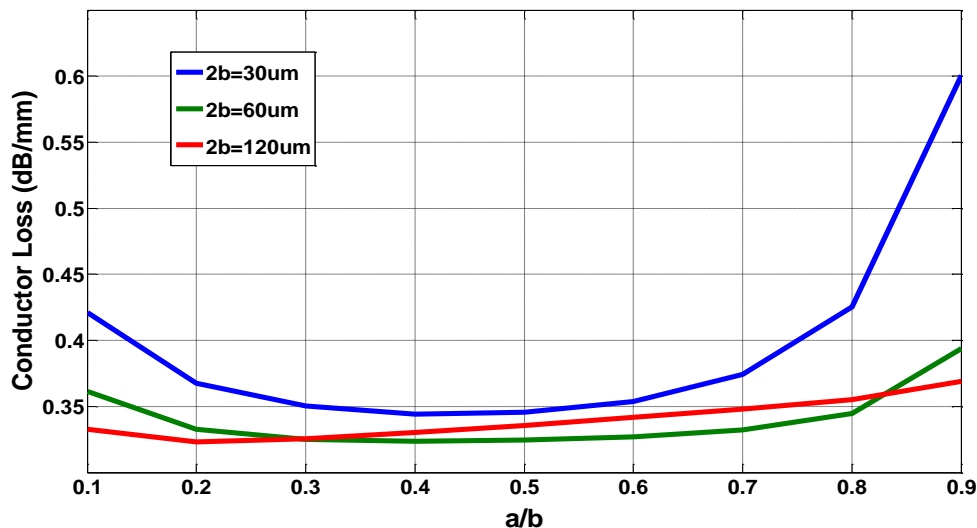


Figure 6.10: Simulated conductor loss of EGCPW lines with three different lateral dimensions ($2b$) of 30, 60 and 120 μm for various ratios of signal width to lateral dimensions (a/b). GaAs substrate is used with thickness of 600 μm and loss tangent of zero.

It can be seen in Fig.6.10 that, unlike CPW, ECPW and SECPW lines, for larger lateral dimensions, the EGCPW conductor loss is almost independent of the size of the signal and gap widths. However, by decreasing the lateral dimension of the lines, the sizes of gap and signal width are seen to have more of an effect on the conductor loss of the EGCPW structure. In these cases, the narrow gaps (b-a) are more effective in increasing the conductor loss than the narrow signal traces (2a). As with the other elevated lines, the conductor loss of the EGCPW line is much lower than the conductor loss in conventional CPW lines. In comparison with ECPW and SECPW lines, elevated grounded CPW has broadly similar conductor losses for lower lateral dimensions e.g. $30\mu\text{m}$. However, for larger lateral dimensions, e.g. $120\mu\text{m}$, the EGCPW structure shows greater conductor loss than the two other elevated lines. This may be due to the effect of the additional lower ground plane in EGCPW which can be physically close to the signal trace and cause some edge effects.

The substrate loss (without radiation) of the EGCPW line is essentially zero due to the complete shielding of the dielectric substrate from the fields between the signal and ground traces.

In order to investigate the effect of elevation height on the attenuation of EGCPW lines, the plots of conductor loss for lines with three different elevation heights- 5, 10 and $15\mu\text{m}$ - are shown in Figure 6.11.

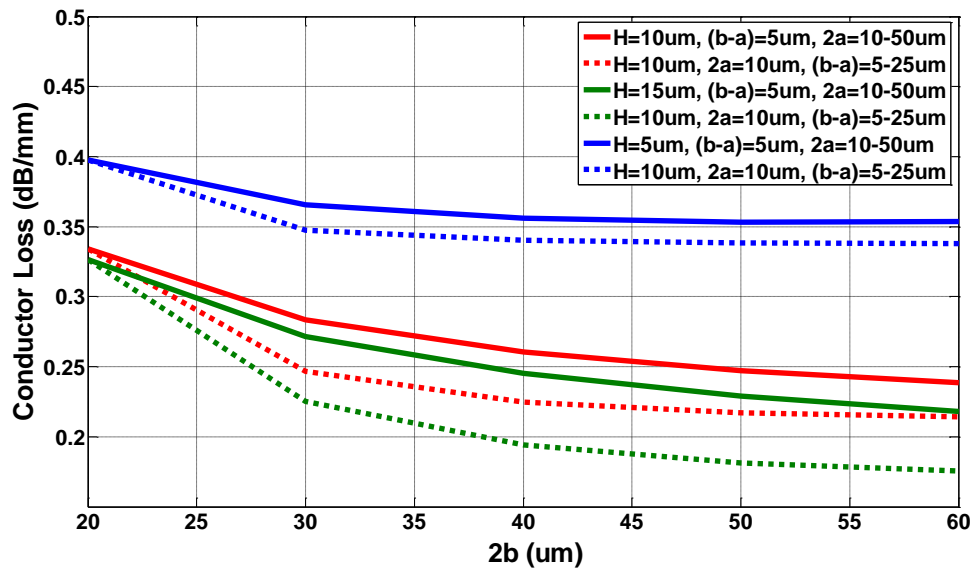


Figure 6.11: Simulated conductor loss of EGCPW lines for various lateral dimensions ($2b$) and three elevation heights of 5, 10 and 15 μm . The range of lateral dimensions is maintained by once keeping the signal width ($2a$) constant and varying the gap size ($b-a$) and once varying the signal width when the gap size is constant.

These data are compiled by varying the lateral dimensions from 20 to 60 μm in two distinct ways: i) the signal width, $2a$, is held constant and the gap size, $b-a$, changed and ii) The gap size held constant and the signal width changed. The results show the significant reduction in conductor loss achieved by increasing the elevation from 5 μm to 10 μm . Note that, whilst the reduction in conductor loss is significant as the elevation increases from 5 μm to 10 μm , there is comparatively little reduction in this loss as the elevation increases from 10 μm to 15 μm . Unlike all of the other previously discussed lines, the conductor loss for an EGCPW line with 5 μm elevation does not increase as the gap size is reduced. This can be an advantage in achieving a low loss/low impedance line. Unlike the SECPW line, as the elevation height in EGCPW is increased, the increased loss due to smaller gaps becomes more pronounced. However, the negative impact of smaller gaps is still less significant than with CPW and ECPW.

In order to investigate the radiation characteristics of the elevated grounded CPW structure the 2-D and 3-D simulation results of the lines with lateral dimensions of $120\mu\text{m}$ and $30\mu\text{m}$ are compared, Fig.6.12 and Fig.6.13.

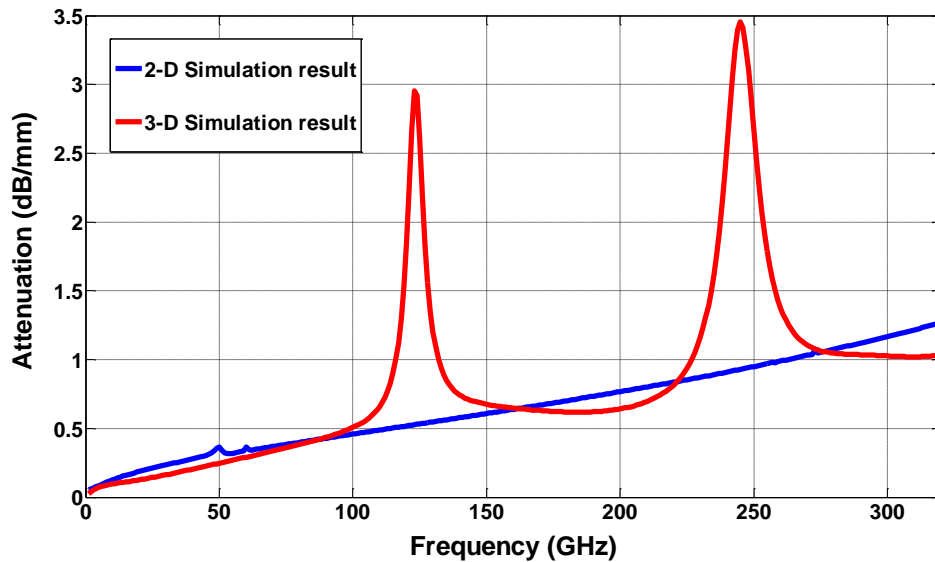


Figure 6.12: 2-D and 3-D Simulation plots of total attenuation of a $5\mu\text{m}$ -elevated EGCPW line with $120\mu\text{m}$ lateral dimension without added supporting posts.

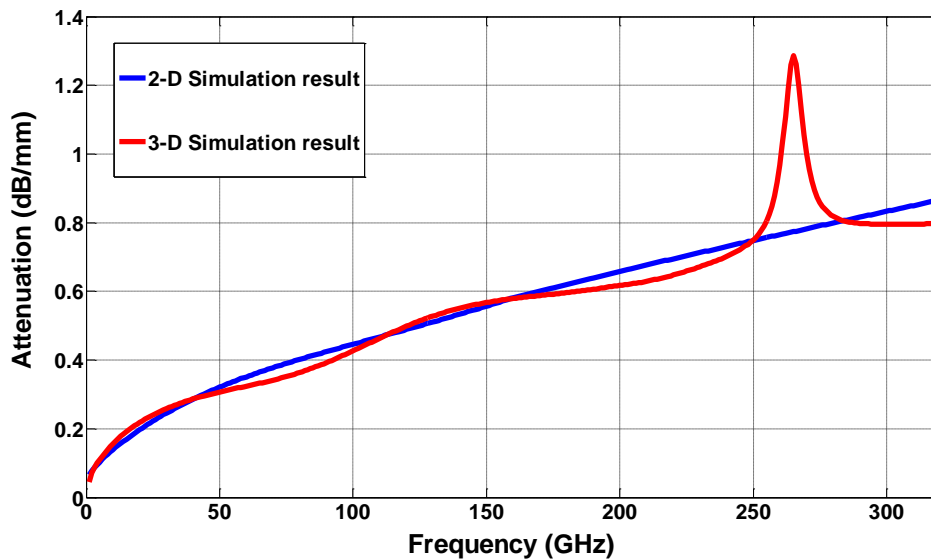


Figure 6.13: 2-D and 3-D Simulation plots of total attenuation of a $5\mu\text{m}$ -elevated EGCPW line with $30\mu\text{m}$ lateral dimension without added supporting posts.

In the 3-D results for lines with lateral dimensions of $120\mu\text{m}$, Fig.6.12, and $30\mu\text{m}$, Fig.6.13, resonances are observed which are, of course, not shown by the quasi-static 2-D simulation results. As mentioned earlier, the EGCPW line is in fact a conductor-backed CPW (CBCPW) structure filled with air as a substrate. It was discussed earlier in chapter 2 that the CBCPW lines with thin substrates can behave similarly to overmoded patch antennas, with resonances occurring in the transmission and reflection characteristics. This same behaviour can be seen here in the ideal EGCPW line because the distance between bottom ground and CPW traces is only $5\mu\text{m}$. It was discussed earlier that using via holes through the substrate to connect the top and bottom grounds at the same potentials is a way of suppressing the unwanted resonances in CBCPW lines. In practical EGCPW lines the supporting posts are required to keep the elevated traces above the substrate. These supporting posts in EGCPW are actually playing the same role as via holes in CBCPW and keep the different grounds at the same potential. Therefore, the resonance phenomena should not be a problem in EGCPW lines in the real world. Fig.6.14 shows the EGCPW line of lateral dimension $30\mu\text{m}$ with the addition of supporting posts at each end of the line.

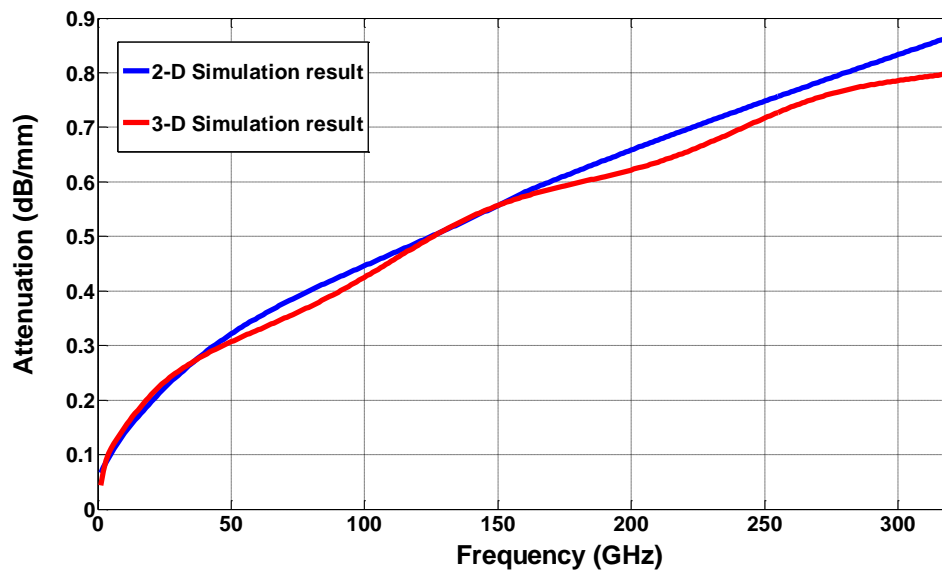


Figure 6.14: 2-D and 3-D Simulation plots of total attenuation of a $5\mu\text{m}$ -elevated EGCPW line with $30\mu\text{m}$ lateral dimension and added supporting posts to connect ground planes.

This Figure illustrates that adding the supporting posts of the EGCPW line, which are unavoidable in real life, can remove the resonance effect completely and the line shows extremely low loss (<half the equivalent CPW losses) up to frequencies as high as 320GHz. This is a pronounced advantage of EGCPW over ECPW and SECPW lines as adding supporting posts to the ground planes increases the mechanical stability of the line without introducing additional loss.

The superiority of elevated grounded CPW lines over other structures becomes clear when looking at the results of the line with $120\mu\text{m}$ lateral dimension, Figure 6.15.

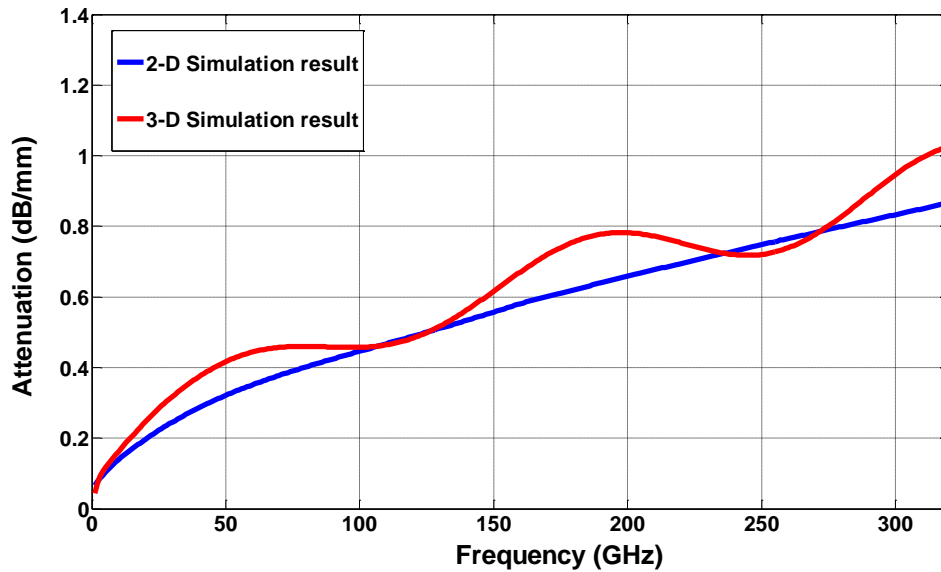


Figure 6.15: 2-D and 3-D Simulation plots of total attenuation of a 5 μm -elevated EGCPW line with 120 μm lateral dimension and added supporting posts to connect ground planes.

As was discussed in chapter 2, conventional CPW with 120 μm lateral dimension suffers from excessive loss at high frequencies due to the radiation of the signal into free space or the substrate. Similarly high losses are observed for the all-elevated and signal-elevated CPW lines at high frequencies due to non-complete isolation from the substrate. However, The elevated grounded CPW shows a superior performance for a given lateral dimension with the total attenuation as low as 1dB/mm at 300GHz which is 9 times less than with CPW, 8 times less than SECPW and 7 times less than ECPW. Simulation results for different lateral dimensions show similar low losses. Therefore, using elevated grounded CPW gives considerable freedom to MMIC designers to design lines with varying dimensions and impedances without increasing losses significantly. This is the great potential that elevated grounded CPW has to meet the requirements of future sub-millimetre wave circuits.

In order to investigate the performance of EGCPW line in real life, the next section gives experimental results obtained from measurements of fabricated structures.

6-3 Modelling and measurement of elevated-grounded CPW transmission line

Fig.6.16 shows a micrograph of the elevated grounded CPW from different angles.

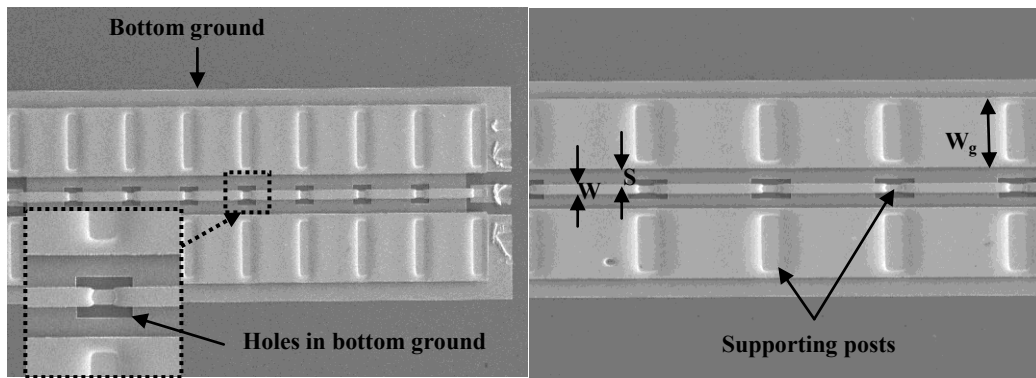


Figure 6.16: Top view micrograph of EGCPW transmission line. The line dimensions are: $W=24$, $S=25$ and $W_g=105$. All dimensions are in micron

A series of EGCPW transmission lines with various dimensions were designed and fabricated for subsequent measurement and analysis. An approximately 54Ω EGCPW transmission line, which was the closest to a 50Ω line of the fabricated structures, was chosen for the results shown in this section. The designed dimensions of this transmission line are: $W=19\mu\text{m}$, $S=30\mu\text{m}$ and $W_g=100\mu\text{m}$. The fabricated dimensions are different due to the fabrication tolerances and they are as follows: $W=24\mu\text{m}$, $S=25\mu\text{m}$ and $W_g=105\mu\text{m}$. The elevation height for this is almost $6\mu\text{m}$. These dimensions were chosen based on initial simulations to achieve a near 50Ω transmission line.

In this section, the attenuation characteristics of the elevated grounded CPW line are investigated by carefully simulating the transmission line and comparing measured/simulated data for EGCPW lines with that for conventional CPW lines.

Fig.6.17 shows the simulation and measurement results for the insertion and reflection loss of an approximately 54Ω EGCPW transmission line up to 320GHz. The results obtained for the EGCPW line are also compared with those for a 50Ω conventional CPW line in this graph.

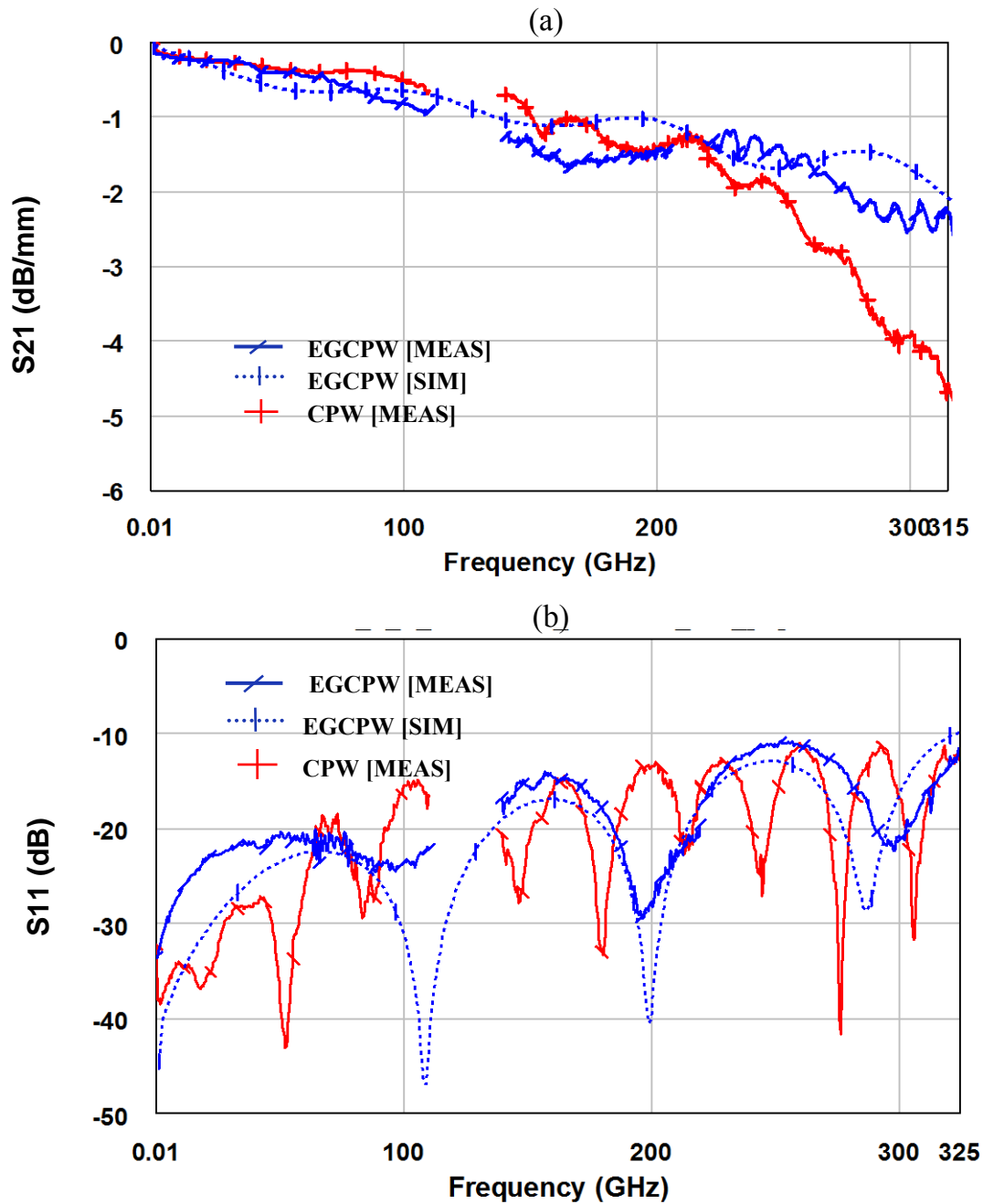


Figure 6.17: Measured and simulated S-parameters for a EGCPW and CPW (a) Insertion loss per mm (b) Reflection Coefficient (dB)

For this measurement, probing was done on top of the elevated traces of EGCPW line by placing two post sections close enough together to form a stable landing pad. This is shown in Figure 6.18.

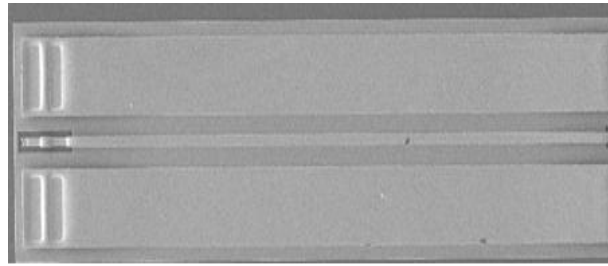


Figure 6.18: Micrograph of a EGCPW line with supporting posts placed in close distance to support probing on top of the elevated structure

Comparison of these EGCPW and CPW measured results, Fig.6.17, indicate that, at low frequencies, where the dielectric losses are relatively small and attenuation is dominated by conductor loss, the attenuation is roughly comparable. However, at high frequencies (especially above 200GHz), when the radiation and dielectric losses of CPW become significant, for any given physical length the EGCPW line has the advantage. The EGCPW line, unlike a conventional CPW line, has essentially zero dielectric loss and does not radiate significantly. The post and feed sections, however, do have losses, but because the majority of the line consists of elevated sections, the overall losses are still lower than for other lines.

To eliminate the effect of any characteristic impedance discrepancy, the loss factor of the EGCPW line is now compared with that for the CPW transmission line in Figure 6.19.

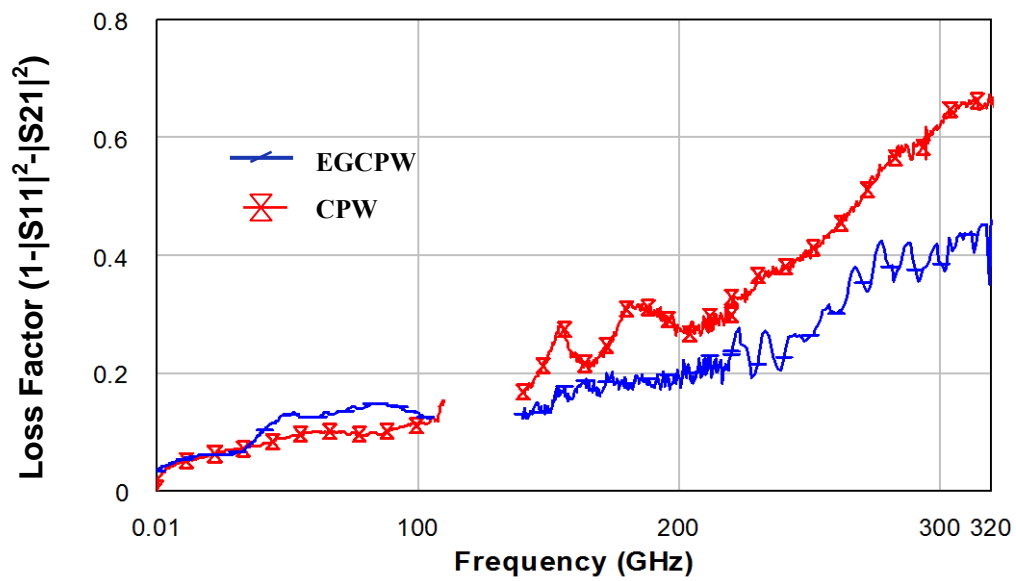


Figure 6.19: Measured loss factor of EGCPW and CPW transmission lines

It can be seen that by using a elevated grounded CPW structure, improvements in the line performance in terms of loss/mm as well as loss factor can be achieved – especially at frequencies above 200GHz.

In addition, the performance of elevated grounded CPW line is compared with CPW and previously mentioned elevated CPW (SECPW and ECPW) lines in terms of loss per unit wavelength, Fig. 6.20.

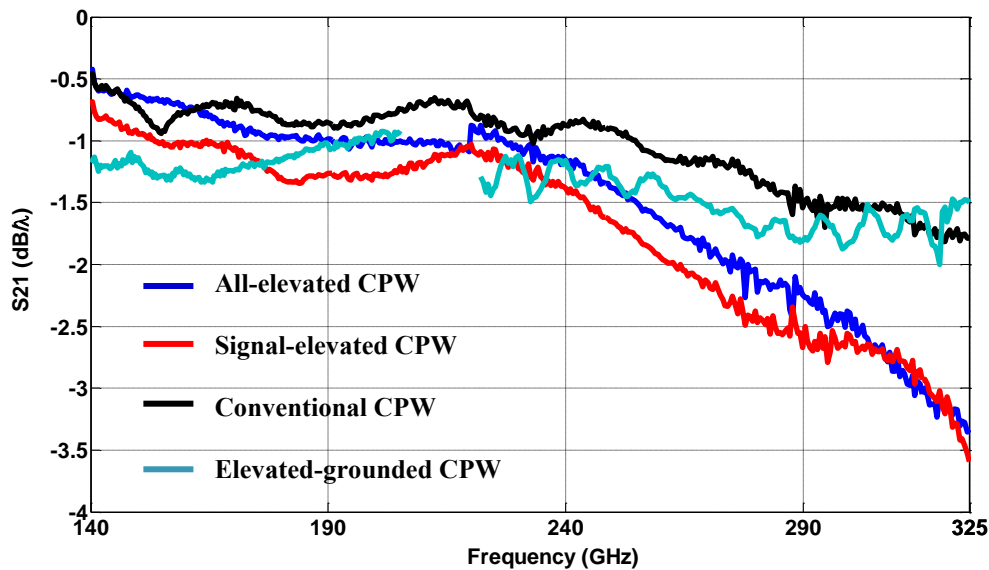


Figure 6.20: Measured loss factor of EGCPW and CPW transmission lines

Figure 6.20 reveals that although EGCPW has much lower effective permittivity and therefore longer wavelength than CPW line, it still shows comparable loss per unit wavelength with CPW structure, specially at H-band frequency range. Also, these results indicate a high improvement in less per unit wavelength when elevated-grounded CPW structure is used instead of other mentioned elevated CPW transmission lines, signal-elevated and all-elevated.

6-3-1 Transition to Coplanar waveguide

Elevated CPW lines cannot be suspended in air over their entire length but must include post and feed sections- not only for mechanical reasons but so they can be connected to transistors and/or passive components.

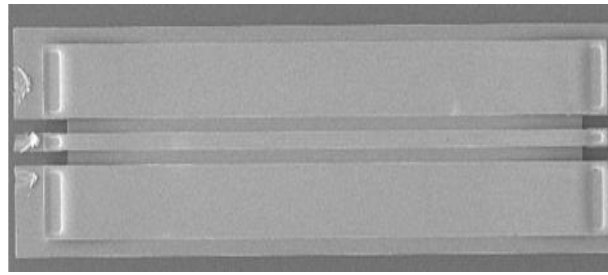


Figure 6.21: Micrograph of EGCPW line with transition pads to Coplanar waveguide

In Fig.6.22, measurements for a EGCPW line with transitions to CPW are compared with the results of a line with the transition de-embedded.

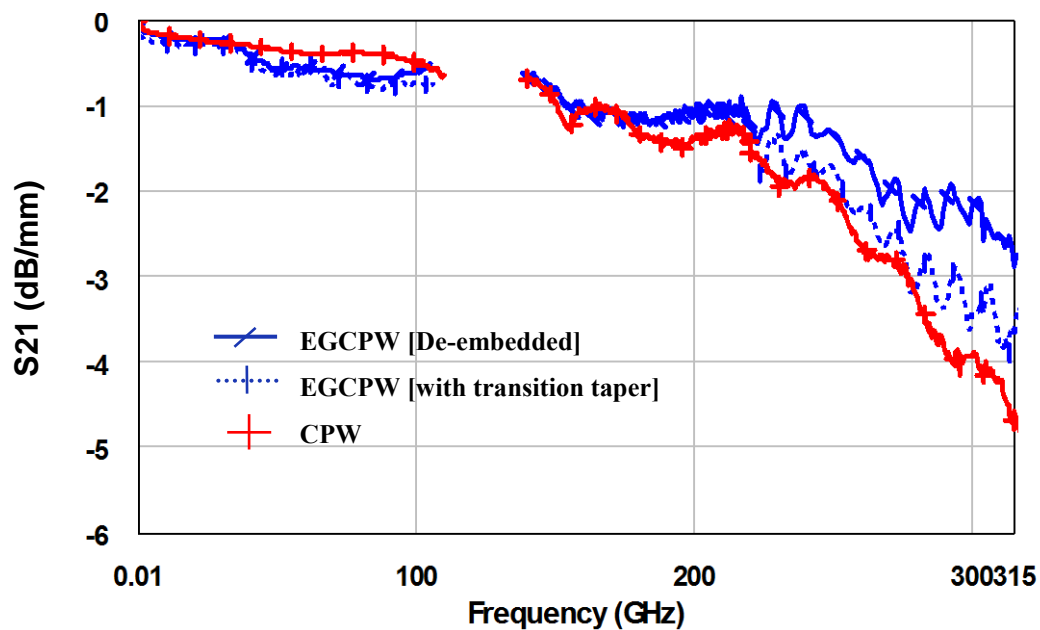


Figure 6.22: Measured S-parameters for a tapered EGCPW, de-embedded EGCPW and CPW transmission lines insertion loss/mm.

Fig.6.22 clearly shows the deleterious effect of the transition pad on the performance of EGCPW line. Comparing the measured insertion loss for the EGCPW line in Fig.6.17(a) with that of Fig.6.22 it can be seen that the two methods of removing the effect of the transition are in close agreement. Moreover, the effect shown in Fig.6.22 in the measured EGCPW line without de-embedding and the CPW line – that of a sudden

increase in attenuation above 210GHz – is shown to disappear using both techniques. The effect of the transition on the overall performance of EGCPW becomes more significant at the frequencies for which CPW performance degradation is more pronounced. The de-embedded elevated grounded CPW line shows very low loss/mm at high mm-wave regimes – almost half the loss for the CPW line with the same characteristic impedance. Note that a rigorous optimization has not been conducted in the design of the CPW transitions and our design is based on a simple matching of quasi-static characteristic impedances. In real applications, transition pads are unavoidable in circuit designs since they provide the connection of EGCPW structures to the other passive and active components. We believe that optimising the transition pads in such a way that they provide a better match with the line impedance could improve the loss performance of the EGCPW line. However, we expect that the destructive effect of transition pad will never be completely eliminated. This is due to the inherent lossy behaviour of CPW structures at high frequencies due to the non-zero isolation from the substrate. Therefore, further research must be carried out to consider ways to optimise them in such a way so as to minimise the deleterious effect of the transition.

Some aspects of the discussed measurement results deserve further comment. The wavelength in the EGCPW with air dielectric is longer than in a CPW line with GaAs dielectric. Measured results for the CPW line reveal that the loss, in dB per wavelength, at 260GHz, is about $1.3\text{dB}/\lambda_g$ whilst for the EGCPW line the figure is $1.6\text{dB}/\lambda_g$. The same measurement at 70GHz shows $1.9\text{dB}/\lambda_g$ for CPW line while $1.6\text{dB}/\lambda_g$ is observed for EGCPW. These results show that, in terms of loss per wavelength and considering the effects of measurement error, the two lines are broadly comparable over the d.c.–

320GHz range but that, for a fixed length, the EGCPW line exhibits considerably less loss. The real advantage of the EGCPW line compared with CPW is the potential to realize extremely wide impedance ranges by varying the elevation height and the parameters a and b without significantly increasing the losses of the line. Further advantages are found in the design of passive circuit components such as the resonators and filters described in the following sections.

The results presented here suggest that elevated grounded CPW has a performance comparable with conventional CPW at lower frequencies. Furthermore, the absence of high losses well into the sub-millimetre wave regions of the electromagnetic spectrum suggest reduced dielectric-related radiation and substrate-conductance losses.

6-4 Elevated-grounded CPW (EGCPW) resonators

To investigate the performance of EGCPW in the implementation of passive components, a set of quarter-wavelength short and open-circuited resonators are designed and their high frequency performances are measured up to 320GHz. These components are also used later to implement band-pass and band-stop filters.

6-4-1 Quarter-wavelength EGCPW Short-circuited stub

The short circuited shunt stub matching network (quarter-wavelength resonator), is a useful topology for a variety of circuits including band-pass filters, diode detectors and matching/d.c. return networks. Fig.6.23 is a micrograph of such a network implemented using EGCPW.

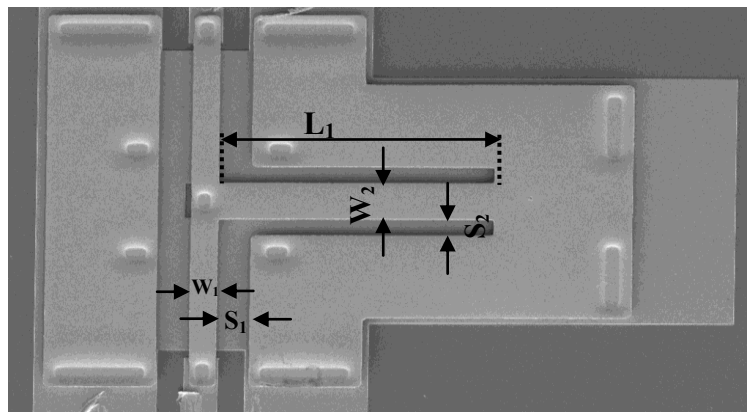


Figure 6.23: Micrograph of EGCPW short circuited stub. The stub dimensions are $L_1=251$, $S_1=30$, $W_1=24$, $S_2=19.5$ and $W_2=44.8$. All dimensions are in microns.

Simulated and measurement results of this short circuit stub with an elevation of $6\mu\text{m}$ are shown in Fig.6.24 and are in very good agreement.

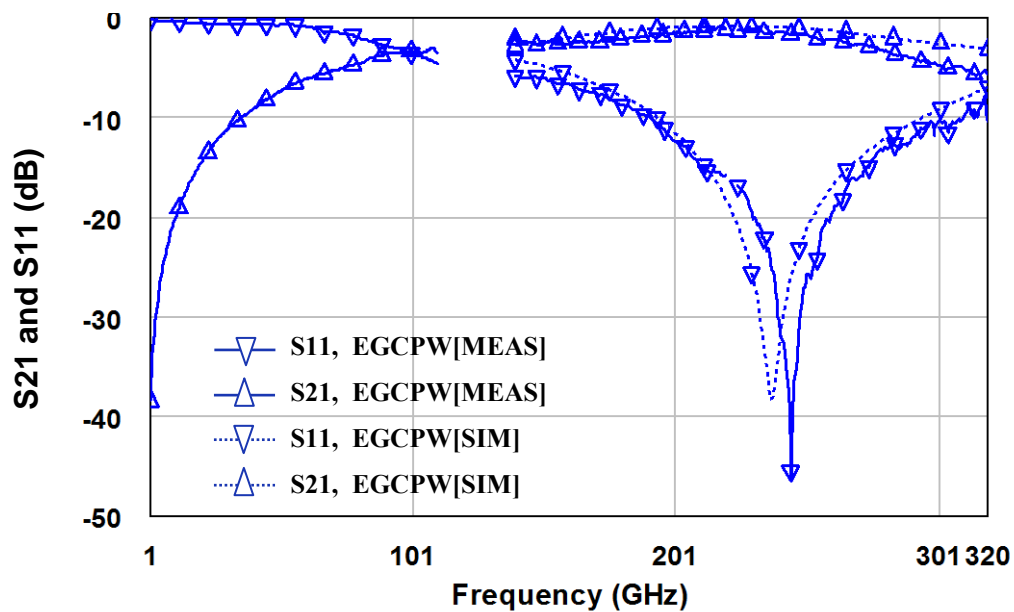


Figure 6.24: Measured and simulated S-parameters for EGCPW short-end shunt stub with $6\mu\text{m}$ elevation.

This stub shows an insertion loss of -1dB and very sharp rejection at the centre frequency of 245GHz . The 3dB bandwidth is 219GHz (89% fractional bandwidth) and quality factor of 1.1.

The performance of CPW short circuit matching stubs at high frequencies was investigated in Chapter 2. It was shown that, due to unwanted substrate effects at high frequencies, the CPW short circuit stub designed for 240GHz exhibits a very large bandwidth and ripples in its reflection coefficient. The loss at the centre frequency is -1.8dB. Fig.6.25 compares the measured results for CPW and EGCPW short circuited matching stubs. The elevated grounded CPW short circuited stub with a center frequency of 245GHz and an elevation of $6\mu\text{m}$ exhibits lower in-band insertion loss at the centre frequency with an improved roll-off characteristic and better matching to 50Ω than the CPW short circuit stub. This stub shows reduced fractional bandwidth by 29% and improved loaded and unloaded quality factor by 27% compared with CPW short stub. This is shown in Fig.6.25.

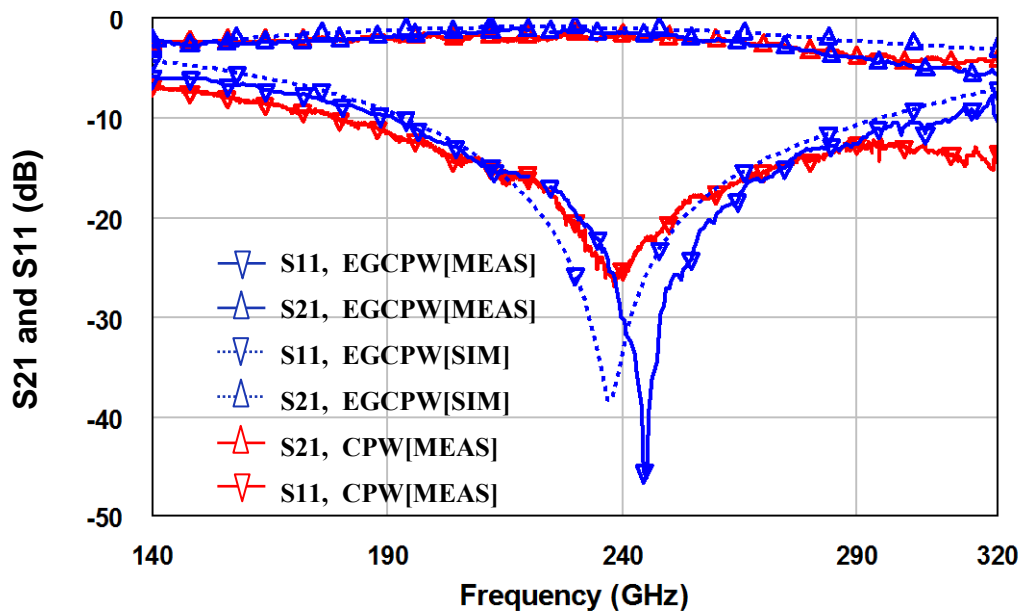


Figure 6.25: Measured and simulated S-parameters for a $6\mu\text{m}$ -elevated EGCPW short-end shunt stub compared with the measured S-parameters for a CPW short stub.

However, by increasing the elevation height to $13\mu\text{m}$, the performance of the short circuited matching stub improves drastically. An insertion loss of 0.7dB at a centre

frequency of 204GHz and a very narrow bandwidth are achieved. The results along with those for a CPW stub resonating at a slightly lower frequency are shown in Fig.6.26.

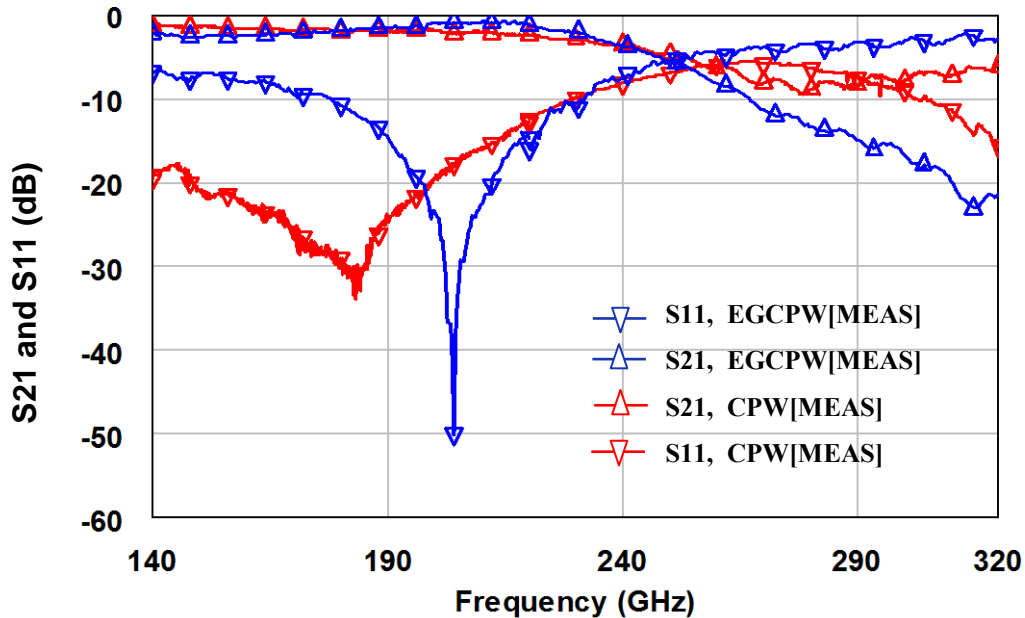


Figure 6.26: Measured and S-parameters for EGCPW short-end shunt stub with 13 μ m elevation compared with CPW short-circuited stub.

In Fig.6.26, the EGCPW stub has -0.7dB loss at the centre frequency of 204GHz compared to -1.8dB loss for the CPW stub at the centre frequency of 185GHz. The EGCPW short stub shows 50% fractional bandwidth (104GHz 3dB bandwidth), loaded quality factor of 2.1 and unloaded Q of 25.8 compared with CPW short stub with fractional bandwidth of 118% , Q_L of 0.8 and Q_u of 4.5. This shows 82.5% improvement in unloaded quality factor for short-circuited stub by using 13 μ m-elevated EGCPW instead of CPW structure.

Using a balanced short-circuited stub with 13 μ m elevation increases the insertion loss at the centre frequency to -1.35dB and reduces the 3-dB bandwidth to 77GHz. The increased loss in this case is mainly attributable to the increase in overall conductor loss

and the decrease in bandwidth, as discussed in chapter 2, is due to the lower overall impedance achieved at the stub by using two short circuited stubs in parallel.

It should be mentioned that increasing the elevation height in EGCPW short-circuited stubs results in a shift of resonance to lower frequencies. Considering the fact that the effective permittivity of the EGCPW structure is always 1 regardless of the elevation height, a series of simulations was carried out to investigate this effect. It was found that, with an increase in elevation, the parasitic (lumped) capacitance of the supporting post sections of the signal trace coupled with the exposed areas of substrate, which increase the effective permittivity, are the effective factors in lowering the resonance frequency. Increasing the elevation height results in an increase in capacitance between the supporting posts and the bottom ground of the EGCPW structure and hence a shifting of resonance to a lower frequency. A similar phenomenon has been observed for open-circuited matching stubs, band-pass and band-stop filters implemented with a EGCPW structure.

Important design note:

It was discussed earlier that using airbridges at CPW matching stubs is necessary to suppress the parasitic slotline mode at discontinuities [140,141]. It was shown that in all-elevated and signal-elevated CPW matching stubs, underbridges can be used to suppress the unwanted slotline mode at discontinuities. In elevated grounded CPW matching stubs, additional supporting posts were used to connect the top and lower ground planes at the junctions to keep the ground planes at the same potential and suppress the unwanted mode, Fig.6.27(a). We tried stubs without these additional connecting posts and the response was very different from those shown in Figure 6.25.

The bandwidth was much larger and the insertion loss was increased by -1.3dB. Figure 6.27(b) shows the performance of the short circuit stub without additional posts at the junction. The stub dimensions are similar to the dimensions of the stub in Figure 6.23 (with $10\mu\text{m}$ less in stub length-i.e. $240\mu\text{m}$). The elevation height is $6\mu\text{m}$.

From the fabrication point of view, both CPW and the previously discussed elevated CPW (ECPW and SECPW) structures need additional fabrication stage(s) to shape airbridge or underbridges at the junctions and discontinuities. The fabrication process for EGCPW structures is inherently more complex, but doesn't need any additional stages to shape airbridge or underbridges. Additional posts considered in EGCPW structures in order to eliminate the slotline mode at discontinuities can be made at the same time as the supporting posts used to elevate the CPW traces.

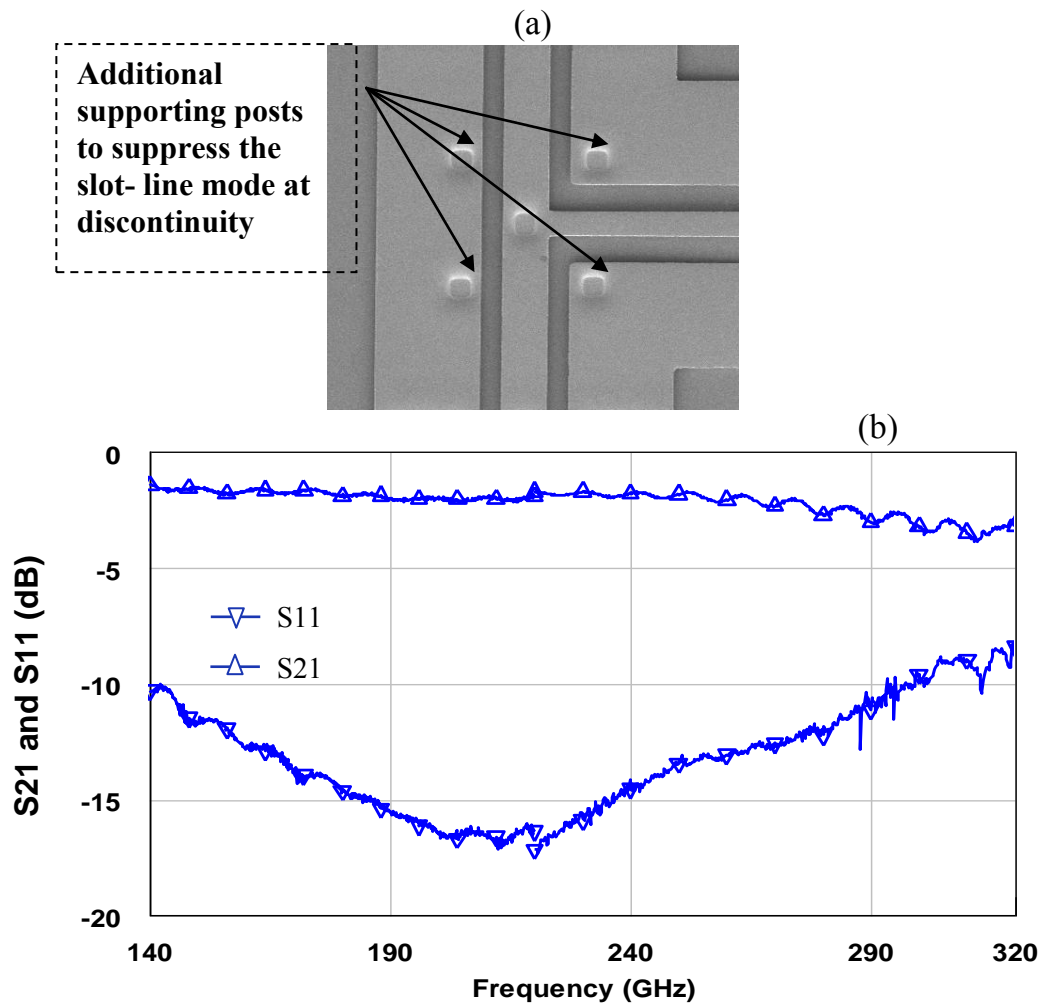


Figure 6.27: (a) Micrograph of an EGCPW stub at the junction with additional supporting posts in order to suppress the unwanted modes. (b) Measured results of the EGCPW short circuit stub without supporting posts at the junction

6-4-2 Quarter-wavelength EGCPW open-circuited stub

One of the coplanar waveguide components whose performance can be improved is the open circuited matching network. To study the performance of the open circuit stub using elevated grounded CPW, a series of open circuited 90° shunt stubs were designed

and fabricated with different centre frequencies. A micrograph of an implemented EGCPW matching network incorporating an open circuited stub is shown in Fig.6.28.

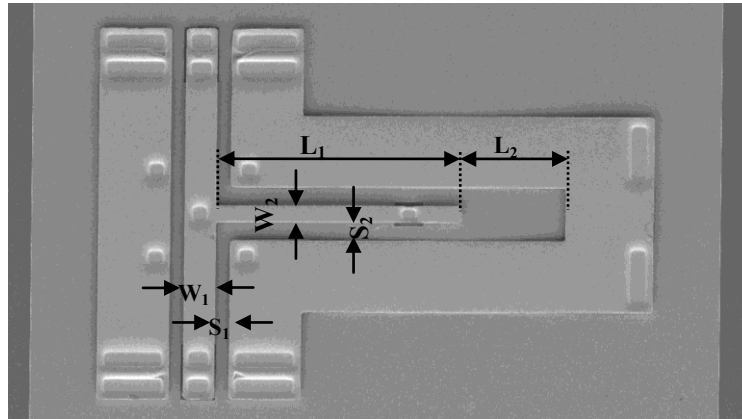


Figure 6.28: Micrograph of a EGCPW open-circuited stub. The stub dimensions are $L_1=350$, $L_2=145$, $S_1=19.5$, $S_2=26$, $W_1=45$, and $W_2=23.5$. All dimensions are in microns.

Figure 6.29 shows simulation and measurement results of the EGCPW open circuit stub.

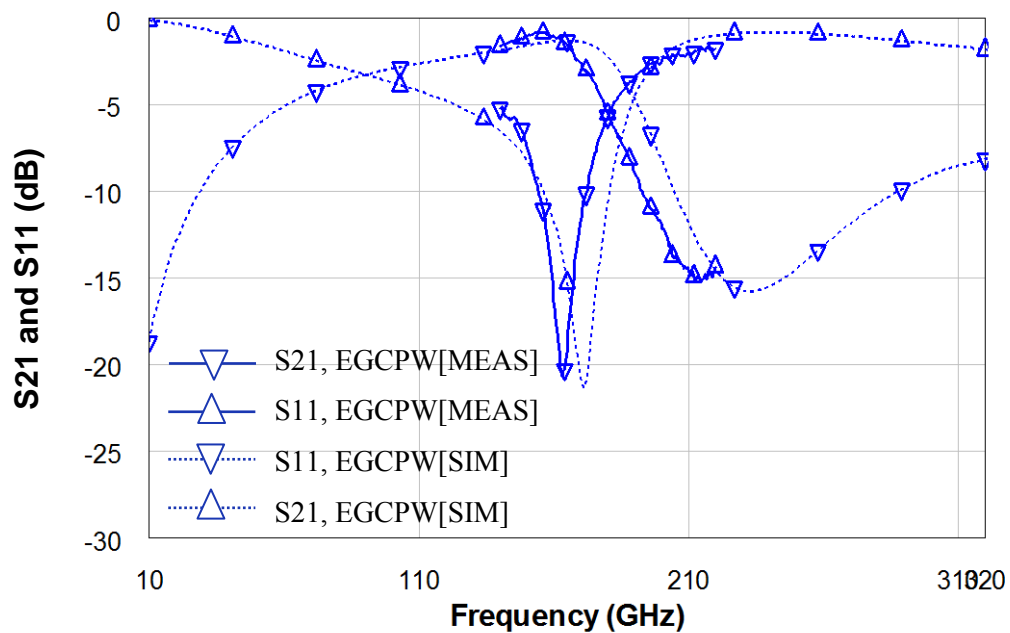


Figure 6.29: Measured and simulated S-parameters for a EGCPW open-end shunt stub.

To demonstrate the stub characteristics, a comparison between the measured and modelled characteristics of a matching network using EGCPW and the measured results of one implemented using CPW is given in Fig.6.30. The EGCPW network shows a return loss at the 90° frequency (163GHz) of the stub of 0.9dB and a 3dB-bandwidth of 95GHz (fractional bandwidth of 58%). The CPW open stub shows a return loss of 1.58dB at the frequency of 152GHz and a 3dB-bandwidth of 81GHz(54%). This is a reduction in loss of around 0.7dB while the bandwidths are comparable. The EGCPW open stub has a loaded quality factor of 1.7 and unloaded Q of 17.2 compared with 1.7 and 8.08 for CPW stub.

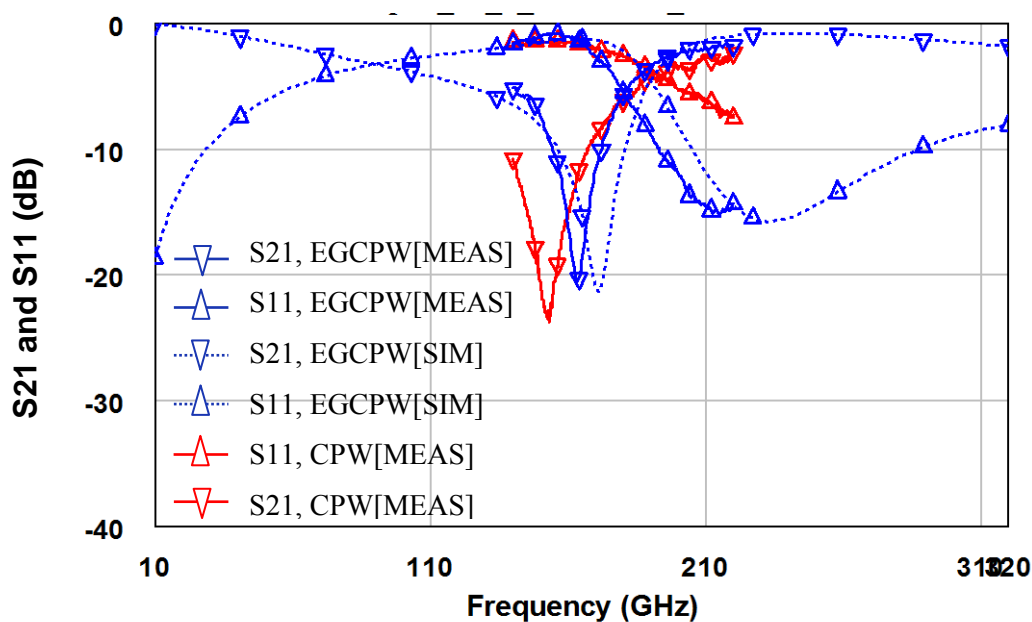


Figure 6.30: Measured and simulated S-parameters for a EGCPW open-end shunt stub compared with the measured S-parameters for CPW open-end stub.

To achieve optimum performance for the particular EGCPW network just discussed, we designed the shunt connected line to have a higher impedance than the series lines. However, even a non-optimized EGCPW network exhibits good performance with 1dB

return loss at centre frequency and a bandwidth of 105GHz. The impedance of EGCPW lines used for feed lines is roughly 35Ω and for stub is around 55Ω .

Increasing the elevation height from $6\mu\text{m}$ to $13\mu\text{m}$ yields an in-band return loss of 1dB at centre frequency of 147GHz with a bandwidth of 60GHz. Compared with low elevations, EGCPW open stub with higher elevation shows narrower fractional bandwidth of 39% and higher loaded quality factor of 2.5 and unloaded quality factor of 22.9. Also measurement results for identical structures with the only difference being the elevation height shows that almost doubling the elevation height ($6\mu\text{m}$ to $13\mu\text{m}$) leads to a trivial shift in resonance frequency of open stub (around 6GHz), Figure 6.31. This is because, unlike ECPW and SECPW structures, the effective permittivity of EGCPW structure remains the same regardless of the elevation. The shift to lower values in resonance frequency, as explained in previous section, is due to the increase in parasitic capacitance of the supporting posts of signal trace with the lower ground as a result of higher elevation. However, this shift is less pronounced here since the resonant frequency of an open-circuited stub, unlike that of a short-circuited stub, is only determined by the electrical length of the stub section and not the length of the feed sections. Changes in the supporting posts of the open-circuited stub slightly change the parasitic capacitance of this section situated at some point along the length of the stub. This results in a small shift in resonance frequency, from 153 to 147GHz, as can be clearly seen in Figure 6.31.

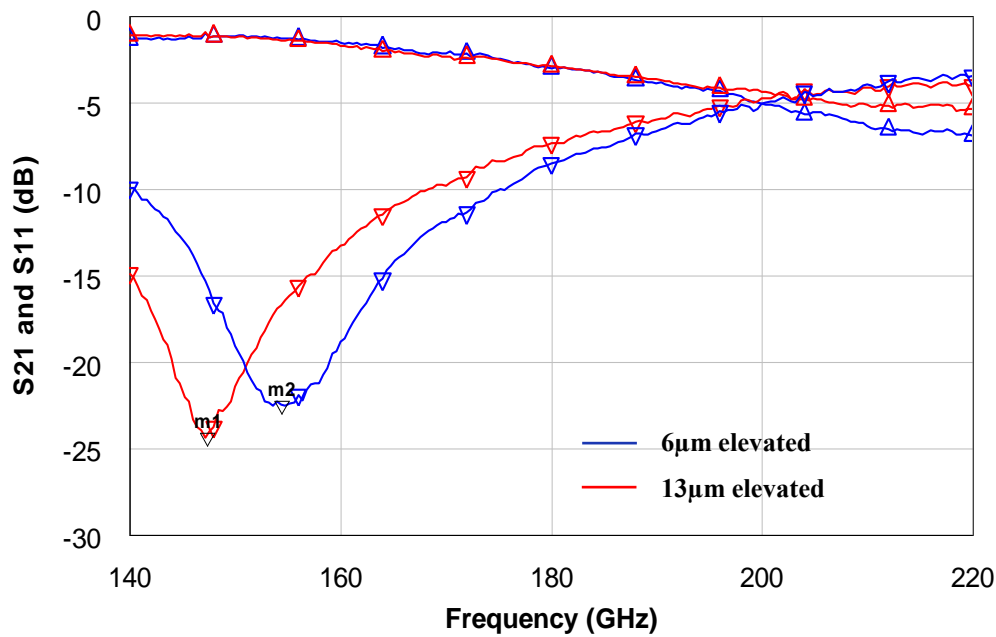


Figure 6.31: Measured S-parameters for EGCPW open-end shunt stub with different elevation heights. (m1: -24.3dB@147.32GHz, m2: -22.45dB@153.38GHz)

In general, the performance and also the resonant frequency of an open circuited stub implemented using EGCPW is insensitive to the elevation height and, therefore, low elevations (i.e $6\mu\text{m}$) can be used. A lower elevation is advantageous in terms of yield, mechanical strength and fabrication complexity.

6-5 Elevated-grounded CPW quarter-wavelength resonator filter

6-5-1 Quarter-wavelength EGCPW Band-pass filter

A third order quarter-wavelength band pass filter was designed by cascading 3 double short circuited stubs. Figure 6.32 shows a micrograph of the filter.

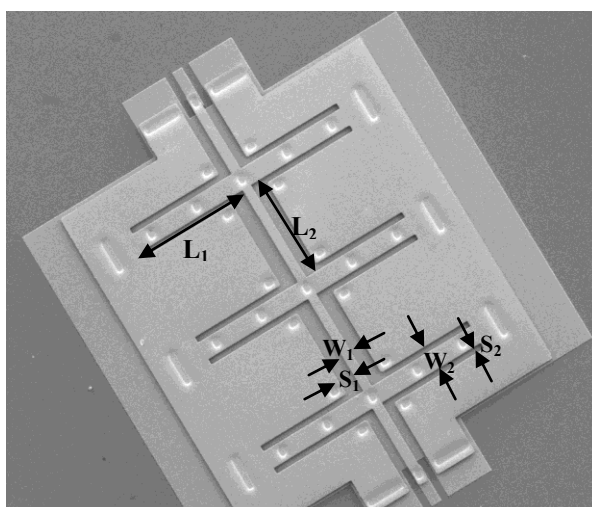


Figure 6.32: Micrograph of the 3rd-order EGCPW quarter-wavelength band-pass Filter. The filter dimensions are $L_1=270$, $L_2=252$, $S_1=37$, $S_2=14$, $W_1=21$, and $W_2=44.5$. All dimensions are in microns.

The measured/ simulated results of the filter are presented in Figure 6.33.

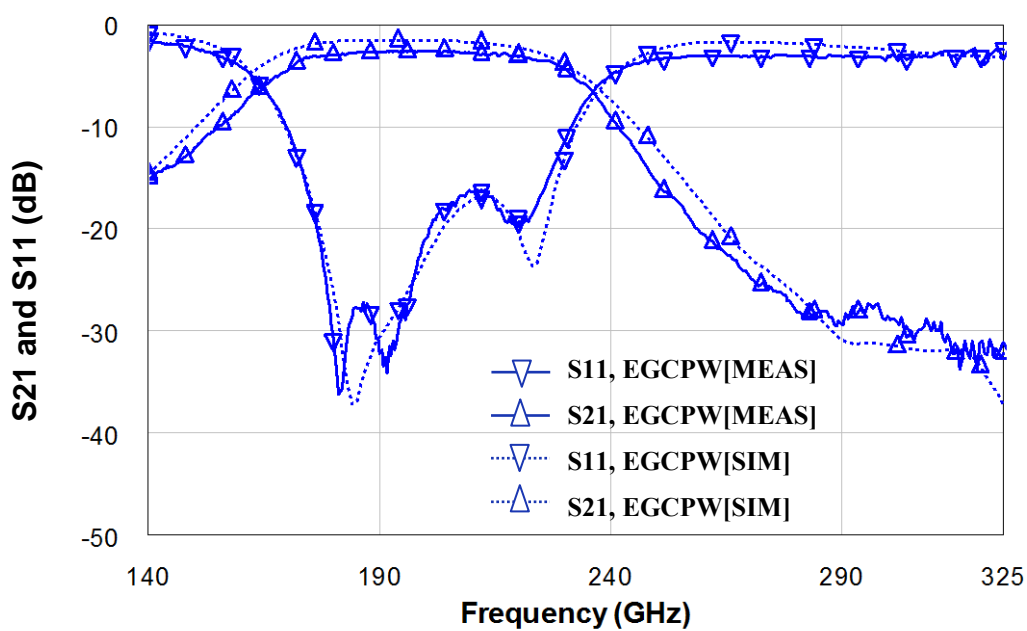


Figure 6.33: Measured and simulated S-parameters for a EGCPW band-pass filter.

Using elevated grounded CPW with very low radiation and attenuation characteristics results in a very low pass-band insertion loss for filters. With reference to Fig.6.34, a EGCPW 3rd-order band-pass filter with a centre frequency of 200GHz, has an insertion

loss of -2.6dB at the centre frequency with a 3dB-bandwidth of 66GHz (fractional bandwidth of 33%). Measurement/simulation results show very poor performance for the 3rd-order band-pass filter designed with CPW transmission media [chapter2], with an insertion loss of -6.19dB at the centre frequency of 220GHz and 3dB-bandwidth of 93GHz (45%).

There is thus an advantage in using elevated grounded CPW for sub-millimetre wave transmission line-based filters in preference to conventional CPW. Filters using these two structures (CPW and EGCPW) are compared in Fig.6.34.

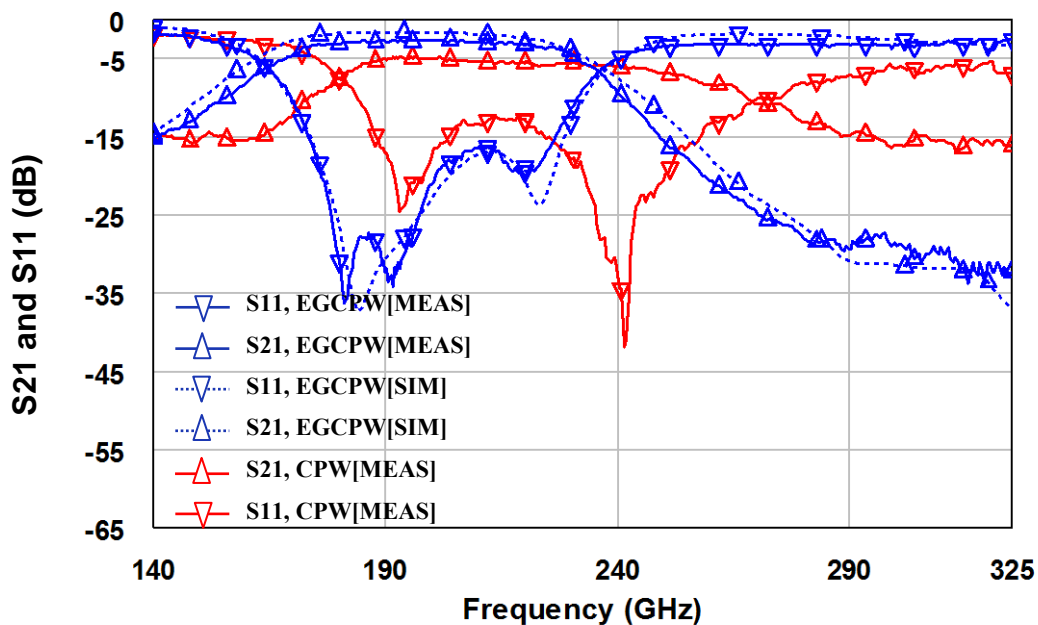


Figure 6.34: Measured and simulated S-parameters for a EGCPW band-pass filter compared with the measured S-parameters for CPW band-pass filter.

It was also observed that increasing the elevation height from $6\mu\text{m}$ to $13\mu\text{m}$ reduces the insertion loss to -1.9dB without significant change in the 3dB-bandwidth (69GHz). Similar to the open and short-circuited stubs, an increase in elevation height shifts the centre frequency of the band-pass filter to a lower value (by 11GHz) as a result of the effect of supporting posts at the centre trace.

6-5-2 Quarter-wavelength EGCPW Band-stop filter

By cascading multiple open circuited EGCPW shunt stubs, it is quite simple to realize a band stop filter. Accordingly, a third order quarter wavelength band-stop filter was designed and fabricated using EGCPW.

Using this circuit topology, however, did not yield performance greatly superior to the CPW implementation. Instead, a combination of short and open circuited shunt stubs, as discussed in chapter 2, is more effectively used to realize the band-stop filter, see Fig.6.35. This improves the performance of the filter with higher insertion loss in the stop-band and better roll-off characteristics.

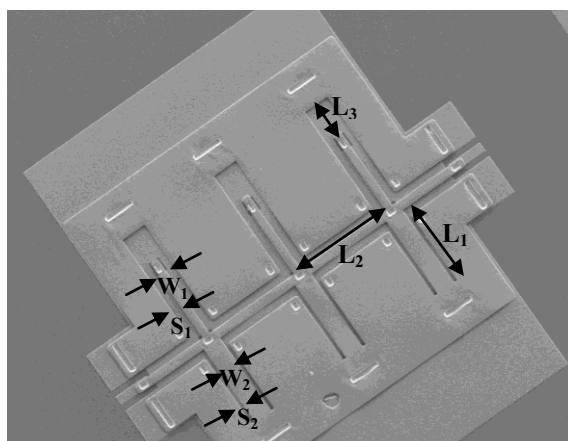


Figure 6.35: Micrograph the 3rd-order EGCPW quarter-wavelength band-stop Filter. The stub dimensions are $L_1=243$, $L_2=220$, $L_3=150$, $S_1=28$, $S_2=12.5$, $W_1=21$, and $W_2=51$. All dimensions are in microns.

Figure 6.36 shows the simulated/ measured results of this optimised EGCPW filter;

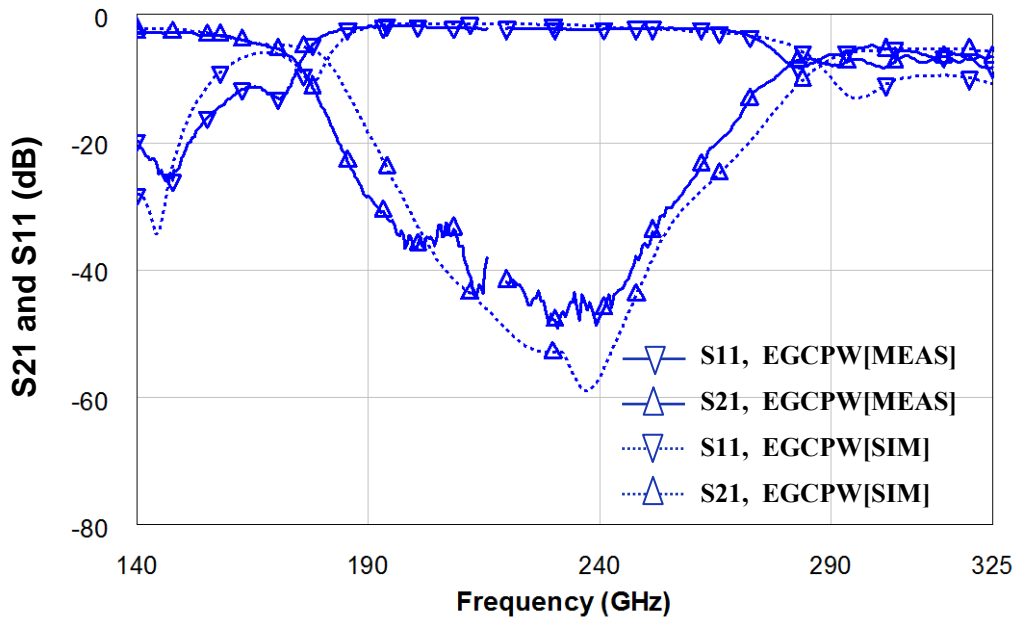


Figure 6.36: Measured and simulated S-parameters for a EGCPW band-stop filter.

From Fig.6.36, good agreement is observed between simulated and measured data. This filter, when implemented with $6\mu\text{m}$ elevation, shows a return loss of 2.1dB and insertion loss more than -40dB at the centre frequency of 224GHz and with a 3dB bandwidth of 102GHz (45%). Increasing the elevation height to $13\mu\text{m}$ shifts the resonant frequency down by 4GHz and reduces the return loss to 1.8dB at a centre frequency of 220GHz. The bandwidth stays the same at $6\mu\text{m}$ and $13\mu\text{m}$ heights.

The performance of this filter is also compared with the 3rd-order quarter wavelength CPW bandstop filter which uses only open circuit stubs in its configuration, Fig.6.37(a), as well as CPW filter with similar configurations, Fig.6.37(b).

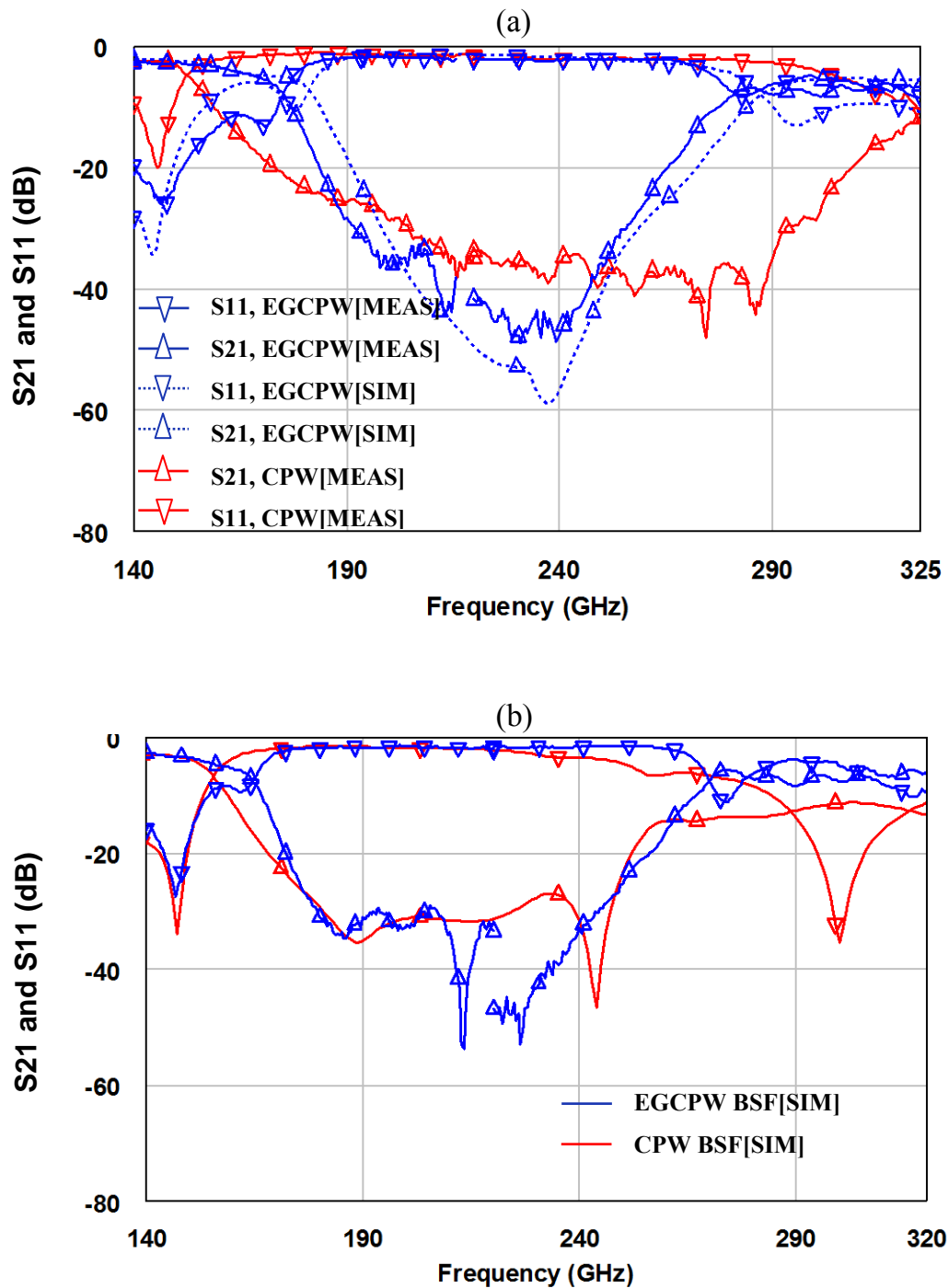


Figure 6.37: Measured and simulated S-parameters for a EGCPW band-stop filter compared with (a) measured CPW band-stop filter with just open stubs in its configuration and (b) modelled CPW band-stop filter with same configuration.

It can be seen in both cases, Fig.6.36 (a) and (b), that EGCPW band-stop filter shows better performance than the CPW band-stop filter. The performance degradation which

is observed at the upper band of simulated CPW band-stop filter with open/short configuration, Fig.6.37(b), is not monitored in the EGCPW filter and this filter, otherwise, show a very good upper band performance with a sharp roll-off characteristic.

6-7 Summary

A new type of elevated CPW transmission line, Elevated grounded CPW (EGCPW), has been investigated via analysis as well as by modelling and experiment, at frequencies up to 320GHz. Simple equations have been formulated to facilitate design work and show good agreement with simulation results. They indicate that the EGCPW structure, unlike ECPW which is advantageous mainly for high impedance transmission lines, can support wide impedance ranges from as low as 5Ω to as high as 100Ω . It was shown that the effective permittivity of the EGCPW stays approximately one regardless of line dimensions and elevation. Static loss analysis (carried out via a series of 2-D simulations) shows zero dielectric loss and lower conductor loss (almost half) for EGCPW lines compared with CPW. 3-D simulation shows very low losses for EGCPW up to very high frequencies (320GHz). Furthermore, the simulations show that while the loss mechanism of CPW and previously reported elevated CPW structures (ECPW and SECPW) depends on the lateral dimension of the line, the loss mechanism of EGCPW is almost entirely independent of geometry. This is a significant advantage of EGCPW over other CPW-based transmission lines since small lateral dimensions are not required to minimise the radiation loss which gives more freedom in the design and fabrication of this structure. 3-D simulations show that the supporting posts used to connect the top and bottom ground planes are necessary in EGCPW structures to eliminate the

resonances caused by an effective thin (air) substrate. It has been also shown that fabricated MMIC compatible EGCPW structures offer an extremely low insertion loss (2.5dB/mm) at 320GHz which is almost 2.5dB less than the insertion loss of an equivalent CPW line and 3.3dB less than an elevated CPW line at the same frequency. Although EGCPW transmission line examined in this work shows performance enhancement compared with CPW and previously reported elevated lines, still the design of supporting post placement has to be done well - perhaps by using continuous posts - to best optimise the EGCPW transmission line.

Circuit components such as short and open circuited resonators, band-pass filters and band-stop filters were designed using the EGCPW structure. Extra posts were used to connect the top and bottom grounds in all of the structures to eliminate the slotline modes at the junctions. Both short-circuited and open-circuited matching stubs were designed using high and low impedance transmission lines to reduce the bandwidth without introducing additional loss. In fact it is in the implementation of low-loss high and, especially, low impedance transmission lines that the advantage of EGCPW over CPW becomes most pronounced. The short circuited stub implemented by 6 μ m elevated EGCPW structure shows around 1dB less insertion loss at the centre frequency with the reduction in 3dB fractional bandwidth by 29% and improvement in quality factor by 27% when compared with CPW short stub. By increasing the elevation height from 6 to 13 μ m, significant improvement in the performance of EGCPW short circuit stub is observed. 13 μ m elevated EGCPW short shows 68% lower fractional bandwidth and 62% higher loaded quality factor and 82.5% higher unloaded quality factor compared with CPW counterpart. The 6 μ m elevated EGCPW open stub also shows better performance with lower in-band return loss by 0.7dB at centre frequency

compared with CPW open stub. By increasing the elevation height to $13\mu\text{m}$, the performance of the open stub is also improved. $13\mu\text{m}$ elevated EGCPW open stub has 3dB bandwidth of 60GHz (39% fractional bandwidth) and quality factor of 2.5. This shows improvement of 15% in bandwidth and 32% in loaded quality factor and 64.7% in unloaded quality factor compared with CPW open stub. Although higher elevated structures are showing higher quality factors, the structures with lower elevations are advantageous in terms of fabrication yield and mechanical strength. In general, all of the passive structures show a performance enhancement, compared with CPW counterparts, up to 320GHz. In particular, a EGCPW band-pass filter shows around 4dB reduction in in-band loss and around 30GHz(12%) reduction in 3-dB bandwidth compared with the CPW counterpart. The superior performance of the MMIC-compatible EGCPW structure in the implementation of transmission lines and basic passive components and also its ability to cover a wide range of impedances without introducing significant additional loss, makes it a near-perfect candidate for sub millimetre wave circuits and systems. Also, the EGCPW structure doesn't require additional fabrication process and is easily combined with CPW or other elevated CPW structures such as SECPW and ECPW.

Chapter 7

Conclusions and Future Work

7-1 Conclusions

The continued growth in millimetre and sub-millimetre wave applications for imaging and communication systems and the advent of HEMTs and HBTs with operating frequencies above 400GHz, has raised the need for transmission media with desirable electrical characteristics at these high frequencies. As discussed in the introduction, a key element in the implementation of high gain/high efficiency sub-millimetre wave circuits, is provision of high-Q /low loss passive networks.

The aim of this work was to conduct research into novel, low loss, transmission lines and distributed passive networks – specifically by analysing, modelling and realizing high quality passive distributed networks with operating frequencies up to 320GHz using air-bridge technologies.

7-1-1 Coplanar Waveguides

Background issues underlying the realisation of high quality transmission lines and other passive distributed networks were explored in depth.

Coplanar waveguides (CPW) suffer from high attenuation above approximately 100GHz, primarily due to radiative substrate leakage. In addition, practical CPW suffers from increased conductor losses due to increased resistivity of the narrow centre conductor for high impedance waveguides and high current density in narrow gaps for low impedance lines. In-depth simulations showed radiative losses to be most important at high frequencies, and whilst decreasing CPW lateral dimensions were shown to reduce this attenuation, fabrication limits severely constrain a designer's ability to achieve practical high and low impedance lines. Simulation, experimental and theoretical results also showed that through-substrate vias – a suggested technique for conductor-backed CPW transmission lines in practical systems – do not suppress resonances over the whole design frequency band, even using densely spaced vias. The conclusions of our investigation confirmed that new variations of CPW with better substrate isolation and more generous fabrication constraints are desirable for mm-wave applications.

In addition, problems with conventional CPW were discovered in the implementation of essential passive networks. Specifically, short-circuited matching stubs with centre frequencies of 180 and 240 GHz, designed with 50Ω transmission lines showed very poor performance with very wide bandwidth (~ 115 - 118%) and high insertion loss (~ 1.8 dB) at the centre frequency with loaded quality factor of approximately 0.8 and unloaded quality factor of 8.08. Deficient performance was also observed in quarter-wavelength band-pass and band-stop filters at a centre frequency of 240GHz. For example, a 3rd order quarter-wavelength band-pass filter with a centre frequency of 220GHz shows a 3-dB bandwidth of 103GHz (45% fractional bandwidth) and a high pass-band insertion loss of around 7dB. Low loss lines with high and low impedances

are required to achieve high-Q passive networks, and these cannot be obtained using conventional CPW.

7-1-2 Elevated Waveguides

The high frequency performance of three different elevated CPW structures utilising air-bridge technology – all-elevated CPW (ECPW), signal-elevated CPW(SECPW) and ground-elevated CPW(GECPW) – were investigated due to their potential in achieving substrate isolation. GECPW was shown to have poorer performance than the other elevated structures and was not considered further. Our development of improved fabrication processes allowed structures with elevation heights from 2 to 13 μm to be constructed and measured. Quasi-static analysis of all-elevated CPW lines was performed using conformal mapping to obtain analytic and semi-analytic results for line characteristic impedance and effective permittivity. These were augmented by 2-D simulations (with excellent agreement between analysis, simulation and measurement), and full 3-D simulation to correctly capture losses at high frequency.

SECPW showed slightly lower characteristic impedance and slightly higher effective permittivity than ECPW for comparably dimensioned lines. In general, low impedance transmission lines were shown to be easier to implement by SECPW than by ECPW. The loss mechanisms of ECPW and SECPW were investigated at low and high frequencies and compared with those for conventional CPW. Although ECPW and SECPW lines showed lower losses than CPW line at lower frequencies, at frequencies around 240GHz, their performance begins to degrade rapidly and becomes comparable with CPW attenuation at frequencies around 320GHz ($\sim 6\text{dB/mm}$). Attenuation due to radiation begins in SECPW at lower frequencies than in ECPW and in both cases is the result of the non-complete isolation of the CPW traces from the substrate. Loss analyses

for different geometries revealed that, by keeping the lateral dimensions of the line small, one can reduce the total attenuation at high frequencies, but at the expense of less freedom in the design and significantly poorer yield.

To investigate the sources of attenuation in practical elevated structures, ECPW and SECPW lines were designed and fabricated with different structures to investigate the effect of elevation height, CPW/ECPW transition pads, size and distance of supporting posts. For example, structures with the elevation height of 6 and 13 μm with supporting posts having different sizes i.e. $7 \times 7\mu\text{m}$ and $15 \times 22\mu\text{m}$ and various distances i.e. 90 μm \square 1mm, were fabricated. It was shown that the radiation characteristics are insensitive to variations in these parameters, with few further gains available, and it is concluded that a structure which is completely isolated from the substrate is required to remove the performance roll-off.

7-1-3 Elevated Passives

In addition, the performance of elementary distributed passive networks was investigated using elevated CPW structures. A set of short and open-circuited quarter-wavelength resonators implemented by ECPW and SECPW structures were designed, fabricated, measured and compared with their CPW counterparts. ECPW short circuited stubs showed superior performance to CPW equivalents, with narrower bandwidths and better matching to 50 Ω at the centre frequencies of 150GHz and 240GHz. A 6 μm elevated ECPW short-circuited stub designed for 240GHz, showed a reduction in bandwidth by 15GHz and a 33.5% higher loaded and 50% higher unloaded quality factors compared with a CPW short-circuited stub. The effect of parameters such as elevation height, CPW/ECPW transition and size and distance of supporting posts were found to be significant. By increasing the elevation height from 6 μm to 13 μm and/or

decreasing the size and number of supporting posts, improvements in the performance of the elevated CPW short-circuited stub are possible. An ECPW short-circuit stub with $13\mu\text{m}$ elevation showed 73GHz (30%) bandwidth, compared with 210GHz (115%) for CPW, loaded quality factor of 3.2, compared with 1.2 for CPW, and unloaded quality factor of 17.09, compared with 4.27 for its CPW-counterpart.

Similarly improved performance was observed for SECPW short-circuited stubs - as long as high elevations, such as $13\mu\text{m}$, are used. For example, a $13\mu\text{m}$ elevated SECPW short-circuited stub has a 3dB bandwidth of 76GHz and a loaded quality factor of 3 and unloaded Q of 17.83. This is an 85% reduction in 3dB fractional bandwidth and a 73% improvement in quality factor compared with the reference CPW short-circuited stub.

On investigating quarter-wavelength open-circuited resonators, it was observed that open-circuited stubs implemented by mid-range impedance, i.e. 60Ω elevated CPW, do not show as significant a performance improvement over CPW open stubs as was observed for short-circuited stubs. A bandwidth reduction of around 11GHz and a 22-27% improvement in loaded and unloaded quality factors were achieved for the open-stub by using either ECPW or SECPW instead CPW. Optimising the elevated CPW open-circuit stubs by using high impedance lines at the stub and low impedance lines at the feeds results in a lower bandwidth without significant increase to in-band loss, while applying the same rule to a CPW open-circuited stub decreases the bandwidth but results in a significant in-band loss and performance degradation. This is due to the high attenuation of the CPW transmission line at low and high impedance ranges.

In addition, the performance of quarter-wavelength band-pass and band-stop resonator filters implemented in ECPW was investigated. An ECPW band-pass filter with a centre frequency of 240GHz shows significant performance improvement its CPW counterpart, with a 25GHz (8%) narrower bandwidth and an in-band loss reduction of

4dB. The advantages of all-elevated CPW in realising sub-millimetre wave band-stop filters were also presented.

To summarise, it is in the implementation of low loss distributed passive networks, matching stubs and filters that the main advantages of elevated CPW structures were discovered. Elevated CPW structures offer low loss even at extremes of characteristic impedance and higher Q networks follow as a result. It should be mentioned though, that, while achieving high impedances is very easy in elevated structures, implementing low impedances can be more challenging.

7-1-4 Elevated-Grounded Waveguides

Although all-elevated CPW was shown to be advantageous to conventional CPW in many cases, it is still not an ideal transmission media for sub-millimetre wave structures due to its tendency to radiate at sufficiently high frequencies for practical circuit dimensions. A structure with a more complete isolation from the substrate, elevated grounded CPW (EGCPW), was developed and investigated for sub-millimetre wave applications.

EGCPW was analysed in terms of characteristic impedance and effective permittivity, and simple formulas along with a synthesis technique based on Newton's method were developed to facilitate circuit design using the technology. It was shown that EGCPW can conveniently support a wide range of impedances (as low as 5Ω to as high as above 100Ω), whilst its effective permittivity stays close to 1.0 regardless of elevation height and line geometry.

Static analysis showed a dielectric loss of zero and conductor losses slightly higher than ECPW but much lower than CPW. The main advantage of EGCPW was shown to be very low attenuation at high frequencies regardless of the lateral line geometry. In

addition, it was found that the supporting posts which are used to elevate the ground planes, not only do not degrade performance, but are actually integral in keeping the top and bottom grounds at the same potential, preventing resonances in the structure. These supporting posts act in a similar way to via holes in conductor-backed CPW, but the air-bridge fabrication process is much simpler than the fabrication process of adding via holes to a thin dielectric substrate. Using air-bridge technology also lets us to have a structure with air substrate in this case while this is not possible to achieve when the process of adding via holes is been used.

To investigate the performance of the EGCPW line in real life, a set of transmission lines with various geometries were designed, fabricated, and measured. The experimental results agree with simulation and show the extremely low attenuation at high frequencies. An insertion loss for 50Ω EGCPW line is 2.5dB/mm at 320GHz which is 2.5dB/mm less than CPW and around 3.3dB/mm less than the insertion loss of ECPW.

7-1-5 Elevated-Grounded Passives

Quarter-wavelength short and open-circuited resonators, band-pass and band-stop filters were designed and fabricated. In the design of quarter-wavelength resonators and filters, additional posts were considered in order to keep the grounds at the same potential at junctions. This, unlike with CPW and other elevated CPW structures, does not require additional fabrication steps.

Compared with CPW, all of these passive components showed superior performance, with reductions in bandwidth and in-band loss. At an elevation of $6\mu\text{m}$, the EGCPW short-circuited shunt stub showed 1dB less insertion loss, 29% less fractional bandwidth and 27% better quality factor than its CPW counterpart. The EGCPW open-circuited

stub showed 0.7dB less return loss and a higher insertion loss at the centre frequency than the CPW stub. On increasing elevation to 13 μ m, the EGCPW short circuit stub showed superior performance with 3dB bandwidth of 102GHz(50%), with 0.7dB insertion loss at the centre frequency of 204GHz and a loaded quality factor of 2. This is a 108GHz lower bandwidth, 1.1dB less insertion loss and 60% higher loaded and 82.5% higher unloaded quality factor than the CPW equivalent. This stub also shows 34% higher unloaded quality factor than 13 μ m elevated ECPW and SECPW short-circuited stubs which is also the highest unloaded quality factor achieved in this work.

The 13 μ m elevated EGCPW open stub has a bandwidth of 60GHz (20GHz less than CPW), a loaded quality factor of 2.5 and unloaded quality factor of 22.9, which are the highest quality factors for an open stub amongst all of the open stubs which were investigated in this work – 64.7% higher Q_u than CPW and 47.6% higher Q_u than other ECPW and SECPW open stubs.

Both EGCPW band-pass and band-stop filters show significant performance improvement compared with CPW filters and better performance than the ECPW filters. A 220GHz EGCPW band-pass filter shows a 3dB bandwidth of 66GHz (33% fractional bandwidth) and insertion loss of 2.5dB at centre frequency. This is 37GHz (12%) narrower in bandwidth and 4.5dB lower in insertion loss than CPW band-pass filters and 12GHz(4%) narrower in bandwidth and 0.5dB lower in insertion loss than the ECPW band-pass filter. Also, by implementing the EGCPW band-stop filter with a new combination of open and short- circuited quarter-wavelength stubs, a filter with 109GHz (49% fractional) 3dB bandwidth with low return loss and high in-band insertion loss was achieved. This filter shows a 45GHz lower bandwidth with much better roll-off characteristics than the CPW filter implemented by using quarter-wavelength open stubs. It should be mentioned that in the design of all of the EGCPW

resonators and filters, combinations of low and high impedance transmission lines have been used. This increased the quality factor of the components without introducing significant additional loss. In fact it is in this implementation of low-loss high and, especially, low impedance transmission lines that the advantages of EGCPW over CPW become even more pronounced.

Due to the superior performance of the MMIC-compatible EGCPW structure in the implementation of transmission lines and, also, basic distributed passive networks, as well as the ability to provide a high range of characteristic impedances, this structure is suggested for use in sub-millimetre wave circuits in order to increase the efficiency and reduce loss. Due to the almost complete isolation of this structure from the substrate, it can be used to implement the components and circuits on any substrate, such as low resistivity Silicon, to maintain low cost and high functionality. This is a significant advantage of this structure over CPW and previously reported elevated CPW structures. Also, this structure can be easily combined with other elevated CPW structures such as ECPW and SECPW in the circuits to make the best use of each lines advantages and obtain maximum efficiency as a result.

7.2 Future work

It is expected that when fully integrated with active components, the structures developed in this work will form a platform for the realisation of high efficiency, high gain circuits. Suggestions for future work which should directly follow from this project are:

- Fabrication and optimisation of elevated grounded CPW using *continuous* supporting posts connecting the top and bottom ground planes, which are likely to further improve the performance of this type of structure.
- Realisation of substrate-isolated elevated grounded CPW on different substrates (e.g. Silicon) in order to investigate its electrical properties when constructed on more cost effective materials.
- Implementation of passive distributed networks such as couplers and phase shifters.
- Integration of passive components with active devices to realise integrated high gain/high efficiency circuits and systems.

There is growing interest in pushing technologies to sub-millimetre wave frequencies due to the benefits that can result in areas such as: passive/active imaging, and next generation high data rate communications. Research into active devices in the sub-millimetre regime has led to the development of transistors with operating frequencies above 400GHz, and this work describes developments in the passive networks necessary to support integrated circuits and systems with high gain and maximum functionality – and since these novel passive structures are substrate-isolated, they can be integrated with the active devices without significant performance degradation. However, continued improvements in device technology will require further breakthroughs in transmission line and passive network technologies, pushing in the long term to yet higher frequencies. Even within the sub 400GHz frequency bands, this work has enabled considerable medium term research opportunity in the detailed work of optimising the integration of active and passive devices into highly functional MICs, MMICs and SMMICs (Sub-mm-wave ICs) – especially in the low cost, and high efficiency regimes.

References

- [1] D. M. SHEEN, D. L. MCMAKIN, AND T. E. HALL, "Three-Dimensional Millimeter-wave Imaging for Concealed Weapon Detection," *IEE Trans. on Microwave Theory and Techniques*, vol.49, no. 9, 1581-1592, Sep 2001.
- [2] T. GLOBUS, D. L. WOOLARD, A. C. SAMUELS, B. L. GELMONT, J. HESLER, T.W.CROWE, AND M. BYKHOVSKAIA, "Submillimeter-wave FTIR spectroscopy of DNA macromolecules and related materials," *Journal of Applied Physic.*, vol. 91, no. 9, pp. 6106–6113, 2002.
- [3] Y. OGAWA, K. KAWASE, M. YAMASHITA, AND H. INOUE, "Non-destructive inspection techniques for illicit drugs using terahertz imaging," in *Proc. Conf. Lasers and Electro-Optics*, vol. 1, pp. 3, May 2004.
- [4] R. APPLEBY, R.N. ANDERTON, "Millimeter-Wave and Submillimeter-Wave Imaging for Security and Surveillance," *proc. IEEE*, vol. 95, Aug. 2007, pp. 1683 - 1690.
- [5] B.D. NGUYEN, C. MIGLIACCIO, CH. PICHOT, K. YAMAMOTO, AND N. YONEMOTO, "W-Band Fresnel Zone Plate Reflector for Helicopter Collision Avoidance Radar," *IEEE Trans. on Antennas and propagation.*, vol. 55, pp. 1452 - 1456, May 2007.
- [6] M. J. ROSKER, "Technologies for Next Generation T/R Modules," *Proc. Conf of IEEE, Radar Conference*, pp. 944-947, June 2007.

- [7] T. G. PHILLIPS AND J. KEENE, “ Sub-Millimeter Astronomy,” *Proc. Conf of IEEE*, vol. 80, pp. 1662-1678, Aug 2002.
- [8] F. K. Y. LO, “ALMA and Sub-Millimeter Astronomy,” *Proc. Conf. IRMMW-THz*, pp. 3, 2006.
- [9] J. C. DICKINSON, T. M. GOYETTE, AND J. WALDMAN, “High resolution imaging using 325 GHz and 1.5 THz transceivers,” *presented at the 15th Int. Symp. Space Terahertz Technology*, Northampton, 2004.
- [10] K. ELGAID, D. MORAN, H. MCLELLAND, M. HOLLAND, AND I. G. THAYNE, “Low noise high performance 50nm T-gate metamorphic HEMT with cut-off frequency fT of 440GHz for millimeter wave imaging receivers applications,” *International conference on Indium phosphide and related materials*, no.10, pp. 141-143, May 2005.
- [11] V. RADISIC, D. SAWDAI, D. SCOTT, W. R. DEAL, DI. LINH DANG LI, J. CHEN, A. FUNG, L. SAMOSKA, T. GAIER, AND R. LAI, “Demonstration of a 311-GHz Fundamental Oscillator Using InP HBT Technology,” *IEE Trans. on Microwave Theory and Techniques*, vol. 55, 2329-2335, Nov 2007.
- [12] H. EISELE AND R. KAMOUA, “Submillimeter-wave InP Gunn devices,” *IEEE Trans. Microw. Theory Tech.*, vol. 52, no. 10, pp. 2371–2378, Oct 2004.
- [13] M. URTEAGA, D. SCOTT, T. MATHEW, S. KRISHNAN, Y. WEI, AND M.J.W. RODWELL, “Single-Stage G-band HBT Amplifier with 6.3dB gain at 175GHz,” *Gallium Arsenide Integrated Circuit (GaAs IC) Symp, 23rd Annual technical Digest*, pp. 83-87, Oct 2001.
- [14] A. TESSMANN, “220-GHz Metamorphic HEMT Amplifier MMICs for High-Resolution Imaging Applications,” *IEEE Journal of Solid-State Circuits*, vol. 40, o. 10, pp. 2070-2076, Oct 2005.

- [15] W. R. DEAL, X. B. MEI, V. RADISIC, W. YOSHIDA, P. H. LIU, J. UYEDA, M. BARSKY, T. GAIER, A. FUNG, L. SAMOSKA, AND R. LAI, "Demonstration of a 270GHz MMIC Amplifier using 35-nm InP HEMT Technology," *IEEE Microwave and Wireless Components Lett*, vol.17, no. 5, pp. 391-393, May 2007.
- [16] T. GAIER, L. SAMOSKA, A. FUNG, W. R. DEAL, V. RADISIC, X. B. MEI, W. YOSHIDA, P. H. LIU, J. UYEDA, M. BARSKY, AND R. LAI, "Measurement of a 270GHz Low Noise Amplifier With 7.5dB Noise Figure," *IEEE Microwave and Wireless Components Lett*, vol.17, no. 7, pp. 546-548, July 2007.
- [17] X. B. MEI, W. YOSHIDA, W.R. DEAL, W. H. LIU, J. LEE, J. UYEDA, J. DANG, J. WANG, W. LIU, D. LI, M. BARSKY, Y. M. KIM, M. LANGE, T. P. CHIN, V. RADISIC, T. GAIER, A. FUNG, L. SAMOSKA, AND R. LAI, "35-nm InP HEMT SMMIC Amplifier with 4.4-dB Gain at 308GHz," *IEEE Electron Device Lett*, vol.28, no. 6, pp. 470-472, June 2007.
- [18] W. R. DEAL, X. B. MEI, V. RADISIC, W. YOSHIDA, P. H. LIU, J. UYEDA, M. BARSKY, T. GAIER, A. FUNG, AND R. LAI, "Demonstration of a S-MMIC LNA with 16-dB Gain at 340GHz," *IEEE Compound Semiconductor Integrated Circuit Symposium*, pp. 1-4, Oct 2007.
- [19] V. RADISIC, X. B. MEI, W. R. DEAL, W. YOSHIDA, P. H. LIU, J. UYEDA, M. BARSKY, L. SAMOSKA, A. FUNG, T. GAIER, AND R. LAI, "Demonstration of Sub-Millimeter-wave Fundamental Oscillators Using 35-nm InP HEMPT Technology," *IEEE Microwave and Wireless Components Lett*, vol.17, no. 3, pp. 223-225, March 2007.

- [20] A. ARBABIAN, AND ALI. M. NIKNEJAD, "A Tapered Cascaded Multi-Stage Distributed Amplifier with 370GHz GBW in 90nm CMOS," *Radio Frequency Integrated Circuits Symposium, 2008 RFIC*, pp. 57-60, April 2008.
- [21] R. LAI, X. B. MEI, S. SARKOZY, W. YOSHIDA, P. H. LIU, J. LEE, M. LANGE, V. RADISIC, K. LEONG, W. DEAL, "Sub 50 nm InP HEMT with $f_T=586$ GHz and Amplifier Circuit gain at 390GHz for Sub-millimeter Wave Applications," *International Conference on, Indium Phosphide & Related Materials (IRRM)*, pp. 1-3, May 2010.
- [22] L. SAMOSKA, D. PUKALA, M. SORIA, AND G. SADOWY, "A G-band Multi-Chip T/R Module for Radar Applications," *33rd International Conference on Infrared, Millimeter and Terahertz Waves, IRMMW-THZ 2008*, pp. 1-2, Sep 2008.
- [23] A. TESSMANN, I. KALLFASS, A. LEUTHER, H. MASSLER, M. KURI, M. RIESSLE, M. ZINK, R. SOMMER, A. WAHLEN, H. ESSEN, V. HURM, M. SCHLECHTWEG, AND O. AMBACHER, "Metamorphic HEMT MMICs and Modules for use in a High-Bandwidth 210GHz Radar," *IEEE Journal of Solid-State Circuits*, vol. 43, pp. 2194-2205, Oct 2008.
- [24] R. LAI, AND S. SARKOZY, "HEMT MMW MMICs for Radiometer Sensor Application," *Microwave Symposium Digest (MTT), 2010 IEEE MTT-S International*, pp. 832-835, July 2010.
- [25] Z. LIU, J. C. MIDKIFF, H. XU, T. W. CROWE, AND R. M. WEIKLE, "Broadband 180 phase-shifters using integrated submillimeter-wave Schottky diodes," *IEEE Trans. on Microwave Theory and Techniques.*, vol. 53, No. 9, Sep 2005.

- [26] J. D. PARK, S. KANG, AND ALI. M. NIKNEJAD, "A 0.38THz Fully integrated Transceiver Utilizing Quadrature Push-Push Circuitry," *VLSI Circuits (VLSIC), 2011 Symposium on*, pp. 22-23, Aug 2011.
- [27] L. P. B. KATEHI, "Novel transmission lines for the submillimeter-wave region," *Proceedings of the IEEE*, vol. 80, no. 11, pp. 1771-1787, Nov 1992.
- [28] H. J. CHENG, J. F. WHITAKER, T. M. WELLER, AND L. P. B. KATEHI, "Terahertz-Bandwidth Characteristics of Coplanar Transmission Lines on Low Permittivity Substrate," *IEE Trans. on Microwave Theory and Techniques*, vol. 42, no. 12, pp. 2399-2406, Dec 1994.
- [29] D. M. POZAR, *Microwave Engineering*, pp. 56, New York, MA : John Wiley and sons, 2nd edition, 1998.
- [30] K. CHANG, I. BAHL, AND V. NAIR, *RF and Microwave Circuit and Component Design for Wireless Systems*, pp.105, New York, MA : John Wiley and sons, 2001.
- [31] R.M. BARRETT, "Microwave Printed Circuits - A Historical Survey," *IRE Trans. on Microwave Theory and Techniques*, vol. 3, pp. 1-9, March 1955.
- [32] D. D. GRIEG, AND H. F. ENGELMANN, "microstrip- A New Transmission Technique for the Klilomegacycle Range," *Proceeding of the IRE*, vol. 40, pp. 1644-1650, 1952.
- [33] S. B. COHN, "Slot Line on a Dielectric Substrate," *Microwave Symposium, G-MTT International*, pp.99-105, 1969.
- [34] J. I. SMITH, "The Even- and Odd- Mode Capacitance Parameters for Coupled Lines in Suspended Substrate," *IEE Trans. on Microwave Theory and Techniques*, vol. 19, pp. 424-431, 1971.

- [35] R. W. JACKSON, "Considerations in the Use of Coplanar Waveguide For Millimeter-Wave Integrated Circuits," *IEE Trans. on Microwave Theory and Techniques*, v. 34, no. 12, pp. 1450-1456, Dec 1986.
- [36] C. P. WEN, " Coplanar Waveguide: A Surface Strip Transmission Line Suitable for Nonreciprocal Gyromagnetic Device Applications," *IEEE Trans. on Microwave Theory and Techniques*, vol. 17, pp.1087-1090, December 1969.
- [37] R. A. PUCEL, "Design Considerations for Monolithic Microwave Circuits," *IEEE Trans. on Microwave Theory and Techniques*, vol. MTT. 29, no. 6, pp. 513-534, June 1981.
- [38] J. BROWNE, "Broadband Amps Sport Coplanar Waveguide," *Microwaves RF*, vol. 26, no. 2, pp. 131-134, Feb 1987.
- [39] J. BROWNE, "Coplanar MIC Amplifier Bridges 0.5 To 18.0 GHz," *Microwaves RF*, vol. 26, no. 6, pp. 194-195, June 1987.
- [40] R. E. STEGENS AND D. N. ALLISS, "Coplanar Microwave Integrated Circuit for Integrated Subsystems," *Microwave Sys. News Comm. Tech.*, vol. 17, no. 11, pp. 84-96, Oct 1987.
- [41] M. MURAGUCHI, T. HIROTA, A. MINAKAWA, K. OHWADA, AND T. SUGETA, "Uniplanar MMIC's and Their Applications," *IEEE Trans. on Microwave Theory and Techniques*, vol. 36, no. 12, pp. 1896-1900, Dec 1988.
- [42] M. RIAZIAT, E.PAR, G. ZDASIUK, S. BANDY, AND M. GLENN, "Monolithic Millimeter Wave CPW Circuits," *IEEE MTT-S International, Microwave Symposium Digest*, vol. 2, pp. 525-528, Dec 1989.
- [43] J. BROWNE, "Broadband Amp Drops through Noise Floor," *Microwaves RF*, vol. 31, no. 2, pp. 141-144, Feb 1992.

- [44] M. Y. FRANKEL, "Terahertz Attenuation and Dispersion Characteristics of Coplanar Transmission Lines," *IEEE Transactions on microwave theory and techniques*, vol.39, no.6, 1991.
- [45] H. CHENG, J. F. WHITAKER, T. M. WELLER, AND L. P. B. KATEHI, "Terahertz-Bandwidth Characterization of Coplanar Waveguide on Dielectric Membrane via Time-Domain Electro-optic Sampling," *IEEE MTT-S International Microwave Symposium Digest*, vol.1, pp. 477 - 480, 1994.
- [46] J. ZHANG, S. ALEXADROU, AND T. Y. HSIANG, "Attenuation Characteristics of Coplanar Waveguides at Subterahertz Frequencies," *IEEE Transactions on microwave theory and techniques*, vol.53, no.11, 2005.
- [47] N. I. DIB, W. P. HAROKOPUS, W.P., P. B. KATEHI, C. C. LING, AND G. M. REBEIZ, "Study of A Novel Planar Transmission Line," *Microwave Symposium Digest*, IEEE MTT-S International, vol. 2, pp. 623-626, June1991.
- [48] F. SCHNIEDER, R. DOERNER, AND W. HEINRICH, "High-Impedance Coplanar Waveguide with Low Attenuation," *IEEE Microwave and Guided Wave Letters*, vol. 6, no. 3, pp. 117-119, March 1996
- [49] E. RIUS, G. PRIGENT, H. HAPPY, G. DAMBRINE, S. BORET, AND A. CAPPY, "Wide- and narrow-band bandpass coplanar filters in the W-frequency band," *IEEE Transactions on microwave theory and techniques*, vol. 51, no. 3, March 2003.
- [50] G. WOLF, G. PRIGENT, E. RIUS, S. DEMICHEL, R. LEBLANC, G. DAMBRINE, AND H. HAPPY, "Band-pass coplanar filters in the G-frequency band," *IEEE Transactions on microwave theory and techniques*, vol. 15, no. 11, Nov 2005.

- [51] W. HEINRICH, F. SCHNIEDER, AND T. TISCHLER, "Dispersion and radiation characteristics of conductor-backed CPW with finite ground width," *in IEEE Int. Microwave Symp. Dig.*, Boston, pp. 1663-1666, Jun 2000.
- [52] W. H. HAYDL, "On the use of vias in conductor-backed coplanar circuits," *IEEE Transactions on microwave theory and technique*, vol. 50, pp. 1571-7, Jun 2002.
- [53] A. G. ENGEL, JR. AND P. B. KATEHI, "Low-Loss monolithic transmission lines for sub-mm and terahertz frequency applications," *IEEE Trans. on Microwave Theory and Techniques*, vol. 39, pp. 1847-1854, Nov 1991.
- [54] E. KIM AND G. M. REBEIZ, "Micromachined Waveguides", *Radiation Lab Report*. no. RL-881, Feb 1992.
- [55] M. YAP, Y-C TAI, W. R. MCGRATH, AND C. WALKER, "Silicon micromachined waveguides for millimeter and submillimeter wavelengths," *presented at the 3rd International Symposium on Space Terahertz Technology*, Ann Arbor, MI, Mar 1992.
- [56] N. I. DIB, W. P. HAROKOPOUS, P. B. KATEHI, C. C. LING, AND G. M. REBEIZ, "Study of a novel planar transmission line," *presented at the 1991 International Symposium of IEEE Microwave Theory and Techniques Society*, Boston, MA, June 1991.
- [57] H. M. HEILIGER, M. NAGEL, H. G. ROSKOS, H. KURZ, F. SCHNIEDER, AND W. HEINRICH, "Thin-film microstrip lines for MM and sub-MM/wave on-chip interconnects," *IEEE Int. Microwave Symp. Digest, IEEE MTT-S International*, pp. 421-424, vol. 2, Jun. 1997.
- [58] K. HETTAK, M. G. STUBBS, K. ELGAID, AND I. G. THAYNE, "Design and characterization of elevated CPW and thin film microstrip structures for

- millimeter-wave applications,” *IEEE Microwave Conference, European*, pp. 2598-2602, Oct 2006.
- [59] J. H. PARK, B. W. CHANG, J. SANGHWA, T. HONG, K. YOUNGWOON, K. K. YONG, “Novel Micromachined CPW transmission lines for application in millimeter-wave circuits,” *IEEE International Conference, Microprocessors and Nanotechnology*, pp. 4-7, Oct. 2005.
- [60] S. N. LEE, J. LEE, Y. J. KIM AND J. G. YOON, “Micromachined elevated CPWs for high performance microwave circuits,” *Journal of Micromechanics and Microengineering*, pp. 2598-2602, Oct 2006.
- [61] A. G. ENGEL, JR. AND P. B. KATEHI, "Analysis of microstrip Structures on and near Dielectric Ridges Using an Integral Equation-Mode Matching Technique," *IEEE Int. Microwave Symp. Digest, IEEE MTT-S International*, pp. 135-138, Jun. 1991.
- [62] W. V. MCLEVIGE, T. ITOH, AND R. MITTRA, “New Waveguide Structures for Millimeter-Wave and Optical Integrated Circuits,” *IEEE Transactions on microwave theory and techniques*, vol. 23, pp. 788-794, Oct 1975.
- [63] K. OGUSU, “Numerical Analysis of the Rectangular Dielectric Waveguide and its Modifications,” *IEEE Transactions on microwave theory and techniques*, vol. 25, pp. 874-885, Nov 1977.
- [64] K. SOLBACH, I. WOLFF, “The Electromagnetic Fields and the Phase Constants of Dielectric Image Lines,” *IEEE Transactions on microwave theory and techniques*, vol. 26, pp. 266-274, Apr 1978.
- [65] T. ITOH, “Trapped Image Guide For Millimeter-Wave Circuits,” *IEEE Transactions on microwave theory and techniques*, vol. 28, pp. 1433-1436, Dec 1980.

- [66] W. TAICHI, AND S. E. SCHWARZ, "Design of Dielectric Ridge Waveguides for Millimeter-Wave Integrated Circuits," *IEEE Transactions on microwave theory and techniques*, vol. 31, pp. 128-134, Jan 2003.
- [67] A. G. ENGEL, JR. AND P. B. KATEHI, "Frequency and Time Domain Characterization of microstrip-Ridge Structures," *IEEE Transactions on microwave theory and techniques*, vol. 41, pp. 1251-1262, Aug 1993.
- [68] A. G. ENGEL, N. I. DIB, L. P. B. KATEHI, "Characterization of a Shielded Transition to a Dielectric Waveguide," *IEEE Transactions on microwave theory and techniques*, vol. 42, pp. 847-854, May 1994.
- [69] K. Y. LEE, N. LABIANCA, S. A. RISHTON, S. ZOLGHARNAIN, J. D. GELORME, J. SHAW, AND T. H. P. CHANG, "Micromachining applications of a high resolution ultrathick photoresist," *Journal of Vacuum Science & Technology B*, vol. 13, pp. 3012-3017, 1995.
- [70] S. W. MOON, C. M. MANN, B. J. MADDISON, I. C. E. TURCU, U. ALLOT, S. E. HUG, AND N. LISI, "Terahertz waveguide components fabricated using 3-D X-ray microfabrication technique," *Electronic letters*, vol. 32, pp. 1794-1795, Sep 1996.
- [71] C. E. COLLINS, J. W. DIGBY, R. D. POLLARD, R.E. MILES, G. M. PARKHURST, J.M. CHAMBERLAIN, D. P. STEENSON, N. J. CRONIN, L. S. KARATZAS, AND J. W. BOWEN, "W-band measurement of 100 μ m height micro-machined air-filled rectangular waveguide," *IEEE MTT-S International, Microwave Symposium Digest*, vol. 3, pp. 1439-1442, Jun1997.
- [72] C. E. COLLINS, R. E. MILES, J. W. DIGBY, G. M. PARKHURST, R. D. POLLARD, J. M. CHAMBERLAIN, D. P. STEENSON, N. J. CRONIN, S. R. DAVIES, AND J. W. BOWEN, "A new micro-machined millimeter-wave and terahertz snaptogether

- rectangular waveguide technology," *IEEE Microwave and Guided Wave Letters*, vol. 9, pp.63-65, Feb. 1999.
- [73] K. K. MA, T. D. DRYSDALE, AND R. S. CUMMING, "A novel silicon micromachining process for sub-millimeter rectangular waveguide fabrication," *Proceeding of SPIE*, vol. 4407, pp. 372-379, 2001.
- [74] G. T. A. KOVACS, N. I. MALUF, AND K. E. PETERSEN, "Bulk Micromachining of Silicon," *Proceedings of the IEEE*, vol.86, pp. 1536-1551, Aug 2002.
- [75] S. BIBER, J. SCHUR, A. HOFMANN, L. P. SCHMIDT, "Design of New Passive THz Devices Based on Micromachining Techniques," *IEEE 5th International Kharkov Symposium, Physics and Engineering of Microwaves, Millimeter, and Submillimeter Waves*, vol. 1, pp. 26-31, Oct 2004.
- [76] Y. LEE, J. P. BECKER, J. R. EAST, L. P. B. KATEHI, "Fully Micromachined Finite-Ground Coplanar Line-to-Waveguide Transitions for W-band Applications," *IEEE Transactions on microwave theory and techniques*, vol. 52, pp. 1001-1007, March 2004.
- [77] M. VAHIDPOUR, K. SARABANDI, "Fabrication and performance evaluation of micromachined cavity-backed co-planar waveguide to rectangular waveguide transition at Y-band frequencies," *IEEE Antennas and Propagation Society International Symposium*, pp. 1-4, July 2010.
- [78] N. I. DIB, R. F. DRAYTON, AND L. P. B. KATEHI, "A theoretical and experimental study of microshield circuit components," *journal of Microwave and Optical Technol. Lett.* vol. 6, pp. 333-339, 1993.
- [79] N. YUAN, C. RUAN, AND W. LIN, "Analytical analysis of v, elliptic, and circular-shaped microshield transmission lines," *IEEE Trans. on Microwave Theory and Techniques*, vol. 42, no.5, pp. 855-859, May 1994.

- [80] M. HELAL, J. F. LEGIER, P. PRIBETICH, AND P. KENNIS, "Analysis of planar transmission lines and microshield lines with arbitrary metallization cross sections using finite elements method," *IEEE MTT-S International, Microwave Symposium Digest*, vol. 2, pp. 1041-1044, 1994.
- [81] T. M. WELLER, L.P. B. KATEHI, AND G.M.REBEIZ, "High performance microshield line components," *IEEE Trans. on Microwave Theory and Techniques*, vol. 43, no.3, March 1995.
- [82] T. M. WELLER, L.P. B. KATEHI, AND G.M.REBEIZ, "A 250-GHz microshield bandpass filter," *Microwave and Guided Wave Letters*, vol. 5, Issue.5, pp.153-155, May 1995.
- [83] S. V. ROBERTSON, L.P. B. KATEHI, AND G.M.REBEIZ, "Micromachined W-Band Filters," *IEEE Trans. on Microwave Theory and Techniques*, vol. 44, no.4, April. 1996.
- [84] O. DUPUIS, J. CARBONELL, P. MOUNAIX, O. VANBESIEN, AND D. LIPPENS, "High Speed-Low Loss Micromachined Coplanar Waveguides in GaAs Technology," *IEEE Microwave Conference, 28th European*, vol. 1, pp. 695-700, Oct 1998.
- [85] V. K. VARADAN, K. J. VINOY, AND K. A. JOES, *RF MEMS and Their Applications*, pp.318, New York, John Wiley and sons, 2002.
- [86] H. ROSKOS, M. NUSS, K. GOOSSEN, D. KISKER, A. WHITE, K. SHORT, D. JACOBSON, AND J. M. POATE, "Propagation of picosecond electrical pulses on a silicon-based microstrip line with buried cobalt silicide ground plane," *Applied Physics Letters*, pp. 2604-2606, vol. 58, Jun. 1991.
- [87] F. SCHNIEDER, AND W. HEINRICH, "Model of Thin-Film microstrip Line for Circuit Design," *IEEE Transactions on microwave theory and techniques*, vol. 49, no. 1, pp. 104-110, Jan 2001.

- [88] F. SCHNIEDER, AND W. HEINRICH, "Thin-film microstrip lines and coplanar waveguides on semiconductor substrates for sub-mm wave frequencies," *Journal of Frequenze*, vol. 59, no. 5-6, 2005.
- [89] K. HETTAK, G. A. MORIN, AND M. G. STUBBS, "The Integration of Thin-Film microstrip and Coplanar Rechnologies for Reduced Size MMICs," *IEEE Transactions on microwave theory and techniques*, vol. 53, no. 1, pp. 283-289, Jan 2005.
- [90] G. SIX, G. PRIGENT, R. ERIC G. DAMBRINE, AND H. HAPPY, "Fabrication and Characterization of Low-loss TFMS on Silicon Substrate up to 220GHz," *IEEE Transactions on microwave theory and techniques*, vol. 53, no. 1, pp. 301-305, Jan 2005.
- [91] J. MAENG, J. NAMCHEOL, S. SANGSUB, AND S. KWANGSEOK, "W-Band Cross-Coupled Filters and a Duplexer on a Thin-Film Substrate for Low-Cost Front-End Integration," *Electronic Components and Technology Conference, ECTC*, pp. 1594-1598, May 2009.
- [92] H. KAMITSUNA, "A very small, low loss MMIC rat-rate hybrid using elevated coplanar waveguides," *IEEE Microwave Guided Wave Lett.*, vol. 2, no. 8, pp. 337-339, Aug 1992.
- [93] U. BHATTACHARYA, S. T. ALLEN, AND M. J.W. RODWELL, "DC- 725 GHz sampling circuits and subpicosecond nonlinear transmission lines using elevated coplanar waveguide," *IEEE Microwave Guided Wave Lett.*, vol. 5, pp. 50-52, Feb 1995.
- [94] F. SCHNIEDER, R. DOERNER, AND W. HEINRICH, "High impedance coplanar waveguides with low attenuation," *IEEE Microwave Guided Wave Lett.*, vol. 6, pp. 117-119, Mar 1996.

- [95] H. T. KIM, S. JUNG, J.H PARK, C.W. BAEK, Y. K. KIM AND Y. KWON, "A new micromachined overlap CPW structure with low attenuation over wide impedance ranges," *IEEE Transactions on microwave theory and techniques*, vol. 49, no. 9. 2001
- [96] K. HETTAK, R. AMAYA, AND G. MORIN, "A novel compact three-dimensional CMOS branch-line coupler using the meandering ECPW, TFMS, and buried micro coaxial technologies at 60 GHz," *Microwave Symposium Digest (MTT), 2010 IEEE MTT-S International*, pp. 1576-1579, July. 2010.
- [97] J. ZEHENTNER, AND J. MACHAC, " Properties of CPW In The Sub-mm Wave range and Its Potential To Radiate," *IEEE MTT-S International Microwave Symposium Digest*, vol.2, pp. 1061 - 1064, 2000
- [98] K. C. GUPTA, R. GRAG AND I. J. BAHL, *Microstrip Lines and Slotlines*, Dedham, MA : Artech House, 1979.
- [99] G. GHIONE AND C. NALDI, "Coplanar Waveguides for MMIC applications: Effect of Upper Shielding, Conductor Backing, Finite-Extent Ground Planes, and Line-to Line Coupling," *IEEE Trans. On Microwave Theory and Techniques*, Vvol.35, pp.260-267, March 1987.
- [100] C. VEYRES, AND V. F. HANNA, "Extensions of the Application of Conformal Mapping Techniques to Co Planar Lines with Finite Dimensions" *Int. J. Electron*, vol. 48, pp. 47-56, 1980.
- [101] C. N. CHEN, Y. WONG AND C. H. CHEN, "Hybrid Quasi static Analysis for Multilayer Coplanar Lines," *IEE Proceedings-H*, pp. 307-312, Aug. 1991.
- [102] S. S. BEDAIR AND I. WOLFF, "Fast, Accurate and Simple Approximate Analytic Formulas for Calculating the Parameters of supported Coplanar Waveguides",

- IEEE Trans. On Microwave Theory and Techniques*, vol. MTT-40, pp. 41 - 48, 1992.
- [103] D. ROW AND B. LAO, "Numerical Analysis of Shielded Coplanar Waveguides," *IEEE Trans. On Microwave Theory and Techniques*, pp. 911-915, Nov. 1983.
- [104] D. MARCUSE, "Electrostatic Field of Coplanar Lines Computed with the Point Matching Method," *IEEE J. Of Quantum Electronics*, pp. 939-947, May 1989.
- [105] F. ALESSANDRI, U. GOEBEL, F. MELAI AND R. SORRENTINO, "Teoretical and Experimental Characterization of Nonsymmetrically Shielded Coplanar Waveguides for Millimeter-Wave Circuits," *IEEE Trans. On Microwave Theory and Techniques*, pp. 2020-2026, Dec. 1989.
- [106] C. N. CHEN, Y. WONG AND C. H. CHEN, "Hybrid Quasistatic Analysis for Multilayer Coplanar Lines," *IEE Proceedings-H*, pp. 307-312, Aug. 1991.
- [107] J. KNORR AND K. KUCHLER, "Analysis of Coupled Slots and Coplanar Strips on Dielectric Substrate," *IEEE Trans. On Microwave Theory and Techniques*, pp. 541-548, July 1975.
- [108] Y. FUJIKI, M. SUZUKI, T. KITAZAWA, AND Y. HAYASHI, "Higher Order Modes in Coplanar-Type Transmission Lines," *Electronics and Communications in Japan*, no. 2, pp. 47-81, 1975.
- [109] J. DAVIES AND D. MIRSHKAR-SYAHKAL, "Spectral Domain Solution of Arbitrary Coplanar Transmission Line with Multilayer Substrate," *IEEE Trans. On Microwave Theory and Techniques*, pp. 538-540, June 1982.
- [110] G. HASNAIN, A. DEINES AND J. WHINNERY, "Dispersion of Picosecond Pulses in Coplanar Transmission Lines," *IEEE Trans. On Microwave Theory and Techniques*, pp. 738-741, June 1986.

- [111] C. NGUYEN, *Analysis methods for RF, Microwave, and millimetre-wave planar transmission line structures*, Texas A&M university, John Wiley and sons, 2000.
- [112] G. GHIONE AND C. NALDI, "Parameters of Coplanar Waveguides with lower Ground Plane," *Electronics Letters*, vol.19, pp. 734-735, 1983.
- [113] CH. BOWICK. J. BLYLER, AND C. AJLUNI, *RF Circuit Design*, pp. 2, Oxford, Elsevier, 2nd edition, 2007.
- [114] R. N. SIMONS, *Coplanar Waveguide Circuits, Components, and Systems*, pp. 206, John Wiley and sons, 2001.
- [115] *ibid.* 98, pp. 416
- [116] R. W. JACKSON, "Considerations in the use of coplanar waveguide for millimetre-wave integrated circuits," *IEEE Transactions on microwave theory and techniques*, vol. MTT-34, no. 12, 1986
- [117] R.W. JACKSON, "Mode conversion at discontinuities in finite-width conductor backed coplanar waveguide," *IEEE Trans. Microwave Theory & Techniques*, vol. 37, no. 10, pp. 1582-1589, 1989.
- [118] M. RIAZIAT, R. MAJIDI-AHY AND I. J. FENG, "Propagation modes and dispersion characteristics of coplanar waveguides," *IEEE Transactions on microwave theory and techniques*, vol. 38, no. 3, 1990.
- [119] *ibid.* 98, pp. 425
- [120] W. R. DEAL, S. DIN, J. PADILLA, V. RADISIC, G. MEI, W. YOSHIDA, P. S. LIU, J. UYEDA, M. BARSKY, T. GAIER, A. SAMOSKA, A. LORENE, AND R. LAI, "Demonstration of a sub-millimeter wave integrated circuit (S-MMIC) using InP HEMT with a 35-nm gate," in *Compound Semiconductor IC Symp.*, pp. 33-6, Nov 2006.

- [121] J. CAPWELL, T. WELLER, D. MARKELL AND L. DUNLEAVY, "Automation and Real-time Verification of Passive Component S-Parameter Measurements Using Loss factor Calculation," *Microwave Journal*, vol. 47, no. 3, pp. 82-90, 2004.
- [122] F. BRAUCHLER, S. ROBERTSON, J. EAST, L. P. B. KATEHI, "W-band finite ground coplanar (FGC) line circuit elements," *IEEE Intl. Microwave Symp.*, *San Francisco, CA*, pp. 1845-8, Jun. 1996
- [123] G. HAMMER, S. WUENSCH, M. ROESCH, K. IL'IN AND M. SIEGEL, "Quarter Wavelength Resonators With Ultra High Quality Factor," *2nd Superconducting Resonator Workshop, Utrecht, NL*. 2008.
- [124] K. BEILENHOF, H. KLINGBEIL, W. HEINRICH, H. L. HARTNAGEL, "Open and short circuits in coplanar MMICs," *IEEE Transactions on microwave theory and techniques*, vol.41, no.9, pp. 1534-1537, Sep 1993.
- [125] G. MATTHAEI, L. YOUNG, AND E. M. T. JONES, *Microwave Filters, Impedance-Matching Network, and Coupling Structures*, Artech House, 2nd edition, 1964.
- [126] *ibid.* 114, pp. 206
- [127] S. THOMS AND D. MACINTYRE, "Electron beam lithography course," 2010. [Online]. Available: <http://www.elec.gla.ac.uk/jwnc/ebeam docs>.
- [128] R. PETHRICK AND K. RANKIN, "Criteria for uniform thin film formation for polymeric materials," *Journal of Materials Science: Materials in Electronics*, vol. 10, no. 2, 141-144, 1999.
- [129] *ibid.* 127, pp. 8
- [130] S. THOMS, "Belle documentation," 2007. [Online]. Available: <http://www.elec.gla.ac.uk/jwnc/vb6docs>.

- [131] K. ELGAID, *A Ka-Band GaAs MESFET monolithic downconverter*, PhD thesis, University of Glasgow, 1998.
- [132] AZ 4500 Series Thick Film Photoresists ,2011. [online] Available: http://www.first.ethz.ch/infrastructure/Chemicals/Photolithography/Data_AZ4500.pdf
- [133] S. H. JEONG, S. J. YOON, J. G. YOON, S. G. LEE, AND Y. J. KIM, "Elevated-CPW for high-speed digital interconnects," *Antennas and Propagation Society International Symposium. IEEE*, vol.3, pp. 541 - 544, July 2001.
- [134] S. HOFSCHEIN, I. WOLFF, "Simulation of an elevated coplanar waveguide using 2-D FDTD," *IEEE Microwave and guided wave letters*, vol. 6, PP. 28 - 30 , Jan. 1996.
- [135] G. GHIONE, M. GOANA, G. L. MADONNA, G. OMEGNA, M. PIROLA, S. BOSSO, D. FRASSATI, AND A. PERASSO, "Microwave modeling and characterization of thick coplanar waveguides on oxide-coated lithium niobate substrates for electrooptical applications," *IEEE Transactions on microwave theory and techniques*, vol. 47, no. 12, pp. 2287–2293, Dec. 2002.
- [136] G. GHIONE AND M. GOANA, "Revisiting the partial-capacitance approach to the analysis of coplanar transmission lines on multilayered substrates," *IEEE Transactions on microwave theory and techniques*, vol. 51, no. 9, pp. 2007–2014, Sep. 2003.
- [137] I. MCGREGOR, F. AGHAMORADI, AND K. ELGAID, "An approximate analytical model for the quasi-static parameters of elevated CPW line," *IEEE Transactions on microwave theory and techniques*, vol. 58, pp. 3809-3814, 2010.

- [138] W. HILBERG, "From approximations to exact relations for characteristic impedances," *IEEE Transactions on microwave theory and techniques*, vol. MTT-17, no. 5, pp. 259–265, May 1969.
- [139] W. R. EISENSTADT, Y. EO, "S-parameter-based IC interconnect transmission line characterization," *IEEE Transactions on components, Hybrids, and manufacturing technology*, vol. 15, 06 Aug 2002.
- [140] N. I. DIB, G. E. PONCHAK, AND L. P. B. KATEHI, "A theoretical and experimental study of coplanar waveguide shunt stubs," *IEEE Transactions on microwave theory and techniques*, vol. 41, no. 1, Jan 1993.
- [141] C.Y. LEE, Y. LIU, AND T. ITOH, "The effect of the coupled slotline mode and air-bridges on CPW and NLC waveguide discontinuities," *IEEE Transactions on microwave theory and techniques*, vol. 43, no. 12, Dec 1995.
- [142] F. AGHAMORADI, I. MCGREGOR, S. ROY, AND K. ELGAID, "Low-Loss Grounded Elevated Coplanar Waveguide for Sub-Millimeter wave MMIC Applications," *Progress in Electromagnetic Research Journal, PIER B*, vol. 34, pp. 103-123, 2011.
- [143] W.C. TANG, AND Y.L. CHOW, "CAD formulas and their inverses for microstrip, CPW and conductor-backed CPW, by successive synthetic asymptotes," *Antennas and Propagation Society International Symposium*, vol.3, pp.394-397, 2001.
- [144] W. H. CHANG, "Analytic IC-metal-line capacitance formulas," *IEEE Trans. Microwave Theory Tech.*, vol. MTT-24, pp. 608-611, 1976, also vol. MTT-25, p. 712, 1977.

- [145] T. HIROTA, Y. TARUSAWA, AND H. OGAWA, "Uniplanar MMIC Hybrid-A Proposed New MMIC Structure," *IEEE Trans. Microwave Theory Tech.*, vol. 35, pp. 576-581, Jun 1987.
- [146] M. HOUDART AND C. AURY, "Various Excitations of Coplanar Waveguide," *IEEE MTT-S International Microwave Symposium Digest*, pp. 116-119, 1979.